

**Molecular Mechanisms during**  
**Amplification of Chirality in Organometallic Systems:**  
***In Situ* Studies by X-ray Absorption Spectroscopy**

A thesis submitted to the University of Manchester for the degree of Doctor of  
Philosophy in the Faculty of Engineering and Physical Sciences.

**2010**

**Luanga Nforba Nchari**

School of Chemical Engineering and Analytical Science  
The University of Manchester

## Table of Contents

<b>LIST OF FIGURES .....</b>	<b>5</b>
<b>LIST OF TABLES .....</b>	<b>11</b>
<b>LIST OF ABBREVIATIONS.....</b>	<b>12</b>
<b>ABSTRACT .....</b>	<b>13</b>
<b>DECLARATION.....</b>	<b>14</b>
<b>ACKNOWLEDGEMENTS.....</b>	<b>15</b>
<b>1. INTRODUCTION.....</b>	<b>17</b>
1.1 ENANTIOMERS AND CHIRAL MOLECULES .....	17
1.2 ENANTIOMERISM: THE DISCOVERY.....	21
1.3 THE BIOLOGICAL IMPORTANCE OF CHIRALITY.....	22
1.4 THE PHYSICAL PROPERTIES OF STEREOISOMERS .....	24
1.5 CHEMICAL PROPERTIES OF ENANTIOMERS.....	27
1.6 METHODS OF OBTAINING OPTICALLY ACTIVE COMPOUNDS .....	28
1.6.1 <i>The Chiral Pool</i> .....	30
1.6.2 <i>Separation of enantiomers</i> .....	31
1.6.3 <i>Resolution by chromatography on chiral materials</i> .....	34
<i>R enantiomer reaches the</i> .....	34
1.6.4 <i>Asymmetric synthesis</i> .....	35
<b>2. ASYMMETRIC AUTOCATALYSIS .....</b>	<b>36</b>
2.1 NONLINEAR EFFECTS IN ASYMMETRICAL STEREOSELECTIVE REACTIONS .....	37
2.1.1 <i>The Frank Model</i> .....	38
2.1.2 <i>The Kagan Model</i> .....	41
2.1.3 <i>The Noyori Model</i> .....	44
2.2 THE SOAI AUTOCATALYTIC REACTION.....	46
2.2.1 <i>Introduction</i> .....	46
2.2.2 <i>Discovery and development of highly enantioselective asymmetric autocatalysis</i> .....	48
<b>3. MECHANISTIC APPROACHES TO UNDERSTANDING THE SOAI AUTOCATALYTIC REACTION.....</b>	<b>52</b>
3.1 THE BLACKMOND MODEL .....	52
3.1.1 <i>Dimer Model</i> .....	52
3.1.2 <i>Tetramer</i> .....	64
3.2 THE SOAI MODEL .....	65
3.3 THE BUHSE MODEL .....	70
3.4 THE BROWN MODEL.....	73

3.5	RESEARCH OBJECTIVE.....	84
<b>4.</b>	<b>EXPERIMENTAL .....</b>	<b>86</b>
4.1	X-RAY ABSORPTION SPECTROSCOPY (XAS).....	86
4.1.1	<i>Principles of X-ray absorption spectroscopy.....</i>	86
4.1.2	<i>XANES and EXAFS.....</i>	88
4.1.3	<i>Physical principles.....</i>	90
4.1.4	<i>EXAFS equation.....</i>	91
4.1.5	<i>Data analysis .....</i>	91
4.2	MINIATURIZED CONTINUOUS FLOW REACTION VESSELS.....	96
4.2.1	<i>Introduction .....</i>	96
4.2.2	<i>Fabrication of microreactors.....</i>	97
4.2.3	<i>Microfluidic handling and effects of downsizing .....</i>	98
4.3	XAFS MEASUREMENT EXPERIMENTAL SET UP .....	100
4.3.1	<i>The influence of ambient conditions on XAFS study of dialkylzinc .....</i>	
4.3.2	<i>Non-flow Reactor for XAFS Studies of Organometallic Reactions.....</i>	
4.3.3	<i>Continuous flow Reactor for XAFS Studies of Organometallic Reactions .....</i>	108
4.3.4	<i>Continuous Tubular Reactor for XAFS Studies of Organometallic Reactions: Possibilities and Limitations for Studies of the Soai Reaction.....</i>	109
4.4	UV MEASUREMENTS .....	116
<b>5.</b>	<b>THE INFLUENCE OF SOLVENTS ON ASYMMETRIC AMPLIFICATION .....</b>	<b>120</b>
5.1	INTRODUCTION .....	120
5.2	EXPERIMENTAL.....	123
5.3	RESULTS AND DISCUSSION.....	124
5.3.1	<i>i-Pr<sub>2</sub>Zn in toluene and THF .....</i>	124
5.3.2	<i>Diethylzinc in different THF/toluene ratios .....</i>	132
5.3.3	<i>Diethylzinc in THF at different concentrations .....</i>	136
5.3.4	<i>Concentration versus solvent ratio of diethylzinc.....</i>	138
5.3.5	<i>Interaction of dialkylzincs with different solvent .....</i>	140
5.3.6	<i>Comparing diethylzinc in THF and toluene at ESRF, ANKA and APS .....</i>	141
5.3.7	<i>Comparing the XANES of diethyl-, dimethyl- and diisopropylzinc.....</i>	143
5.3.8	<i>EXAFS analysis of diethylzinc in solvents .....</i>	145
5.3.9	<i>Kinetic simulation studies of diethylzinc in solvents.....</i>	152
5.4	CONCLUSION.....	154
<b>6.</b>	<b>CHARACTERISATION OF A LIGAND AND ALKYLZINC COMPLEX .....</b>	<b>156</b>
6.1	INTRODUCTION .....	156
6.2	EXPERIMENTAL.....	159
6.3	RESULTS AND DISCUSSION .....	159

6.3.1	<i>i-Pr<sub>2</sub>Zn and 2-Butanol</i> .....	159
6.3.2	<i>Et<sub>2</sub>Zn and DMAE</i> .....	163
6.4	CONCLUSION.....	169
<b>7.</b>	<b>CHARACTERISATION OF THE ALKYLATION OF ALDEHYDES .....</b>	<b>171</b>
7.1	INTRODUCTION .....	171
7.2	EXPERIMENTAL.....	173
7.3	RESULTS AND DISCUSSION .....	173
7.3.1	<i>i-Pr<sub>2</sub>Zn and Benzaldehyde</i> .....	173
7.3.2	<i>i-Pr<sub>2</sub>Zn and pyrimidyl aldehyde</i> .....	175
7.3.3	<i>Et<sub>2</sub>Zn and pyrimidyl aldehyde</i> .....	185
7.3.4	<i>Et<sub>2</sub>Zn, DMAE and cinnamaldehyde</i> .....	192
7.3.5	<i>Characterisation of dimer species formed in the Soai reaction</i> .....	198
7.4	CONCLUSION.....	204
<b>8.</b>	<b>ADDITIONAL WORK.....</b>	<b>207</b>
8.1	EXPERIMENTAL .....	207
8.2	RESULTS AND DISCUSSION .....	210
8.2.1	<i>Alkylating agents</i> .....	210
8.2.2	<i>Solvent effect</i> .....	211
8.2.3	<i>Ethylation with paracyclophane based and dimethylaminoethanol ligands</i> .....	213
8.2.4	<i>Diethylzinc addition to Imines</i> .....	215
8.2.5	<i>EXAFS Refinement of ANKA data</i> .....	217
8.3	CONCLUSION.....	217
<b>9.</b>	<b>SUMMARY.....</b>	<b>220</b>
<b>10.</b>	<b>FUTURE WORK .....</b>	<b>224</b>
<b>11.</b>	<b>PEER REVIEWED WORK .....</b>	<b>226</b>
<b>12.</b>	<b>REFERENCES .....</b>	<b>227</b>

## List of figures

Figure 1.1: Soai autocatalytic reaction <sup>[1]</sup> .....	17
Figure 1.2: Subdivision of isomers. <sup>[3]</sup> .....	19
Figure 1.3: (a) Models of 2-Butanol enantiomers. (b) Non superimposable models .....	20
Figure 1.4: Relationship of enantiomers.....	21
Figure 1.5 Chiral forms of Thalidomide .....	23
Figure 1.6: Chiral forms of Limonene in Lemon and Orange .....	24
Figure 1.7 S-Stereoconfiguration of alanine <sup>[11]</sup> .....	25
Figure 1.8 Schematic of a polarimeter.....	26
Figure 1.9: Schematic of polarimeter <sup>[13]</sup> .....	26
Figure 1.10: (S)-Ibuprofen (left), antiinflammatory and (R)-Fluoxetine (right), antidepressant. <sup>[13]</sup> ...	27
Figure 1.11: Structure and shape of hexachloroethane (left) and cyclooctane (right). <sup>[13]</sup> .....	28
Figure 1.12: Methods of producing optically active compounds. <sup>[8]</sup> .....	30
Figure 1.13 Preparation of $\alpha$ – Methyl-L-Dopa <sup>[9]</sup> .....	32
Figure 1.14: Epoxidation reaction of only one enantiomer <sup>[9]</sup> .....	33
Figure 1.15: Separation of enantiomers by chromatography. <sup>[15]</sup> .....	34
Figure 1.16: Asymmetric synthesis scheme.....	35
Figure 2.1: Non-linear effects with partially resolved chiral auxiliaries <sup>[17]</sup> .....	37
Figure 2.2: Sketch of general form of solutions of equations 2.2 and 2.3 <sup>[16]</sup> .....	40
Figure 2.3: Outline of Kagan $ML_2$ mechanism .....	41
Figure 2.4: Illustration of the mechanism developed by Noyori et al to explain amplification of ee...	45
Figure 2.5: An example of the Soai autocatalytic reaction <sup>[1]</sup> .....	47
Figure 2.6: Dialkylzinc addition to aldehydes using chiral catalysts. <sup>[22]</sup> .....	48
Figure 2.7 Enantioselective addition of dialkylzincs to pyridine aldehydes. <sup>[22]</sup> .....	49
Figure 2.8: Enantioselective alkylation of pyrimidine aldehyde <sup>[22]</sup> .....	50
Figure 2.9: Practically perfect asymmetric autocatalysis in which the product is used as the asymmetric autocatalyst for the next run. <sup>[22]</sup> .....	50
Figure 2.10: Consecutive asymmetric autocatalysis of (S)-16 with amplification of enantiomeric excess. <sup>[22]</sup> .....	51
Figure 3.1: Reaction heat flow against time of differing enantiomeric excess: 97%, 43% and 0% <sup>[42]</sup>	53
Figure 3.2: Simplified Kagan and Noyori mechanisms. <sup>[43]</sup> .....	54
Figure 3.3: Amplification of enantiomeric excess in a 1 molar solution of S and R monomers through RS heterodimer formation (Noyori model). The lines represent increasing values of the equilibrium constant $K_{hetero}$ for heterodimer formation (see inset for values of $K_{hetero}$ ). .....	56
Figure 3.4 : Blackmond's proposed active metal catalyst. <sup>[42]</sup> .....	61
Figure 3.5: Formation of dimer species from monomeric alkoxides. <sup>[45]</sup> .....	62
Figure 3.6: Experimental kinetic data and dimer model calculations for reactions at 22% and 6% initial ee Initial concentrations $[A] = 0.2M$ ; $[Z] = 0.4M$ ; catalyst 10%. <sup>[44]</sup> .....	62

Figure 3.7: Blackmond's dimer model. <sup>[44]</sup> .....	63
Figure 3.8: Reaction rate as a function of aldehyde. Blue circles: Experimental data; dash black line: Equation 3.1; solid pink line: Equation 3.2. <sup>[40]</sup> .....	64
Figure 3.9: Aldehyde- $iPr_2Zn$ complex <sup>[40]</sup> .....	65
Figure 3.10: Scheme proposed by Soai and coworkers <sup>[19]</sup> .....	65
Figure 3.11: Comparison of simulation (solid lines) with experimental points. $T = 273K$ ; $A_0 = 2.08 \times 10^{-2} M$ ; $Z_0 = 3.13 \times 10^{-2} M$ ; $P_0 = 2.08 \times 10^{-4} M$ . Broken line represents simulation assuming a first-order autocatalytic reaction. <sup>[19]</sup> .....	67
Figure 3.12: Model proposed by Soai and coworkers. <sup>[32]</sup> .....	68
Figure 3.13: Comparison of simulation [yield: broken line; ee: solid line] with experimental points [yield: hollow circles; ee: filled circle] on asymmetric autocatalysis with initial ee of 59.4% at $-25^\circ C$ . <sup>[32]</sup> .....	70
Figure 3.14: Proposed kinetic model. $k$ : rate constant <sup>[47]</sup> .....	71
Figure 3.15: Frank model. <sup>[48]</sup> .....	72
Figure 3.16: Noyori model. <sup>[48]</sup> .....	72
Figure 3.17: Kagan model <sup>[48]</sup> .....	73
Figure 3.18: Fundamentals of Noyori and Kitamura model <sup>[51]</sup> .....	74
Figure 3.19: Double resonance from homochiral to heterochiral <sup>[51]</sup> .....	75
Figure 3.20: Proposed square planar homo- and hetero- dimer <sup>[50]</sup> .....	76
Figure 3.21: Dynamic exchange between homo- and hetero- dimer a) A: Observed B: Calculated b) Arrhenius plot. Half life approx. 14s at 293 K. <sup>[51]</sup> .....	77
Figure 3.22: Chemical shift of binding of diisopropylzinc to pyrimidine aldehyde. <sup>[51]</sup> .....	78
Figure 3.23: Enthalpy of binding $ZnMe_2$ to pyrimidine aldehyde (Units: kcal/mol). N- preferred over O- complexation. <sup>[51]</sup> .....	79
Figure 3.24: Closed cyclic dimers derived by DFT. <sup>[51]</sup> .....	80
Figure 3.25: DFT calculated ground state conformations (preferred) of $iPr_2Zn$ derived homo- (Ar, Ar' syn) and hetero- (Ar, Ar' anti) dimers. <sup>[51, 52]</sup> .....	81
Figure 3.26: (a) Four closed tetramers with alkyl substituents removed; (b) Space filling model of cube and square-capped macrocycle (both homochiral). <sup>[51, 52]</sup> .....	82
Figure 4.1: Illustration of X-ray absorption process in an atom <sup>[55]</sup> .....	86
Figure 4.2: Spectrum of photon energy in wavelength and frequency <sup>[55]</sup> .....	87
Figure 4.3: Plot of XANES and EXAFS region. <sup>[54]</sup> .....	89
Figure 4.4: (a) Photoelectric effect in terms of excitation of different orbital or different energy levels. (b) Illustration of neighbouring shells of atoms about the absorber. Interference between outgoing photoelectron wave and backscattered off neighbouring atoms shell. <sup>[56]</sup> .....	90
Figure 4.5: a) Pt edge fluorescence data for Pt complex. The $\mu_{vic}$ function better represents the 'fall off' of the atomic background absorption $\mu_0$ with increasing energy than $\mu_{spline}$ . b) Transmission L edge data showing that $\mu_{spline}$ can be a good approximation to $\mu_{vic}$ and $\mu_0$ . <sup>[59]</sup> .....	94

Figure 4.6: Radial distribution function after Fourier transformation of Pt foil. Absolute (full line) and imaginary (- - -). <sup>[56]</sup>	95
Figure 4.7: Photolithographic fabrication of channel networks in glass. <sup>[67]</sup>	97
Figure 4.8: (a) Microreactors used in chemical synthesis; (b) dependence of the product yields from the reaction time. <sup>[63]</sup>	99
Figure 4.9: Schematic of XAS experiment <sup>[69]</sup>	101
Figure 4.10: Optics and detectors <sup>[69]</sup>	101
Figure 4.11: XANES spectra of dialkylzincs in toluene and water.	102
Figure 4.12: Zinc K-edge EXAFS spectra of decomposed Et <sub>2</sub> Zn exposed to air. Fit with zinc hydroxide coordination numbers fixed. Dash lines are the experimental data and the solid lines are the best theoretical fit.	104
Figure 4.13: Zinc K edge EXAFS spectra of decomposed Et <sub>2</sub> Zn exposed to air. Fit with zinc oxide coordination numbers fixed. Dotted lines are the experimental data and the solid lines are the best theoretical fit.	105
Figure 4.14: XANES spectra of 0.1 M Et <sub>2</sub> Zn in non-flow reactor (microcentrifuge) over 2 days	107
Figure 4.15: Testing the continuous flow Al reactor with colour dyes.	108
Figure 4.16: Schematic arrangement of the PTFE tubular flow reactor mounted on a heatable Al frame; also shown are representative in situ Zn K-edge FY XANES data taken at positions A1, D2 and C4 during the Soai reaction with a 1:1 volume mixture of 0.1 mol L <sup>-1</sup> diisopropylzinc and pyrimidyl aldehyde solutions.	110
Figure 4.17: Tubular flow reactor assembled at station 9.3, SRS Daresbury, UK.	110
Figure 4.18: Electron microscopy and EDX analysis of the organozinc wall deposit on the inside of the PTFE reactor tube.	112
Figure 4.19: In situ transmission XANES (BM29, ESRF) obtained in microcentrifuge tubes. From top to bottom: Zn K-edge XANES spectra of a toluene solution containing 0.1 M diisopropylzinc; the supernatant of a solution formed by reacting 0.1 M diisopropylzinc and 0.1 M pyrimidine aldehyde in toluene; the sediment formed in this solution; a toluene solution containing 0.1 M diisopropylzinc and 2 M pyrimidine aldehyde; the spectrum labelled C4 in figure 1 (measured at the SRS); a spectrum of ZnO.	114
Figure 4.20: Overview of '5 cuvette' platform, (a) camera, (b) flow cuvettes in aluminium frame, (c) collimating lens, (d) monochromator & light source, (e and f) syringe pump dosing system with stock solutions and (g) control PC. <sup>[73]</sup>	117
Figure 4.21: Aluminium frame containing cuvettes <sup>[73]</sup>	118
Figure 4.22: Image of monochromatic light through five sample cells <sup>[73]</sup>	118
Figure 4.23: Determination of light intensity through sample cells at a range of wavelengths by image analysis software. <sup>[73]</sup>	119
Figure 5.1: Product ee against initial catalyst ee in toluene, diethylether, Et <sub>2</sub> O/toluene and THF. <sup>[45]</sup>	121
Figure 5.2: Zn K-edge XANES spectra of 0.1 M i-Pr <sub>2</sub> Zn in toluene, THF and toluene/THF (1:1)...	125

Figure 5.3: Zn K-edge EXAFS spectra and FT of <i>i</i> -Pr <sub>2</sub> Zn in toluene. Dash lines: Experimental data and solid lines: best theoretical fit. ....	126
Figure 5.4: Zn K-edge EXAFS spectra and FT of <i>i</i> -Pr <sub>2</sub> Zn in toluene and THF. Dash lines: experimental data and solid lines: best theoretical fit. ....	127
Figure 5.5: Models of <i>i</i> Pr <sub>2</sub> Zn in toluene and THF from EXAFS calculations .....	129
Figure 5.6: Ligand field splitting of Zn <sup>2+</sup> 4p orbitals as a function of site geometry. <sup>[79]</sup> .....	131
Figure 5.7: XANES spectra of 0.1M DEZ at different THF/toluene ratios .....	133
Figure 5.8: XANES spectra of 0.1 M DEZ in toluene and THF. Calculated XANES in 1:1 (toluene:THF) included .....	134
Figure 5.9: Comparing the experimental and fitted XANES of 0.1 M Et <sub>2</sub> Zn at different THF/toluene ratios (vol %). ....	135
Figure 5.10: XANES spectra of DEZ in THF at different concentrations.....	137
Figure 5.11: XANES spectra of DEZ in THF/toluene mixture at different concentrations.....	139
Figure 5.12: XANES spectra of 0.1 M dialkylzincs in THF, toluene and water.....	140
Figure 5.13: Comparing the dipole moment of water, THF, diethyl ether and toluene. ....	141
Figure 5.14: Comparing the XANES spectra of 0.1M DEZ obtained at different synchrotrons. ....	142
Figure 5.15: Zn K-edge spectra of 0.1 M dimethyl-, diethyl and diisoproylzinc in toluene.....	144
Figure 5.16: Zinc K edge EXAFS spectra of Et <sub>2</sub> Zn in Toluene. Dotted lines are the experimental data and the solid lines are the best theoretical fit.....	145
Figure 5.17: Model of diethyl zinc in toluene from EXAFS calculations. ....	147
Figure 5.18: EXAFS fits of diethylzinc in THF (a) linear (b) dimer and (c) tetramer. ....	148
Figure 5.19: Structural calculated model of diethylzinc in THF (Dimer model). ....	149
Figure 5.20: Structural calculated model of diethylzinc in THF (Tetramer model). ....	150
Figure 5.21: Kinetic simulation of DEZ, solvent and the complex. Initial concentration 0.1mol/l....	153
Figure 6.1: Catalytic cycle proposed by Noyori. <sup>[18]</sup> .....	157
Figure 6.2: Noyori's DAIB and the dimer-monomer equilibrium of homochiral zinc chelate complexes. <sup>[87]</sup> .....	157
Figure 6.3: XANES Zn K-edge spectra of 0.1 M <i>i</i> -Pr <sub>2</sub> Zn : 2-butanol molar ratios.....	160
Figure 6.4: Zinc K edge EXAFS spectra of 0.1M <i>i</i> -Pr <sub>2</sub> Zn with 2-butanol in 1:1 molar ratio in toluene (dimer and tetramer). Dotted lines are the experimental data and the solid lines are the best theoretical fit. ....	161
Figure 6.5: EXAFS calculated structural dimer and tetramer model of <i>i</i> -Pr <sub>2</sub> Zn with 2-butanol in 1:1 molar ratio. ....	163
Figure 6.6: XANES Zn K-edge spectra of 0.1 M Et <sub>2</sub> Zn and DMAE. ....	165
Figure 6.7: Structure of 2-butanol (left) and DMAE (right). ....	166
Figure 6.8: Zn K-edge EXAFS of 0.1 M Et <sub>2</sub> Zn/DMAE in 1:1 ratio (toluene) in k and R space. (a) monomer (b) dimer (c) tetramer. Dash lines are the experimental data and the solid lines are the best theoretical fit. ....	167



Figure 6.9: Zn K-edge EXAFS parameters of 0.1 M Et <sub>2</sub> Zn/DMAE in 1:1 ratio in toluene (different models).	168
Figure 6.10: Monomer, Dimer and Tetramer structural models proposed from EXAFS parameters of 0.1 M Et <sub>2</sub> Zn/DMAE in 1:1 ratio (toluene).	169
Figure 7.1: The increase in the amounts of S and R pyrimidyl alcohol in consecutive asymmetric autocatalysis. <sup>[102]</sup>	172
Figure 7.2: Zinc K-edge of 0.1 M i-Pr <sub>2</sub> Zn:BA in toluene.	174
Figure 7.3: Zinc K-edge spectra of 0.1 M i-Pr <sub>2</sub> Zn:PA in toluene.	176
Figure 7.4: Zinc k-edge EXAFS spectra of i-Pr <sub>2</sub> Zn with pyrimidyl aldehyde in 1:1 molar ratio (toluene). Dash lines are the experimental data and the solid lines are the best theoretical fit.	177
Figure 7.5: Zinc K edge EXAFS spectra of i-Pr <sub>2</sub> Zn with pyrimidyl aldehyde in 1:1 molar ratio (precipitate). Dotted lines are the experimental data and the solid lines are the best theoretical fit.	179
Figure 7.6: EXAFS model of i-Pr <sub>2</sub> Zn with pyrimidyl aldehyde in 1:1 molar ratio. Model of dimer alkoxide in solution.	180
Figure 7.7: Zinc K edge EXAFS spectra of i-Pr <sub>2</sub> Zn with pyrimidyl aldehyde in 2:1 molar ratio (solution) at t <sub>0</sub> (initial). Dotted lines are the experimental data and the solid lines are the best theoretical fit.	181
Figure 7.8: Zinc K edge EXAFS spectra of i-Pr <sub>2</sub> Zn with pyrimidyl aldehyde in 2:1 molar ratio (solution) after 3 hours. Dash lines are the experimental data and the solid lines are the best theoretical fit.	182
Figure 7.9: EXAFS model of i-Pr <sub>2</sub> Zn with pyrimidyl aldehyde in 2:1 molar ratio in solution at start and after 3 hours.	183
Figure 7.10: Zinc K edge EXAFS spectra of i-Pr <sub>2</sub> Zn with pyrimidyl aldehyde in 1:2 molar ratio (precipitate). Dash lines are the experimental data and the solid lines are the best theoretical fit.	184
Figure 7.11: EXAFS model of i-Pr <sub>2</sub> Zn with pyrimidyl aldehyde in 1:2 molar ratio (precipitate).	185
Figure 7.12: Zinc K-edge XANES spectra of 0.1 M DEZ:PA in toluene.	186
Figure 7.13: Zinc k edge EXAFS spectra of 0.1 M DEZ with pyrimidyl aldehyde in 1:1 molar ratio (toluene). Dotted lines are the experimental data and the solid lines are the best theoretical fit.	187
Figure 7.14: EXAFS model of DEZ with pyrimidyl aldehyde in 1:1 molar ratio (solution).	189
Figure 7.15: Zinc k edge EXAFS spectra of DEZ with pyrimidyl aldehyde in 2:1 molar ratio (toluene). Dotted lines are the experimental data and the solid lines are the best theoretical fit.	190
Figure 7.16: EXAFS model of DEZ with pyrimidyl aldehyde in 2:1 molar ratio (solution).	191
Figure 7.17: Possible model of DEZ with surplus pyrimidyl aldehyde in solution.	192
Figure 7.18: Zinc k-edge spectra of 0.1 M DEZ:DMAE:CA in toluene.	193
Figure 7.19: Absorption Spectra of reaction of DMAE and cinnamaldehyde	195
Figure 7.20: Absorption Spectra of reaction of DMAE, cinnamaldehyde and DEZ	196
Figure 7.21: Zinc K edge EXAFS spectra of 0.1 M DEZ:DMAE:CA (2:1:2) in toluene. Dotted lines are the experimental data and the solid lines are the best theoretical fit.	197

Figure 7.22: Zinc K-edge spectra of 0.05M $i\text{-Pr}_2\text{Zn}$ and different aldehydes (molar ratio 1:1 in toluene). Reaction products of $i\text{-Pr}_2\text{Zn}$ with A: pyrimidyl- B: methoxypyrimidyl- C: methoxypyridyl- D: benzaldehyde (APS). .....	199
Figure 7.23: Structure of the different aldehydes. A: pyrimidyl- B: methoxypyrimidyl- C: methoxypyridyl- D: benzaldehyde. ....	200
Figure 7.24: Zn K-edge EXAFS and Fourier Transform of 0.5 M $i\text{-Pr}_2\text{Zn}$ and different aldehydes (A, B, C and D) in 1:1 molar ratio in k and R space in toluene. ....	202
Figure 7.25: EXAFS model of alkoxide model from $i\text{-Pr}_2\text{Zn}$ with pyrimidyl aldehyde in 1:1 molar ratio. Pyrimidylalkoxide dimer (APS). ....	203
Figure 8.1: (a) Ionisation chambers(IC) (b) Sample holder between IC .....	208
Figure 8.2: Air free sample preparing set up.....	209
Figure 8.3: XANES of different alkylzincs in Toluene. APS-labeled; ANKA-unlabeled .....	210
Figure 8.4: Comparing XANES of diethylzinc in Toluene and THF. (APS/ANKA data) .....	212
Figure 8.5: XANES spectra of 0.1 M diethylzinc with ligands and Ketone (ANKA data). ....	214
Figure 8.6: XANES spectra of diethylzinc addition to imines (ANKA data). ....	216

## List of tables

Table 1.1 Representative substances from the chiral pool <sup>[9]</sup> .....	31
Table 1.2: Drugs prepared via Classical Resolution <sup>[9]</sup> .....	33
Table 3.1: Binding enthalpies of tetrameric compared to dimeric structures <sup>[52]</sup> .....	83
Table 4.1: EXAFS parameters of exposed DEZ in air (set as zinc hydroxide solid).....	103
Table 4.2: EXAFS of DEZ in toluene exposed in air (set as zinc oxide) .....	104
Table 4.3: Local structure of ZnO and Zn(OH) <sub>2</sub> derived from this EXAFS and other studies .....	106
Table 5.1: Asymmetric autocatalysis reaction with autocatalytic reaction with (S)- and (R)-2 with > 99.5% ee. <sup>[36]</sup> .....	120
Table 5.2: Comparing the ee and % product in solution and the precipitate for the Soai reaction. <sup>[45]</sup> .....	122
Table 5.3: Zinc K edge EXAFS parameters of i-Pr <sub>2</sub> Zn in toluene and THF .....	128
Table 5.4: Comparison of bond distances in i-Pr <sub>2</sub> Zn gas phase and solution. Gas phase: Haaland's study, <sup>[78]</sup> Solution: EXAFS calculation.....	130
Table 5.5: EXAFS parameters of diethylzinc in toluene .....	146
Table 5.6: EXAFS parameters of diethylzinc in THF.....	149
Table 6.1: Effect of aldehyde: dialkylzinc: DAIB ratio on reactivity. <sup>[18]</sup> .....	158
Table 6.2: Zn K-edge EXAFS parameter of 0.1 M i-Pr <sub>2</sub> Zn with 2-Butanol in 1:1 molar ratio in toluene .....	162
Table 7.1: Zn K-edge EXAFS parameter of 0.1 M i-Pr <sub>2</sub> Zn with PA in 1:1 molar ratio in toluene. ...	177
Table 7.2: Zinc K edge EXAFS parameters of i-Pr <sub>2</sub> Zn with pyrimidyl aldehyde in 1:1 molar ratio (precipitate).....	178
Table 7.3: Zinc K edge EXAFS parameter of i-Pr <sub>2</sub> Zn with pyrimidyl aldehyde in 2:1 molar ratio (solution) at t <sub>0</sub> (initial).....	181
Table 7.4: Zinc K-edge EXAFS spectra of i-Pr <sub>2</sub> Zn with pyrimidyl aldehyde in 2:1 molar ratio (solution) after 3 hours.....	182
Table 7.5: Zinc K edge EXAFS spectra of i-Pr <sub>2</sub> Zn with pyrimidyl aldehyde in 1:2 molar ratio (precipitate).....	183
Table 7.6: Zinc K edge EXAFS spectra of DEZ with pyrimidyl aldehyde in 1:1 molar ratio (toluene). .....	188
Table 7.7: Zinc K edge EXAFS spectra of DEZ with pyrimidyl aldehyde in 2:1 molar ratio (toluene). .....	190
Table 7.8: Colour change at different molar ratios of DEZ:DMAE:CA after 36 hours .....	194
Table 7.9: Zinc K edge EXAFS spectra of DEZ, DMAE and CA. ....	198
Table 7.10: Zn K-edge EXAFS parameters of iPr <sub>2</sub> Zn and aldehyde A. s: fixed.....	204
Table 8.1: Chemicals used during experiment .....	209
Table 9.1: Comparing the 1 <sup>st</sup> shell coordination number analysed by the XANES and EXAFS. ....	223

## List of Abbreviations

NMR	Nuclear magnetic resonance
XAFS	X-ray absorption fine spectroscopy
APS	Advance Photon Source
ESRF	European Synchrotron Radiation Facility
ANKA	Angstrom-Quelle Karlsruhe
<i>ee</i>	Enantiomeric excess
HPLC	High performance liquid chromatography
THF	Tetrahydrofuran
DFT	Density functional theory
XANES	X-ray absorption near edge spectroscopy
EXAFS	Extended X-ray absorption fine structure
UV	Ultra violet spectroscopy
DEZ	Diethylzinc
MEZ	Monoethylzinc
LCF	Linear combination fit analysis
DMAE	Dimethylaminoethanol
BA	Benzaldehyde
PA	Pyrimidylaldehyde
CA	Cinnamaldehyde
IR	Infra red
XRD	X-ray diffraction

## Abstract

The alkylation of pyrimidyl aldehyde by diisopropylzinc has received immense attention over the last decade. This is mainly because the reaction which was discovered by Soai and coworkers is capable of achieving a homochiral product from an essentially achiral precursor. The strong amplification of the enantiomeric excess occurs because of a transition state complex which is responsible for autocatalysis.

Clarifying the structural nature of the organometallic species involved in the reaction is vital for understanding the mechanism of the chiral amplification process. Known mechanistic details are patchy and based on studies that address molecular level details by NMR, computational chemistry, calorimetric and kinetic studies. The studies reported in this thesis for the first time directly addressed the nature of the intermediate by structural analysis with X-ray Absorption Fine Structure (XAFS) Spectroscopy at the Zn K-edge. These measurements provide bond distances, local coordination numbers and the geometry of ligands in the local environment around the Zn centres.

First, the molecular level origin of the solvent dependencies in the asymmetric amplification by the Soai process is elucidated. A rationale for the behaviour of dialkylzinc compounds in polar and non-polar solvents is reported. Structural causes for often observed chirality depletion in polar solvents are elucidated.

Further studies then examined the nature of the products formed by the reaction of various chiral ligands and dialkylzinc compounds. Different chiral ligands are examined and the complex structure was determined.

Finally, first results of *in situ* studies of the reaction progress in continuous flow channel cells are reported.

## Declaration

The following four notes on copyright and the ownership of intellectual property rights must be included as written below:

- (1) The author of this thesis (including any appendices and/or schedules to this thesis) owns certain copyright or related rights in it (the “Copyright”) and s/he has given the University of Manchester certain rights to use such Copyright, including for administrative purposes.
- (2) Copies of this thesis, either in full or in extracts and whether in hard or electronic copy, may be made only in accordance with Copyright, Designs and Patents Act 1988 (as amended) and regulations issued under it or where appropriate, in accordance with licensing agreements which the University has from time to time. This Page must form part of any such copies made.
- (3) The ownership of certain Copyright patents, designs, trademarks and any and all other intellectual property rights except for the copyright (the “Intellectual Property Rights”) and any reproductions of copyright works, for example graphs and tables (“Reproductions”), which may be described in this thesis, may not be owned by the author and may be owned by thirds parties. Such Intellectual Property Rights and Reproductions cannot and must not be made available for use without the prior written permission of the owner(s) of the relevant Intellectual Property Rights and/or Reproductions.
- (4) Further information on the conditions under which disclosures and commercialization of this thesis, the Copyright and any Intellectual Property and/or Reproductions described in it may take place is available in the University IP policy (see <http://www.campus.manchester.ac.uk/medialibrary/policies/intellectualproperty.pdf>) in any relevant Thesis restriction declarations deposited in the University Library. The University Library’s regulation (see <http://www.manchester.ac.uk/library/aboutus/regulations>) and in the University's policy on presentation of theses.

## **Acknowledgements**

I dedicate this work to my parents Anthony Nforba Nchari of blessed memory and Mary Kinyuy Nchari.

I owe my deepest gratitude to my honorific supervisor, Dr Sven L.M. Schroeder who accepted me as a PhD student in his group. His wisdom, knowledge and commitment inspired and motivated me.

I extend thanks to the Engineering and Physical Science Research Council for awarding me a scholarship to pursue this research degree. This opportunity has given me the possibility to engage in funded research.

I also appreciate the support of the International Union of Crystallography and the University of Manchester in granting me a scholarship to attend and present during the XAFS 14 International Conference in Camerino, Italy. I also appreciate supported provided by Leech trust towards my PhD.

I am grateful to Drs Guy Hembury, Angela Beesley, Nick Lockyer and Norbert Weiher. Their mentorship was paramount in providing a well rounded experience.

I am also indebted to Professors Pat Bailey and his research assistants in the University of Manchester: Dr Ben Lam and Dr Richard Price. My access to their laboratory and resources was vital in appreciating the chemistry of the Soai reaction.

I am also thankful to Professor Stephan Braese and Sefer Ay of the Technical University of Karlsruhe, Germany for their excellent collaboration.

Special thanks goes to the beam line scientists at APS (Argonne-USA), ESRF (Grenoble-France), ANKA (Karlsruhe-Germany), SRS (Daresbury-UK) and Maxlab (Lund-Sweden) who provided immense assistance.

Special thanks as well to my PhD student colleagues: David Meehan, Matthew Thomason, Hamizah Mohd Zaki, Joanna Stevens, Vicky Fawcett, Matthew Hudson, Nikolaos Tsapataris, Hamid Esfahanian who created a fun and stimulating environment necessary for growth in learning.

I appreciate the collaboration of MSc students I supervised: Devon Indar and Mahmoud Gawish. They both worked intensively on the kinetic simulation of the Soai Autocatalytic Reaction and showed keen interest.

I owe great thanks to my family and friends. This especially goes to my lovely wife, daughter, brother, sister, cousins and in laws, who have been a great source of encouragement and enthusiasm.



## 1. Introduction

The remarkable Soai autocatalytic reaction which is capable of amplifying chirality is the main focus of this project. This thesis for the first time examines the mechanism underlying chiral amplification in asymmetric synthesis mainly using X-ray absorption spectroscopy. This reaction which has intrigued numerous scientists begins with a very minute enantiomeric excess in the chiral initiator (**4**) which catalyses its own formation in greatly amplified enantiomeric excess (**4**).<sup>[1-6]</sup>

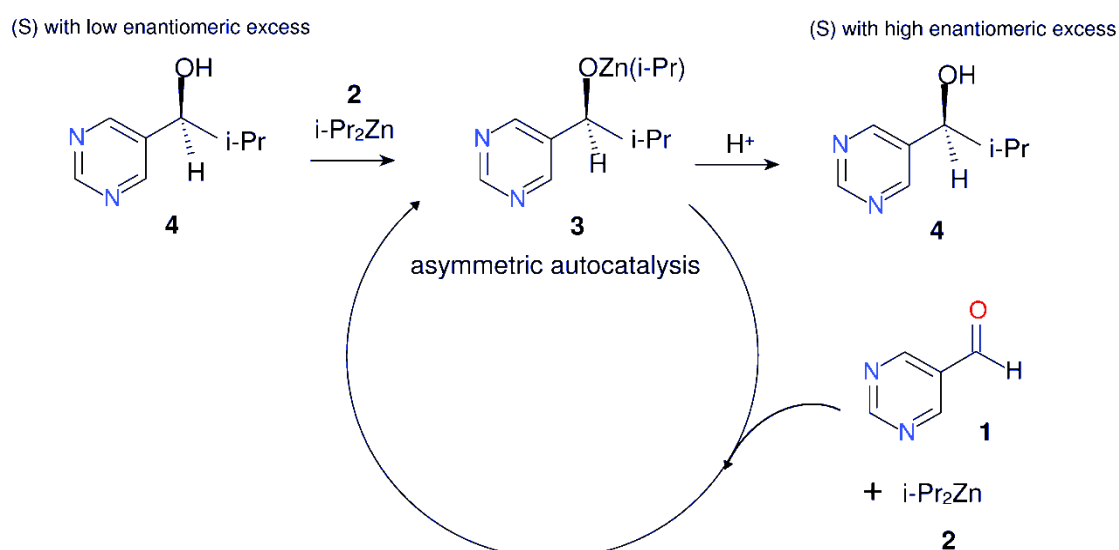


Figure 1.1: Soai autocatalytic reaction<sup>[1]</sup>

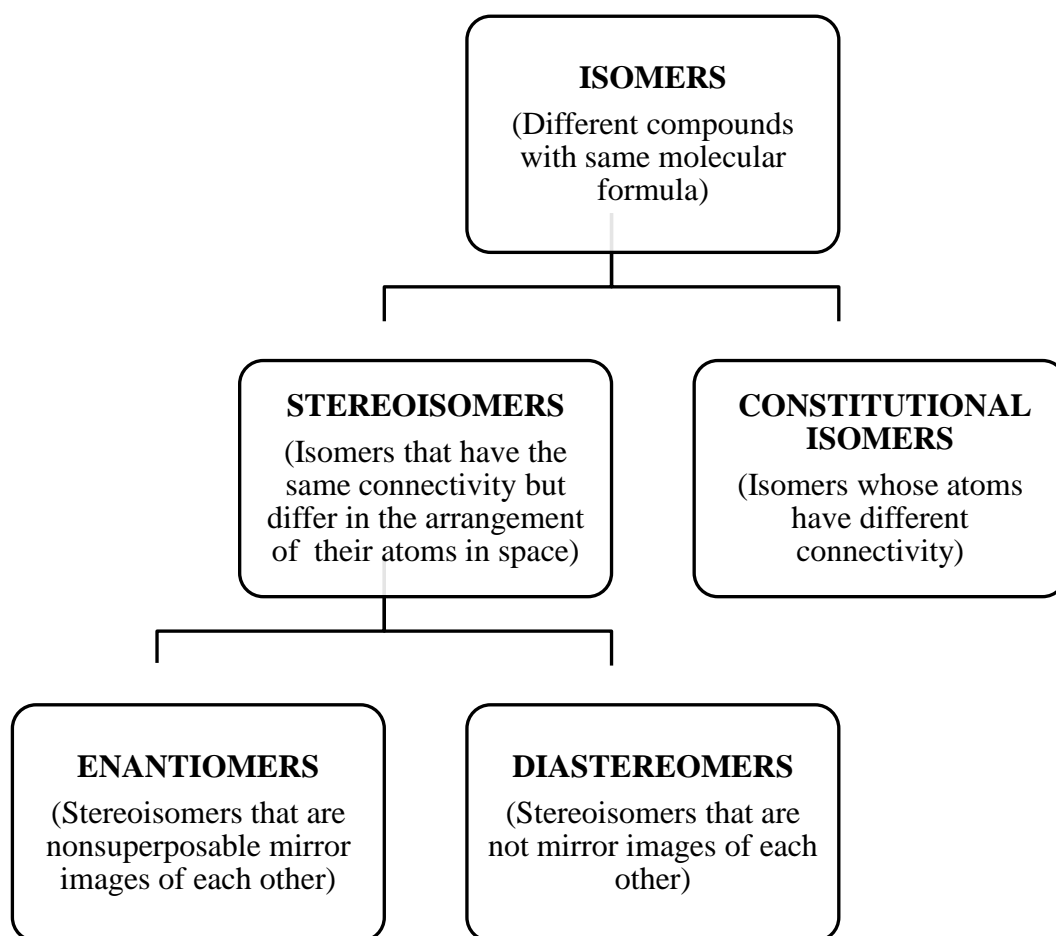
Prior to the details of this research, this chapter embarks on the principles of stereoisomerism and conventional approaches of generating chiral compounds.

### 1.1 Enantiomers and chiral molecules

Stereochemistry (Greek: *stereos*, solid) considers the geometry of molecules in three dimensions. Stereoisomerism describes compounds that have the same chemical formula but a geometrically different arrangement of the atoms in space. Enantiomers are a subset of stereoisomers as seen in the classification below (Figure 1.2)<sup>[2]</sup>. An enantiomer is one of two stereoisomers that are chiral, i.e., they are mirror

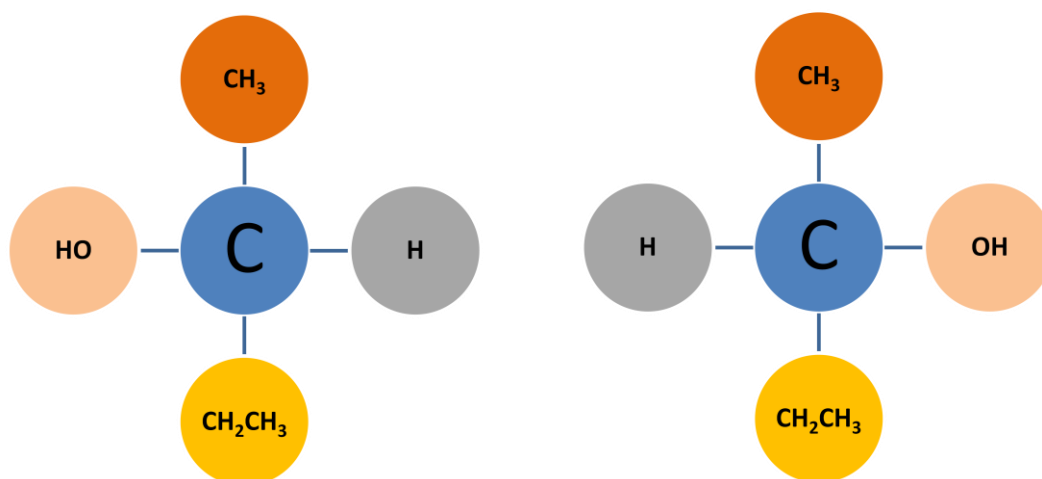
images of each other are "non-superposable" (not identical), similar to one's left and right hands are "the same" but opposite. The word chiral is derived from the Greek word *cheir*, which meanings "hand." The expression chiral, describes molecules of enantiomers since they are related in the same manner that a right hand is related to a left hand.<sup>[3]</sup>

Samples with molecules of the same chirality are enantiopure compounds. Enantiomers can be distinguished using different nomenclature. The nomenclature initially used was (+) and (-) signs or *d(dextro)* or *l(levo)*. (+) or *d(dextro)* implies rotation of plane polarized light to the right (clockwise) and (-) or *l(levo)* to the left or anticlockwise. The notation which has almost replaced the *d/l* notation is the Cahn-Ingold-Prelog (CIP) convention. Instead R and S are assigned according to CIP in which the order of priority of the substituents on the centre of chirality is determined on the basis of decrease in the atomic number of the atoms directly bonded to the centre of chirality. The heaviest atomic number is given the highest priority.<sup>[4]</sup>

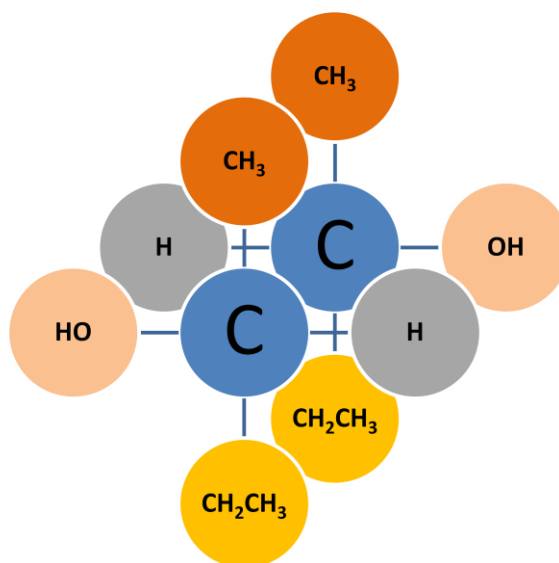


**Figure 1.2: Subdivision of isomers.**<sup>[3]</sup>

The chirality of simple molecules can be illustrated with 2-butanol,  $\text{CH}_3\text{CH}(\text{OH})\text{CH}_2\text{CH}_3$ . Molecules of 2-butanol are chiral because their enantiomers are non-superimposable as shown in the models in Fig. 1.3.



(a)

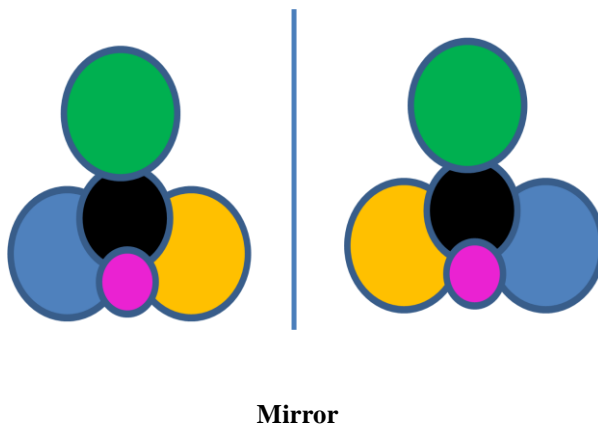


(b)

**Figure 1.3: (a) Models of 2-Butanol enantiomers. (b) Non superimposable models**

A pair of enantiomers can be recognized by the attachment of four different groups to the stereocenter which in the illustration above is carbon (blue). One enantiomer is

a non-superimposable mirror image of the other as seen in the three dimensional illustration below.



**Figure 1.4: Relationship of enantiomers**

Both enantiomers have different spatial arrangements and consequently cannot be superimposed on each other.

## **1.2 Enantiomerism: the discovery**

Optical isomerism was discovered by the French chemist Jean-Baptiste and has been known since 1815. Louis Pasteur discovered enantiomerism and is the founder of stereochemistry. His discovery resulted from the separation of a racemic form of tartaric acid in 1848 at Ecole Normale in Paris. Pasteur repeated the early work of a chemist on salts of tartaric acid and found something nobody had noticed. He found that optically inactive ammonium tartrate existed as a mixture of two types of crystals which were mirror images of each other. Pasteur used a hand lens and a pair of tweezers to separate the mixture into two: one right handed and the other left handed crystals. The original mixture was found optically inactive, the separated piles of crystals dissolved in water were found to be active. In addition it was noticed that the specific rotation of both solutions were equal but opposite in sign. Pasteur concluded that it was a property not of the crystals but the molecules since the

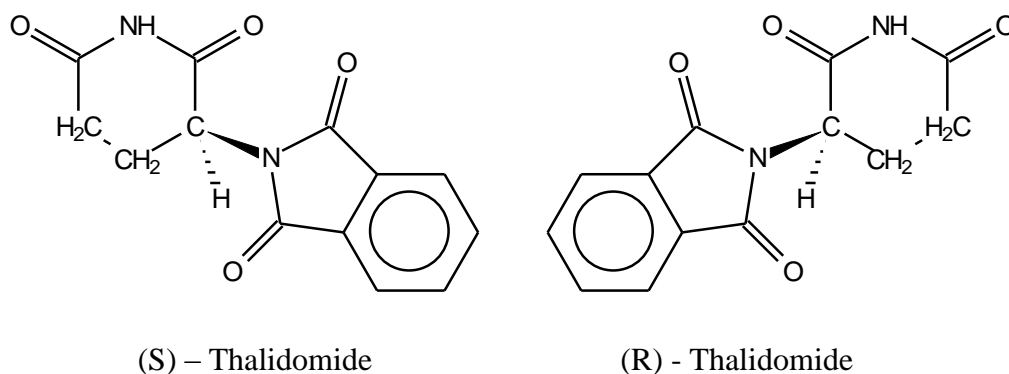
distinction in optical activity was noticed in solution. He then proposed that the two piles of crystals were composed of molecules which were mirror images to each other. Pasteur proposed the existence of isomers that have differing mirror images with a difference in the direction of rotation of plane polarized light. The discovery of enantiomerism by Louis Pasteur led to the proposal of a tetrahedral structure of carbon by van't Hoff and Le Bel in 1874. Van't Hoff in 1901 was the first recipient of the Nobel Prize in Chemistry.<sup>[2, 3]</sup>

### **1.3 The biological importance of chirality**

Out of the 20 amino acids that make up naturally occurring proteins all but one are chiral. All naturally occurring amino acids are left handed. On the other hand naturally occurring sugars are right handed.<sup>[3, 5-7]</sup>

The important applications of chiral isomers today are in the pharmaceutical, agrochemical, food, environment and petrochemical industry. Chirality in the pharmaceutical industry received much attention through the thalidomide tragedy in the 1960s, when an unfortunate outcome of stereochemistry was revealed. Thalidomide was administered to pregnant women in the late 1950s in its racemic form to cure morning sickness. The consequence was birth defects and deaths as a result of the harmful (S) isomer. The (R) isomer was the effective drug. This tragedy has led to approved and strict guidelines for the development of new drugs. The physiological effects of enantiomers of chiral drugs must be fully understood to avoid any harmful effects. This revelation was as a result of the keen interest of Francis Kelsey, a researcher at the U.S Food and Drug Administration. The

restriction of thalidomide from the work of Kelsey was due the high rate of abortions in rats.<sup>[8-10]</sup>

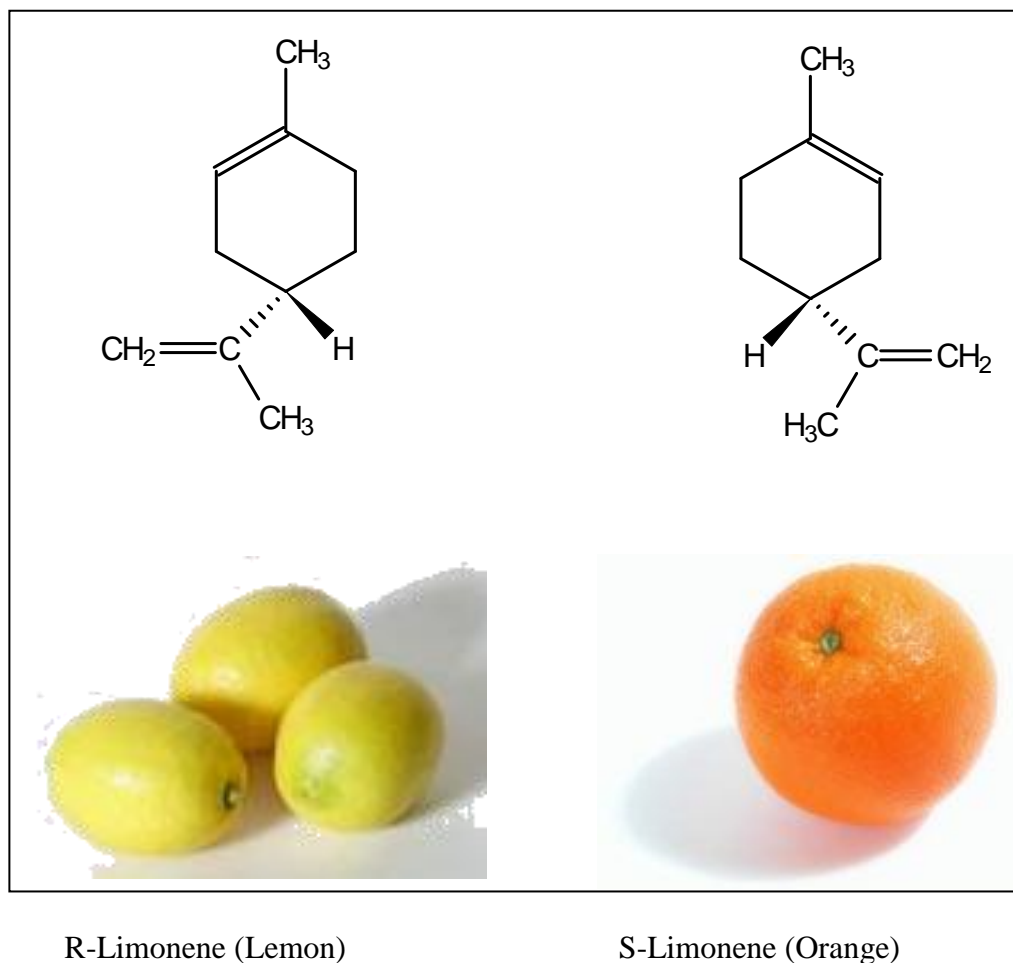


**Figure 1.5 Chiral forms of Thalidomide**

Some reasons for synthesizing optically active pure materials are:

- i. The biological activity may be attributed to only one enantiomer.
- ii. The separation of effects of differing enantiomers; both of which may be beneficial or one may be beneficial and the other not.
- iii. Some optical active compounds are twice as active as the racemate due to antagonism.
- iv. Some enantiomers, when compared to their racemates, possess physical properties which may give development and formulation advantages.

Examples of the differing properties of enantiomers are abundant and remarkable as seen below in the case of Limonene present in the flavour of lemon and orange. One enantiomeric form is responsible for the zest of oranges while the other enantiomer is responsible for the zest of lemons.



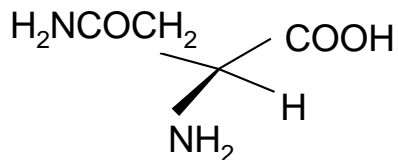
**Figure 1.6: Chiral forms of Limonene in Lemon and Orange**

## 1.4 The physical properties of stereoisomers

Two enantiomers possess different physical properties which include melting point, boiling point, solubility, similar IR and NMR spectra. These properties do not include how they differ in plane polarized light. As previously seen, chiral molecules have non superimposable mirror images contrary to achiral compounds which are superimposable.<sup>[9]</sup> Several compounds may be found in two forms with a different molecular three dimensional geometry that are mirror images. Both forms are enantiomers as seen in the former section. Other enantiomers include amino acids e.g. alanine, which has two mirror image forms. The relative configuration of an enantiomer can be determined by firstly identifying the stereogenic atom, which has



non identical groups attached. In the case of alanine, the central carbon atom bears four different groups.<sup>[11-13]</sup>

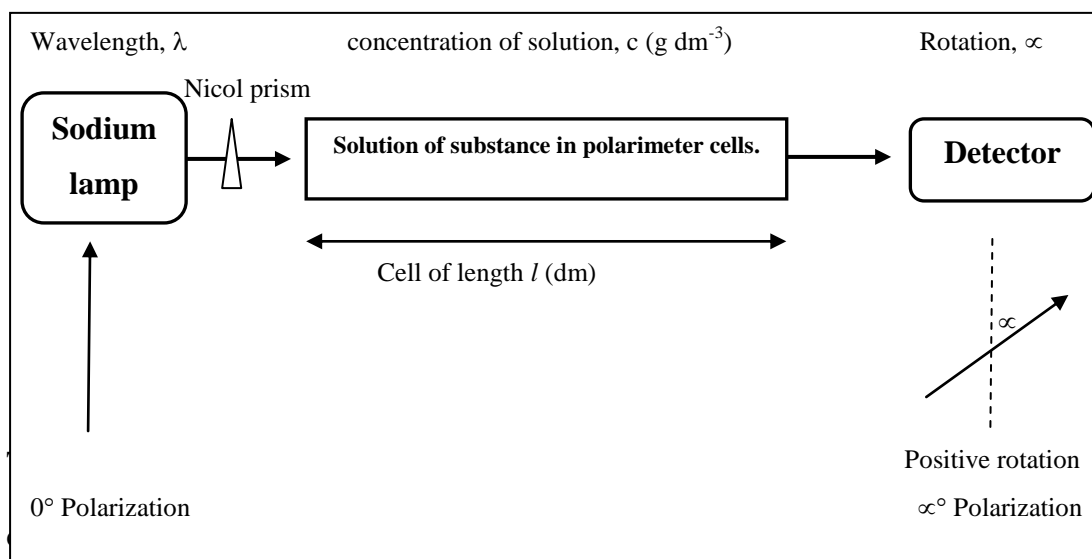


**Figure 1.7 S-Stereoconfiguration of alanine<sup>[11]</sup>**

Enantiomers however differ in the rotation of plane polarized light and this is the basis of the nomenclature of enantiomers. Plane polarized light rotation is measured by a polarimeter as seen below, where the angle of rotation ( $\alpha$ ) is defined as:

$$[\alpha]_D = \alpha_{\text{obs}}/lc \quad 1.1$$

$[\alpha]_D$  is the specific rotation at a specific temperature of the D-line of sodium light;  $\alpha_{\text{obs}}$  is the observed angle of rotation;  $l$  is the length of the medium (decimetres) and  $c$  is the concentration of the medium ( $\text{g/dm}^3$ ).



**Figure 1.9: Schematic of polarimeter<sup>[13]</sup>**

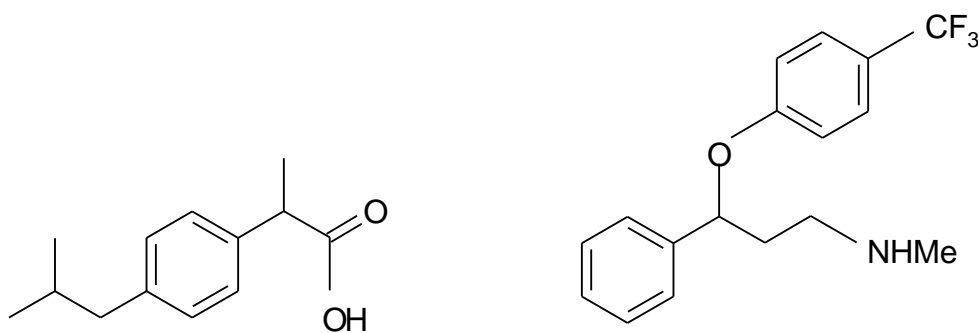
An equal amount of two enantiomers is a racemic mixture or a racemate. Racemic mixtures are optically inactive. The enantiomeric excess  $ee$  (also called optical purity) gives information on the excess of one enantiomer over the other.<sup>[13]</sup>

$$\text{Enantiomeric Excess} = \frac{([R] - [S])}{([R] + [S])} \quad 1.2$$

The electric field in light waves oscillates in different directions perpendicular to the direction in which it propagates. Plane polarized light on the other hand oscillates in one direction and is created by passing ordinary radiation through a Nicol prism (placed between lamp and sample).<sup>[8]</sup>

## 1.5 Chemical properties of enantiomers

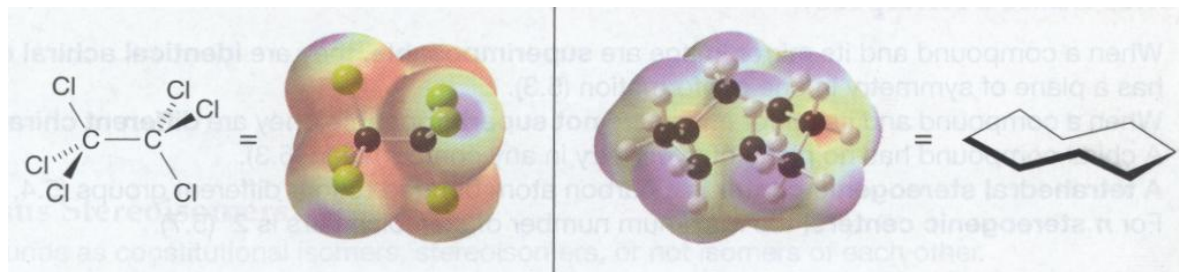
The rate of reaction of two enantiomers with an achiral molecule is the same. However, the rate of reaction changes when they react with chiral or non racemic reagents. In this section some applications will be visited. Living organisms are composed of chiral molecules. Most drugs which are chiral must interact with a chiral receptor or chiral enzyme to be effective. One enantiomer has the potential of curing an illness whereas the other does not. (S)-Ibuprofen is the active substance in Motrin and Advil (both anti inflammatory agents). (R)-Fluoxetine is the active ingredient of Prozac (antidepressant).



**Figure 1.10: (S)-Ibuprofen (left), antiinflammatory and (R)-Fluoxetine (right), antidepressant.<sup>[13]</sup>**

(S)-Naproxen is also an anti-inflammatory agent, but the (R) enantiomer has been established to be harmful to the liver. Because of the change in orientation of both enantiomers the biological activity is modified leading to unwanted side effects. The sale of chiral drugs would be preferred to be delivered as the single active enantiomer. The process of separating from a racemic mixture is rather expensive and would be reflected on the sale of chiral drugs.

In addition to chiral drugs, enantiomers have a specific odour. This is caused by their shape. Hexachloroethane and cyclophane are dissimilar in structure but have a similar odour because of their similarity in shape.



**Figure 1.11: Structure and shape of hexachloroethane (left) and cyclooctane (right).**<sup>[13]</sup>

The difference in smell is caused by the difference in interaction of the enantiomers with chiral receptors in the nose. An example is seen in Figure 1.6 which shows the chiral forms of limonene found in lemon and orange. The enantiomers are responsible for the difference in odour and taste.

## 1.6 Methods of obtaining optically active compounds

The pharmaceutical industry remains the key driver for chiral compound development with an estimated 80% of chiral intermediates and related products going into the pharmaceutical market.<sup>[8]</sup> 15% of optical active intermediates are used in chemical building blocks, auxiliaries or advanced intermediates. The fraction of chiral compounds in the pharmaceutical industry will increase with the enforcement of the stricter regulations by the US Food and Drug Administration (FDA). Authorities responsible for the registration of new active compounds have emphasized the demand to increase the targeted synthesis of one enantiomer. The FDA and the European Committee for Proprietary Medicinal Products since 1992 have stipulated that the physiological action of each enantiomer must be fully

understood. In addition since 1997 the emergence of the fast track single isomer program of FDA has been a driving force for pharmaceutical companies to convert racemic active compounds into enantiomerically pure forms. This trend is also found in the agrochemical industry in order to improve economics and reduce quantities applied, thus reducing the environmental impact.

The synthesis of active pharmaceutical and agricultural products can be achieved from optically active important compounds which include amines, alcohols and carboxylic acids. The development of new technologies focuses on large scale industrial processes prior to previous times. This has opened up new opportunities and economically attractive methods for the production of optically active compounds.<sup>[14]</sup>

Three primary sources of pure enantiomers include:

- i. Extraction of naturally occurring molecules from plants.
- ii. By the de novo fermentation process of inexpensive available feedstocks.
- iii. Synthesis of optically active compounds from the above two or prochiral starting materials.

The above three methods are schematically characterized below.

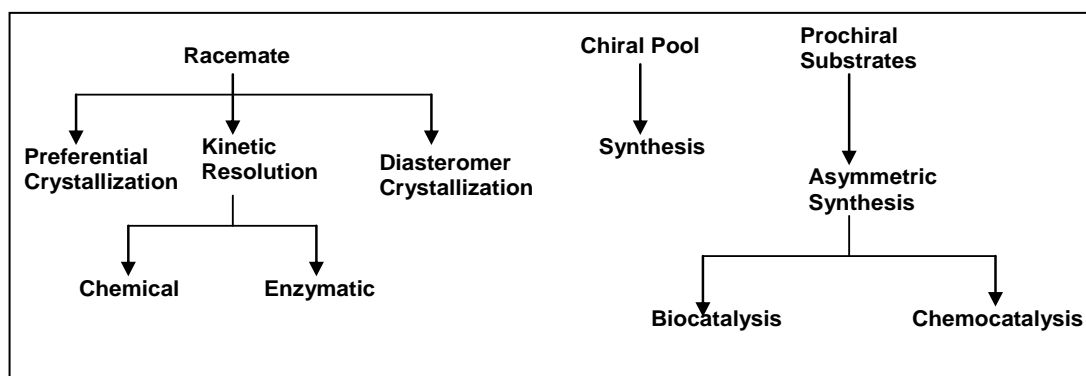


Figure 1.12: Methods of producing optically active compounds.<sup>[8]</sup>

### 1.6.1 The Chiral Pool

A group of inexpensive readily available optical natural products comprise a chiral pool which mainly includes chemicals such as carbohydrates, amino acids, hydroxyl acids, terpenes and alkaloids.<sup>[8]</sup>

*Carbohydrates* form the largest group of chiral compounds found in nature predominantly with a D configuration.

*Amino acids* constitute the most valuable chemicals in the chiral pool. They are desirable because they are simple in structure i.e. one or two chiral centres and can easily be functionally modified. Significant quantities of natural  $\alpha$ -amino acids can be produced by biological processes, fermentation and hydrolyzing plant and animal proteins.

*Hydroxy acids* are produced by fermentation of glucose or microbial oxidation of aliphatic acids. Chiral  $\alpha$ - and  $\beta$ - hydroxy acids are a good source for synthesizing optically active products and preparing pharmaceutical intermediates respectively.

*Terpenes* are extracted from natural sources. They are the starting material for the preparation of resolving agents and chiral ligands in asymmetric synthesis.<sup>[9]</sup>

*Alkaloids* are the most expensive compounds of the chiral pool. They are extracted from plants and are used primarily in resolving racemic mixtures. Their use in asymmetric synthesis as chiral ligands is growing.

Compound	Price, US (\$/kg)
Ascorbic acid	13
(+)- Calcium pantothenate	16
(-)- Carvone	23
Ephedrinehydrochloride	62
(+)- Limonene	3
L-Lysine	3.2
L-Tryptophan	68
Quinidine sulphate	130
Quinine sulphate	75
L-Threonine	12-50

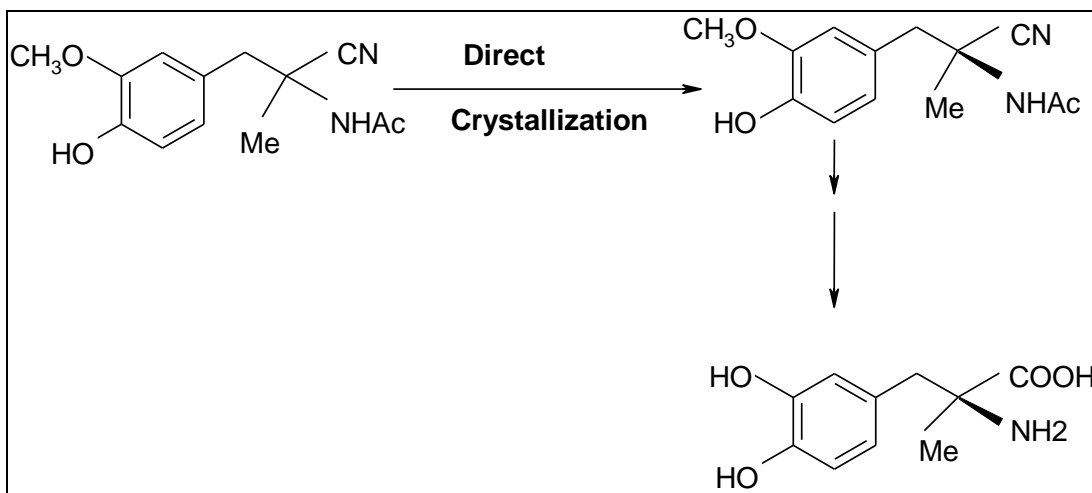
**Table 1.1 Representative substances from the chiral pool<sup>[9]</sup>**

### 1.6.2 Separation of enantiomers

The separation of enantiomers can be achieved by four resolution processes which include preferential crystallization, diastereomeric salt crystallization, kinetic resolution and HPLC.

*Preferential crystallization*, separates racemates that exist as a conglomerate. Only 10% of all compounds, exists as conglomerates implying that this technique is not usable for the other 90% of racemates referred to as racemic compounds. The process involves the pumping of a supersaturated solution through chambers in contact with crystals of the pure isomers responsible for seeding. The removed

substance is substituted as a racemic mixture in another chamber prior to re-cooling and repeating the process.  $\alpha$  – Methyl-L-Dopa is prepared using this method as seen in the scheme.



**Figure 1.13 Preparation of  $\alpha$  – Methyl-L-Dopa<sup>[9]</sup>**

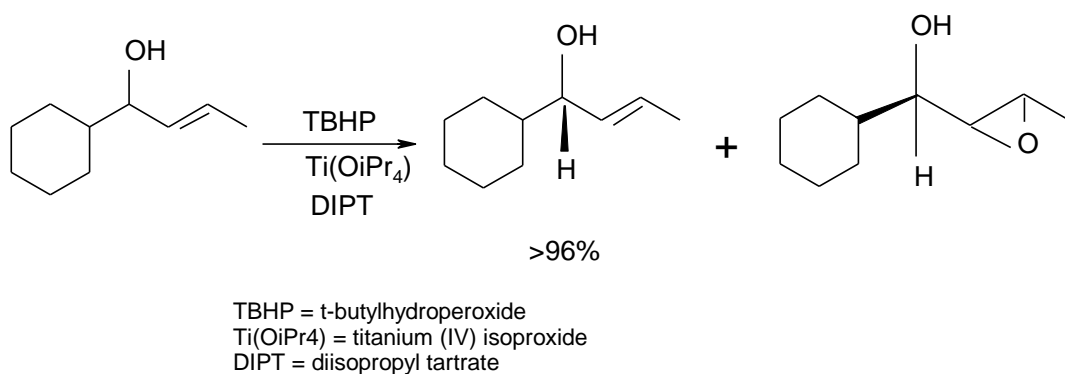
*Diastereomer crystallization* involves the crystallization of diastereomeric salts to prepare optically active compounds which are mostly pharmaceuticals. The resolving agent, solvent composition and recovery of chiral auxiliary are crucial in deciding the effectiveness of the process. The table includes some drugs and resolving agents used in diastereomer crystallization.



Drug	Resolving Agent	Activity
Ampicillin	D-camphosulfonic Acid	Antibiotic
Ethambutol	L-(+)-tartaric Acid	Tuberculostatic
Choramphenicol	D-camphosulfonic Acid	Anti-infective
Fosfomycin	R-(+)-phenethylamine	Antibiotic
Thiampenicol	D-(-)-tartaric Acid	Antiinfective
Naproxen	Cinchonidine	Anti- inflammatory
Diltiazem	R-(+)-phenethylamine	Calcium antagonist

**Table 1.2: Drugs prepared via Classical Resolution<sup>[9]</sup>**

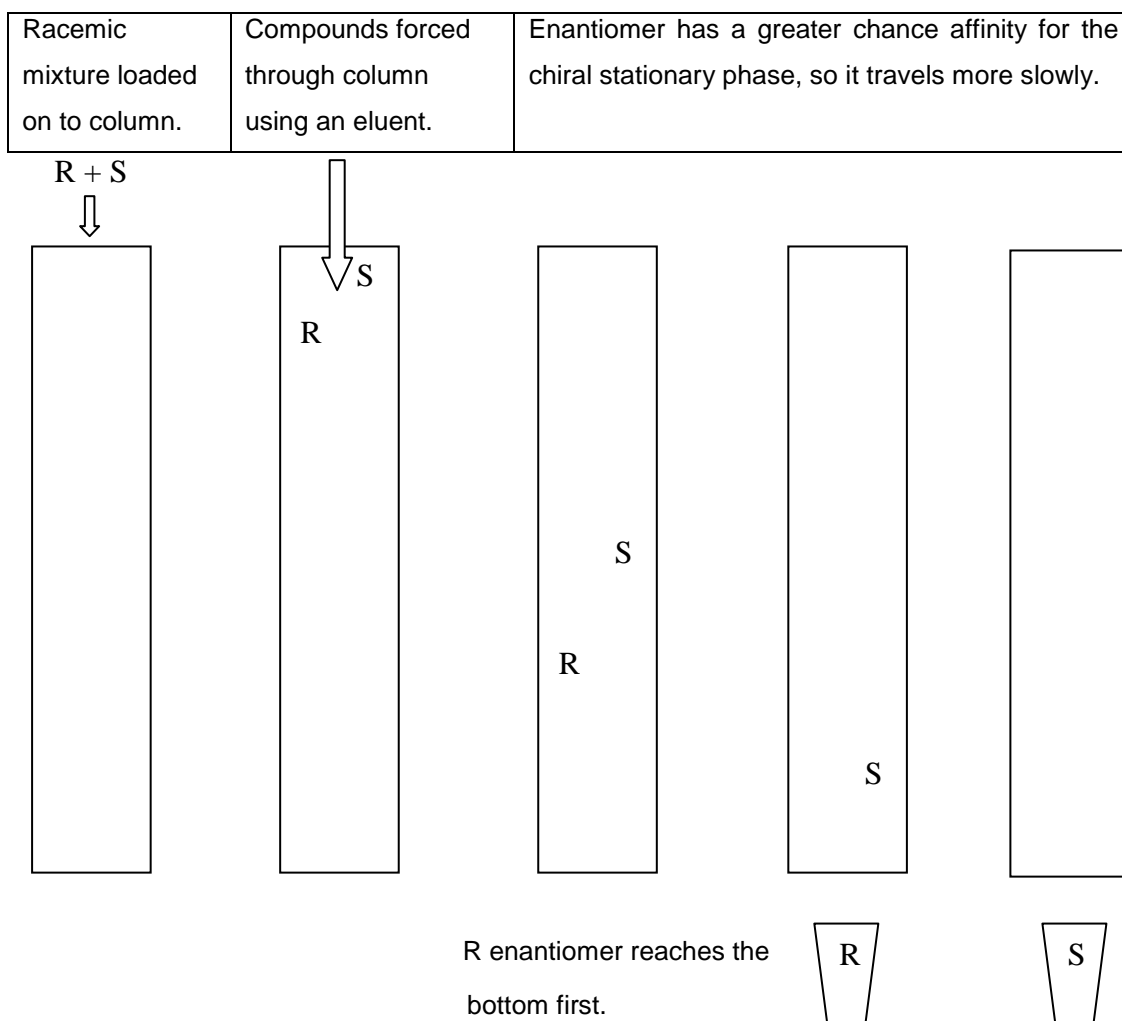
*Kinetic resolution* is another method of resolving enantiomers. One enantiomer reacts quicker than the other resulting in two products i.e. an unreacted enantiomer and a formation of a new product. The purity of the wanted enantiomer is influenced by the degree of conversion. This method is both chemically and enzymatically possible. An example of this is Sharpless epoxidation as seen in the scheme below.



**Figure 1.14: Epoxidation reaction of only one enantiomer<sup>[9]</sup>**

### 1.6.3 Resolution by chromatography on chiral materials

Enantiomers have difference physical properties. In addition they have different affinities to adhere to a chiral stationary phase. One chiral form can be achieved by passing the racemic mixture through a chiral column.



**Figure 1.15: Separation of enantiomers by chromatography.**<sup>[15]</sup>

Chromatography is especially crucial for enantiomers which have no functional groups suitable for the development of further derivatives.<sup>[15]</sup>

#### 1.6.4 Asymmetric synthesis

Asymmetric synthesis is the main method studied in this research study. Prochiral substrates are converted into optically active compounds.

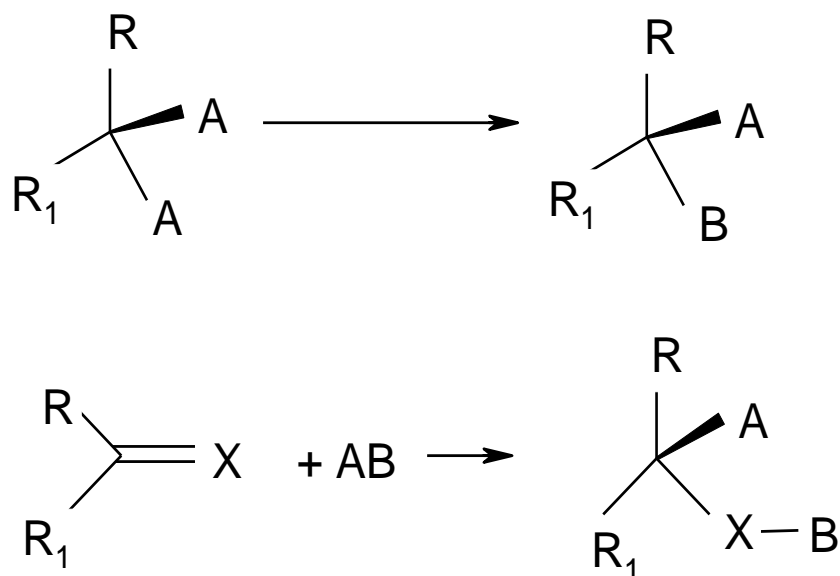


Figure 1.16: Asymmetric synthesis scheme

This reaction could either be homogeneous or heterogeneous. Organometallic catalysts have a wider reactivity application compared to enzymes. Catalysts are more stable and have higher levels of enantioselectivity. Transition metals are predominantly used as catalysts in asymmetric synthesis for the following reasons:

- i. The existence of several different oxidation states permits the addition and elimination of substrates, reactants and products.
- ii. Transition metals coordinate to ligands and ascertain stereo- and regioselectivity.

They possess the ability to stabilize reactive intermediates which are not probable via other synthetic methods.

## 2. Asymmetric Autocatalysis

This section explains the principles of asymmetric autocatalysis and some important reaction examples. It includes different models that describe the process of amplifying chirality. Frank postulated an autocatalytic process for the amplification of chirality in the 1950s, even though no actual reaction capable of amplifying chirality was known at the time.<sup>[16]</sup> Kagan and coworkers later discovered the first examples of reactions in which positive nonlinear effects achieve the amplification of chirality.<sup>[17]</sup> Noyori successfully studied the positive nonlinear effect of the alkylation of benzaldehyde in the presence of a chiral catalyst.<sup>[18]</sup> Finally, the autocatalytic asymmetric reaction developed by Soai and coworkers will be explored because it is the focus of the investigations in this thesis.<sup>[1, 19-27]</sup>

Central to a discussion of chiral amplification is the concept of the enantiomeric excess,  $ee$  (see equation 1.2). It can vary from 0 (100% racemic) to 1 (100% enantiopure). In asymmetrical stereoselective synthesis, enantiomeric excess of the product ( $ee_{\text{prod}}$ ) is not always proportional to that of the auxiliary ( $ee_{\text{aux}}$ ), as shown in the equation below.

$$ee_{\text{prod}} = ee_0 \times ee_{\text{aux}} \quad 2.1$$

Whereby,

$ee_{\text{prod}} = ee$  in reaction product

$ee_0 = ee$  in reaction product if enantiopure reagents are used (normally 100%)

$ee_{\text{aux}} = ee$  of chiral auxiliary

A graphical representation is shown below that illustrates the linear relationship.<sup>[17]</sup>

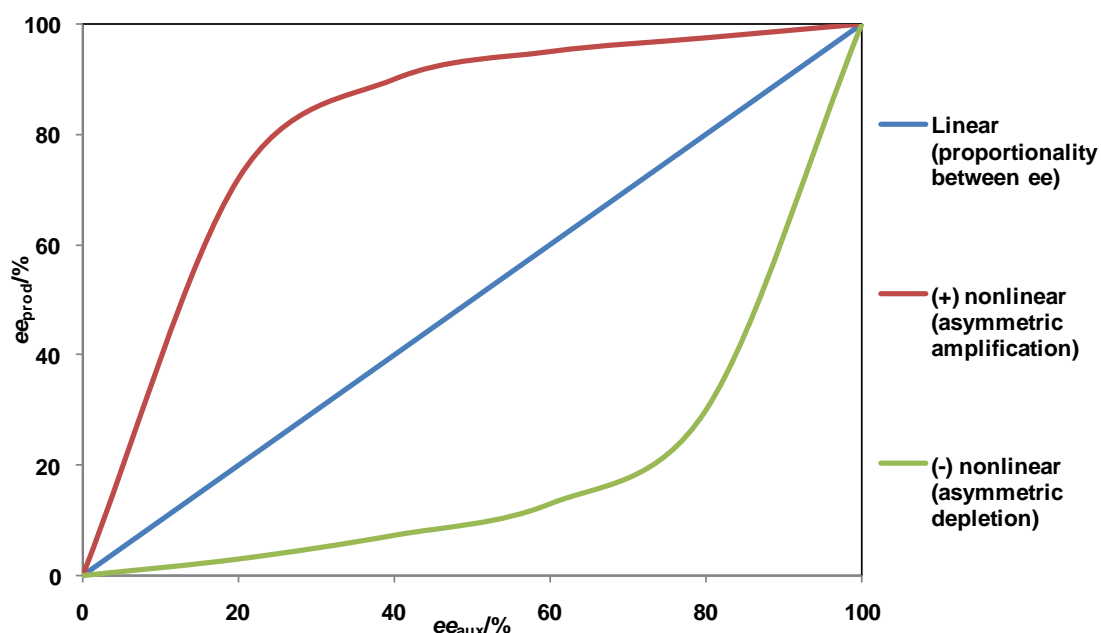


Figure 2.1: Non-linear effects with partially resolved chiral auxiliaries<sup>[17]</sup>

From the above illustration, the deviation from linearity is either positive (amplification) if the  $ee_{\text{prod}}$  is higher than  $ee_{\text{aux}}$  as seen in red curve or negative (depletion) if the  $ee_{\text{prod}}$  is lower than  $ee_{\text{aux}}$  as seen in the green curve. The blue curve represents the proportionality between  $ee_{\text{prod}}$  and  $ee_{\text{aux}}$ .

Systems that deviate from the linear relationship have a Non Linear Effect (NLE). An excess in the  $ee$  of the product over the chiral catalysts is known as Positive NLEs or (+)-NLEs. The studies presented in this thesis focus on such a system, which possesses the potential of amplifying  $ee$ . The negative NLEs or (-)-NLEs on the other hand represents a system with the chiral product having a lower  $ee$  than the chiral catalyst as seen in the above figure.

## 2.1 Nonlinear Effects in Asymmetrical Stereoselective Reactions

The enantiomeric excess of the product,  $ee_{\text{prod}}$  is not directly proportional to the enantiomeric excess of the auxiliary,  $ee_{\text{aux}}$  for most asymmetrical stereoselective

synthesis. The models below represent the special cases where non-linear amplification effects are present.

### 2.1.1 The Frank Model

Frank proposed a mechanism for asymmetric autocatalysis decades before the Soai reaction was discovered. His work led the way to a feasible mechanism for asymmetric autocatalysis. The mechanism was purely theoretical and not designed for any particular chemical reaction.<sup>[16]</sup> This mechanism is a plausible explanation of homochirality as well as amplification of chirality in the Soai autocatalytic reaction.

Frank's mechanism describes the process as "a chemical substance which is a catalyst for its own production and an anti-catalyst for the production of its optical antimer."<sup>[16]</sup> His postulate suggests that if it is possible to suppress one reaction route compared to the other, the *ee* multiplies increasingly as autocatalytic amplification emphasizes. He describes the rate of increase of each enantiomer with the following differential equations:

$$dn_1/dt = (k_1 - k_2n_2)n_1 \quad 2.2$$

$$dn_2/dt = (k_1 - k_2n_1)n_2 \quad 2.3$$

Where

1 and 2 are optical antimers

$k_1$  and  $k_2$  are positive rate constants

$n_1$  and  $n_2$  are concentrations

The negative terms of both equations represent the interaction parameters of the enantiomers which may be considered for each enantiomer to decrease the rate of formation of the opposite enantiomer.

Subtracting the above two equations we get:

$$d(n_1 - n_2)/dt = k_1(n_1 - n_2) \quad 2.4$$

implying

$$(n_1 - n_2) = (n_{01} - n_{02})e^{k_1 t} \quad 2.5$$

Where  $n_{01}$  and  $n_{02}$  are initial concentrations of the antimers: there is an exponential increase of the difference in antimer concentration.

Dividing equation 2.2 and 2.3 results in:

$$dn_1/dn_2 = [(k_1 - k_2 n_2)n_1]/[(k_1 - k_2 n_1)n_2] \quad 2.6$$

hence

$$n_1/n_2 = (n_{01}/n_{02}) \exp [k_2(n_1 - n_2 - n_{01} + n_{02})(e^{k_1 t} - 1)] \quad 2.7$$

Combining equation 2.5 and 2.7

$$n_1/n_2 = (n_{01}/n_{02}) \exp [k_2(n_{01} - n_{02})(e^{k_1 t} - 1)] \quad 2.8$$

An exponential increase in the concentration ratio is the case when  $n_{01} - n_{02}$  is positive. The corresponding decrease occurs if this difference is negative as illustrated in the figure below.

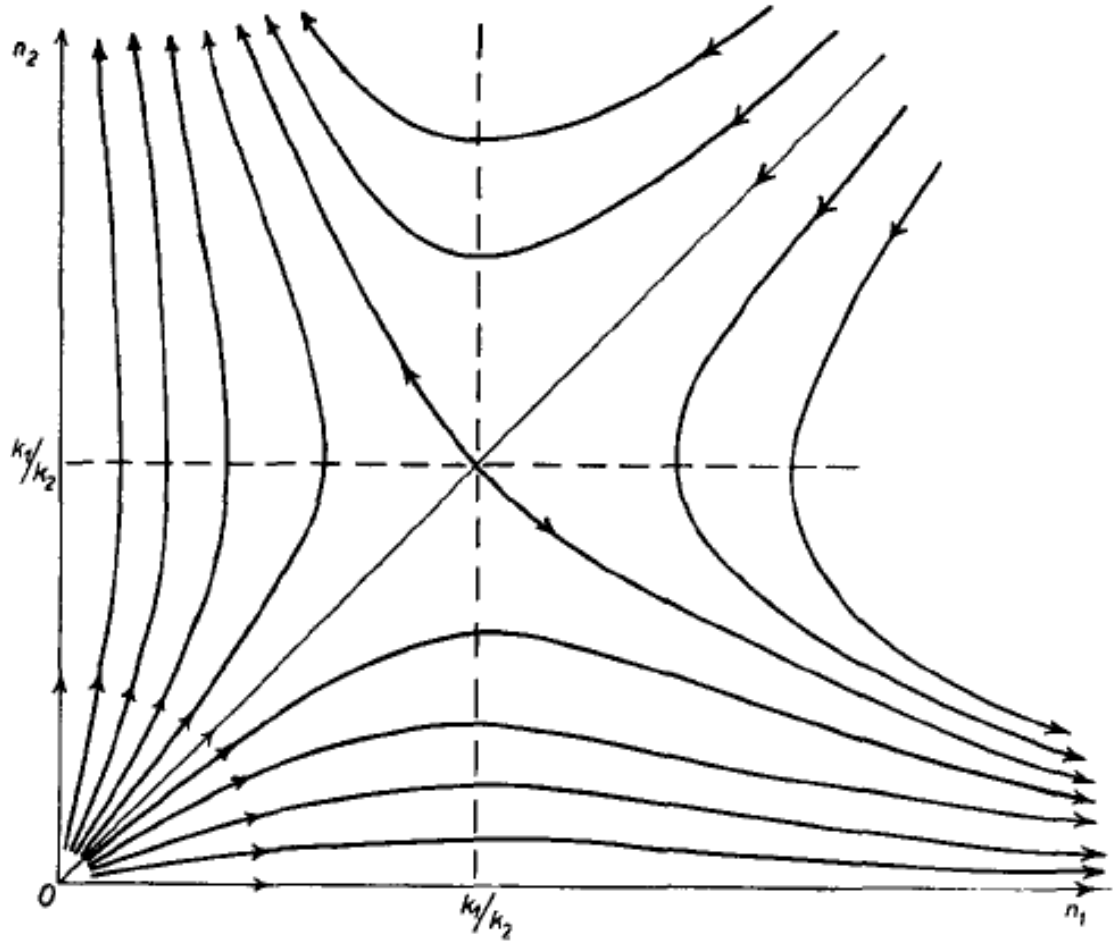


Figure 2.2: Sketch of general form of solutions of equations 2.2 and 2.3<sup>[16]</sup>

The above plot shows the relationship of time to the logarithm of the distance and the distance from the line  $n_1 = n_2$ . The difference  $n_1 - n_2$  increases significantly, however there is always the possibility of a reverse in the sign of the difference. An analogy demonstrating this statistical fluctuation is a marble running downhill which is likely to find itself in the gutter on either side of the road. The marble on its path may encounter pebbles which will displace to the opposite side, however it is likely to end up at the side where it is at that time. Even though the travelling path of the marble before finishing off in the gutter is infinite its statistical variation is very limited.<sup>[16]</sup>

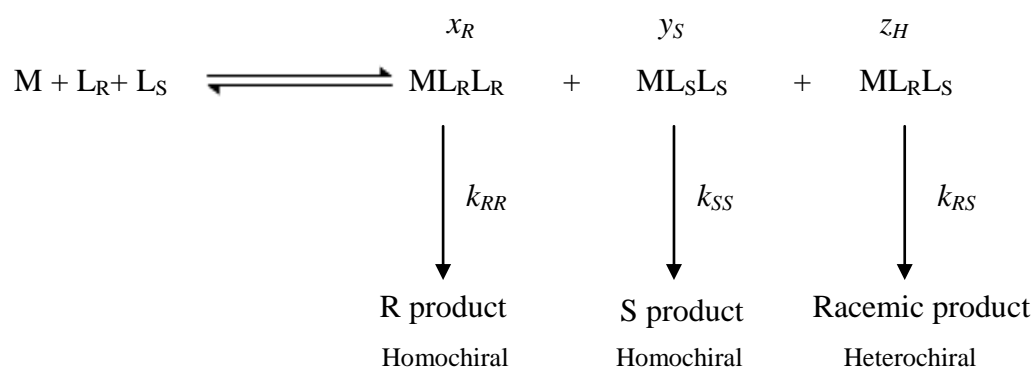


### 2.1.2 The Kagan Model

Kagan put together empirical models for NLEs mainly applied to diastereomeric interactions between metals and chiral ligands.<sup>[17]</sup> Kagan's group has published work on asymmetric autocatalysis since 1986. In recent years, Blackmond *et al* have built on this work in understanding asymmetric autocatalysis.

Kagan argued against the linear relationship between product and starting material *ee* for certain reactions. The mechanisms of the reactions studied by Kagan *et al* in 1986 all required complex intermediates. In conclusion the interactions between reagents, generating diastereoisomeric intermediates, influenced the *ee* of the reaction products.<sup>[29]</sup>

Kagan and co-workers defined a system in which metal atoms form complexes with ligands with the outcome of amplification of *ee*. This system was described as  $ML_n$ , with the  $M$  referring to the metal atom and  $L_n$  referring to  $n$  molecules of the  $L$  ligand. The  $ML_2$  system is likely relevant to the Soai reaction, which will be examined in this thesis in more depth.<sup>[29]</sup>



**Figure 2.3: Outline of Kagan  $ML_2$  mechanism**

Whereby:

$M$  = Metal centre to which ligands attach

$L$  = Ligand (can be either R or S)

$L_R$  = R- enantiomer of the ligand

$L_S$  = S- enantiomer of the ligand

$x_R$  = Steady-state concentration of R homochiral complex (mol dm<sup>-3</sup>)

$y_S$  = Steady-state concentration of S homochiral complex (mol dm<sup>-3</sup>)

$z_H$  = Steady-state concentration of heterochiral complex (mol dm<sup>-3</sup>)

$k_{RR}$  = First order rate constant for formation of R enantiomer (s<sup>-1</sup>)

$k_{SS}$  = First order rate constant for formation of S enantiomers (equal to  $k_{RR}$ ) (s<sup>-1</sup>)

$k_{RS}$  = First order rate constant for formation of racemic product (s<sup>-1</sup>)

The  $ML_2$  mechanism describes a metal binding with 2 chiral ligands to form either homochiral ( $ML_RL_R$  and  $ML_SL_S$ ) or heterochiral ( $ML_RL_S$ ) complexes ( $ML_RL_S$  is considered equivalent to  $ML_SL_R$ ). The assumption is that the homochiral complex catalyses the formation of its respective enantiomer; the heterochiral complex catalyses the formation of a racemic product. Another assumption made was non-dependence of the metal in any of these catalytic reaction steps i.e. first-order reaction.<sup>[29]</sup> From these assumptions the following set of equations relating the *ee* of products to that of the starting materials were derived.

$$ee_{prod} = ee_0 \times ee_{aux} \times \frac{1 + \beta}{1 + g\beta}, \quad 2.9$$

Wherein:

$$\beta = \frac{z_H}{x_R + y_S} \quad 2.10$$

$$g = \frac{k_{RS}}{k_{RR}} \quad 2.11$$

$\beta$  denotes the ratio of heterochiral to homochiral complexes in the reacting mixture, whereas  $g$  denotes the ratio of the activity of heterochiral to homochiral complexes in product formation.

The absence of any heterochiral complexes is represented by the case with  $\beta = 0$ . This according to equation 2.5 would imply a linear relationship between the  $ee$  of the product and the  $ee$  of the starting material. In this case equation 2.1 and 2.5 are similar implying that heterochiral dimers are fundamental for non-linear effects in the mechanism proposed by Kagan because  $\beta$  is not zero.

From equation 2.5 the value of the factor  $[(1 + \beta)/(1 + g\beta)]$  needs to be as large as possible in order to have a large (+)-NLEs. This can be achieved by having a large value for  $\beta$  and a minute value for  $g$ . A large  $\beta$  value would mean there must be a large amount of heterochiral material formed in the reacting mixture; this would consume large amounts of the minor enantiomer. Mostly monomers of the enantiomer and inactive (since  $g$  is very small) heterochiral dimers are present in the reaction mixture. Dimerisation therefore acts to sequester away large quantities of the minor enantiomer into a catalytically inactive heterochiral species. The monomers left behind would gradually unite and develop into homochiral complexes. These formed homochiral complexes catalyse the development of the same enantiomer resulting in amplification of chirality.

Another variable defining the inter-conversion of homochiral and heterochiral dimers was used by Kagan and co-workers to calculate  $\beta$ .<sup>[17]</sup>

$$K_{Kagan} = \frac{z_H^2}{x_R y_s} \quad 2.12$$

$$\beta = \frac{-K_{Kagan} e.e.^2_{aux} + \sqrt{-4K_{Kagan} e.e.^2_{aux} + K_{Kagan}(4 + e.e.^2_{aux})}}{4 + K_{Kagan} e.e.^2_{aux}} \quad 2.13$$

Prior to the above calculation of  $\beta$ , Kagan *et al* suggested a purely statistical distribution of ligands,  $K_{Kagan} = 4$ . Substituting  $K_{Kagan} = 4$  in equation 2.13:

$$\beta = \frac{1 - ee_{aux}^2}{1 + ee_{aux}^2} \quad 2.14$$

Further combination of equation 2.10 and 2.5 acquires:

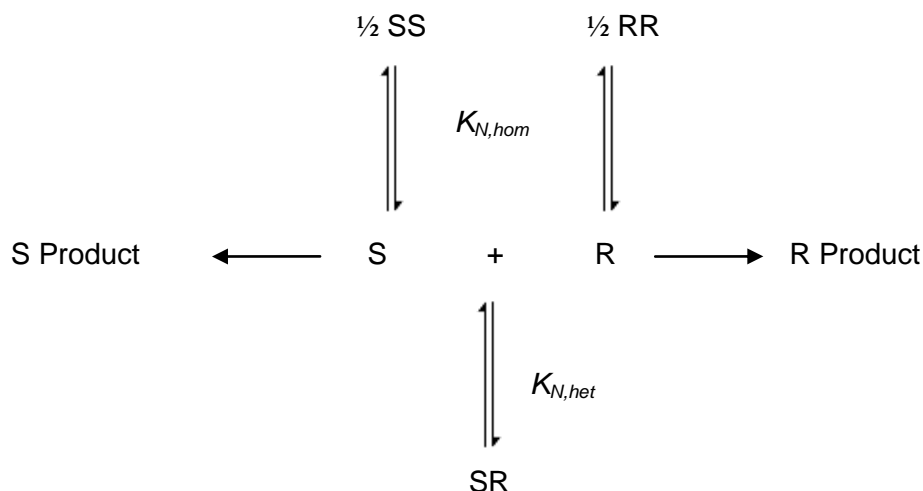
$$ee_{prod} = ee_0 \times ee_{aux} \times \frac{2}{1 + g + (1 - g)ee_{aux}^2} \quad 2.15$$

The above derived equation demonstrates that for a statistical distribution of ligands a non-linear effect exists except in cases where  $g = 1$ . Small values of  $g$  imply large (+)-NLEs; as  $g$  tends to 1, the probability of producing racemic products increases.

### 2.1.3 The Noyori Model

The reaction mechanism of the addition of dialkylzinc compounds to aldehydes using (-)-3-exo-(dimethylamino)isoborneol [commonly called (-)- DAIB] as a chiral catalyst was studied by Noyori and co-workers in 1989.<sup>[18]</sup> The proposed mechanism involves the reaction of DIAB and dialkylzinc to form a product which can either be R or S. Further combination of these products leads either to the formation of homochiral (RR or SS) or heterochiral (RS equivalent to SR) dimeric complexes.

The suggested mechanism is different from the Kagan scheme (Figure 2.3) because the *monomeric* species in the mechanism act as catalysts and the *dimeric* species are totally inactive. Kagan describes the *dimeric* species as catalytically active whereas the *monomers* are inactive.



**Figure 2.4: Illustration of the mechanism developed by Noyori *et al* to explain amplification of *ee*.**

Whereby:

$K_{N,hom}$  = Equilibrium constant for the *dissociation* of homochiral dimers ( $\text{mol dm}^{-3}$ )

$K_{N,het}$  = Equilibrium constant for the *dissociation* of heterochiral dimers ( $\text{mol dm}^{-3}$ )

$SS$  = S-homochiral dimer

$RR$  = R-homochiral dimer

$SR$  = Heterochiral dimer

From Figure 2.4 the dissociation constant values of  $K_{N,hom}$  and  $K_{N,het}$  are extremely important. Noyori *et al* established that if  $K_{N,hom} = 2K_{N,het}$ , the system confirms a linear effect; no amplification or depletion of *ee*. is the case. A positive non-linear effect is observed when  $K_{N,hom} > 2K_{N,het}$  and the *ee* of the product is amplified.<sup>[30]</sup>

For  $K_{N,hom} \gg K_{N,het}$ , the homochiral dimers are less stable than heterochiral dimers. Heterochiral dimers form stable, catalytically inactive species, which would consume most of the minor enantiomer. Mostly inactive heterochiral dimers would be present in the resulting solution with a small amount of active monomers. These active

monomers are derived primarily from the enantiomer which was initially in excess, since the enantiomer which was not in excess would be consumed in heterochiral dimer formation. Dimer formation is therefore necessary in sequestering away the minor enantiomer into an inactive heterochiral species.

Summarily, the required condition of  $K_{N,hom} > 2K_{N,hetero}$  in the Noyori *et al* model is similar to the required condition of  $\beta \gg 1$  in the Kagan *et al* mechanisms. The formation of dimers is preferred to monomers in both mechanisms, because the heterochiral dimers sequester away the minor enantiomer. In the Kagan *et al* mechanisms, the heterochiral dimers are inert, while the homochiral dimers are active catalysts. In the Noyori *et al* mechanism, both heterochiral and homochiral dimers are inert; *monomers* are the active catalysts.<sup>[18]</sup>

## 2.2 The Soai Autocatalytic Reaction

### 2.2.1 Introduction

The Soai Autocatalytic reaction is an example of asymmetric synthesis seen in the previous section. Considerable attention has been paid to understanding the mechanism of this reaction, which was discovered by Kenso Soai and coworkers over a decade ago.<sup>[1, 19-27, 31-33]</sup>

Unlike ordinary asymmetric catalysis, the Soai autocatalytic reaction is special because the chiral auxiliary and the product are identical. As a result, amplification of chirality is possible because the chiral product serves as the catalyst for its own generation. The enantiomeric excess *ee* can therefore be amplified to extremely high values, close to 99%.

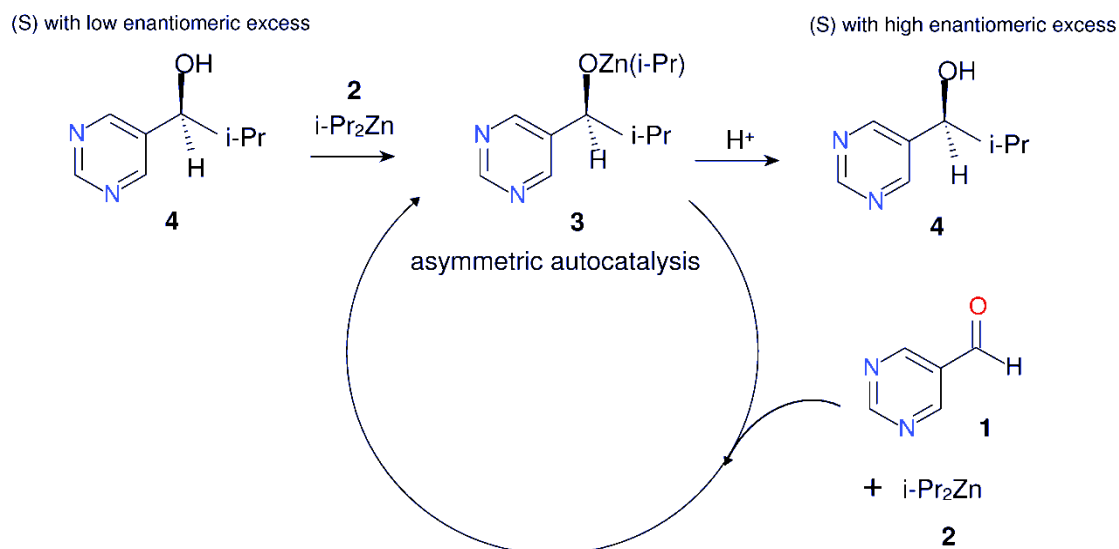


Figure 2.5: An example of the Soai autocatalytic reaction<sup>[1]</sup>

The autocatalytic Soai scheme involves the reaction of the pyrimidyl aldehyde **1** with diisopropylzinc **2** to an organozinc complex **3**, from which the pyrimidyl alcohol (product **4**) can be derived by hydrolysis. The chiral product **3** forms the pyrimidyl alcohol **4**, which further reacts with diisopropylzinc **2** to generate the same product i.e. the product of alkylation **4** and the chiral auxiliary are identical. Chiral amplification is attained because the configuration of the product alcohol leads to increased formation of more product alcohol with the same configuration. The advantages of asymmetric autocatalysis over conventional asymmetric synthesis include:<sup>[26, 27]</sup>

- i. A high efficiency by virtue of the amplification process.
- ii. The chiral catalyst concentration increases in the course of the reaction.
- iii. Separation of the product and the catalysts is not required since both are chemically identical.

### 2.2.2 Discovery and development of highly enantioselective asymmetric autocatalysis

Enormous developments in asymmetric synthesis have been realized over the last decades.<sup>[26, 27, 34-38]</sup> Development is targeted towards achieving high enantioselectivity by designing precursors and chiral catalysts. Within this field of synthetic chemistry research, the automultiplication of chiral compounds has been regarded as kind of molecular replication that has attracted scientists including Soai and co-workers.

Soai and co-workers reacted aldehydes with dialkylzincs in the presence of  $\beta$ -amino alcohols as chiral catalysts. Examples of such chiral catalysts include N,N-dibutylnorephedrine (DBNE) **1**, 1-phenyl-2-(1-pyrrolidiny)-1-propanol (PPP) **2** and diphenyl(1-methylpyrrolidin-2-yl)methanol (DPMPM) **3**.<sup>[22]</sup>

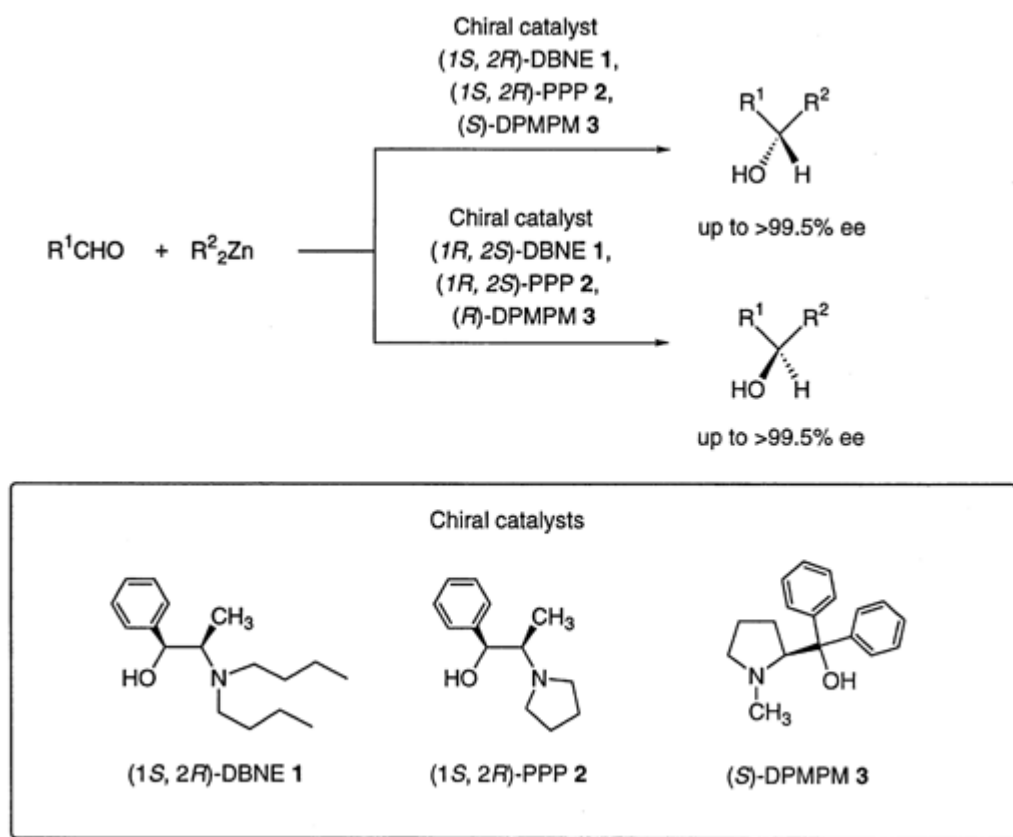
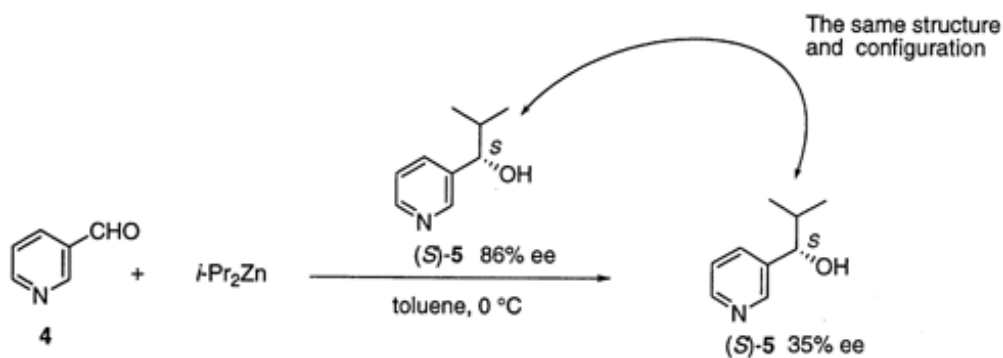


Figure 2.6: Dialkylzinc addition to aldehydes using chiral catalysts.<sup>[22]</sup>



Further studies revealed that the reaction of diethylzinc with pyridine-3-carbaldehyde, a nitrogen-containing aldehyde, at 0°C in the presence of DBNE **1** (chiral catalyst), reached completion 16 times faster than a similar reaction utilizing benzaldehyde. A possible reason for this may be ethylzinc alkoxide of 3-pyridyl alkanol **5**, acting as an asymmetric autocatalyst. This observation was the breakthrough of the first asymmetric autocatalytic reaction involving the enantioselective addition of diisopropylzinc (*i*-Pr<sub>2</sub>Zn) to pyridine-3-carbaldehyde **4** with a 35% *ee* of (*S*)-3-pyridyl alkanol **5**.



**Figure 2.7** Enantioselective addition of dialkylzincs to pyridine aldehydes.<sup>[22]</sup>

Chiral 5-pyrimidyl alkanol **7** which comprises two nitrogen atoms on the aromatic ring acts as a highly enantioselective asymmetric autocatalyst. In the case of (*S*)-2-methyl-5-pyrimidyl alkanol **7** up to 98% *ee* is attainable with the same structure as the autocatalyst.

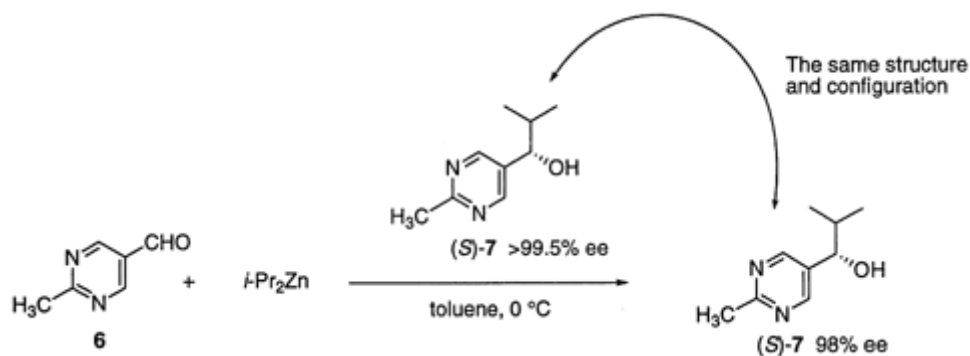


Figure 2.8: Enantioselective alkylation of pyrimidine aldehyde<sup>[22]</sup>

Interestingly the R group of the pyrimidyl aldehyde influences the degree of enantioselectivity. Practically perfect asymmetric autocatalysis was found to be the case when **10** is the autocatalyst with up to >99.5% *ee*.

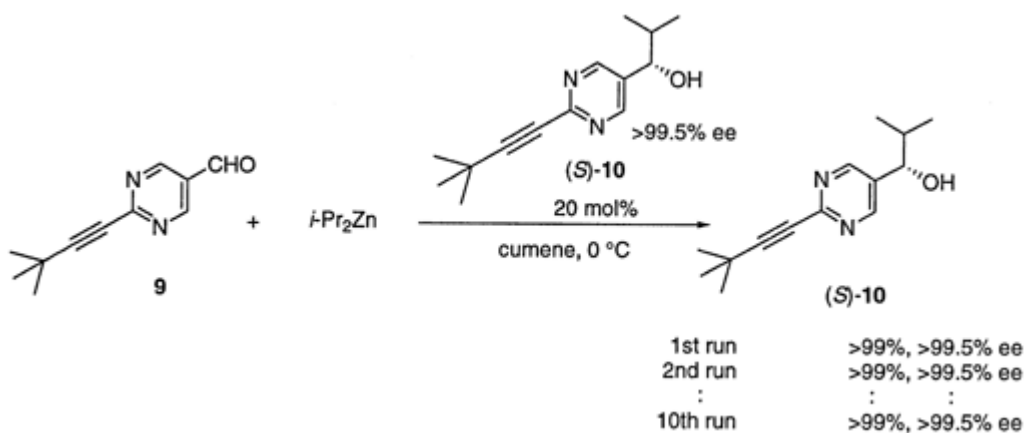
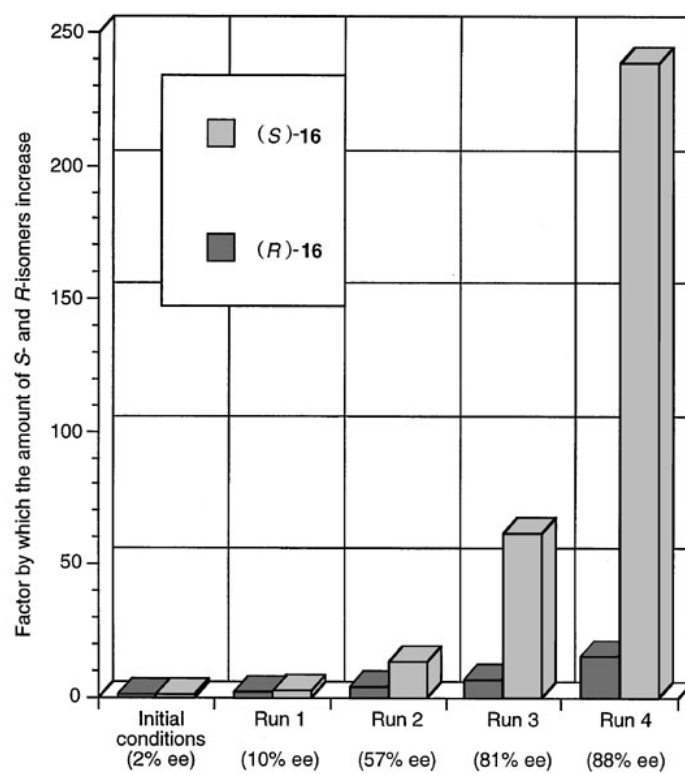


Figure 2.9: Practically perfect asymmetric autocatalysis in which the product is used as the asymmetric autocatalyst for the next run.<sup>[22]</sup>

The positive non-linear effect in the above is obvious with the *ee* of the produced pyrimidyl alcohol higher than the asymmetric autocatalyst. Consecutive asymmetric autocatalysis was found to achieve a high *ee* with minute initial amounts of the autocatalyst.



**Figure 2.10:** Consecutive asymmetric autocatalysis of (S)-16 with amplification of enantiomeric excess.<sup>[22]</sup>

### 3. Mechanistic approaches to understanding the Soai autocatalytic reaction

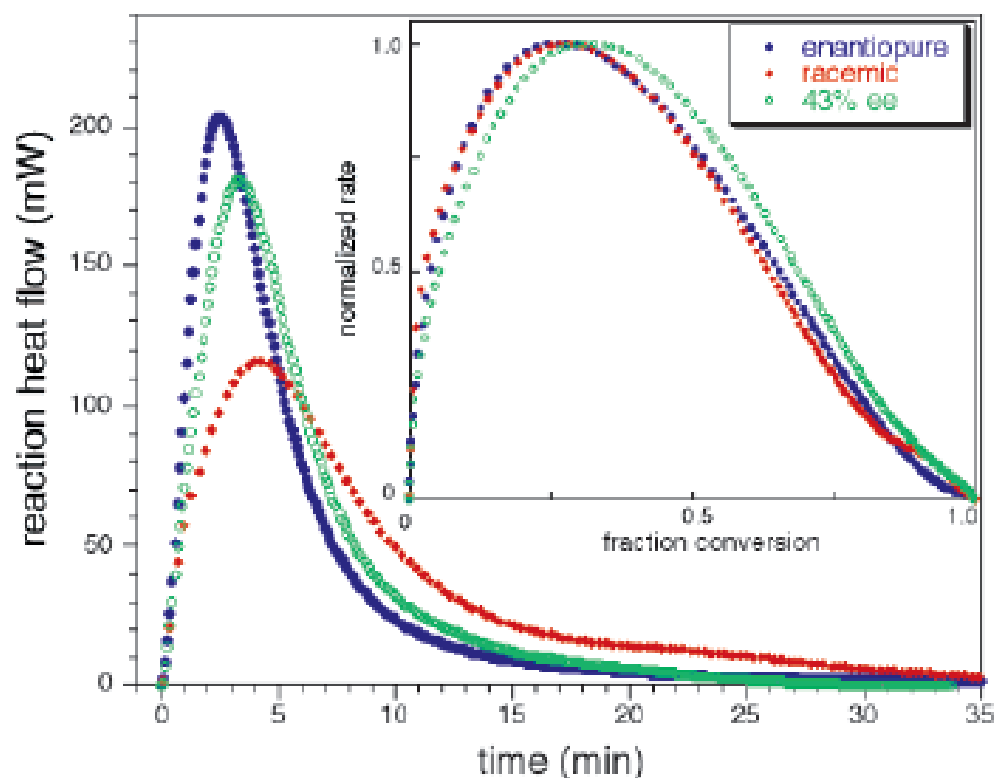
A summary of recently proposed mechanisms for the Soai autocatalytic reaction is visited in this section. Of particular importance are the mechanisms proposed by Blackmond, Brown, Soai, Buhse and co-workers. The essence of this section is to obtain knowledge that so far contributes to the understanding of the molecular mechanism behind amplification of chirality.

#### 3.1 The Blackmond Model

Blackmond's first publication on non-linear effects was built on the Kagan  $ML_2$  and  $ML_3$  models (introduced in section 2.1.2),<sup>[39]</sup> which were evaluated using experimentally determined rates of asymmetric synthesis reactions. These studies formed the foundation for subsequent mechanistic studies of the Soai reaction, which will be summarised further below.<sup>[40, 41]</sup>

##### 3.1.1 Dimer Model

The foundation of the dimer model as the active catalyst is based on its suitability when compared with experimental data. Reaction microcalorimetry (Omnical CRC90) at room temperature has been used as a kinetic tool to follow the progress of the Soai reaction.<sup>[41-44]</sup> Three optical purities were tested, with autocatalyst of 97% *ee*, 43% *ee* and a racemic autocatalyst mixture. As can be seen in Figure 3.1 the rate of reaction is higher with an enantiopure catalyst and least with a racemic catalyst. However, after normalisation to relative conversion the kinetic profiles of the different autocatalyst are very similar.<sup>[42]</sup>



**Figure 3.1:** Reaction heat flow against time of differing enantiomeric excess: 97%, 43% and 0%<sup>[42]</sup>

In fact, the normalized rate profiles for the 97% *ee* and racemic autocatalyst mixtures were found to be almost identical. This suggests that the kinetic order and hence the reaction mechanism is similar. Very significantly, the reaction rate observed with the 97% enantiopure autocatalyst was approximately twice that of the rate observed with the racemic system. This indicates that the concentration of the active catalyst is influenced by the catalyst *ee*, supporting the view that the action of some components in the racemic system, are suppressed. The system therefore appears to exhibit features intrinsic to the Kagan and Noyori models discussed in section 2.1 above.

Predictions derived from the amplification mechanisms proposed by Kagan and Noyori (section 2.1.3 above) were therefore discussed in light of the experimentally

derived dependence of the reaction rate on enantiopurity.<sup>[42]</sup> The main features of the Noyori and Kagan schemes are summarised once more in Figure 3.3 below, which indicate the role of monomer and dimer catalysts respectively.

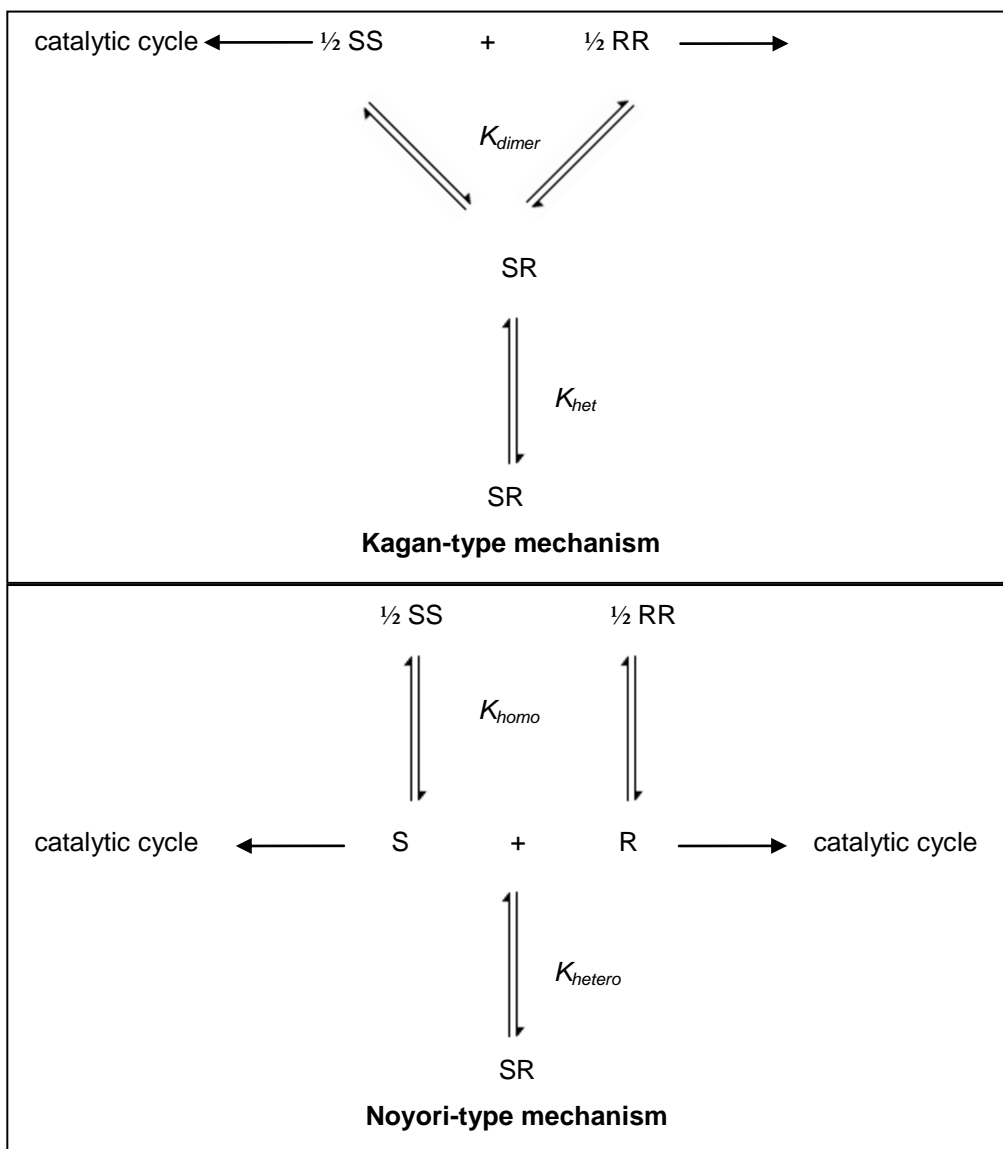


Figure 3.2: Simplified Kagan and Noyori mechanisms.<sup>[43]</sup>

The Noyori scheme contains the equilibrium constant for the dissociation of homochiral dimers,  $RR$  and  $SS$  ( $\text{mol}^{-1} \text{dm}^3$ )

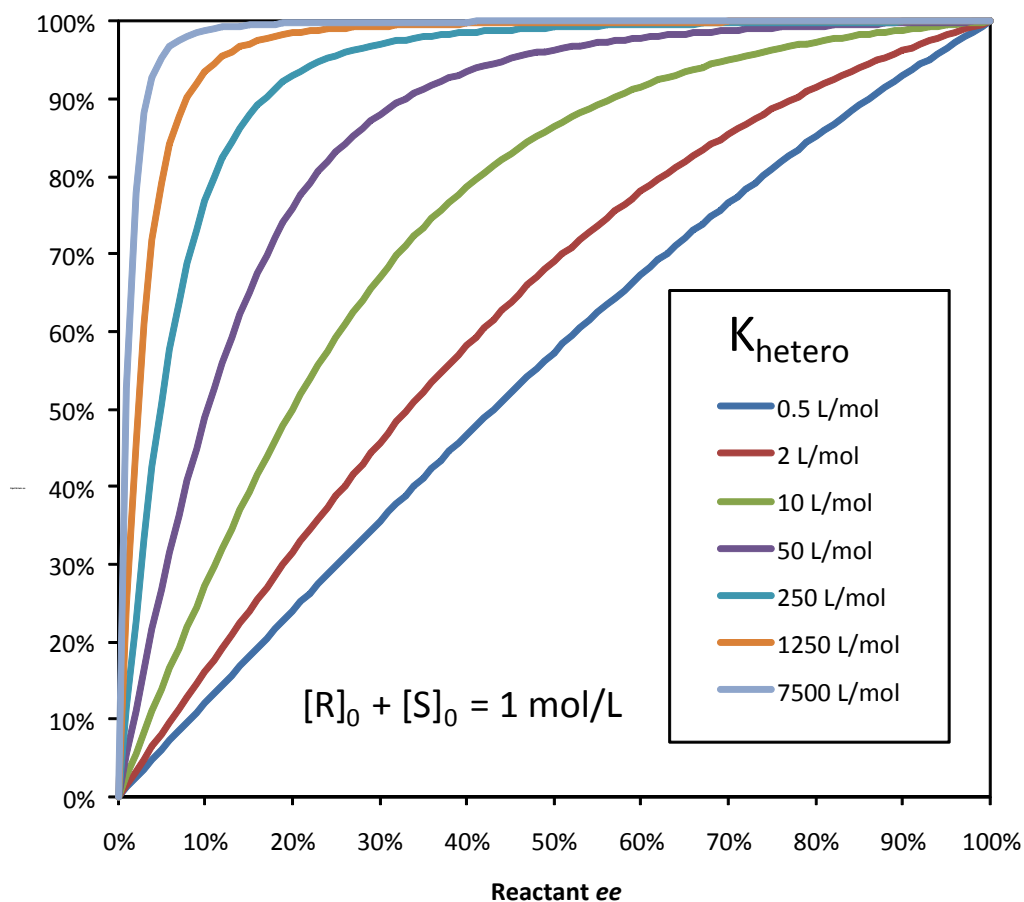
$$K_{\text{homo}} = \frac{[RR]}{[R]^2} = \frac{[SS]}{[S]^2},$$

and the equilibrium constant for the dissociation of heterochiral dimers, RS and SR

$$(\text{mol}^{-1} \text{ dm}^3)$$

$$K_{\text{hetero}} = \frac{[RS]}{[R][S]}$$

It can be seen that in the Noyori scheme formation of catalytically inactive homodimers according to the equilibrium constant  $K_{\text{homo}}$  lowers the concentration of both monomeric enantiomers, but without any influence on enantiomeric excess in the reactant solution. Amplification of enantiomeric excess can occur when the equilibrium constant for the formation of the RS heterodimer is sufficiently high: removal of equal amounts of minor and major enantiomer in the form of the RS dimer then depletes the concentration of the minor enantiomer relatively more than that of the major enantiomer. The reactant solution then has a lower total concentration  $[S] + [R]$  of the monomers, but a higher enantiomeric excess. For this effect to become significant a reasonably high value of  $K_{\text{hetero}}$  is necessary. The dependence on the magnitude of  $K_{\text{hetero}}$  is illustrated quantitatively (Figure 3.3).



**Figure 3.3: Amplification of enantiomeric excess in a 1 molar solution of S and R monomers through RS heterodimer formation (Noyori model). The lines represent increasing values of the equilibrium constant  $K_{\text{hetero}}$  for heterodimer formation (see inset for values of  $K_{\text{hetero}}$ ).**

Blackmond *et al* suggested that the observed doubling of the reaction rate when replacing the racemic mixture with an enantiopure reactant (Figure 3.1) can be reconciled with the Noyori mechanism only if all three types of dimers are formed with equal probability. Such a purely statistical (‘non-selective’) distribution would imply the absence of any free energy difference between hetero- and homochiral dimers, and the concentrations of SS, RS and RR dimers formed in the racemate would follow a distribution of 1:2:1, respectively. Half of the dimers would be RS, while RR and SS dimers contribute 25% of the total dimer population. As will be



shown in the next section, the equilibrium constants  $K_{hetero}$  and  $K_{homo}$  for a purely statistical dimer distribution are related through  $K_{hetero} = 2K_{homo}$ . Blackmond *et al* appear to be arguing that the halving of the reaction rate in the racemic system is due to removing ~50% of the monomeric S and R molecules from the available pool as RS dimers. By implication, if dimer formation were indeed non-selective, the remaining 25% each of R and S molecules would have to form quantitatively RR and SS dimers. To achieve such quantitative turnover into dimers the absolute values of the equilibrium constants for heterodimer formation,  $K_{hetero}$ , and for homodimer formation,  $K_{homo}$ , would have to be very large. To achieve the halved reaction rate of the racemate the homochiral dimer species then would also have to carry the chiral amplification reaction, in contradiction to the original Noyori mechanism, in which all dimer species are presumed inactive.

Blackmond *et al* argue further that amplification of chirality is not possible with a statistical selection of dimers, with  $K_{hetero} = 2K_{homo}$ . This would indeed be the case if monomers are quantitatively transformed into homochiral and heterochiral dimers, because in this case the diastereomeric distribution of dimers would always mirror the original enantiomeric excess.

It is instructive for further discussions below to derive the relationship  $K_{hetero} = 2K_{homo}$  from first principles, using elementary statistics. For this we consider  $n$  molecule pairs randomly drawn (without replacement) from a pool of  $2n$  molecules, of which  $r$  molecules have R-configuration and  $s$  molecules have S-configuration, with  $2n = r + s$ . If the two types of molecules cannot otherwise be distinguished then the probability of drawing an R molecule from such a pool is  $r/2n$ . The probability of immediately drawing another R molecule is  $(r-1)/(2n-1)$ , hence the probability of forming an RR pair is

$$P(RR) = \frac{r}{2n} \times \frac{r-1}{2n-1} \text{ if } r \geq 2, \text{ and}$$

$$P(RR) = 0 \text{ if } r < 2.$$

On average this probability remains the same for all of the  $n$  pair formation events. Hence the expectation value  $E(RR)$  for forming pairs of RR molecules in  $n$  pairing events will be

$$E(RR) = nP(RR) = n \times \frac{r}{2n} \times \frac{r-1}{2n-1} = \frac{r(r-1)}{2(2n-1)} \text{ if } r \geq 2, \text{ and}$$

$$P(RR) = 0 \text{ if } r < 2.$$

The expectation value for pairs of SS molecules can now be calculated with the equivalent formula, as

$$E(SS) = \frac{s(s-1)}{2(2n-1)} \text{ if } s \geq 2$$

and the expectation value for RS pairs follows as

$$E(RS) = n - E(RR) - E(SS),$$

Or, with  $s = 2n - r$ ,

$$E(RS) = n - \frac{r(r-1)}{2(2n-1)} - \frac{s(s-1)}{2(2n-1)} = 2E(RR) \times \frac{2n-r}{r-1}.$$

For a racemate ( $n = r$ ) this expression becomes  $E(RS) \approx 2 E(RR)$ .

We also find that

$$\frac{E(RS)}{E(RR)} = 2 \times \frac{2n-r}{r-1},$$

which is an expression useful for showing why the equilibrium constant for homodimer formation in a non-selective system is always half that of heterodimer formation. For this we consider the ratio between  $K_{\text{hetero}}$  and  $K_{\text{homo}}$

$$\frac{K_{\text{hetero}}}{K_{\text{homo}}} = \frac{[RS]}{[R][S]} \times \frac{[R]^2}{[RR]} = \frac{[RS]}{[RR]} \times \frac{[R]}{[S]}.$$

The ratio between the concentrations of hetero- and homodimers concentrations is equal to the ratio between their statistical expectation values,

$$\frac{E(RS)}{E(SS)} = \frac{[RS]}{[RR]},$$

so we can also write

$$\frac{K_{\text{hetero}}}{K_{\text{homo}}} = \frac{E(RS)}{E(SS)} \times \frac{[R]}{[S]} = 2 \times \frac{2n-r}{r-1} \times \frac{[R]}{[S]}.$$

We now identify  $2n - r$  as just the number of S molecules in SS dimers, which will be proportional to the equilibrium concentration of [S]. Furthermore, for a large population of molecules ( $r \rightarrow \infty$ )  $r - 1 \approx r$ . Because S and R molecules are chemically indistinguishable the proportionality as for  $s$  and [S] applies equally to  $r$  and [R]. For a large population of molecules we can therefore write that

$$\frac{K_{\text{hetero}}}{K_{\text{homo}}} = 2 \times \frac{s}{r-1} \times \frac{[R]}{[S]} \approx 2 \times \frac{[S]}{[R]} \times \frac{[R]}{[S]} = 2,$$

From which follows the expression  $K_{\text{hetero}} = 2K_{\text{homo}}$  used by Blackmond *et al.*

However, within the Noyori monomer catalysis scheme an alternative interpretation of the experimental findings of Blackmond *et al* is possible. If the equilibrium constants for dimerisation were such that 50% of all monomers are removed from the solution then the halving of the reaction rate indicated by the data in Figure 3.1 could be achieved as well, even though monomer catalysis would be taking place. If there was additionally a preference for heterochiral RS dimer formation then chiral amplification similar to that illustrated in Figure 3.3 could be achieved. Such mechanisms have in fact been explored by Buhse and co-workers who have shown

that Noyori-type monomeric chiral amplification is at least theoretically compatible with the rate measurements presented by Blackmond.<sup>[42]</sup> It appears that more detailed further experimental work might be required to identify the species that is actually the catalyst responsible for amplification.

Currently, on balance, the experimental consensus leans towards acknowledging the presence of large quantities of dimer species, and hence the construction of mechanistic scenarios based on dimer catalysis. This is a reasonable choice because large quantities of dimers have been observed by NMR spectroscopic investigations.<sup>[42]</sup> Dimer catalysis is the basis of the Kagan model, in which the homochiral dimers (and not the monomers) are the chiral auxiliaries for amplifying enantiomeric excess.  $K_{\text{dimer}}$  is the dimensionless equilibrium constant for the direct formation of heterochiral dimers from homochiral dimers:

$$K_{\text{dimer}} = \frac{[RS]^2}{[RR][SS]}$$

By simple substitution with the values for  $K_{\text{hetero}}$  and  $K_{\text{homo}}$  (derived above in the context of the Noyori model) it also follows that

$$K_{\text{dimer}} = \frac{(K_{\text{hetero}}[R][S])^2}{(K_{\text{homo}}[R][S])^2} = \left( \frac{K_{\text{hetero}}}{K_{\text{homo}}} \right)^2$$

which implies that  $K_{\text{dimer}} = 4$  based on the proposal that  $K_{\text{hetero}} = 2K_{\text{homo}}$ .

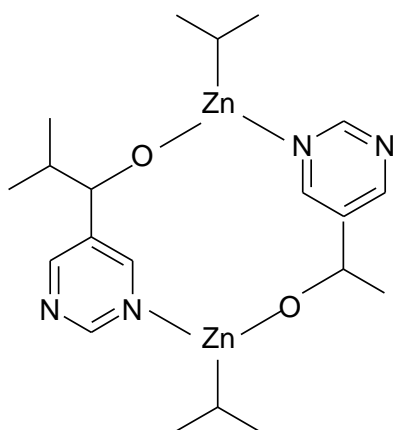
The rate equation in the modified  $ML_2$  Kagan system (considers the homodimer as the active catalysts as seen in section 2.1.2) used by Blackmond *et al* follows as:<sup>[42]</sup>

$$\text{Rate} = k_{1B} \times [\text{Aldehyde}] \times [\text{Pr}_2^i\text{Zn}] \times [\text{Alkoxide}] \times \left( \frac{1 + g\beta}{1 + \beta} \right) \quad 3.1$$

Whereby:

$k_{IB}$  = Reaction rate constant for the rate limiting step in the Blackmond *et al* 2001 mechanism ( $\text{mol}^{-2} \text{dm}^6 \text{s}^{-1}$ )<sup>[42]</sup>

It is necessary that  $g \ll 1$  for amplification of e.e. Blackmond reported that the rate profiles are modelled very accurately by the Kagan  $ML_2$  system and the heterochiral dimers are rendered *completely* inactive (i.e.  $g = 0$ ).<sup>[42]</sup> The proposed bimetallic active catalytic species responsible for the Soai autocatalytic reaction is seen in Figure 3.4.



**Figure 3.4 : Blackmond's proposed active metal catalyst.**<sup>[42]</sup>

Further work by Blackmond refined the dimer-catalysis model, as summarised in Figure 3.5. The formation of the dimers (RR, SS and RS) was again by virtue of a *statistical distribution* (no free energy difference between homo- and heterochiral dimers) and the amplification of *ee* was achieved by the active homochiral dimer catalyst.<sup>[45]</sup>

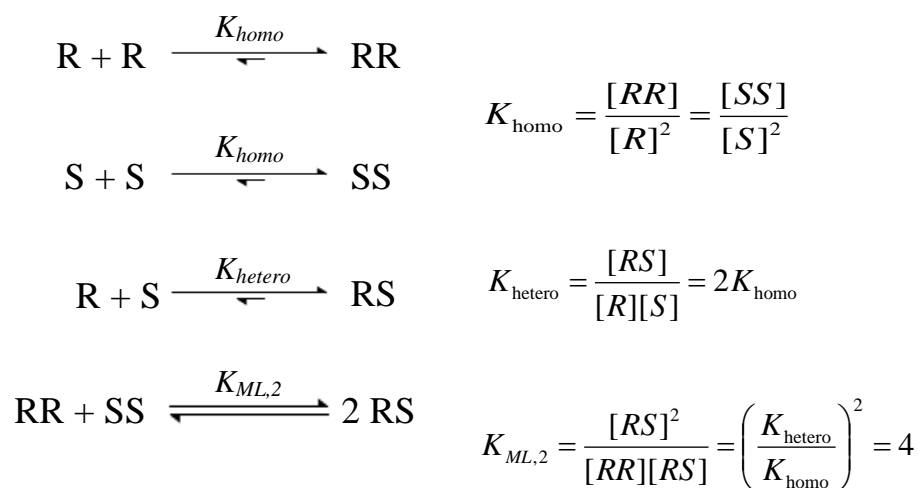


Figure 3.5: Formation of dimer species from monomeric alkoxides.<sup>[45]</sup>

Later in 2006, Blackmond without any given justification decided to neglect the reaction for the direct interconversion of homochiral and heterochiral dimers, i.e.

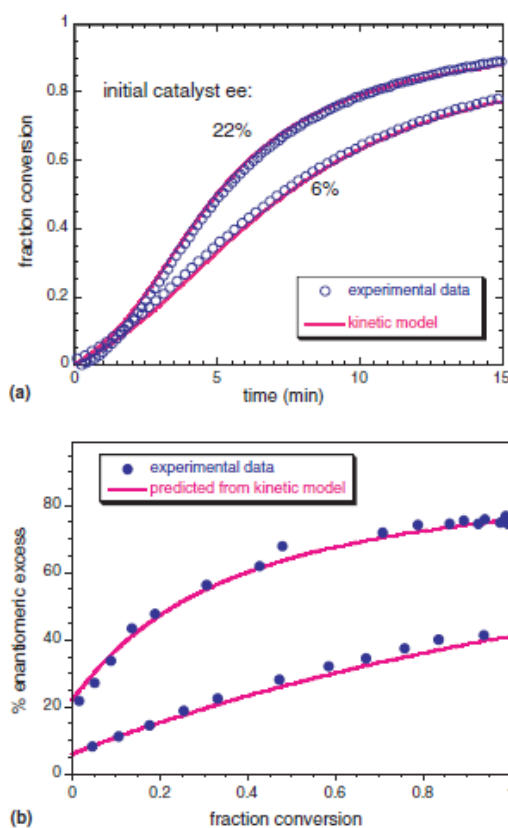
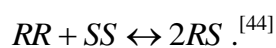
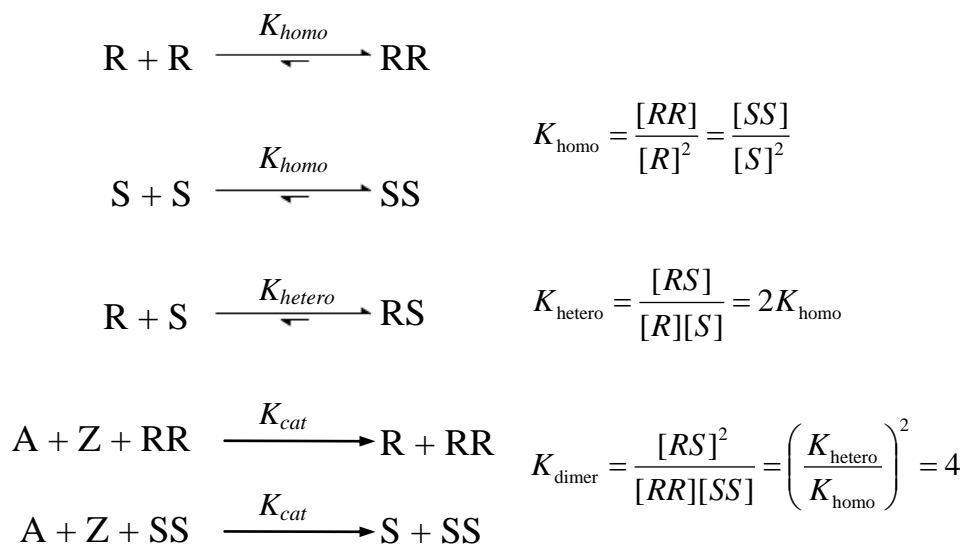


Figure 3.6: Experimental kinetic data and dimer model calculations for reactions at 22% and 6% initial ee Initial concentrations  $[\text{A}] = 0.2\text{M}$ ;  $[\text{Z}] = 0.4\text{M}$ ; catalyst 10%.<sup>[44]</sup>

The kinetic model used to fit experimental data was obtained from the following sequence of equations similar to the model developed in Figure 3.5. However, as previously mentioned the interconversion of homochiral and heterochiral dimers was completely omitted without justification (see Figure 3.7). Blackmond confirmed the *stochastic distribution* of dimer species by proton NMR in which racemic mixtures disclose the existence of heterochiral and homochiral dimers in a 50:50 ratio within experimental error as suggested by the kinetic model i.e.  $K_{dimer}=4$ . Blackmond describes the reaction of an aldehyde A and dialkylzinc Z with homodimers (RR or SS) as the active catalysts to produce alkanol products R and S; RS as the inactive catalytic species.



**Figure 3.7: Blackmond's dimer model.<sup>[44]</sup>**

From the above equations large values of  $K_{homo}$  and  $K_{hetero}$  are necessary for the formation of the hetero- and homodimers which are reported to have equal stability. The enantiomeric excess of the alkanol product is defined as follows:

$$e.e._{prod} = \frac{[RR] - [SS]}{[RR] + [SS] + [SR]} \quad 3.2$$

### 3.1.2 Tetramer

Blackmond also proposed a tetrameric model to explain the Soai autocatalytic reaction rates. The rate equation developed in previous works (equation 3.1) is used but the parameters  $g$  and  $\beta$  are excluded.<sup>[40]</sup>

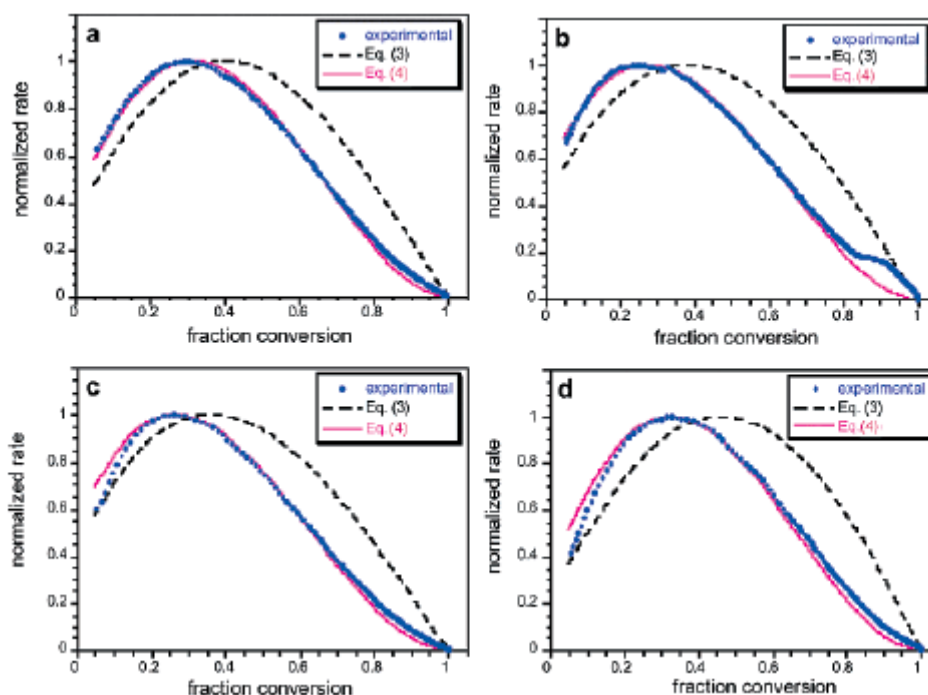
$$\text{Rate} = k_{2B} \times [\text{Aldehyde}] \times [\text{Pr}_2^i\text{Zn}] \times [\text{Catalyst}]_{\text{active}} \quad 3.3$$

Whereby:

$k_{2B}$  = Rate constant in the rate limiting step ( $\text{mol}^{-2} \text{dm}^6 \text{s}^{-1}$ )

$$[\text{Catalyst}]_{\text{active}} = [\text{RR}] + [\text{SS}] \quad 3.4$$

Blackmond and Buono suggested that equation 3.1 is only obeyed for equimolar ratios of the aldehyde and  $i\text{Pr}_2\text{Zn}$ . Figure 3.8 shows the reaction rate and the enantiomeric excess of four reactions with different stoichiometric ratios.



**Figure 3.8:** Reaction rate as a function of aldehyde. Blue circles: Experimental data; dash black line: Equation 3.1; solid pink line: Equation 3.2.<sup>[40]</sup>

The results shown above were obtained in toluene at 298 K and the initial concentration of the aldehyde was 0.1 M, with 10 mol% chiral alcohol catalyst. The



respective conditions of the above profiles are (a)  $ee$  (cat) = 0.22, 1.8 equiv  $iPr_2Zn$ , (b)  $ee$  (cat) = 0.02, 2.0 equiv  $iPr_2Zn$ , (c)  $ee$  (cat) = 0.97, 2.0 equiv  $iPr_2Zn$ , (d)  $ee$  (cat) = 0.22, 3.6 equiv  $iPr_2Zn$ . Blackmond and Buono justify equation 3.3 by proposing the formation of a complex between the aldehyde and  $iPr_2Zn$  (Figure 3.9) before the transfer of the alkyl group. Tetrameric structures are reported to be familiar in the reactions of dialkylzinc and amino alcohols.<sup>[40]</sup>

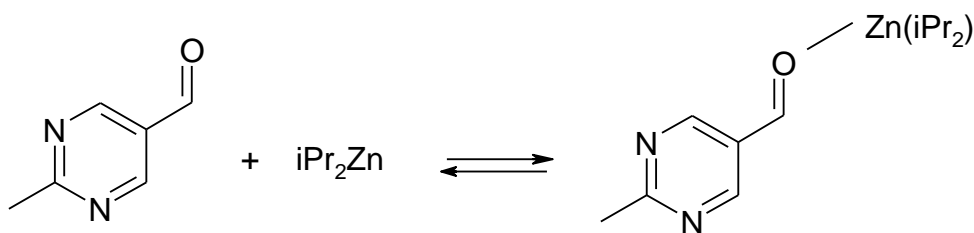


Figure 3.9: Aldehyde-  $iPr_2Zn$  complex<sup>[40]</sup>

### 3.2 The Soai model

Soai and co-workers also made substantial effort in understanding the kinetics of the autocatalytic reaction capable of amplifying chirality using HPLC to determine the yield of the products with naphthalene as an internal standard. They proposed a model that focused on the kinetics and did not cater for the amplification of enantiomeric excess. The kinetic model was developed from different reactions of aldehyde and  $iPr_2Zn$  in the presence of minute amounts of an enantiopure catalyst.<sup>[19]</sup>

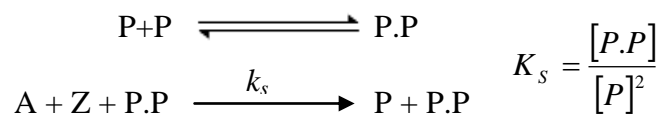


Figure 3.10: Scheme proposed by Soai and coworkers<sup>[19]</sup>

$A$  = Aldehyde;  $Z$  =  $iPr_2Zn$

$P$  = Reaction product (either R or S)

$P.P$  = Dimeric catalyst species (either homochiral or heterochiral)

$k_s$  = Rate constant for dimer-catalysed product formation ( $\text{mol}^{-2} \text{dm}^6 \text{s}^{-1}$ )

$K_s$  = Equilibrium constant for the formation of dimeric catalyst species ( $\text{mol}^{-1} \text{dm}^3$ )

From this scheme the rate of reaction,  $v$  ( $\text{mol dm}^{-3} \text{s}^{-1}$ ) is defined as:

$$v = -\frac{d[A]}{dt} = k_s[A][Z][P.P] = k_s K_s \times [A][Z][P]^2 \quad 3.5$$

Introducing the amount of reactant consumed or product formed results in:

$$-\frac{d[A]}{dt} = k_s K_s [A_0 - x] \times [Z_0 - x] \times [P_0 + x]^2 = \frac{dx}{dt} \quad 3.6$$

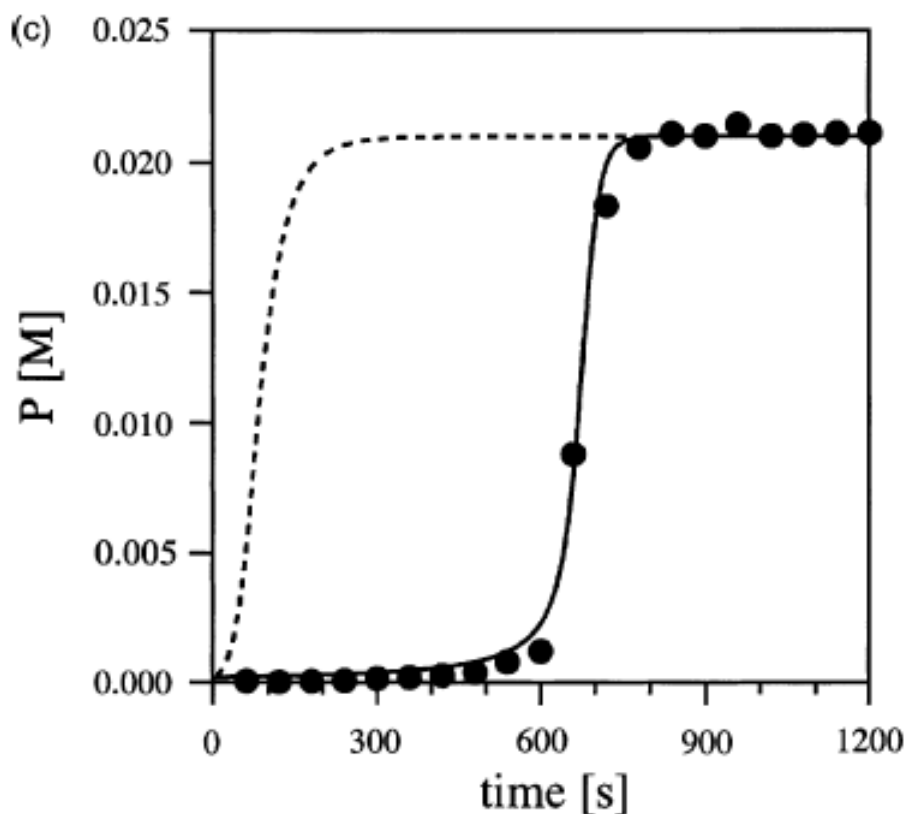
$A_0$  = Initial aldehyde concentration ( $\text{mol dm}^{-3}$ )

$P_0$  = Initial alkoxide product concentration ( $\text{mol dm}^{-3}$ )

$Z_0$  = Initial diisopropylzinc concentration ( $\text{mol dm}^{-3}$ )

$x$  = Amount of reactant consumed / amount of product formed ( $\text{mol dm}^{-3}$ )

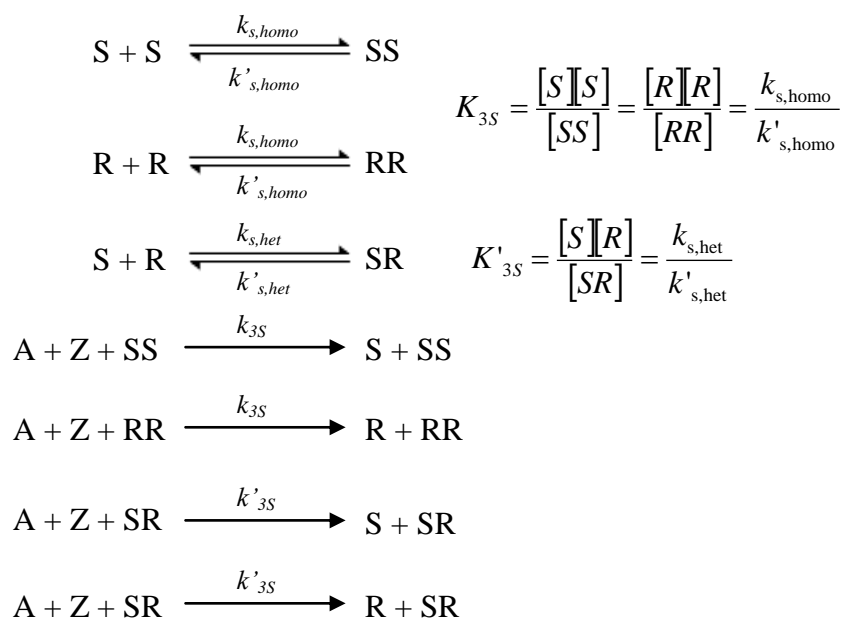
A comparison of kinetic simulation of the derived rate equation and experimental data is shown below. Clearly, it is a second order reaction and not first order as depicted by the simulation represented by dash lines.



**Figure 3.11:** Comparison of simulation (solid lines) with experimental points.  $T = 273\text{K}$ ;  $A_0 = 2.08 \times 10^{-2} \text{ M}$ ;  $Z_0 = 3.13 \times 10^{-2} \text{ M}$ ;  $P_0 = 2.08 \times 10^{-4} \text{ M}$ . Broken line represents simulation assuming a first-order autocatalytic reaction.<sup>[19]</sup>

This model which elucidates the kinetics does not provide information on a model to explain the amplification of *ee* in the reaction. They claim that this dimer model is suitable because of agreement between experimental and calculated data. However this work has been criticized by Blackmond *et al* because of the lack of crucial information on the suppression of a minor enantiomer and stereochemical information.<sup>[46]</sup>

The model was eventually improved by Soai and co-workers by considering amplification of *ee*.<sup>[32]</sup> The newly proposed mechanism shows similarity to that proposed by Blackmond and co-workers in 2001.<sup>[42]</sup> However unlike Blackmond, it is assumed that the heterodimers are active catalysts and there is a free association of dimers implying no statistical distribution.



**Figure 3.12: Model proposed by Soai and coworkers.**<sup>[32]</sup>

$K_{3S}$  = Equilibrium constant for homochiral dimer formation ( $\text{mol}^{-1} \text{dm}^3$ )

$K'_{3S}$  = Equilibrium constant for heterochiral dimer formation ( $\text{mol}^{-1} \text{dm}^3$ )

$k_{3S}$  = Reaction rate constant for homochiral dimer-catalysed alkoxide formation ( $\text{mol}^{-2} \text{dm}^{-6} \text{s}^{-1}$ )

$k'_{3S}$  = Reaction rate constant for heterochiral dimer-catalysed alkoxide formation ( $\text{mol}^{-2} \text{dm}^{-6} \text{s}^{-1}$ )

$k_{s,homo}$  = Reaction rate constant for *association* of homochiral dimers ( $\text{mol}^{-1} \text{dm}^3 \text{s}^{-1}$ )

$k'_{s,homo}$  = Reaction rate constant for the *dissociation* of homochiral dimers ( $\text{s}^{-1}$ )

$k_{s,het}$  = Reaction rate constant for *association* of heterochiral dimers ( $\text{mol}^{-1} \text{dm}^3 \text{s}^{-1}$ )

$k'_{s,het}$  = Reaction rate constant for the *dissociation* of heterochiral dimers ( $\text{s}^{-1}$ )

The parameters  $K_{3S}$  and  $K'_{3S}$  in the above mechanism are similar to  $K_{homo}$  and  $K_{hetero}$  respectively in the models developed by Blackmond *et al* in Figure 3.5. However, there is no statistical distribution i.e.  $K_{hetero} = 2K_{homo}$  in the Soai model. In addition

the Soai model does not include the interconversion of homochiral to heterochiral dimers which agrees with Blackmond's 2006 model.<sup>[44]</sup>

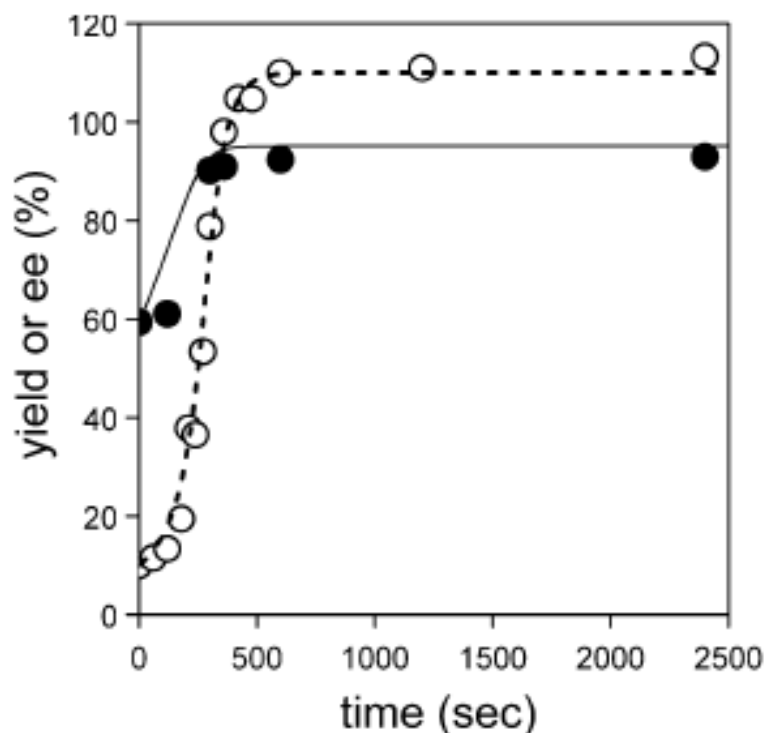
From the model (Figure 3.12) the following equations were derived on the basis that the concentration of the dimer is small relative to the monomer. However, this assumption may not be obeyed at later stages of the reaction.

$$\begin{aligned}\frac{d[S]}{dt} &= k_{3S} [A][Z][SS] + k'_{3S} [A][Z][SR] \\ &= k_{3S} K_{3S} [A][Z][S]^2 + k'_{3S} K'_{3S} [A][Z][S][R]\end{aligned}\tag{3.7}$$

$$\begin{aligned}\frac{d[R]}{dt} &= k_{3S} [A][Z][RR] + k'_{3S} [A][Z][SR] \\ &= k_{3S} K_{3S} [A][Z][R]^2 + k'_{3S} K'_{3S} [A][Z][S][R]\end{aligned}\tag{3.8}$$

$$\gamma = \frac{k_{3S} K_{3S}}{k_{3S} K_{3S} + k'_{3S} K'_{3S}}\tag{3.9}$$

The experimental and calculated results from the above rate equations are illustrated below. Yields and the *ee* (59.4 to 94 %) were found to increase rapidly after short incubation periods.



**Figure 3.13:** Comparison of simulation [yield: broken line; *ee*: solid line] with experimental points [yield: hollow circles; *ee*: filled circle] on asymmetric autocatalysis with initial *ee* of 59.4% at -25°C.<sup>[32]</sup>

It is obvious from this work that Soai and coworkers have proven that their dimer model explains the amplification of *ee* in asymmetric autocatalysis.

### 3.3 The Buhse model

The model proposed by Buhse and co-workers is apparently more realistic than the models earlier proposed by Blackmond<sup>[42]</sup> and Soai<sup>[32]</sup> in 2001 and 2003 respectively. The latter mentioned models consider that the association of  $i\text{Pr}_2\text{Zn}$ , the aldehyde and the dimeric catalysts occurs in one concerted rate limiting step. Buhse basically separated the three molecules in their model into two steps. In their model they assume that two alkoxide molecules combine to form dimeric species; a complex formed between the dimer and aldehyde; the aldehyde-dimer complex then reacts with  $i\text{Pr}_2\text{Zn}$  to form a product.<sup>[47]</sup>

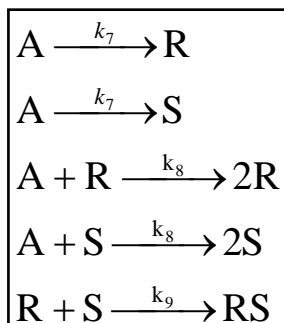
Process	Reaction	Rate Law
Irreversible formation of the zinc alkoxide	$\text{COH} + \text{Zn} \rightarrow \text{COZn}$	$R_1 = k_1[\text{COH}][\text{Zn}]$
	$\text{CHO} + \text{Zn} \rightarrow \text{COZn}$	$R_2 = k_2[\text{CHO}][\text{Zn}]$
Reversible zinc alkoxide dimerization equilibrium	$\text{COZn} + \text{COZn} \rightleftharpoons (\text{COZn})_2$	$R_{3a} = k_3[\text{COZn}]^2$ $R_{3b} = k_{-3}[(\text{COZn})_2]$
Reversible association of the carbaldehyde	$(\text{COZn})_2 + \text{CHO} \rightleftharpoons (\text{COZn})_2\text{-CHO}$	$R_{4a} = k_4[(\text{COZn})_2][\text{CHO}]$ $R_{4b} = k_{-4}[(\text{COZn})_2\text{-CHO}]$
Irreversible catalyzed formation of the zinc alkoxide	$(\text{COZn})_2\text{-CHO} + \text{Zn} \rightleftharpoons (\text{COZn})_2 + \text{COZn}$	$R_5 = k_5[(\text{COZn})_2\text{-CHO}][\text{Zn}]$
Side reaction	$\text{COH} + \text{CHO} \rightarrow \text{Reaction by-product}$	$R_6 = k_6[\text{COH}][\text{CHO}]$

Figure 3.14: Proposed kinetic model. k:rate constant<sup>[47]</sup>

In this model the possibility of an unspecified by product which was not considered by the other mentioned models is taken into account. This consideration evolves from the formation of fewer products than expected from the limiting reagent. In contrast to Blackmond and Soai, Buhse suggested that both homodimers and heterodimers are catalytically active.

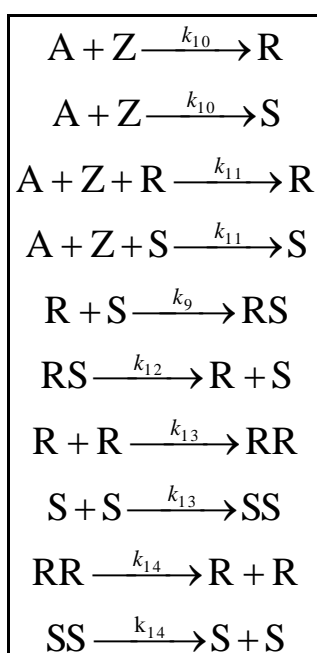
Further kinetic models were developed by Buhse<sup>[48]</sup> which considered the work of Noyori, Frank and Kagan. Three models that incorporate mutual inhibition and chiral autocatalytic steps have been proposed.

*Model 1* which is based on the Frank mechanism is seen below (k: rate constants):



**Figure 3.15: Frank model.**<sup>[48]</sup>

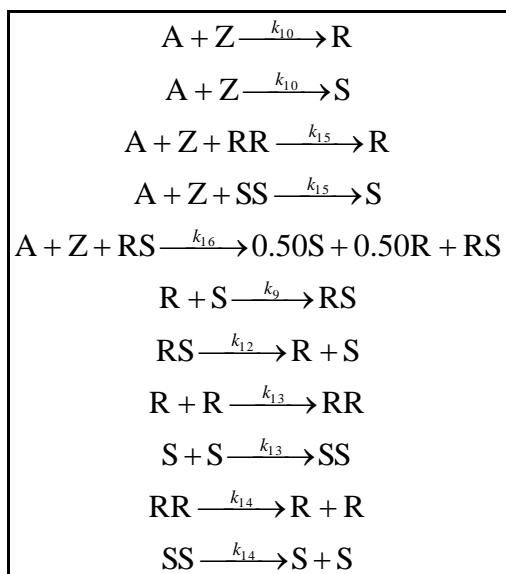
*Model 2* introduces an organozinc reactant Z with uncatalyzed steps. In this model the reversible formation of homochiral and heterochiral zinc alkoxide dimers is assumed based on the work of Noyori and coworkers.



**Figure 3.16: Noyori model.**<sup>[48]</sup>

*Model 3* is based on the work of Kagan and coworkers who began mentioning dimer catalysis to explain amplification of chirality. The monocatalysed steps are then substituted by dimer catalyzed steps.





**Figure 3.17: Kagan model**<sup>[48]</sup>

According to Buhse and co-workers because of more chemical realism, model 1 and 2 are comparable in mirror-breaking and amplification of chirality. However, amongst all three models, model 2 was found to give the best fit of the Soai reaction based on experimental kinetic data.<sup>[48]</sup>

### 3.4 The Brown model

The Soai autocatalytic reaction according to Brown like other scientists does not tally with well studied reactions of dialkylzinc with aldehydes. In contrast the monomeric catalysts cannot be used to explain the amplification process. Brown and co-workers support their studies with kinetic, NMR and computational techniques in order to elucidate possible mechanisms to explain asymmetric autocatalysis.<sup>[34, 49-51]</sup>

The fundamentals of the formation of a chelate complex capable of forming a dimer, is demonstrated by the work of Noyori and Kitamura in the illustration below.

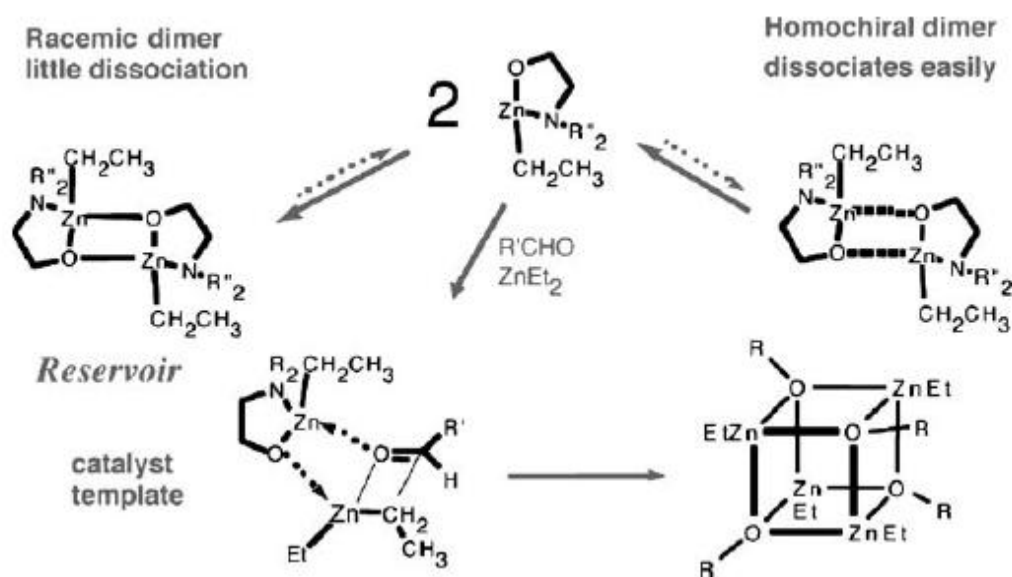
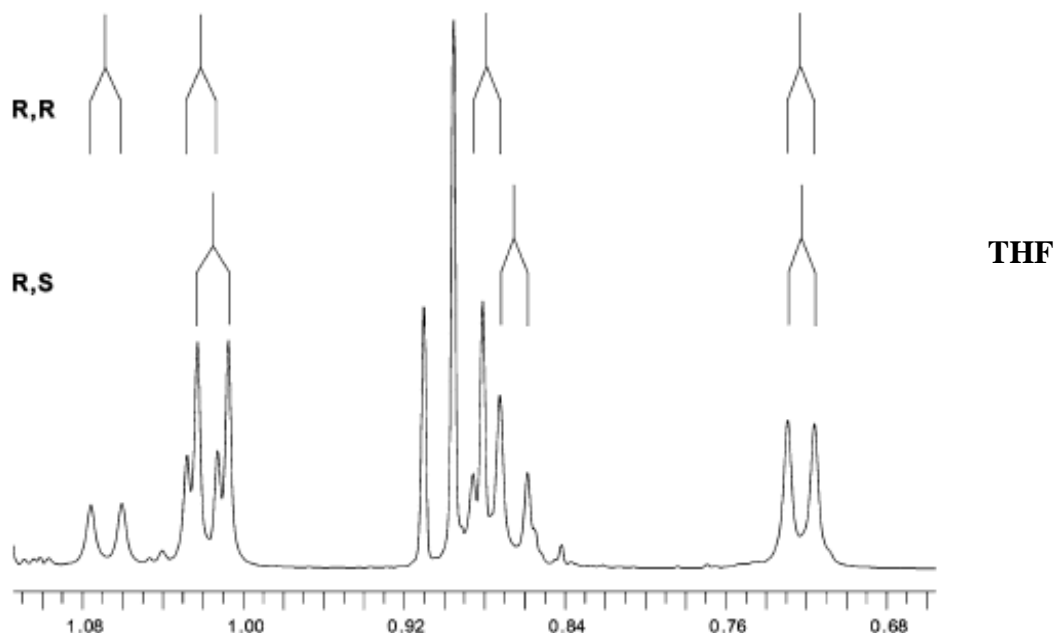


Figure 3.18: Fundamentals of Noyori and Kitamura model<sup>[51]</sup>

The monomer which forms a zinc chelate, is clearly reactive as it provides sites for the carbonyl compound by coordinating with zinc and dialkylzinc through oxygen coordination. The reason given for the high *ee* of the product over the catalyst is suggested to be due to the reservoir dimer behavior that releases the reactive monomer.<sup>[50]</sup> The presence of a ligand is important in identifying accessible sites for reactants and reagents. The catalyst is suggested to be a dimer that acts as a reservoir that releases monomers. The heterodimer which is energetically more stable than the homodimer reduces the concentration of one enantiomer resulting in a higher *ee* of the reactant product than the starting *ee* of the catalysts.

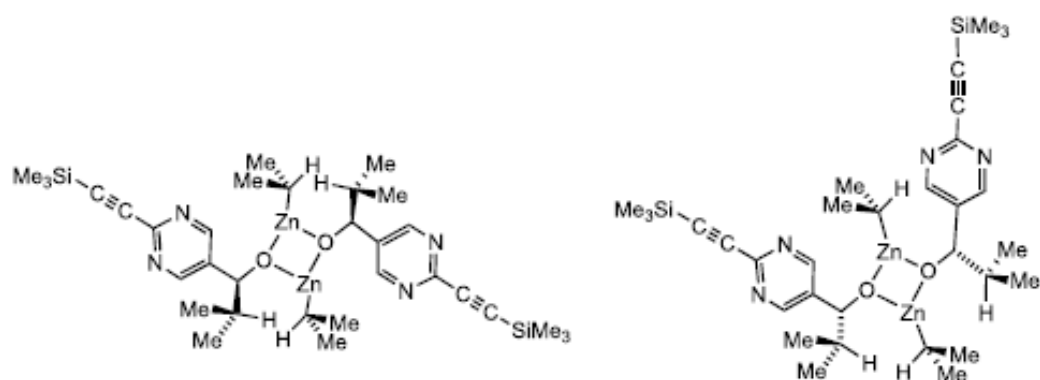
The main technique used to understand the Soai reaction by Brown and co-workers was NMR analyses in which species are identified in solution. Amplification of chirality occurs with non-polar solvents in which precipitation unfortunately occurs. THF which is a polar solvent has a lower tendency to precipitate and is a better

medium to provide interpretable data without difficulty. A spectra of racemic and enantiopure zinc alkoxide showed distinct NMR spectra in THF.



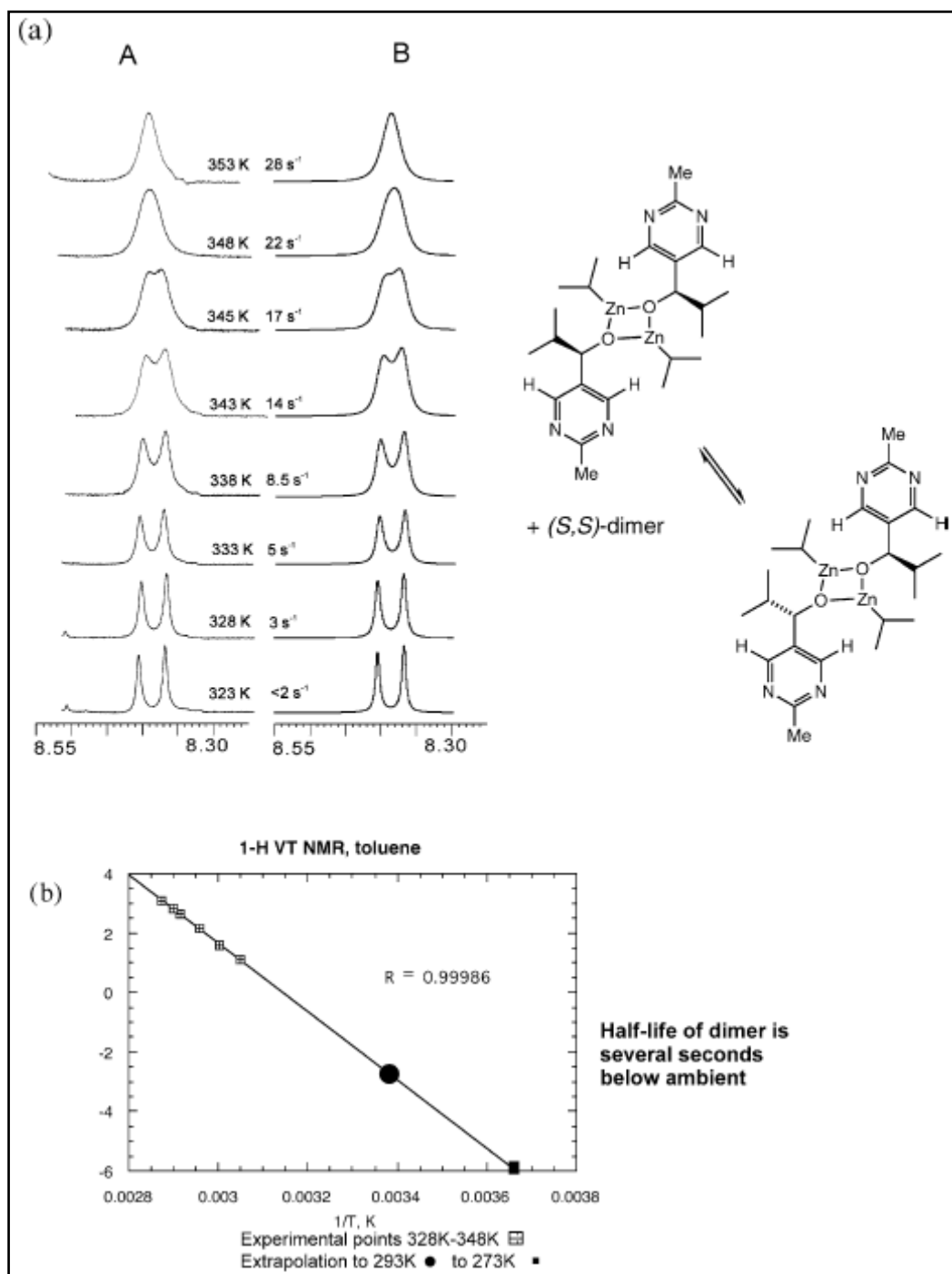
**Figure 3.19: Double resonance from homochiral to heterochiral**<sup>[51]</sup>

Equivalent amounts of homo and heterodimers can be approved by two sets of resonance (evidence of statistical distribution). According to Brown the likelihood of higher oligomers is low since they ought to produce more signals. Further computational studies considered that zinc could be bonded to N or O in pyrimidine carbaldehyde and consequently suggests three possible structures of the dimer. Brown suggests that the most likely dimer from his NMR analyses is a Zn-O square dimer. He also specifies that characteristic conditions for an autocatalytic turnover are 0-25°C, 0.05-0.2M  $i\text{Pr}_2\text{Zn}$ .<sup>[50, 51]</sup>



**Figure 3.20: Proposed square planar homo- and hetero- dimer<sup>[50]</sup>**

At ambient temperature the half life of a dimer molecule is about 15 s and there is equilibrium between the homo- and hetero- dimer.<sup>[34, 49-51]</sup>



**Figure 3.21: Dynamic exchange between homo- and hetero- dimer a) A: Observed B: Calculated b) Arrhenius plot. Half life approx. 14s at 293 K.<sup>[51]</sup>**

From the spectra above it is observed that increasing the temperature causes the broadening and coalescence of singlets. Clearly a monomer is not formed in the equilibrium between the dimers but probably at higher temperatures where small

changes in chemical shift are noticeable suggesting dissociative structural modification. Further NMR studies were carried out to determine zinc site binding to either the pyrimidine nitrogen or carbonyl group by monitoring the  $^{13}\text{C}$ ,  $^1\text{H}$  and  $^{15}\text{N}$  chemical shift changes.

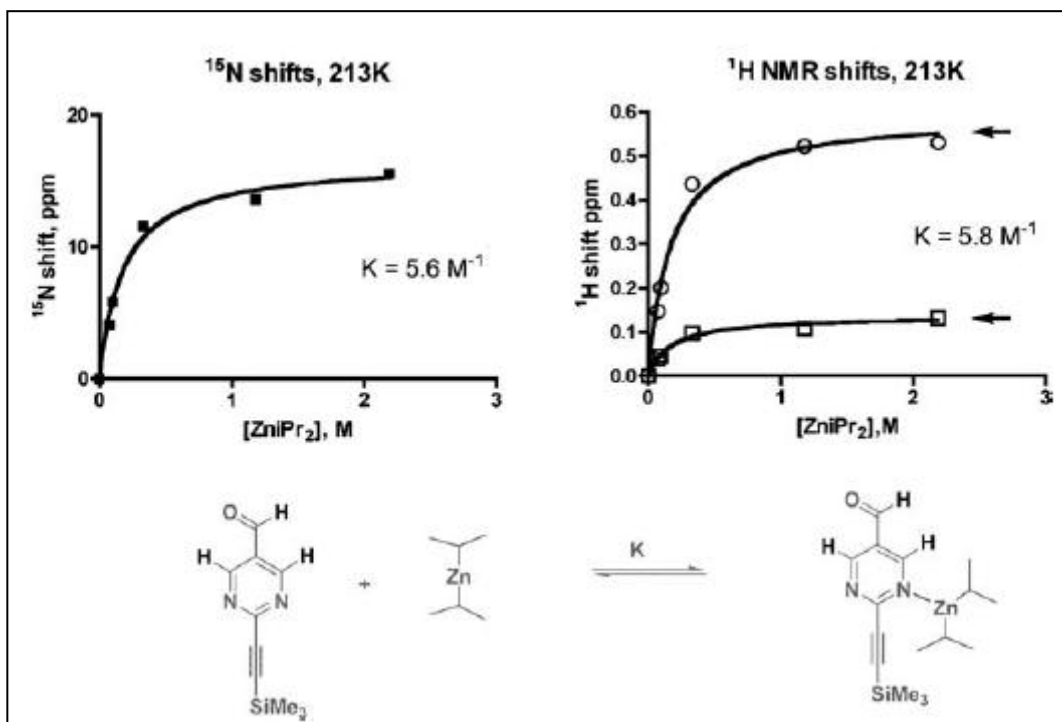
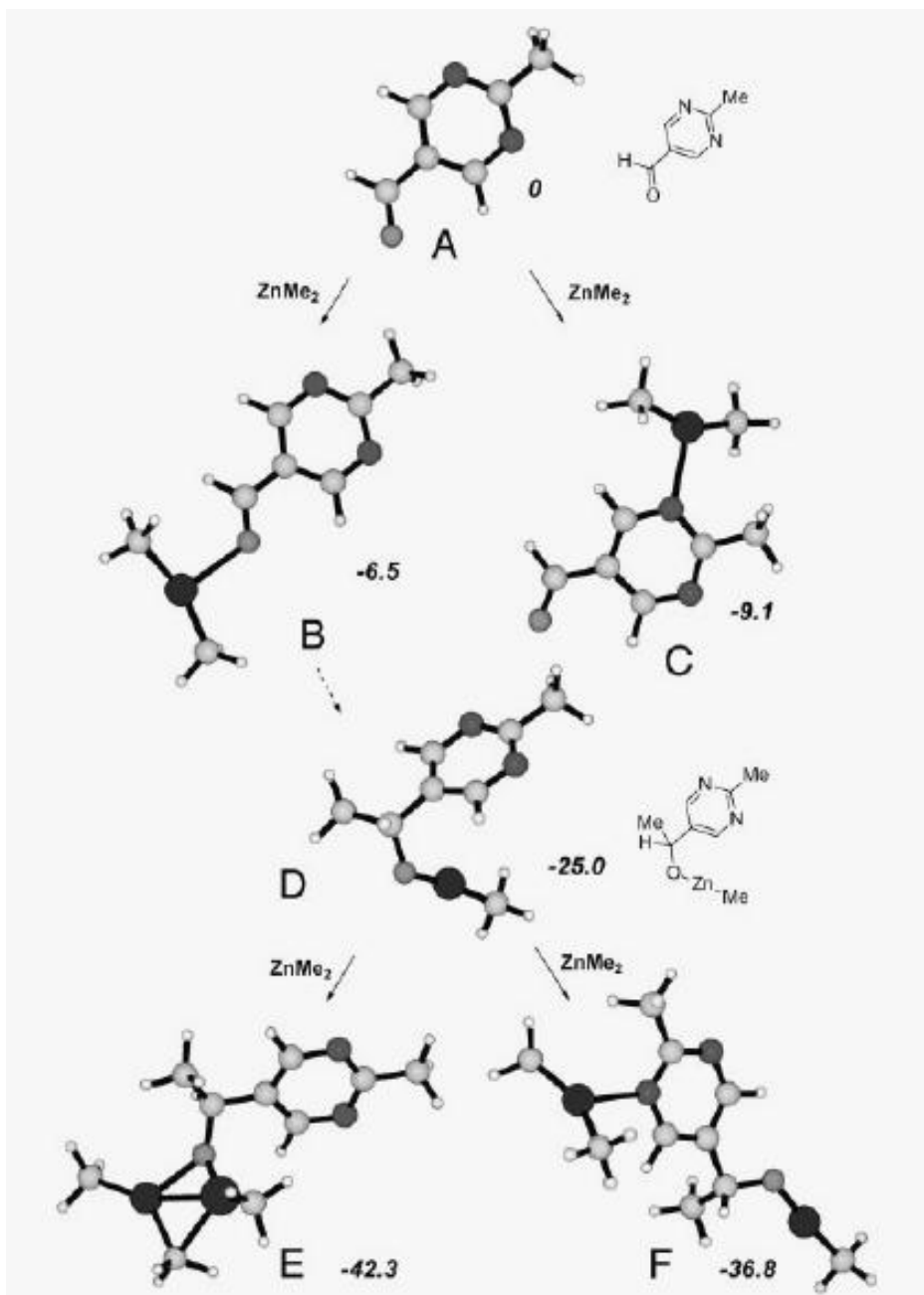


Figure 3.22: Chemical shift of binding of diisopropylzinc to pyrimidine aldehyde.<sup>[51]</sup>

From the above results the site of binding is the pyrimidine nitrogen. Further computational studies were carried out in order to compare with the NMR data.  $i\text{Pr}_2\text{Zn}$  which is used in the Soai autocatalytic reaction was replaced by  $\text{Me}_2\text{Zn}$ . The successive binding with  $\text{Me}_2\text{Zn}$  initially with the aldehyde is seen in the scheme below. The calculations were done by DFT at the B3LYP functional level with 6-31G basis set for all atoms. It is obvious that the experimental and computed results agree with the zinc preferring N- over O- in the pyrimidine aldehyde.<sup>[34, 51]</sup>



**Figure 3.23: Enthalpy of binding  $\text{ZnMe}_2$  to pyrimidine aldehyde (Units: kcal/mol). N- preferred over O- complexation.**<sup>[51]</sup>

The significance of the relative stabilities of dimers was also computationally studied in support of the  $(\text{ZnO})_2$  planar structure over O-Zn-N macrocycles and even more over  $\{\text{OZnO}, \text{NZnN}\}$  isomeric macrocycle. No reported evidence is however present for the existence of a macrocycle from NMR studies.<sup>[51]</sup>

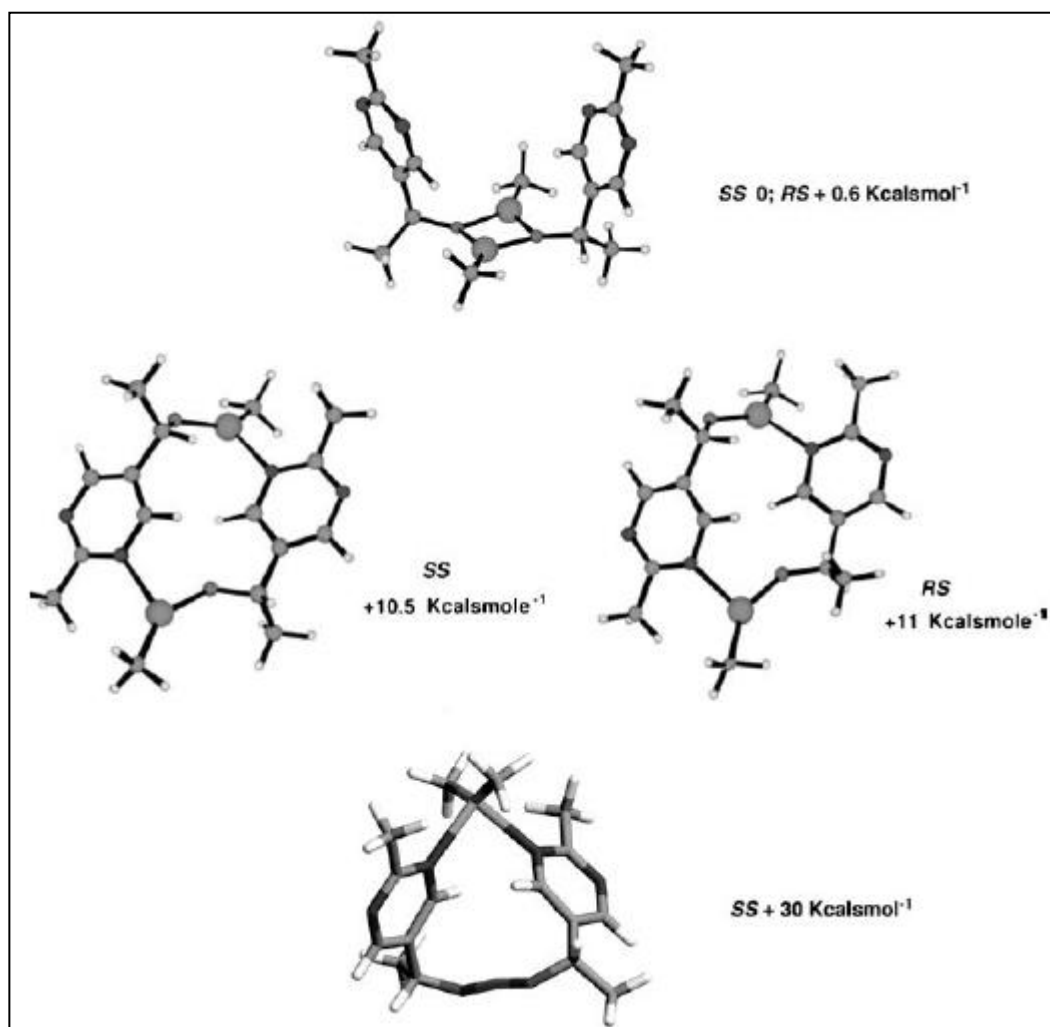
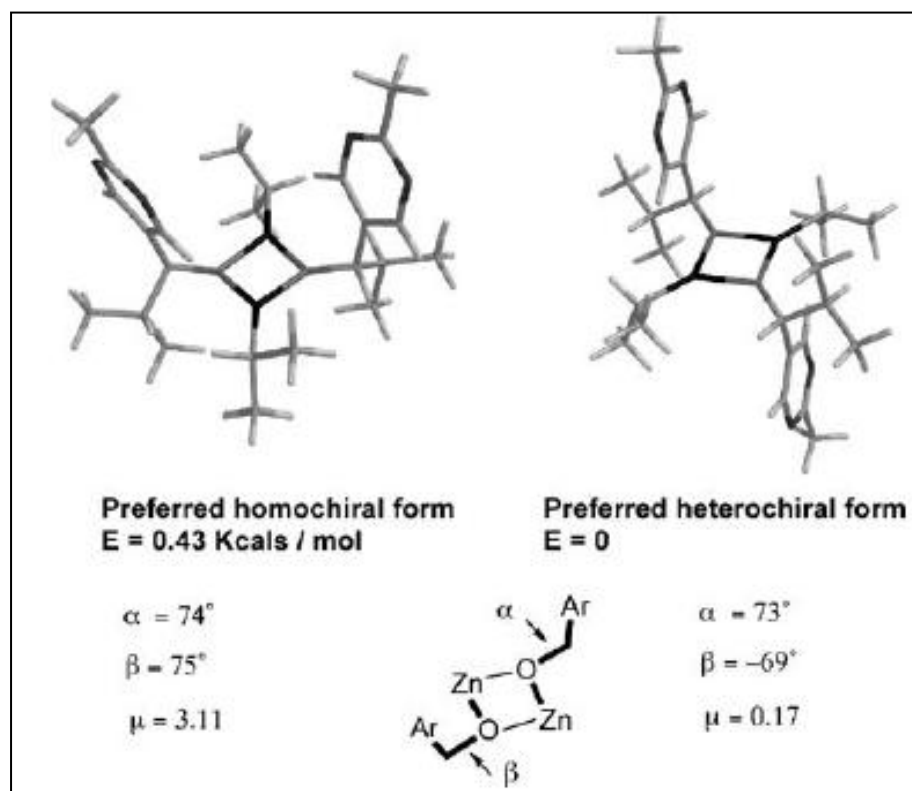


Figure 3.24: Closed cyclic dimers derived by DFT.<sup>[51]</sup>

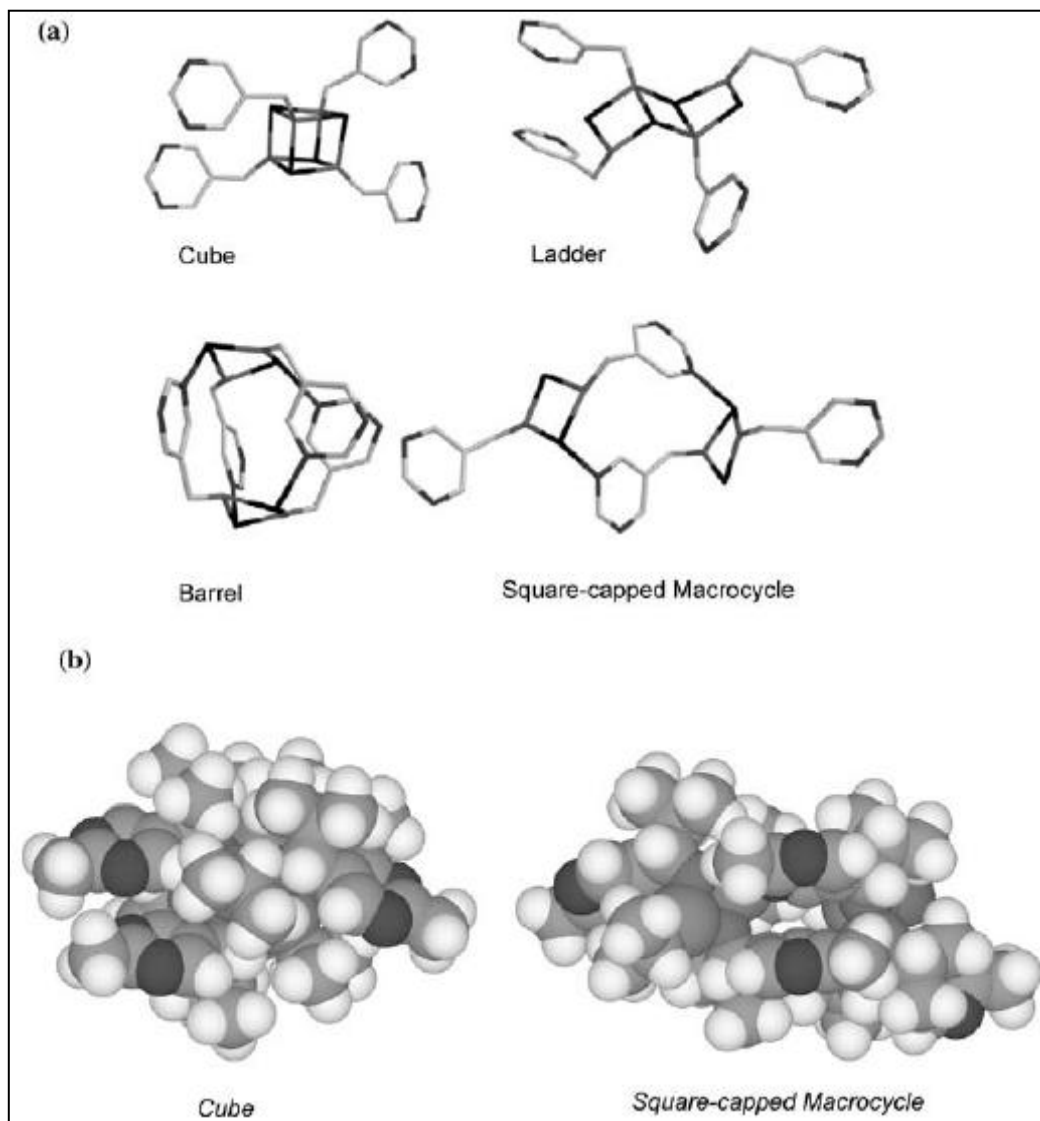
The difference between homochiral and heterochiral dimers in autocatalysis has been studied by Brown *et al.* Based on enthalpy it was found that homodimers dominate with *syn*- pyrimidines whereas heterodimers have *anti*- related pyrimidines as illustrated below. *Syn*- related pyrimidines have a significant dipole moment compared to *anti*- which may explain why they have a role in autocatalysis.<sup>[51]</sup>





**Figure 3.25:** DFT calculated ground state conformations (preferred) of  $i\text{Pr}_2\text{Zn}$  derived homo- ( $\text{Ar}, \text{Ar}'$  *syn*) and hetero- ( $\text{Ar}, \text{Ar}'$  *anti*) dimers.<sup>[51, 52]</sup>

Other possible species which include trimers and tetramers were derived from computational calculations. Adding the aldehyde to the dimeric catalyst and alkyl zinc gives a trimer. The option of tetramers which was earlier visited by Blackmond in this report was also explored by Brown *et al* in the DFT calculations. The tetramers were based on a square dimer template. Four distinct tetramer structures were computationally defined.<sup>[34, 50]</sup>



**Figure 3.26: (a) Four closed tetramers with alkyl substituents removed; (b) Space filling model of cube and square-capped macrocycle (both homochiral).**<sup>[51, 52]</sup>

The cubic tetramer is noted to have tight nonbonding H – H bonding interactions. From DFT calculations, over 40 kcal/mol is lost from going from a methylzinc to an isopropylzinc derived structure due to increased steric hindrance. The isopropyl derived  $[\text{Zn-O}]_2$  square-based tetramer was found to be more strained than its methylzinc counterpart. The isopropyl derived square-capped tetramer is not excessively strained and does not have acute H – H interactions. Two H – H contacts were found less than 2.3 Å. The ladder structured tetramer which lacks one pair of

Zn-O associations and the barrel like structure tetramer are both less stable than the cube tetramer.

Entry <sup>a</sup>	Structure	Binding Energy (Me) kcal mol <sup>-1</sup>	Binding Energy (i-Pr) kcal mol <sup>-1</sup>	Binding Energy (relative to 2x precursor dimer) kcal mol <sup>-1</sup>
1C	Me cube all-R	129.51		39.53
2C	Pr <sup>i</sup> cube all-(S)		91.68	7.46
3C	Me cube (RRSS)	129.58		40.86
4C	Pr <sup>i</sup> cube (RRSS)		91.86	6.78
1L	Me ladder all-S	110.81		20.83
2L	Pr <sup>i</sup> ladder all S		80.88	-3.34
1B	Me barrel all R	128.95		38.97
2B	Pr <sup>i</sup> barrel all R		104.8	20.58
1M	Me SMS all-S	116.02		26.04
2M	Pr <sup>i</sup> SMS all S		101.3	17.11
<sup>a</sup> C = cube, L = ladder, B = barrel, M = (square macrocycle square (SMS))				

**Table 3.1: Binding enthalpies of tetrameric compared to dimeric structures<sup>[52]</sup>**

The most likely active catalyst tetramer has a square-capped structure which remarkably preserves its trigonal unsaturated Zn geometry for coordination. From <sup>1</sup>H NMR studies at low temperature there is evidence of highly dynamic and unsymmetrical tetrameric Zn alkoxide species formed by the association of dimers. It has been noted that the observed *ee* is higher than the *ee* calculated with a dimer catalyst. According to Brown and co-workers, full consideration should be given to higher homochiral oligomers in the explanation of the autocatalytic pathway. Models with higher oligomers as the autocatalysts have been noted to give a higher calculated *ee* for a given level of turnover.<sup>[51, 52]</sup>

An autocatalytic turnover is present only with diisopropylzinc. Other dialkylzinc groups which include cyclopropyl, cyclopentyl or tertbutyl do not perform. According to Klankermayer the bulkiness of the isopropyl group is responsible for its exceptional performance in the autocatalytic amplification of chirality.<sup>[51, 52]</sup> However, *i*Pr and Et are of similar size with respective A-values of 2.21 and 1.79 Å but the presence of longer range H – H interactions changes the setting.

Brown and co-workers have so far done kinetic, computational and NMR studies to understand autocatalytic amplification. The solution structure of the resting state has been well considered, yet Brown suggests that an X-ray structure of the oligomer would be a step forward. No fully agreeable model explaining this process is known at present.<sup>[51]</sup>

### 3.5 Research objective

The objective of this research study is to make a significant contribution to support the numerous models already mentioned. As seen earlier, the nature of the catalyst responsible for amplification of chirality is not definite. The characteristic of the transition state structure has so far been suggested to be a monomer, dimer or tetramer etc. Different techniques have been used to determine the catalyst, but none of these techniques provides electronic and structural information which is necessary in determining the molecular mechanism during amplification of chirality.

X-ray absorption fine structure (XAFS) which is the main technique used in this work, provides structural and electronic information of the solution structure responsible for autocatalysis. It is a powerful probing method for the quantitative determination of structural parameters. Using this method it is possible to probe Zn species in solution to generate structural information during amplification of

chirality. Information such as the oxidation number, coordination number and bond distances can be acquired to build a model after probing the Zn species. Details of the Zn sites which could be linear, trigonal, tetrahedral etc. can be revealed by probing the Zn species. XAFS should be able to determine the transition state structure at an initial stage of the reaction and also at different stages of the reaction. It would be obvious if the central zinc probed has one or more zinc neighbours which would imply the existence of a monomer, dimer etc. Evidence of the characteristic structure of zinc species in toluene and THF is expected to be different using XAFS because THF is a polar solvent and therefore has an affinity for metals. This would confirm the poor performance of the Soai autocatalytic reaction in THF by the provision of a model which has so far not been visited.

It is expected that chapters further in this work provide one model that suitably characterises the Zn catalyst. This is unlike other models proposed earlier in this chapter which suggest different models using the same technique.

## 4. Experimental

### 4.1 X-ray Absorption Spectroscopy (XAS)

X-ray absorption Fine Structure (XAFS) is the main technique used in this study to characterize Zn species in solution. The XAFS is usually divided into two regions, the XANES (X-ray Absorption Near Edge Structure) and EXAFS (Extended X-ray Absorption Fine Structure). The local atomic coordination and chemical/oxidation state of Zn can be calculated using XAFS at low concentrations.<sup>[53, 54]</sup>

#### 4.1.1 Principles of X-ray absorption spectroscopy

X-ray absorption takes place due to the excitation of core level electrons in atoms by X-ray photons.

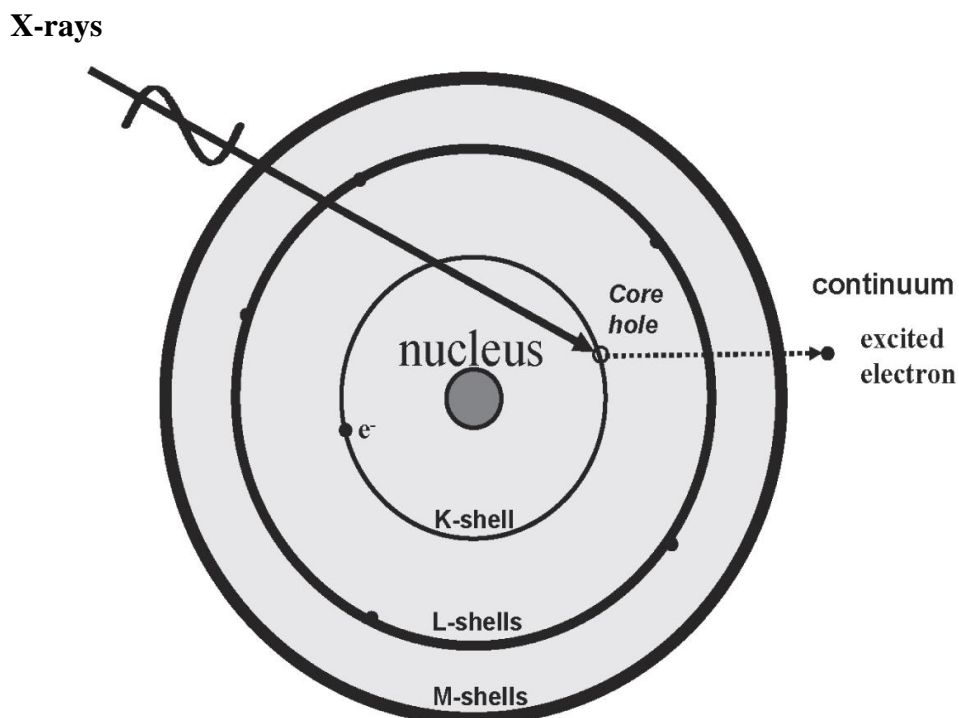
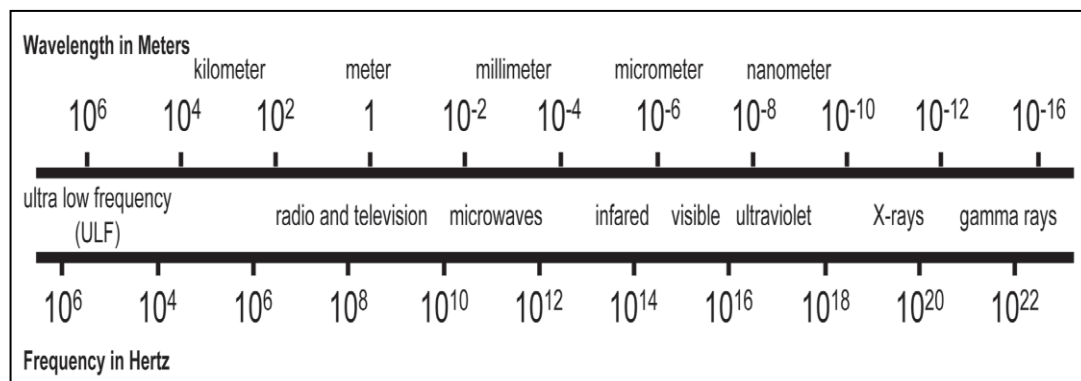


Figure 4.1: Illustration of X-ray absorption process in an atom<sup>[55]</sup>

The more weakly bound valence electrons occupy outer shell orbitals. These electrons take part in chemical bond formation.

*X-rays* are photons, which are electromagnetic radiation. The electromagnetic spectrum includes radio and television waves, microwaves, infrared light, X-rays and gamma rays.



**Figure 4.2: Spectrum of photon energy in wavelength and frequency<sup>[55]</sup>**

Photons possess wave and particle like properties. The energy of X-rays is usually expressed in electron volts (eV). The relation between energy and wavelength is:

$$E = hc/\lambda, \quad (\text{in Joules, J}) \quad 4.1$$

Where  $h$  is Planck's constant and  $c$  is the speed of light.

Three types of *X-ray scattering* are known which include Compton, Rayleigh and X-ray Raman scattering. They all result from the interaction of electrons with X-rays. Compton scattering is an inelastic process in which the X-ray loses energy, whereas Rayleigh scattering is elastic and occurs because the oscillating electric field induces oscillation in the electrons. Stronger elastic X-ray scattering is observed for heavier atoms, because they have more electrons.

When an atom acquires all the energy of an X-ray, *X-ray absorption* occurs. This gained energy excites the core electrons into higher energy unoccupied electron

orbitals or into the continuum where the electron is no longer bound by the atom. The latter free electrons are usually referred to as photoelectrons. When the core electrons are excited, a core hole is left behind. Within less than  $10^{-15}$  s, an electron from a higher energy orbital fills the core hole. This transition results in the release of energy which can be in the form of fluorescence radiation, Auger electron production or secondary electron production.

The filling of a core hole by a more weakly bound electron can also result in *X-ray fluorescence*. The fluorescent X-ray energy is, in a first approximation, the difference between the binding energy of the two core levels involved in the transition. The fluorescence X-ray energy for a given electronic transition is element specific.

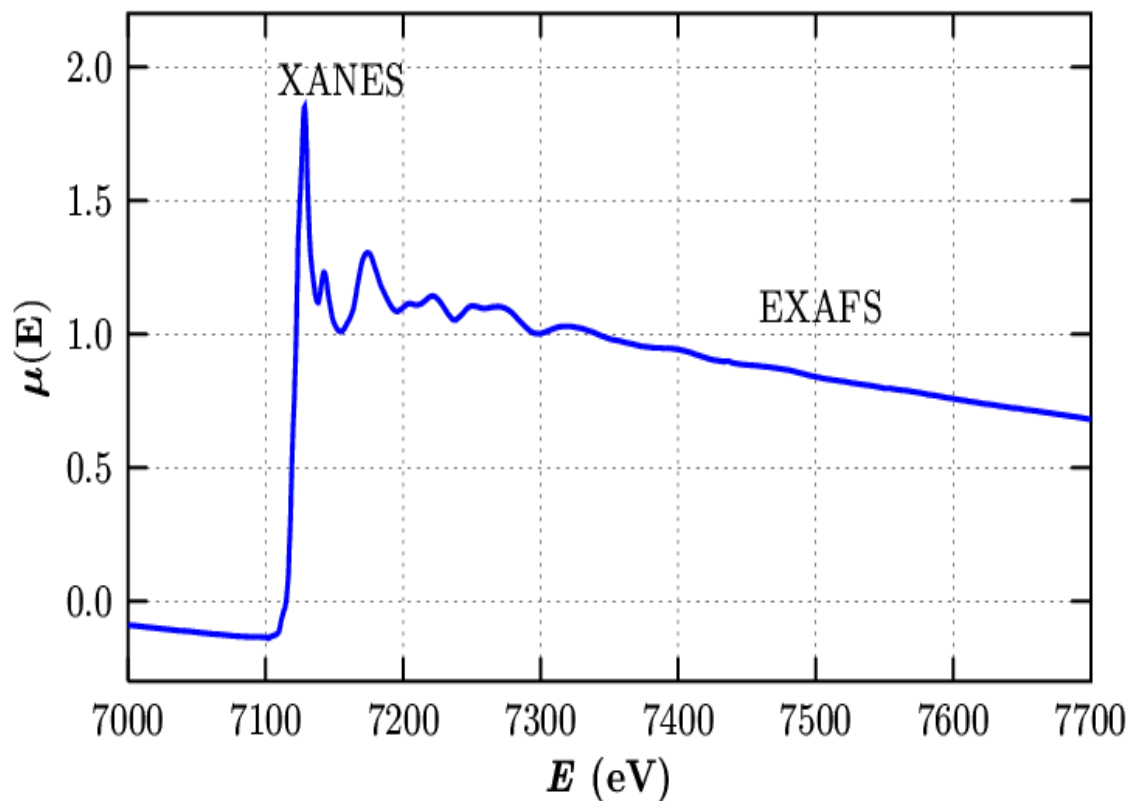
An alternative way for the system to lose energy during the process of core hole deexcitation is the loss of energy by emission of additional electrons, either from the same core levels involved in the deexcitation process or from different shells. This is known as Auger electron production. The final steps of core hole relaxation by electron emission is the production of secondary electrons and lower energy (UV/Vis) photons.<sup>[55]</sup>

#### **4.1.2 XANES and EXAFS**

X-ray absorption spectra are typically acquired from about 200 eV below the absorption edge to 1000 eV above. The X-ray absorption near edge structure (XANES) is the region ranging from the absorption edge to about 40 eV above the edge (Figure 4.3). The near-edge structure is determined by the density of states available to the excited photoelectron. The coordination geometry and oxidation state affect this part of the spectrum. The region after the XANES is known as the



Extended X-ray absorption fine structure (EXAFS). The EXAFS gives information about the local structure which is calculated by curve fitting.



**Figure 4.3: Plot of XANES and EXAFS region.**<sup>[54]</sup>

The information found in the XANES and EXAFS region is different. XAFS spectroscopy gives information on the electronic and structural properties under reaction conditions and in the presence of a catalyst. X-ray diffraction (XRD) also provides geometric information, but it is unsuitable for studying reaction mechanisms in solution because it requires crystalline samples with long range order. X-ray photoelectron spectroscopy (XPS) is not also suitable because it is limited to giving only electronic information specifically under ultra-high vacuum conditions. XAFS technique is widely used in catalysis research and is used to determine the electronic and structural properties of homogeneous and heterogeneous catalysts.

### 4.1.3 Physical principles

An incident beam of X-ray photons of intensity  $I$ , will be decreased by an amount that is determined by the absorption characteristics of the irradiated material. The relation between the path length  $dx$  and intensity is:

$$dI = -\mu(E)I dx \quad 4.2$$

Lambert's law is derived by integrating the above equation considering the total thickness  $x$ :

$$I_t = I_0 e^{-\mu(E)x} \quad 4.3$$

The excitation of an electron from a core to a vacant excited state or the continuum results in a sudden rise (threshold energy or absorption edge) in the absorption intensity. The kinetic energy of the electron ( $E_k$ ) for any energy above the absorption edge is defined by:

$$E_k = h\nu - E_{\text{binding}} \quad 4.4$$

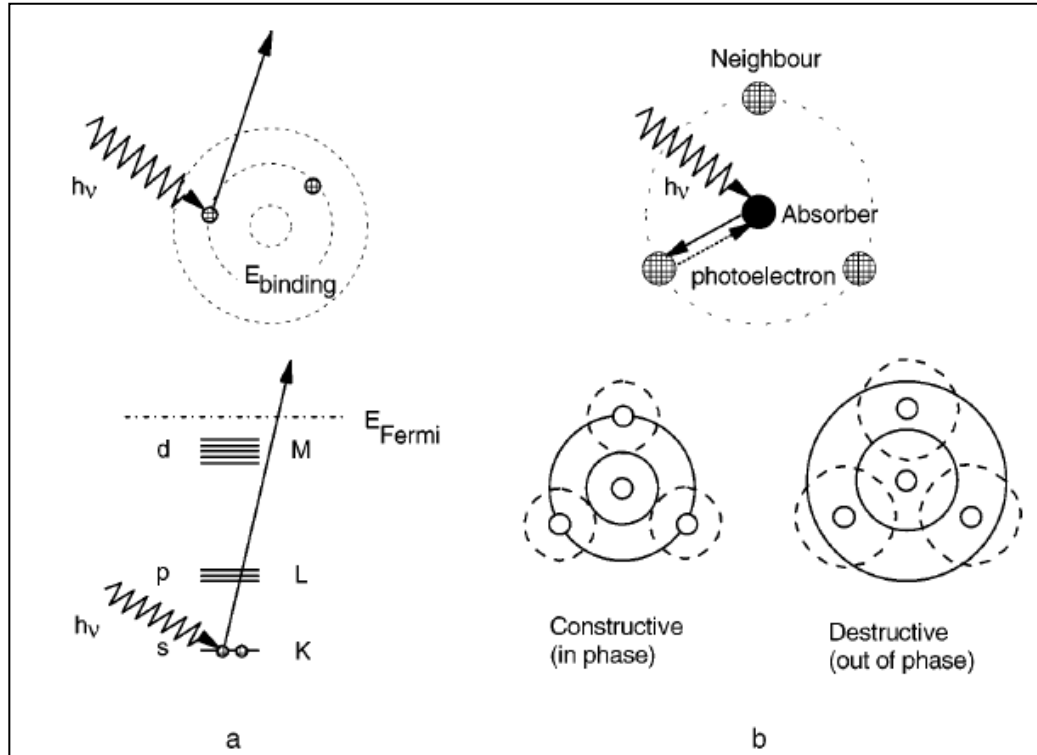


Figure 4.4: (a) Photoelectric effect in terms of excitation of different orbital or different energy levels. (b) Illustration of neighbouring shells of atoms about the absorber. Interference between outgoing photoelectron wave and backscattered off neighbouring atoms shell.<sup>[56]</sup>

#### 4.1.4 EXAFS equation

A scattering theory can be modeled to define the XAFS oscillation,  $\chi_i(k)$ , where  $k$  is the wave number. In the plane wave approximation, the sum of the modified sine waves  $\chi_i(k)$  with different frequency and phase from each backscattering coordination shell  $j$ , around the central atom  $i$  is expressed as:

$$\chi_i(k) = \sum A_j(k) \sin \Phi_j(k) \quad 4.5$$

$A_j(k)$ : Total backscattering amplitude of the  $j^{\text{th}}$  shell of backscattering atoms.

$\Phi_j(k)$ : Total phase function.

The amplitude and phase functions provide structural information. The amplitude  $A_j(k)$  is further defined as:

$$A_j(k) = \frac{N_j}{kR_j^2} S_0^2 F_j(k) e^{-2k^2\sigma_j^2} e^{-2R_j/\lambda k} \quad 4.6$$

$F_j(k)$ : The backscattering amplitude (element specific).  $S_0^2$ : The amplitude reduction factor representing many-body effects such as central atom shake-up and shake-off due to relaxation processes. The finite lifetime of the excited state is justified by the exponential term which includes the photoelectron mean-free path,  $\lambda$ .<sup>[56]</sup>

#### 4.1.5 Data analysis

The XAFS function,  $\chi(k)$ , is defined as:

$$\chi(k) = \frac{[\mu(k) - \mu_0(k)]}{\mu_0(k)} \quad 4.7$$

$\mu$ : Measured absorbance; including all fine structure

$\mu_0$ : The XAFS-free absorbance of a single free atom.

The first step in the extraction of the experimental XAFS function is the pre-edge background removal followed by normalization. The energy is then calibrated

(calibrated with zinc foil in this study) and it is converted to k-space. Several known programs are available to process XAFS data which include Iffefit packages: Athena and Artemis, WinXAS, GNXAS<sup>[57]</sup> and EXAFSPAK. In this work the Iffefit packages: Athena and Artemis are utilized in the extraction of EXAFS oscillation and data refinement.<sup>[58]</sup> Two spectra were collected on an average for XANES and EXAFS during this study and no changes were observed over short periods.

*Background correction:* Correction is necessary to eliminate effects that affect the experimental absorption spectrum. Such effects include instrumental effects, sample cell absorption, effects of other atoms (or electrons) in a sample. Ideally, only the specific absorption of the atom chosen for study should remain for EXAFS analysis. The pre-edge region is fitted with a polynomial (linear or quadratic) function and the fit values are deducted from raw data.

*Normalization:* Normalization ensures that amplitude of the signal is in the right scale and compensates for uncertainties in the concentration and sample thickness. This process is achieved after pre-edge background correction and is done by dividing experimental data collected from a synchrotron by the edge step.<sup>[59]</sup>

*Threshold energy,  $E_0$ :*  $E_0$  is the minimum energy needed to excite a photoelectron and can be correlated to the kinetic energy of the electron.<sup>[60]</sup> The photon energy  $E$  of the incident beam defines the wave vector  $k$  of the photoelectron:

$$k = \{0.2625(E-E_0)\}^{1/2} \quad 4.8$$

$E_0$  is the Fermi energy in version 8 of the FEFF program and is in a first approximation taken as the first maximum derivative of the edge.  $E_0$  can be affected by the oxidation state, covalency in chemical bonds etc.

*Conversion to k-space:* The energy scale can be changed from eV to the photoelectron wave number,  $k$  ( $\text{\AA}^{-1}$ ) by the following correlations:

$$\text{Kinetic energy of the photoelectron, } E - E_0 = 1/2 m_e v^2 = (m_e v)^2 / 2 m_e = P^2 / 2 m_e$$

$$\text{Photoelectron momentum, } P = \hbar \cdot k \quad 4.9$$

$$k = \text{wave vector} = \frac{2\pi}{\lambda_e} = \text{photoelectron wave number} \quad 4.10$$

$$\Rightarrow E - E_0 = \frac{\hbar^2 k^2}{2 m_e} \quad k = \sqrt{\frac{2 m_e (E - E_0)}{\hbar^2}} = \{0.2625(E - E_0)\}^{1/2} \quad 4.11$$

When  $k = 0$ ; the energy is the threshold energy.

*Spline atomic background removal:* The total absorption coefficient  $\mu(k)$  of an isolated atom is expressed as:

$$\mu(k) = \mu_0(k) \{1 + \chi(k)\} \quad 4.12$$

Where  $\chi(k)$  denotes the fractional change (modulation) in the absorption coefficient induced by neighbouring atoms and contains structural information.

XAFS  $\chi(k)$  can therefore be defined as:

$$\chi(k) = \frac{[\mu(k) - \mu_0(k)]}{\mu_0(k)} \quad 4.13$$

$\mu_0(k)$  is the atomic background absorption for an isolated atom at the same energy.

With high  $k$  values the amplitude of the oscillations becomes smaller because of a decrease in absorption with increasing energy. Dividing by  $\mu_0(k)$  normalises the XAFS data. The EXAFS region  $\mu_0(k)$  function is determined by the smooth curve,  $\mu_{\text{spline}}(k)$  fitted from experimental data.  $\mu_{\text{spline}}(k)$  is used as an approximation for  $\mu_0(k)$  during normalization:

$$\chi(k) = \frac{[\mu_{\text{data}}(k) - \mu_{\text{spline}}(k)]}{\mu_{\text{spline}}(k)} \quad 4.14$$

The Victoreen approximation of the absorption coefficient,  $\mu_{\text{vic}}$  which is given by:

$\mu_{\text{vic}} = C_{\text{vic}} \lambda^3 - D_{\text{vic}} \lambda^4$ . The EXAFS function is then defined as:

$$\chi(k) = \frac{[\mu_{data}(k) - \mu_{spline}(k)]}{\mu_{vic}(k)} \quad 4.15$$

The extraction of the XAFS function can be seen in the following figure.

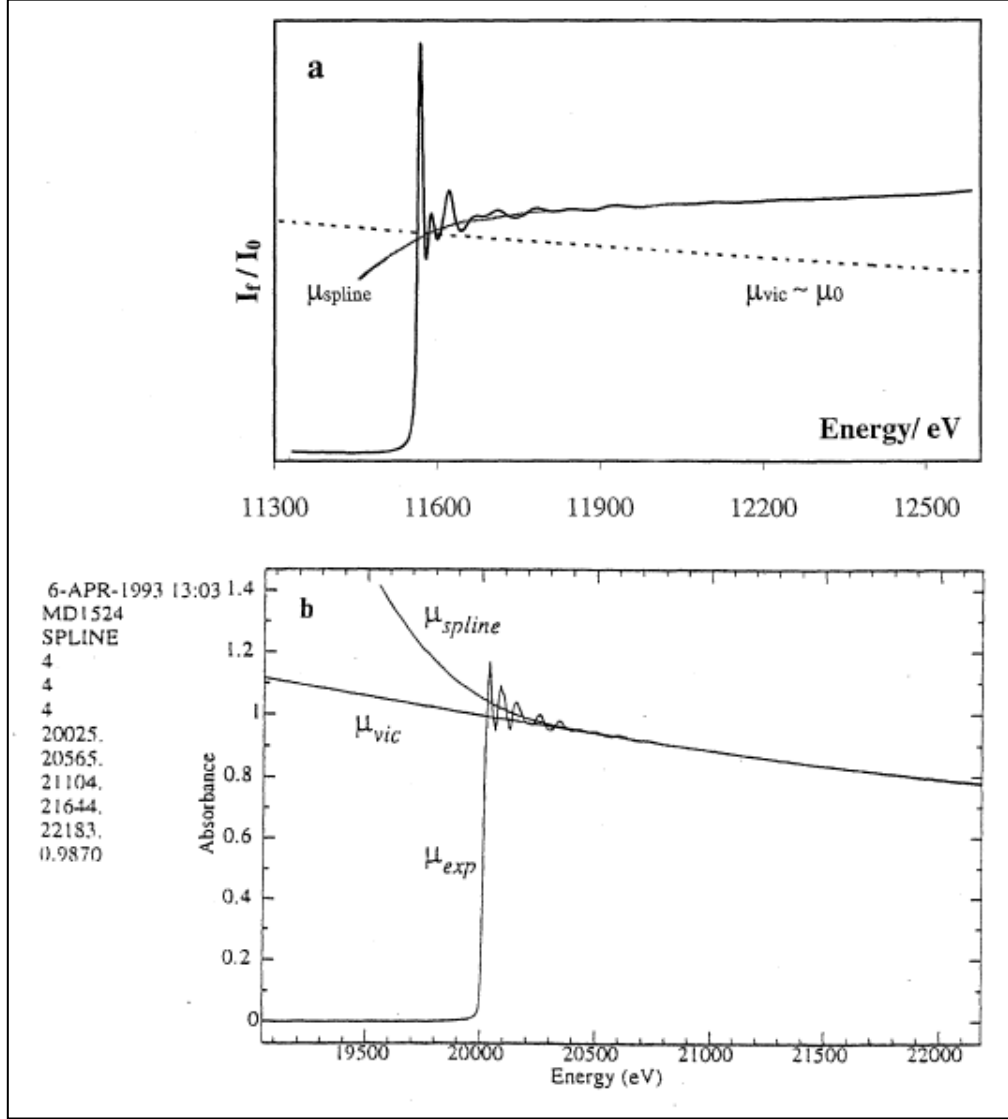
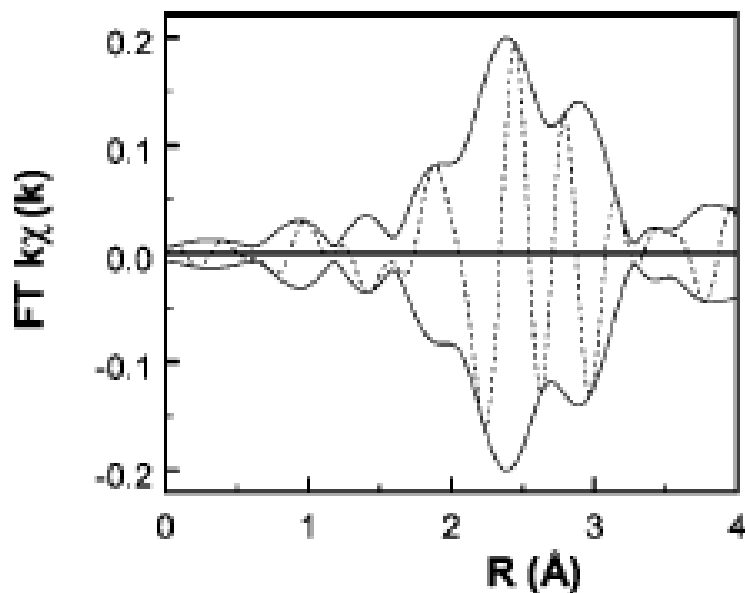


Figure 4.5: a) Pt edge fluorescence data for Pt complex. The  $\mu_{vic}$  function better represents the ‘fall off’ of the atomic background absorption  $\mu_0$  with increasing energy than  $\mu_{spline}$ . b) Transmission L edge data showing that  $\mu_{spline}$  can be a good approximation to  $\mu_{vic}$  and  $\mu_0$ .<sup>[59]</sup>

*Fourier transform:* The Fourier transformation is expressed as

$$FT(R) = \frac{1}{\sqrt{2\pi}} \int_{k_{min}}^{k_{max}} k^n \chi(k) e^{i2kR} dk \quad 4.16$$

An example of the radial distribution function defined in R-space is the distance from the absorber atom. Different  $k$  weightings used to distinguish low mass (e.g. oxygen) and high mass (e.g. Pt). Pt will scatter at higher  $k$ -values as seen below.



**Figure 4.6: Radial distribution function after Fourier transformation of Pt foil. Absolute (full line) and imaginary (- - -).**<sup>[56]</sup>

The Fourier transformation is a complex function that includes an imaginary (Im) and a real part (Re). The absolute part or envelope of the Fourier transform is defined by

$$\text{Absolute part} = \text{Im}^2 + \text{Re}^2 \quad 4.17$$

The number of neighbours and disorder determines the absolute part. An accurate determination of the absorber–scatterer distance can be derived from the imaginary part. The weighting by  $k^2$  or  $k^3$  emphasises the high  $Z$  contributions i.e. high  $Z$  elements have more scattering power at high values of  $k$  than low  $Z$  elements.<sup>[56]</sup>

*FEFF program*: FEFF8 can be used for data analysis. It calculates the phase shifts, effective scattering amplitudes for single and multiple scattering pathways for XAFS and XANES spectra.<sup>[61]</sup>

*ATOMS*: This program converts crystallographic data to a text file that is a Feff input file.<sup>[56, 58, 62]</sup>

## **4.2 Miniaturized continuous flow reaction vessels**

In this study a continuous flow tubular reactor and microcentrifuge tubes are used to measure XAFS data *in situ*. The physical importance of downscaling to miniaturized reactors is explored in this section.

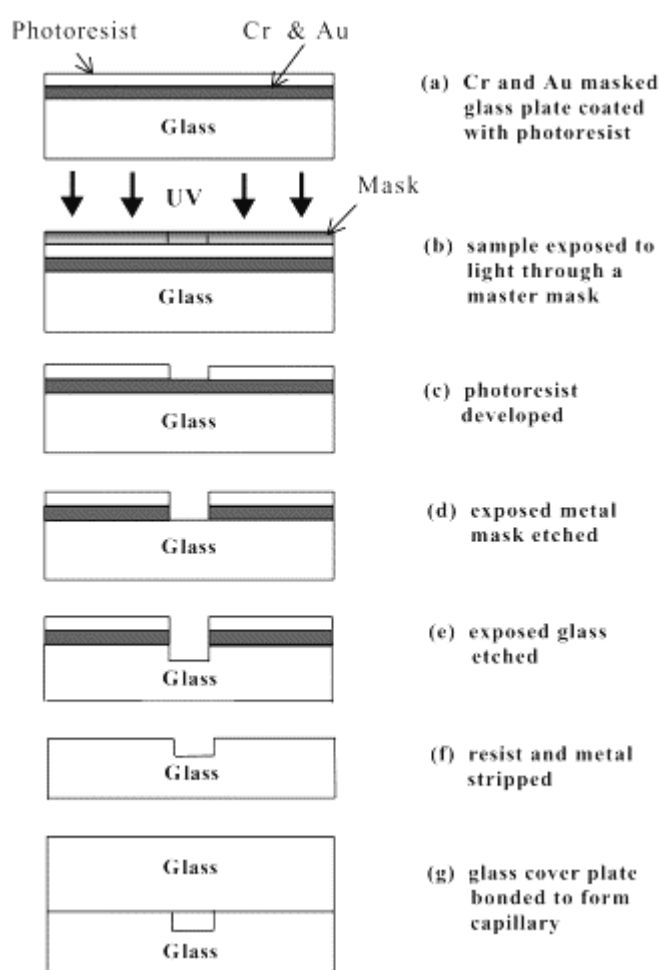
### **4.2.1 Introduction**

In the laboratory reactions are carried out in large volumes from to a few hundred milliliters. Aliquots can be withdrawn from reactions off-line and analyzed batch-wise. The disadvantage of such large quantities is analysis is slow and it takes longer for a homogenous temperature and concentration distribution to be attained. This may however lead to side products giving rise to lower yields and process selectivity.<sup>[63]</sup> Microreactor technology minimizes this problem and is used today by several researchers. It involves a low volume of reagents in a laminar flow in which a thermal and concentration gradient is present. The yield of reactions in microreactors is notably high in much shorter times. Clearly microreactors are a new, safe and efficient method to increase awareness of complex chemical processes.<sup>[64-66]</sup>



#### 4.2.2 Fabrication of microreactors

Several materials are used to build microreactors which include silicon, quartz, glass, metals and polymers. Compatibility of the reagent with the microreactor material is crucial. Microfabrication methods include photolithography, hot embossing, powder blasting, injection moulding and laser micro-forming.<sup>[67]</sup> In this study the material of choice should be compatible with X-ray Absorption Fine Spectroscopy in-situ measurements.



**Figure 4.7: Photolithographic fabrication of channel networks in glass.**<sup>[67]</sup>

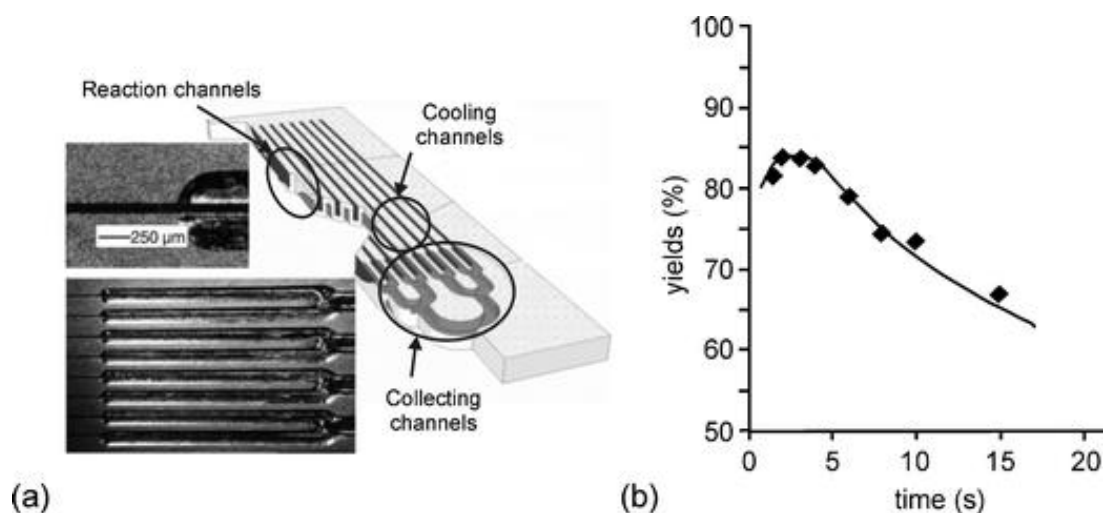
Most organic chemists prefer to use glass microreactors.<sup>[64]</sup> The material of choice should generally be chemically inert, resistant to solvents and transparent for optical

inspection. The material should avoid chemical species absorption and should have suitable thermal and electrical properties.<sup>[63]</sup>

#### **4.2.3 Microfluidic handling and effects of downsizing**

Methods used to drive liquids in microchannels are electrokinetic, pressure driven and flow driven. Driving a liquid through microchannels should target optimal control on reaction conditions. A homogenous flow rate should be provided by the pumping mechanism and this should not be affected by temperature, viscosity or pressure that may change with time. In addition dead volumes due to connections and tubings should be minimized to optimize control.<sup>[63]</sup> In this study a flow driven mechanism is used to pump the liquid through a cell while XAFS measurements are collected. Flow with a high level of control is ensured by the use of syringe pumps or peristaltic pumps and is suitable for time resolved reactions.<sup>[63, 68]</sup>

Reducing the reactor size has the advantage over lab-scale because less space is required, less energy and reagents; and a shorter reaction time is involved. Process safety and higher yields are also more likely. The consequence of downscaling is a large surface to volume ratio which causes a higher mass and heat transfer compared to lab scale reactors. An investigation of a study of the reliance of the reaction yield on the residence times in microreactors under isothermal conditions is illustrated below.



**Figure 4.8: (a) Microreactors used in chemical synthesis; (b) dependence of the product yields from the reaction time.**<sup>[63]</sup>

Diffusion and convection are the first step of any chemical reaction. The mass transport is expected to be faster than the reaction kinetics as expressed by the Damkohler number, which is the ratio of the characteristic time for a chemical reaction and for fluid dynamics. Reaction kinetics is unaffected by downscaling, however mass transfer coefficients are increased as a result of reduced reactor size. Mixing in microreactors is quicker due to shorter diffusion lengths. Characteristic specific surface areas (surface [m<sup>2</sup>]/volume [m<sup>3</sup>]) in microreactors are between 10,000 and 50,000 m<sup>-1</sup>, while those for lab-scale reactors are about 1000 m<sup>-1</sup>.

The Reynold number,  $Re$  is the ratio of the inertia ( $\rho v^2 l^2$ ) to viscous force ( $\mu v l$ ). This ratio quantifies these forces for given flow conditions. When the Reynold number is small,  $Re \ll 1$ , the viscous forces dominate and when  $Re \gg 1$  the inertia forces dominate.

$$Re = \frac{\rho v l}{\mu} \quad 4.18$$

$\rho$  [kg m<sup>-3</sup>] is the mass density,  $v$  [m s<sup>-1</sup>] is the velocity,  $l$  [m] is the length, and  $\mu$  [N s m<sup>-2</sup>] is the dynamic viscosity. In microchannels flow is laminar and mixing is realized by diffusion. The diffusion time is described below:

$$t_d = \frac{L^2}{D} \quad 4.19$$

$t_d$  is the diffusion time,  $L$  [m] is the diffusion distance and  $D$  [m<sup>2</sup> s<sup>-1</sup>] is the diffusion coefficient, in which  $k$  is the Boltzmann constant ( $1.38 \times 10^{-23}$  J K<sup>-1</sup>),  $T$  [K] the absolute temperature,  $\eta$  [kg m<sup>-1</sup> s<sup>-1</sup>] the absolute (solute) viscosity, and  $r$  the hydrodynamic radius [m].

$$D = \frac{kT}{6\pi\eta r} \quad 4.20$$

Based on the assumption that the diffusion coefficient is in the order of  $1 \times 10^{-9}$  m<sup>2</sup> s<sup>-1</sup> for small molecules the mixing time is in the order of seconds (with  $L$  in the order of 100  $\mu$ m) to milliseconds (with  $L$  in the order of 10  $\mu$ m).

### 4.3 XAFS measurement experimental set up

A typical XAS experimental set up is seen below. Data can be collected in transmission and fluorescence mode. There are mainly five parts of the experimental setup, which include the source, the optics, the sample, the detectors and the electronics and computer.

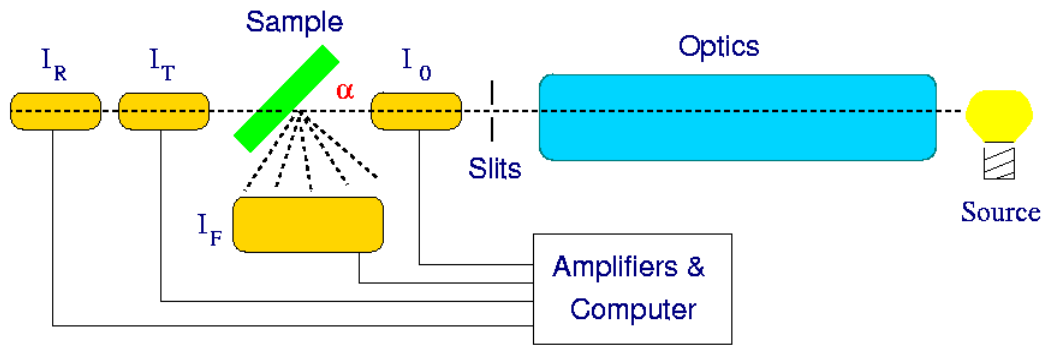


Figure 4.9: Schematic of XAS experiment<sup>[69]</sup>

In terms of the optics and detectors several types are known. The illustration below includes a monochromator and mirrors for harmonic rejection.

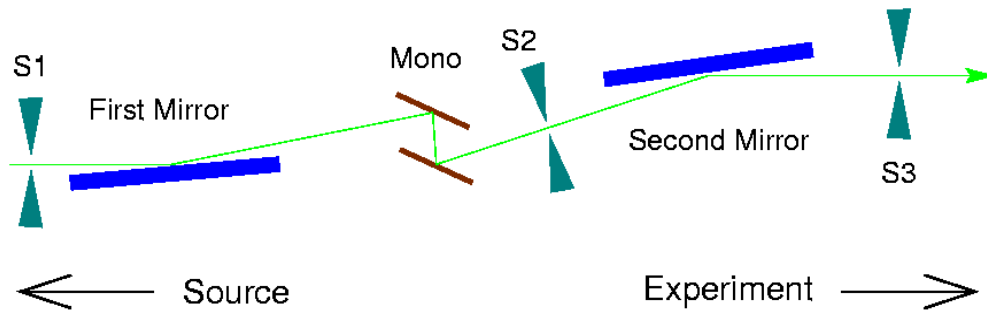


Figure 4.10: Optics and detectors<sup>[69]</sup>

The different sorts of detectors mainly used include ion chambers, diodes, energy discriminating and wavelength dispersive detectors.

XAFS data are acquired in transmission mode by passing the photon beam through the sample, with the intensities of the incident ( $I_0$ ) and the transmitted ( $I_T$ ) beams each collected by an ionization chamber. Fluorescence yield mode takes advantage of the fact that the intensity of characteristic X-ray fluorescence,  $I_F$ , is proportional to the absorption coefficient, so the absorption spectrum is obtained from  $\mu(E) = (I_F/I_0)$ .

#### 4.3.1 Decomposition products of dialkylzinc compounds exposed to ambient conditions

It is intended in this section to show the influence of the environment on dialkylzinc.

It is therefore crucial that experimental conditions are maintained in an oxygen and water free environment to prevent the decomposition as seen in Figure 4.11.

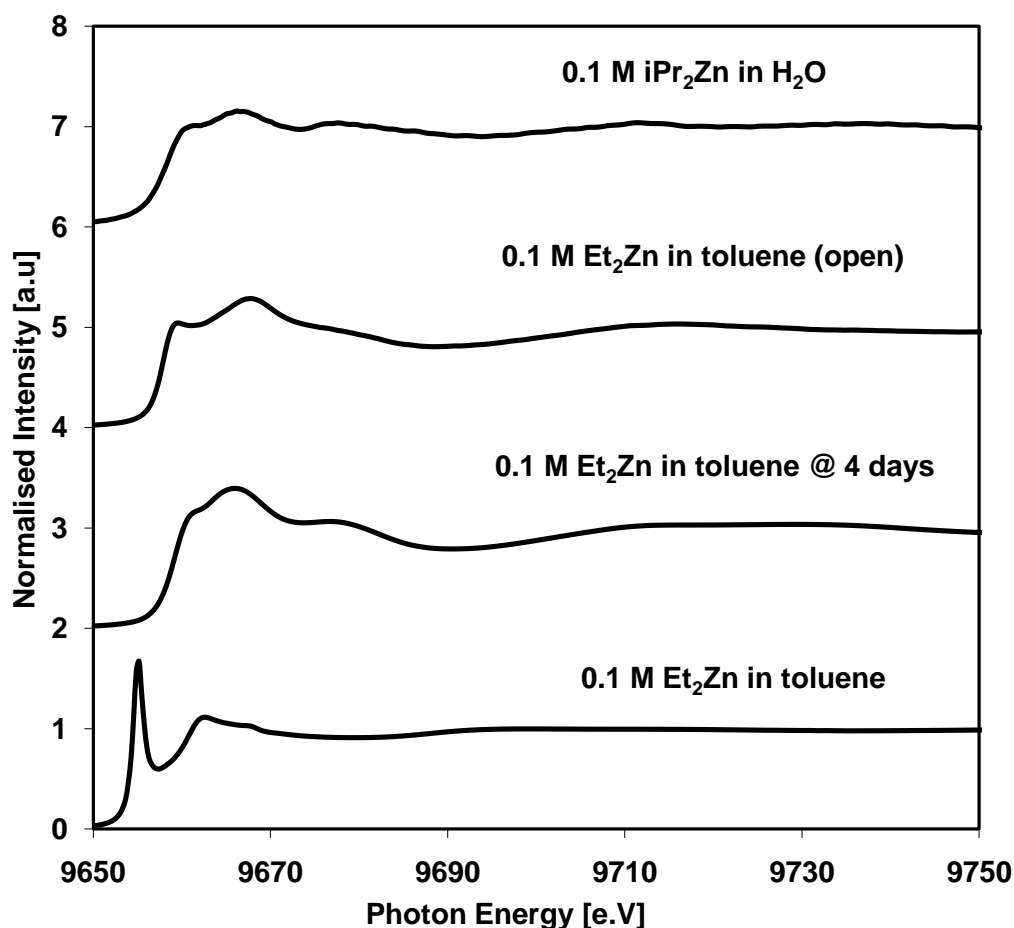


Figure 4.11: XANES spectra of dialkylzincs in toluene and water.

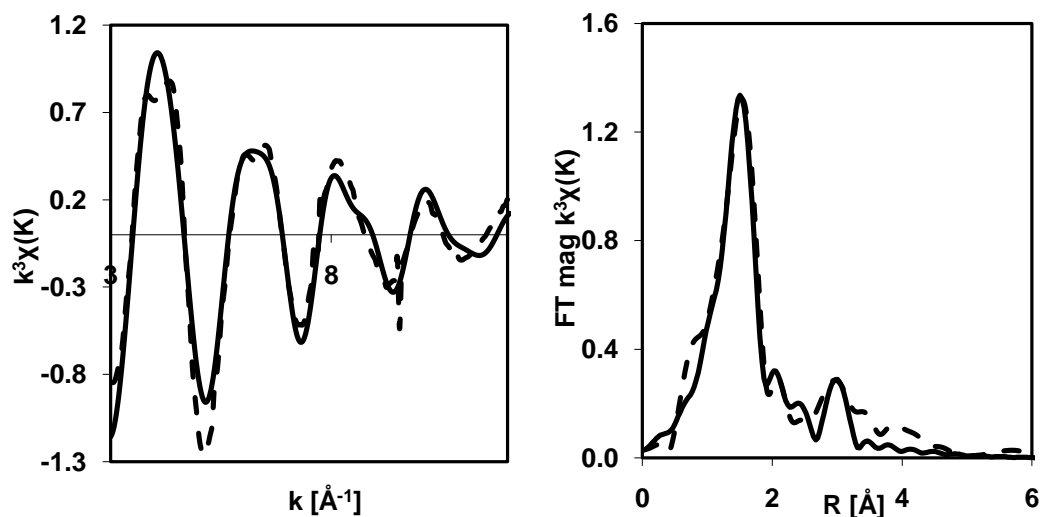
Decomposition of dialkylzinc as seen in the XANES spectra is possible with the presence of oxygen and water from different sources which include air and solvents. 0.1 M DEZ (diethylzinc) in toluene initially has a strong resonance peak which diminishes with the influence of oxidizing agents. It is observed that the resonance peak changes drastically over 4 days and this process is even faster when DEZ is left

open to oxygen with an increased rate of oxidation. Diisopropylzinc in water also results in a drop in the resonance peak with the formation of a precipitate observed to settle at the bottom of the microcentrifuge tube. The change observed is likely from a linear complex in toluene to a tetrahedral coordinated system when oxidized. The interaction with water as impurity in the solvent is possible at low concentrations of dialkylzinc suggesting that very low concentrations of dialkylzinc are not recommended. In this section the possibility of oxidation of the dialkylzinc to zinc oxide or zinc hydroxide is considered. Crystallographic information of zinc oxide and zinc hydroxide was acquired and the acquired coordination numbers of zinc oxide and zinc hydroxide were then fixed in order to get the best possible fit. Other EXAFS studies of both zinc oxide and zinc hydroxide were considered in order to compare the calculated bond distances.<sup>[70, 71]</sup> An EXAFS fit of decomposed DEZ assuming the coordination numbers of zinc hydroxide as the oxidized product is seen in Table 4.1. The coordination numbers of zinc were fixed in the 1<sup>st</sup> shell to 4 i.e. Zn to O and the Zn to Zn was fixed to 2.2 in the 2<sup>nd</sup> shell as expected from crystallographic data and other studies.

Sample	First shell			Second shell							
	(Zn-O/C/N)			(Zn-O/C/N)			(Zn-Zn)				
	N	<i>R</i> (Å)	σ <sup>2</sup> (Å <sup>2</sup> )	N	<i>R</i> (Å)	σ <sup>2</sup> (Å <sup>2</sup> )	N	<i>R</i> (Å)	σ <sup>2</sup> (Å <sup>2</sup> )	E <sub>0</sub> (eV)	R (%)
Et <sub>2</sub> Zn in toluene	4 <sup>s</sup>	1.96 (±0.006)	0.005 (±0.001)				2.2 <sup>s</sup>	3.24 (±0.015)	0.012 (±0.002)	3.16 (±1.027)	3.5

**Table 4.1: EXAFS parameters of exposed DEZ in air (set as zinc hydroxide solid)**

The R-factor of the fit was 3.5 %, which is considered good. However the EXAFS spectra are non identical to that of Zn(OH)<sub>2</sub>. This suggests that the decomposed product is not zinc hydroxide.



**Figure 4.12:** Zinc K-edge EXAFS spectra of decomposed Et<sub>2</sub>Zn exposed to air. Fit with zinc hydroxide coordination numbers fixed. Dash lines are the experimental data and the solid lines are the best theoretical fit.

A similar fit was studied with zinc oxide in which the central zinc atom of decomposed diethylzinc was set to 4 in the 1<sup>st</sup> shell with neighbouring oxygen atoms and 12 in the 2<sup>nd</sup> shell with neighbouring zinc atoms based on other studies.

Sample	First shell (Zn-O/C/N)			Second shell (Zn-O/C/N) (Zn-Zn)							
	N	R(Å)	σ <sup>2</sup> (Å <sup>2</sup> )	N	R(Å)	σ <sup>2</sup> (Å <sup>2</sup> )	N	R(Å)	σ <sup>2</sup> (Å <sup>2</sup> )		
Et <sub>2</sub> Zn in toluene	4 <sup>s</sup>	1.96 (±0.004)	0.005 (±0.0002)				12 <sup>s</sup>	3.26 (±0.013)	0.027 (±0.002)	3.12 (±0.788)	2.1

**Table 4.2:** EXAFS of DEZ in toluene exposed in air (set as zinc oxide)



The EXAFS fit based on zinc oxide has an R-factor of 2.1% implying a better fit compared to zinc hydroxide as seen below.

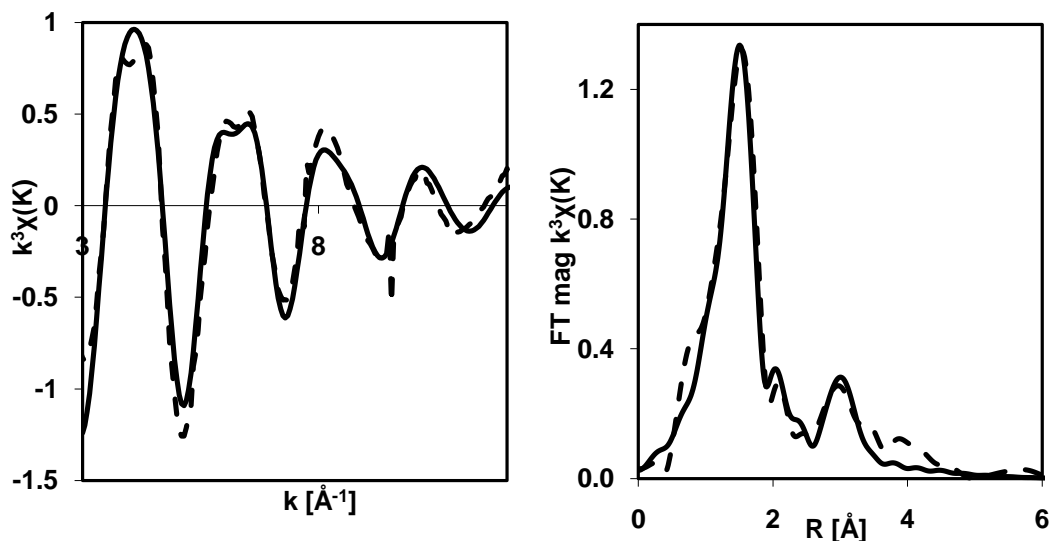


Figure 4.13: Zinc K edge EXAFS spectra of decomposed Et<sub>2</sub>Zn exposed to air. Fit with zinc oxide coordination numbers fixed. Dotted lines are the experimental data and the solid lines are the best theoretical fit.

By virtue of the R-factor of the above EXAFS fits of decomposed DEZ it is likely that the product formed after DEZ oxidation is closer to zinc oxide (The R-factor calculated here is about two times smaller) than zinc hydroxide. It must be noted here that neither of them is the decomposed product. The above two fits have similar Zn-O bond distances in the 1<sup>st</sup> shell at about 1.96 Å with the same coordination number of oxygen (4) around the central zinc atom. There is a slight difference in the Zn..Zn bond distance of 0.02 Å between ZnO and Zn(OH)<sub>2</sub>. The bond distances of this EXAFS calculation are similar to other studies.<sup>[70]</sup>

Compound	Atom	This EXAFS	Other EXAFS <sup>[70]</sup>	XRD <sup>[70]</sup>	
		R (Å)	R (Å)	CN	R (Å)
Zinc Oxide	Zn-O	1.96	1.95	4	1.98
	Zn-Zn	3.26	3.22	12	3.50, 3.66
Zinc Hydroxide	Zn-O	1.96	1.99	4	1.96
	Zn-Zn	3.24	3.29, 3.47	2.2	3.29, 3.50

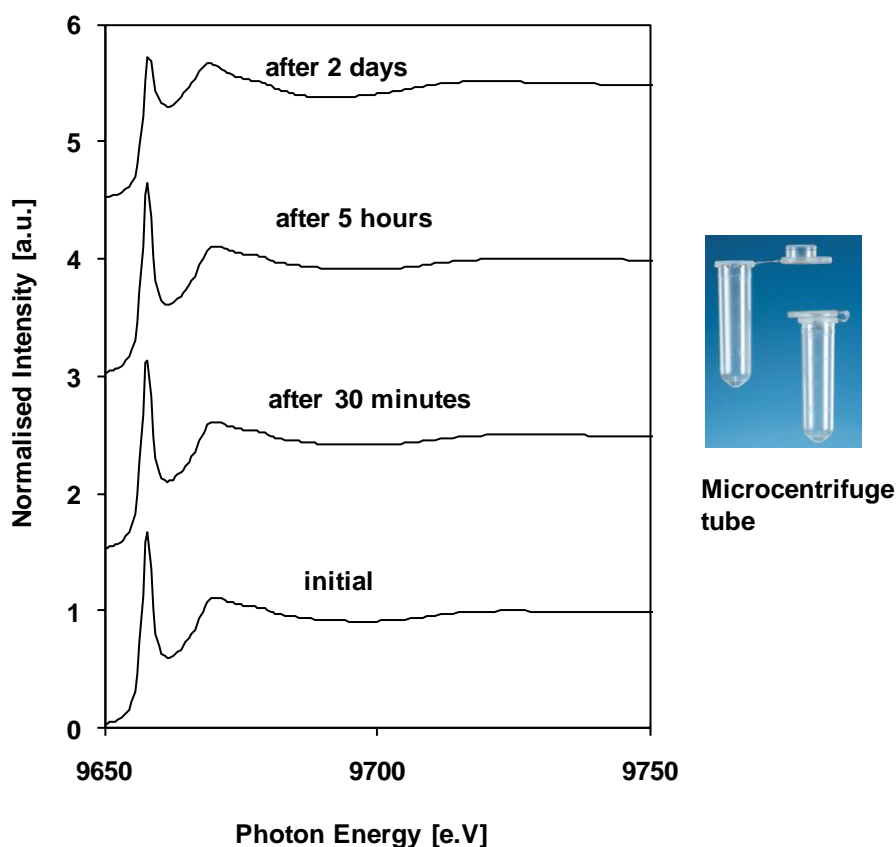
**Table 4.3: Local structure of ZnO and Zn(OH)<sub>2</sub> derived from this EXAFS and other studies**

The table above clearly shows the similarity of bond distances from the XAFS calculations of this study compared to the study by Robert and co-workers<sup>[70]</sup> even though the spectra are different. A comparison is made between the bond distances from EXAFS calculations of this and other work in addition to bond distances derived from XRD measurements. In the case of zinc oxide the Zn-O and Zn-Zn bond distance difference of this study and the above reference are 0.00 and 0.02 Å. The XRD measurements are higher than both EXAFS bond distances. On the other hand, the Zn-O and Zn-Zn bond distances of zinc hydroxide were comparable but lower. This comparison may suggest that the Zn-O and Zn-Zn bond distances and coordination numbers of decomposed DEZ in this EXAFS study are closer to that of ZnO than Zn(OH)<sub>2</sub>. However decomposed DEZ is neither ZnO nor Zn(OH)<sub>2</sub>.

#### **4.3.2 Microcentrifuge Tubes as Batch Reactors for *in situ* XAFS Studies**

1.5 to 2 mL polypropylene microcentrifuge tubes were used as batch or non-flow reactors to collect most of the *in situ* XAFS data in this study. Solutions of the pyrophoric dialkylzinc compounds were dosed into the tubes in an inert gas

environment ensuring the absence of oxygen, either under nitrogen or argon. XAFS experiments were carried out subsequently for a maximum of 3 hours. To ensure that these tubes are sufficiently leak-tight a series of XANES spectra of 0.1 M  $\text{Et}_2\text{Zn}$  were collected as a function of time. (Figure 4.14)

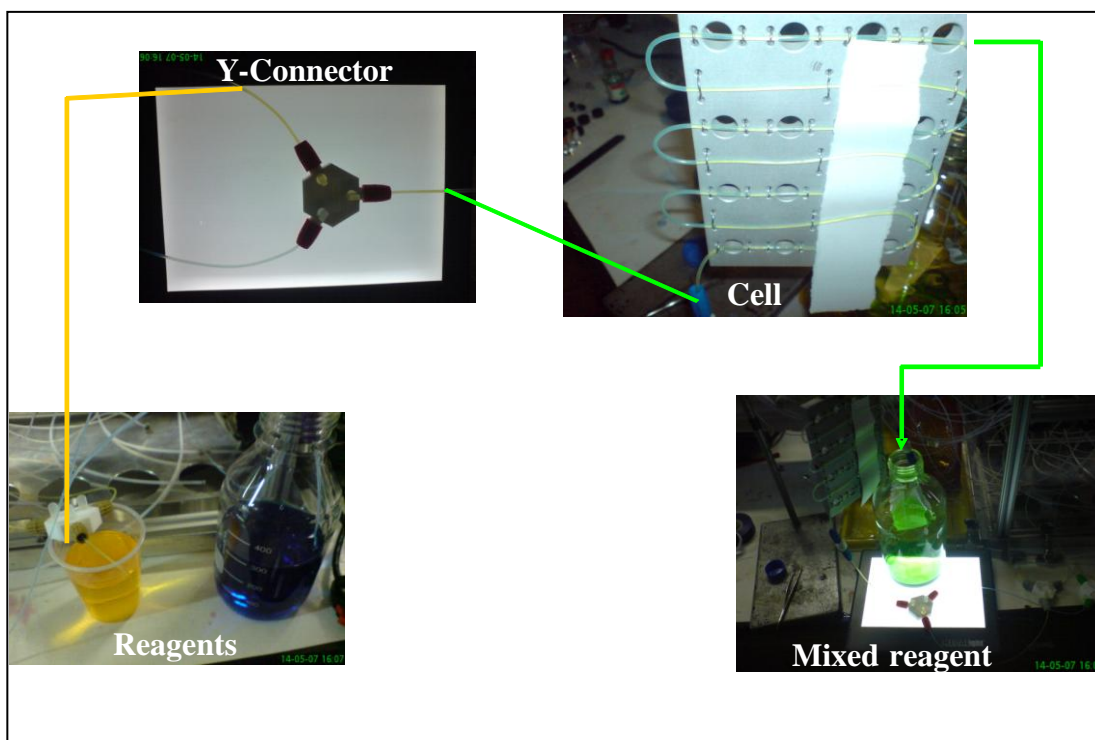


**Figure 4.14: XANES spectra of 0.1 M  $\text{Et}_2\text{Zn}$  in non-flow reactor (microcentrifuge) over 2 days**

It can be seen that  $\text{Et}_2\text{Zn}$  which is very reactive with air remains unreacted for several hours when kept airtight in a polypropylene microcentrifuge tube. A significant reduction is seen in the resonance peak of the XANES after 2 days. The above XANES spectra (Figure 4.14), demonstrates that within periods of a few hours the collected XAFS data are not affected by reactions with air or humidity entering through the push seal or the walls of the tube.

### 4.3.3 Continuous flow Reactor for XAFS Studies of Organometallic Reactions

In this study two main XAFS reactors were used: a simple room temperature batch previously seen in section 4.3.2 and a continuous flow reactor. Both reactors were used to understand the molecular mechanism during the alkylation of aldehydes under an inert environment i.e. Ar or N<sub>2</sub> gas. The batch reactors were a 1.5 - 2 mL microcentrifuge tube chemically resistant to the reagents. An initial design of the continuous flow reactor is illustrated below with the flow of colour dyes through PTFE tubes of internal diameter 1 mm and a perforated Al cell which should allow contact of incident X-rays with the flowing reagent.



**Figure 4.15: Testing the continuous flow Al reactor with colour dyes.**

The internal diameter of 1 mm and slow flow rate permits mixing (yellow and blue give green) to occur by diffusion since flow is laminar as explained earlier in section 4.2. This construction should be suitable to study reaction mechanisms if the mass transport is faster than reaction kinetics. A more detailed description of the

continuous flow reactor as well as the possibilities and limitations of the continuous tubular flow reactor for XAFS studies of organometallic reactions (seen in 4.3.4) has been published as a conference proceeding.<sup>[72]</sup>

#### **4.3.4 Continuous Tubular Reactor for XAFS Studies of Organometallic Reactions: Possibilities and Limitations for Studies of the Soai Reaction<sup>1</sup>**

The *in situ* flow XAFS measurements at the Zn K-edge were performed at station 9.3 of the SRS, UK, and at 12ID-B of the Advanced Photon Source (APS) at Argonne National Laboratory (USA). Supporting work with non-flowing solutions was performed using sealed Eppendorf microcentrifuge tubes at BM29 of the ESRF, Grenoble, France. Solutions were loaded into the microcentrifuge tubes in a glove bag continuously purged with dry N<sub>2</sub>. All reactions were performed at room temperature. At all three beamlines simultaneous measurements in transmission mode with gas ionization chambers and by fluorescence-yield (FY) detection with multielement Ge detectors were performed. Reactants and dry toluene solvent were obtained from Aldrich.

---

<sup>1</sup>This section has been published in the journal of physics conference series. [72] L. N. Nchari, G. A. Hembury, A. M. Beesley, D. J. Meehan, N. Tsapatsaris, M. Hudson, M. Thomason, S. L. M. Schroeder, *14th International Conference on X-Ray Absorption Fine Structure (Xafs14), Proceedings 2009*, 190.

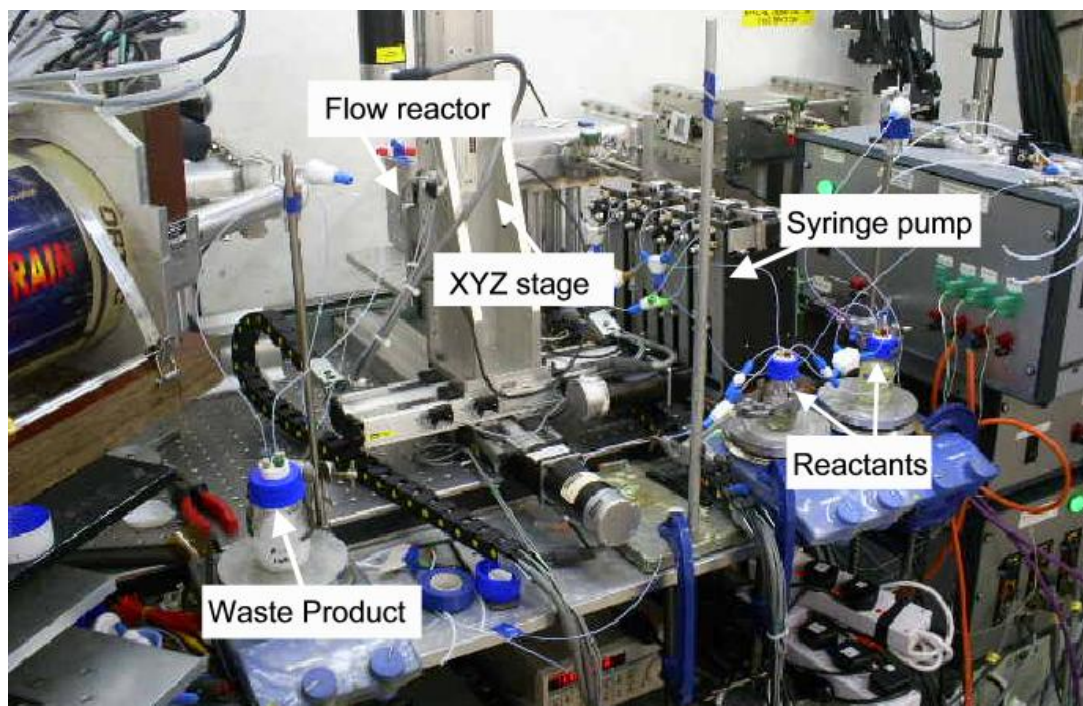


Figure 4.17: Tubular flow reactor assembled at station 9.3, SRS Daresbury, UK.

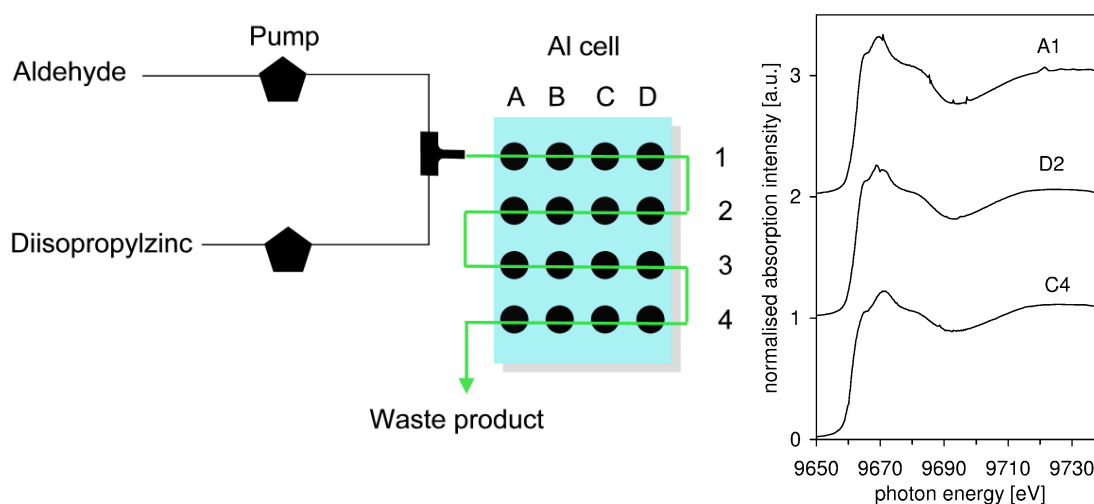


Figure 4.16: Schematic arrangement of the PTFE tubular flow reactor mounted on a heatable Al frame; also shown are representative *in situ* Zn K-edge FY XANES data taken at positions A1, D2 and C4 during the Soai reaction with a 1:1 volume mixture of 0.1 mol L<sup>-1</sup> diisopropylzinc and pyrimidyl aldehyde solutions.

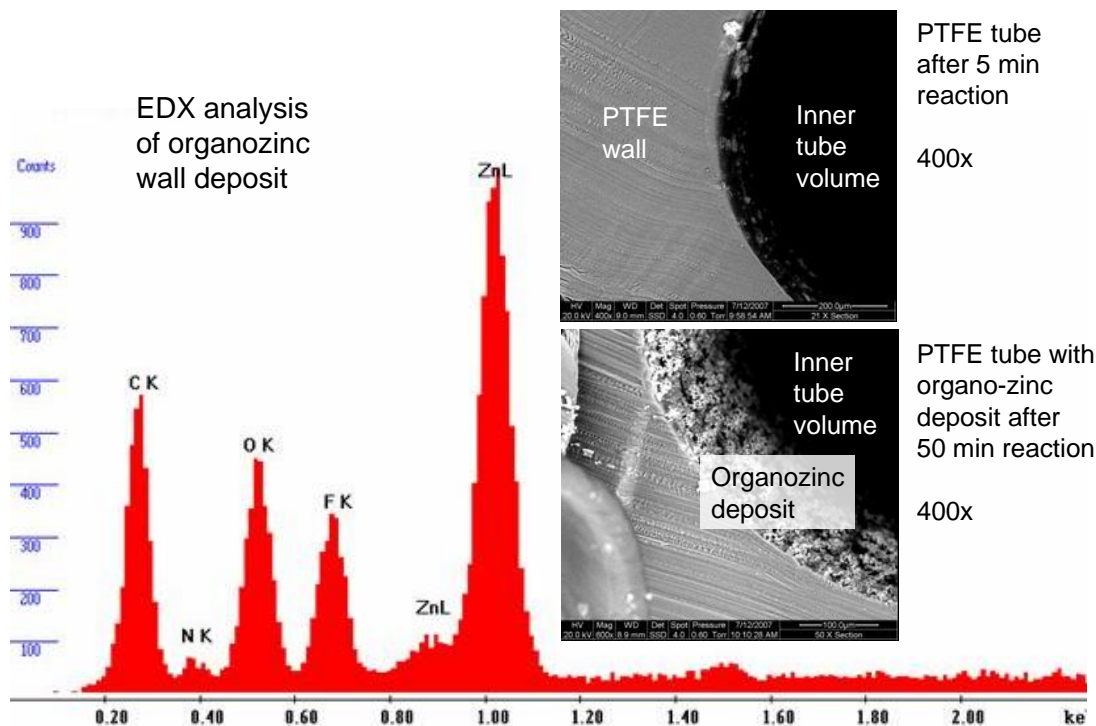
The flow reactor was based on PTFE tubing (1/8 inch outer diameter) attached to an aluminium support frame that had 16 holes in a regular 4×4 pattern machined out of it (Figure 4.16). At the positions of these holes *in situ* monitoring of the reaction progress along the tube was possible by combined transmission and fluorescence-yield detection. For our studies of the Soai reaction the pyrimidyl aldehyde and

diisopropylzinc were mixed at the tube inlet by joining the two solution streams in a PTFE 'T'-piece (Omnifit). The solution streams were provided by syringe pumps (Versa 6, Kloehn) fitted with 1 mL syringes and non-distribution valves; they were controlled remotely *via* a serial interface with a LabVIEW (National Instruments) GUI. A pair of syringe pumps was used for each of the two reactants (0.1 mol L<sup>-1</sup> diisopropylzinc and pyrimidyl aldehyde solutions). Handshaking operation synchronised the pump pairs: while one pump was dispensing the other was aspirating in preparation for subsequent dosing. As mentioned above, due to the oxygen and moisture sensitivity of this iPr<sub>2</sub>Zn solution a nitrogen atmosphere was needed to keep the environment inert within the pump pairs and flow cell apparatus. This was achieved by including a nitrogen feed on the multiport pump-head and purging before introduction of iPr<sub>2</sub>Zn solution. The reactant solutions were also prepared and stored under nitrogen. By varying the flow rate from the dosing pumps it is possible to tune the flow rate in the reactor to obtain information about the nature of metal species as a function of reaction time. Positioning in the X-ray beam was achieved by using a computer controlled XYZ stage calibrated to the dimensions of the reactor system. FY XANES data obtained at the APS during the reaction in a solution containing 0.1 mol L<sup>-1</sup> of pyrimidyl aldehyde and 0.1 mol L<sup>-1</sup> diisopropylzinc are included in Figure 4.16. A photograph of the completely assembled system at station 9.3 of the SRS is shown in Figure 4.17.

#### *Flow Experiments*

The XANES data from Figure 4.19 indicates that under the chosen flow conditions the reaction had progressed almost to completion at the initial measurement point,

A1. Only minor spectral changes occur as the reaction progresses towards positions D2 and C4.



**Figure 4.18: Electron microscopy and EDX analysis of the organozinc wall deposit on the inside of the PTFE reactor tube.**

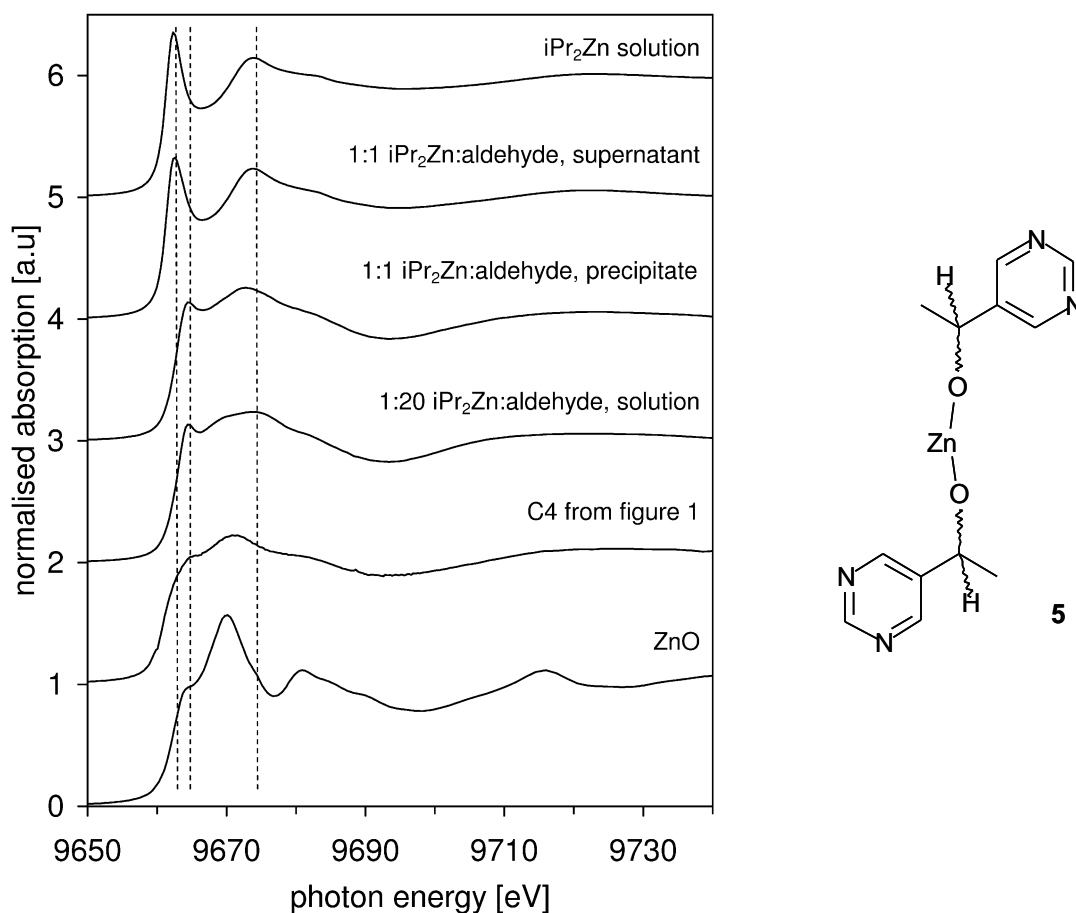
The appearance of occasional ‘spikes’ in the XANES data shown in Figure 4.16 was traced to the formation of small floating particles of a precipitate formed by the Soai process. We found that particles moving into and out of the X-ray beam would cause such distortions of the spectra, which were especially strong in transmission mode. In fact, several runs of experiments were rendered uninterpretable by the resulting presence of strong non-random noise.

In addition to the observed formation of a precipitate a strongly adherent wall deposit became apparent during the flow reactor experiments. These stationary deposits additionally influenced the XANES spectra. They form because the velocity of the flowing solution near the walls is lower than in the inner volume of the tube. The



extent to which wall deposits can grow quickly is illustrated by electron microscopic images in Figure 4.18. The lower of the two images shows that after running the Soai reaction for 50 min the deposit had a thickness of 5  $\mu\text{m}$ . *Ex situ* energy-dispersive X-ray (EDX) analysis (Figure 4.18) confirmed that the deposit contains ZnO and organozinc material. It seems likely that the formation of such wall deposits can only be suppressed if the reactor design is modified to maintain a high space velocity of the reaction medium, for example through strong turbulent flow or shear, near the wall where the XAFS measurements take place. Abrupt changes of flow direction or introduction of constricted regions on the tube may achieve this objective.

The XANES data included in Figure 4.19 are reminiscent of the Zn K-edge XANES of  $\text{Zn}^{2+}$  species in a tetrahedral environment, such as ZnO. This is illustrated in figure 4, in which the spectrum from position C4 is compared to a previously published spectrum of solid crystalline ZnO. It can be seen that the energetic positions of the shoulder at  $\sim 9664$  eV, the main resonance at  $\sim 9669$  eV and the broad resonance around  $\sim 9682$  eV coincide. Note however that the amplitudes of the XANES resonances of the Soai product, and especially the features in the EXAFS region (e.g., at  $\sim 9717$  eV), are strongly reduced, indicating disorder relative to crystalline ZnO on one hand and the presence of a significant self-absorption effect, likely associated with the formation of the observed solid product on the other. It appears that deposition of a poorly ordered ZnO and/or  $\text{Zn}(\text{OH})_2$  product takes place on the wall of the reactor tube and dominates the observed XAFS spectrum. The most likely origin is the presence of residual water and/or  $\text{O}_2$  in the reaction system, decomposing diisopropylzinc to  $\text{Zn}(\text{OH})_2$  and ZnO, respectively.



**Figure 4.19:** *In situ* transmission XANES (BM29, ESRF) obtained in microcentrifuge tubes. From top to bottom: Zn K-edge XANES spectra of a toluene solution containing 0.1 M diisopropylzinc; the supernatant of a solution formed by reacting 0.1 M diisopropylzinc and 0.1 M pyrimidine aldehyde in toluene; the sediment formed in this solution; a toluene solution containing 0.1 M diisopropylzinc and 2 M pyrimidine aldehyde; the spectrum labelled C4 in figure 1 (measured at the SRS); a spectrum of ZnO.

Because of the problems associated with solid product formation the flow reactor turned out to be unsuitable for a number of Soai aldehyde alkylation systems. For this reason we reverted back to a simple static batch reactor experiment with microcentrifuge tubes as described in section 4.3.2 that permitted separation of solution phase and precipitates by gravitational settling.

#### *Products of Soai Process under Non-Flow Conditions*

Experiments with a sealed static reactor cell (a standard Eppendorf polypropylene microcentrifuge tube) allowed us to minimise the formation of wall deposits and to selectively characterise the precipitate formed by the Soai process. This was achieved by allowing sedimentation of the precipitate at the bottom of the microcentrifuge tube, which also enabled us to separately examine the remaining supernatant solution. Figure 4.19 contains the resulting transmission XANES spectra of the sedimented precipitate (3<sup>rd</sup> spectrum from top) and of the supernatant solution (2<sup>nd</sup> spectrum from top) obtained by mixing 0.1 mol L<sup>-1</sup> aldehyde and 0.1 mol L<sup>-1</sup> iPr<sub>2</sub>Zn in toluene in a 1:1 molar ratio. It can be seen by comparison with the spectrum of iPr<sub>2</sub>Zn in toluene (top spectrum) that any Zn species remaining in the supernatant solution stem from unreacted iPr<sub>2</sub>Zn. In contrast, the spectrum of the sedimented precipitate (second spectrum from top) has no strong white line, indicating that p-like valence states are occupied and that the local bonding and/or coordination geometry are fundamentally different from that in iPr<sub>2</sub>Zn. For a 1:1 mixture of iPr<sub>2</sub>Zn and aldehyde one would statistically expect a product mixture containing unreacted iPr<sub>2</sub>Zn as well as the monomeric species **3** and some monomeric dialkoxide species **5** (Figure 4.19). To address which of these species was responsible for the observed spectrum we carried out the reaction of iPr<sub>2</sub>Zn with a 20-fold excess of aldehyde because this reaction is expected to result in the formation of only the dialkoxide **5**. Interestingly, the XANES spectrum of this product (3<sup>rd</sup> spectrum from bottom in Figure 4.19) is very similar to the spectrum of the precipitate formed in the 1:1 mixture, indicating that the dialkoxide is preferentially formed even when understoichiometric amounts of aldehyde are supplied. What is currently not clear is whether the precipitate contains the monomeric species **5** or whether the previously proposed dimers, trimers or

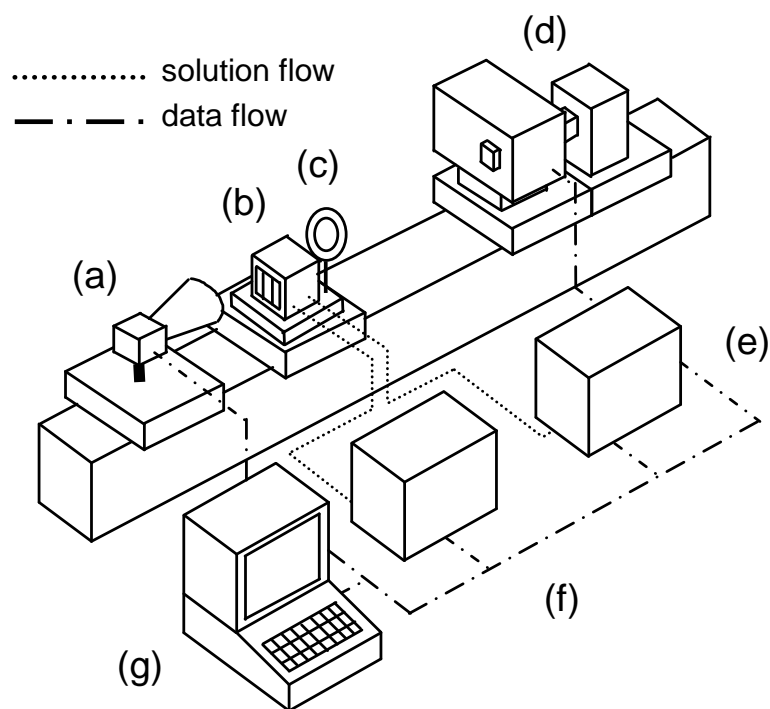
oligomers of **5** are formed. In these products the Zn centres would be in a distorted tetrahedral coordination environment, which is compatible with the overall appearance of the spectra and especially the absence of the strong white line in the XANES spectra of the observed product. (4.3.1)

In summary, fully computer-controlled continuous tubular flow reactor system for time-resolved *in situ* XAFS measurements has been commissioned. Zn K-edge XANES data demonstrate that with 3<sup>rd</sup> generation synchrotron beam spectra of very good quality can be achieved with Zn concentrations in the 100 mmol region. Heterogeneous processes in the Soai reaction lead to considerable complications with the measurements due to the formation of floating particles of the aldehyde/ $i\text{Pr}_2\text{Zn}$  adduct formed in the reaction, while the deposition of solid  $i\text{Pr}_2\text{Zn}$  decomposition products on the walls of the flow reactor dominates the spectra after less than an hour of continuous reaction. The Soai precipitate formed in 1:1  $i\text{Pr}_2\text{Zn}$ :aldehyde mixtures appears to be the dialkoxide complex, while the remaining supernatant still contains unreacted  $i\text{Pr}_2\text{Zn}$ . The XANES data for the dialkoxide do not exclude the presence of non-monomeric species; that a precipitate is observed supports the notion that the formation of dimers, trimers, tetramers or higher oligomers takes place.

#### **4.4 *In situ* UV spectroscopy study in parallel reactors**

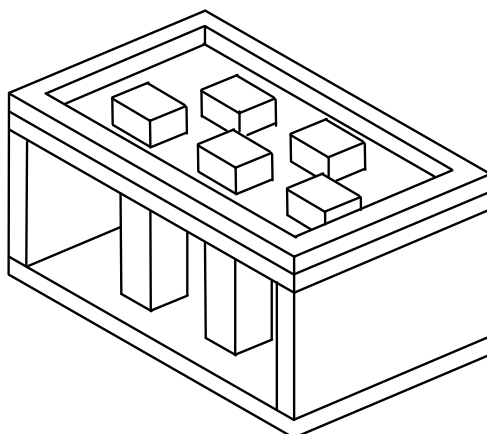
In the course of this study a noticeable colour change was observed with a mixture of cinnamaldehyde, diethylzinc and dimethylaminoethanol. This was quite intriguing and as a result the XAS measurements were complemented with UV measurements. UV measurements were carried using an in house built high throughput system. Different ratios of the mixture of cinnamaldehyde, diethylzinc and

dimethylaminoethanol were considered. The change in the absorption characteristics overtime was observed by simultaneously measuring five samples. The intensity of each cell was measured at intervals of one minute. The illustration below shows the automated system suitable for measuring 5 samples simultaneously.<sup>[73]</sup>



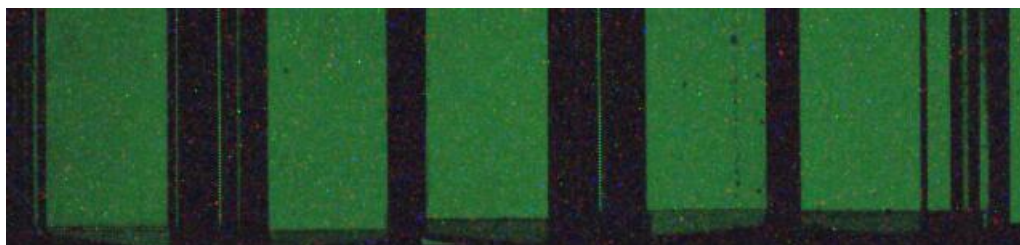
**Figure 4.20: Overview of ‘5 cuvette’ platform, (a) camera, (b) flow cuvettes in aluminium frame, (c) collimating lens, (d) monochromator & light source, (e and f) syringe pump dosing system with stock solutions and (g) control PC.<sup>[73]</sup>**

The scanning monochromatic light (250 W quartz tungsten halogen lamp) was allowed to go through the sample array using a collimating lens. The sample array of five cuvettes (Type 71-V, Starna Scientific), were fixed in an aluminium frame.



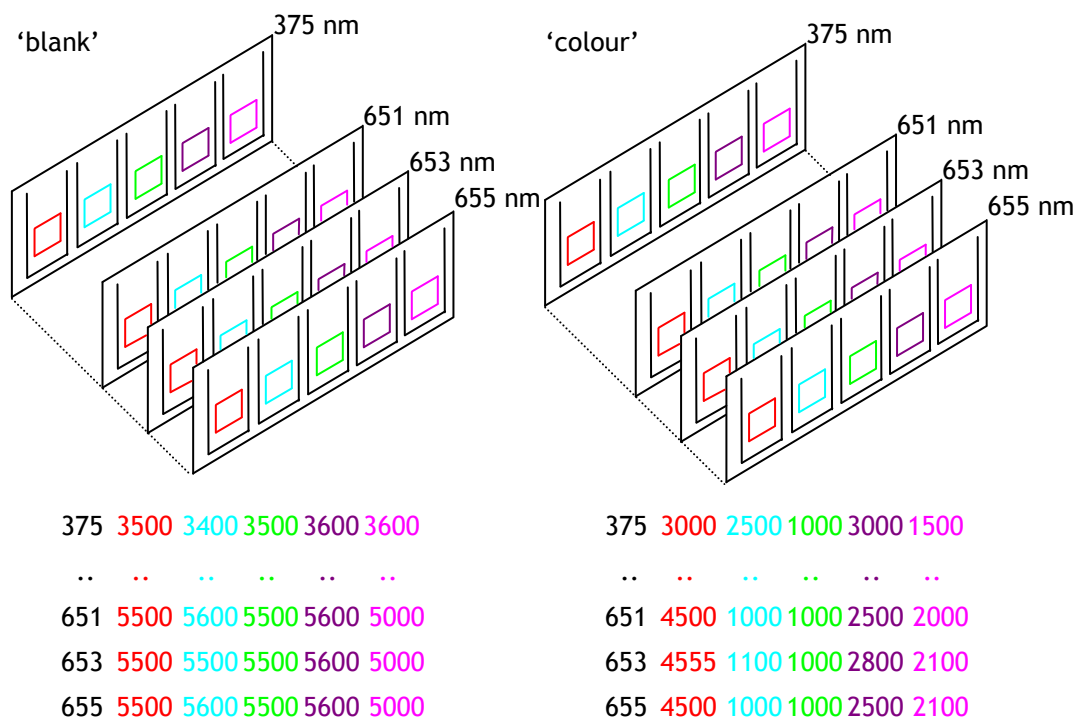
**Figure 4.21: Aluminium frame containing cuvettes<sup>[73]</sup>**

The samples were detected by a CMOS (complementary metal oxide semiconductor) camera (EC640c, Prosilica) combined with a telecentric lens (Visionmes 70/8/0.1, Zeiss). With the aid of a LabVIEW based software, the absorption spectra of all five samples over time is registered.<sup>[73]</sup>



**Figure 4.22: Image of monochromatic light through five sample cells<sup>[73]</sup>**

Scanning was automatically done between 375 – 655 nm at 5 nm intervals as illustrated below.



**Figure 4.23: Determination of light intensity through sample cells at a range of wavelengths by image analysis software.**<sup>[73]</sup>

The summation of pixel intensities gives information about the brightness and the amount of transmitted light. The measurement of 5 samples is compared to a reference image which in this case was toluene at the same wavelength. The absorption is calculated by using the Beer-Lambert equation

$$A = 2 - \log(100 \times I/I_0) \quad 4.21$$

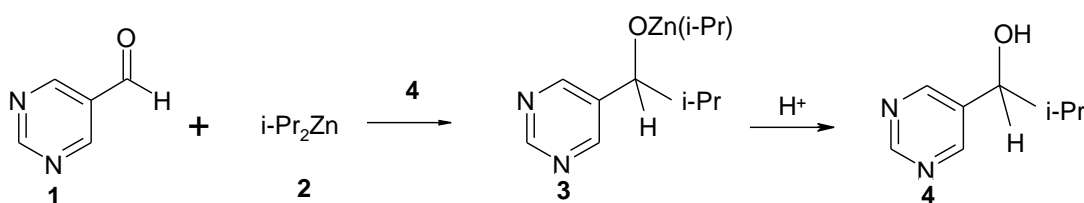
$A$  - Absorption,  $I$  - Measured Intensity and  $I_0$  - Original Intensity

Synchronized images acquired are replicated every minute for 35 minutes in order to produce a time resolved measurement.<sup>[73]</sup>

## 5. The influence of solvents on asymmetric amplification

### 5.1 Introduction

Asymmetric amplification can be strongly influenced by the solvent medium. The influence is more specifically on the enantiomeric excess, *ee* and yield. In the Soai autocatalytic reaction<sup>[20, 36, 38, 41]</sup> it has been reported that cumene is a slightly better solvent than toluene. The *ee* is increased to 99.3% in cumene in the following reaction.



The table below compares solvents that generally give a high *ee* and yield with cumene being the better solvent in the Soai autocatalytic reaction as earlier mentioned.

Entry	X	Solvent	Asym, autocat. and product <i>ee</i> [%]	Yield [%]	<i>ee</i> [%]
1	2.2	Toluene (a)	99.3 (S)	98	99.1 (S)
2	2.2	Cumene (a)	99.4 (S)	98	99.3 (S)
3	2.2	Tert-butylbenzene (a)	99.3 (S)	99	99.1 (S)
4	2.2	Cumene (b)	>99.5 (S)	99	>99.5 (S)
5	1.7	Cumene (b)	>99.5 (S)	>99	>99.5 (S)
6	1.7	Cumene (b)	>99.5 (R)	>99	>99.5 (S)

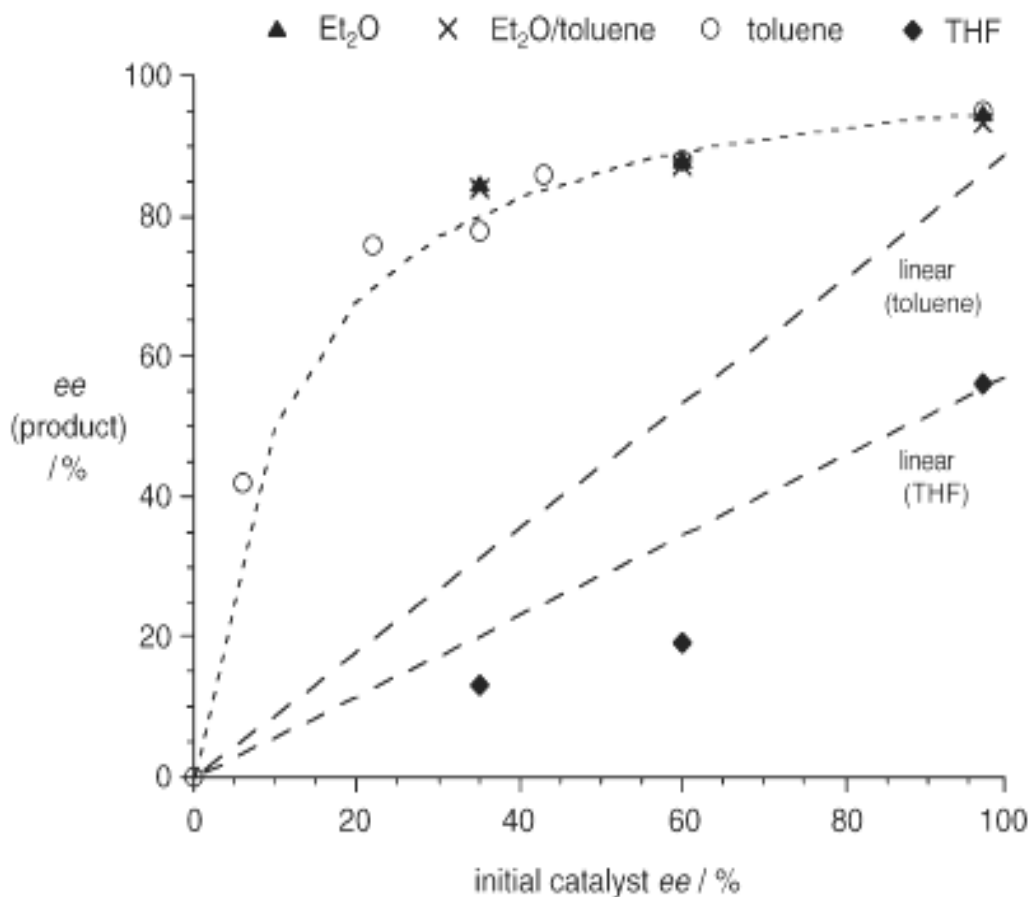
(a) With 1M *i*Pr<sub>2</sub>Zn in toluene

(b) With 1M *i*Pr<sub>2</sub>Zn in cumene

**Table 5.1: Asymmetric autocatalysis reaction with autocatalytic reaction with (S)- and (R)-2 with > 99.5% *ee*.<sup>[36]</sup>**



According to studies done by Blackmond, the Soai autocatalytic reaction performs chiral amplification well in toluene and diethylether (Figure 5.1).<sup>[45]</sup>



**Figure 5.1: Product *ee* against initial catalyst *ee* in toluene, diethylether, Et<sub>2</sub>O/toluene and THF.**<sup>[45]</sup>

Interestingly, THF does not lead to amplification but to promotion of a linear relationship between the *ee* of the product and the initial catalyst. In THF the reaction is also reported to be extremely sluggish. Further studies indicated that product precipitation may be observed during reactions in all solvents.<sup>[45]</sup> The *ee* in solution and the precipitate is solvent dependent. In the case of toluene the *ee* of the precipitate in toluene is lower than that of the solution. This reverses in diethyl ether in which the precipitate gives a higher *ee*. Blackmond has proposed that these results

suggest the physical properties of the heterodimer to be less soluble than homodimer species in toluene whereas in diethylether the heterodimer species is more soluble.<sup>[45]</sup>

Entry	Solvent	% ee (cat.)	% ee (solution)	% ee (precipitate)	% ee (total)	% product in solution
1	toluene	60	95.8	88.3	88.5	42
2	toluene	60	94.3	78.9	85.6	59
3	toluene	60	96.6	69.5	87.2	68
4	toluene	60	96.7	66.2	83.9	46
5	toluene	35	93.2	64.3	79.9	45
6	toluene	35	93.0	61.2	77.3	50
7	toluene	35	94.9	73.1	78.8	24
8	toluene	35	91.4	63.0	78.4	42
9	toluene	35	90.4	64.0	75.1	40
10	Et <sub>2</sub> O	60	63.7	94.4	88.8	16
11	Et <sub>2</sub> O	60	41.8	92.6	90.5	14
12	Et <sub>2</sub> O	60	35.7	91.3	84.8	17
13	Et <sub>2</sub> O	60	51.4	89.4	88.5	14
14	Et <sub>2</sub> O	60	49.5	92.3	88.1	14
15	Et <sub>2</sub> O	35	37.9	88.7	80.3	18
16	Et <sub>2</sub> O	35	54.0	86.3	85.5	7
17	Et <sub>2</sub> O	35	57.3	86.1	86.9	5
18	Et <sub>2</sub> O	35	56.1	86.4	83.3	8
19	Et <sub>2</sub> O/toluene	60	73.3	91.5	89.0	7.5
20	Et <sub>2</sub> O/toluene	60	57.6	91.6	86.5	10.5
21	Et <sub>2</sub> O/toluene	60	58.3	93.5	90.7	12
22	Et <sub>2</sub> O/toluene	60	68.4	90.5	86.4	8.5
23	Et <sub>2</sub> O/toluene	60	58.1	90.9	86.1	20
24	Et <sub>2</sub> O/toluene	60	72.7	90.3	86.7	12
25	Et <sub>2</sub> O/toluene	60	69.3	90.0	87.5	24
26	Et <sub>2</sub> O/toluene	60	72.8	90.2	86.3	14
27	Et <sub>2</sub> O/toluene	35	81.8	85.5	83.8	10
28	Et <sub>2</sub> O/toluene	35	80.3	84.5	83.2	5
29	Et <sub>2</sub> O/toluene	35	82.4	85.8	83.6	10
30	Et <sub>2</sub> O/toluene	35	76.4	85.1	85.1	7
31	Et <sub>2</sub> O/toluene	35	81.9	85.3	83.4	12
32	Et <sub>2</sub> O/toluene	35	81.6	82.5	81.8	19
33	Et <sub>2</sub> O/toluene	35	81.9	83.8	83.7	20
34 <sup>[b]</sup>	THF	96	56	n.d.	56	98
35 <sup>[b]</sup>	THF	60	19	n.d.	19	n.d.
36 <sup>[b]</sup>	THF	35	13	14	13	96
37 <sup>[b]</sup>	THF	10	0	3	1	55

[a] The reactions were carried out in different solvents under conditions similar to those of the reactions shown in Figure 2. Reactions were sampled after 1 hour, except where noted. All reactions exhibited 100% conversion, except where noted. [b] Sampled after 24 h; reaction products other than **2** were observed. Total conversion of aldehyde **1** in reactions in THF after 24 h was < 50%.

**Table 5.2: Comparing the *ee* and % product in solution and the precipitate for the Soai reaction.**<sup>[45]</sup>

Brown also reported the non-occurrence of amplification in THF.<sup>[50]</sup> It was suggested that the strong Lewis basicity of the solvent has an inhibiting effect that causes a slow turnover. Other studies report the binding of the Lewis base to metals.

Using PMR spectroscopy Denisov *et al*.<sup>[74]</sup> examined the formation of complexes of diethylzinc with Lewis bases. They proposed that a donor-acceptor complex causes an internal shift or change in the electronegativity of Zn atom explaining why for complexes with diethylether a small chemical shift is observed than for THF. The decreasing strength of complex formation with Et<sub>2</sub>Zn is in the order THF > propylene oxide > diethyl ether.<sup>[74]</sup> An X-ray absorption spectroscopy study is important to understand the interaction of the solvents with alkyl zinc and to explain the different levels of the *ee* of the product and chiral catalyst.

## 5.2 Experimental

Several concentrations of dialkyl zinc were prepared in 2 mL microcentrifuge tubes. This preparation was done in the presence of nitrogen gas in a glove bag in the absence of oxygen. The behaviour of dialkylzinc was studied in solvents which include toluene, diethylether and tetrahydrofuran. In some experiments the solvents were mixed in specific ratios. X-ray absorption fine structure (XAS) measurements were carried out at the Zn K-edge.<sup>[56]</sup> The monochromator type used was Si (111) and the experiments were performed at beam lines BESSRC 12-BM-B at the Advanced Photon Source (USA), BM29 at the European Synchrotron Research Facility (ESRF), XAS at ANKA (Germany) and 9.3 at SRS (United Kingdom). The X-ray radiation was detected in florescence and transmission mode.

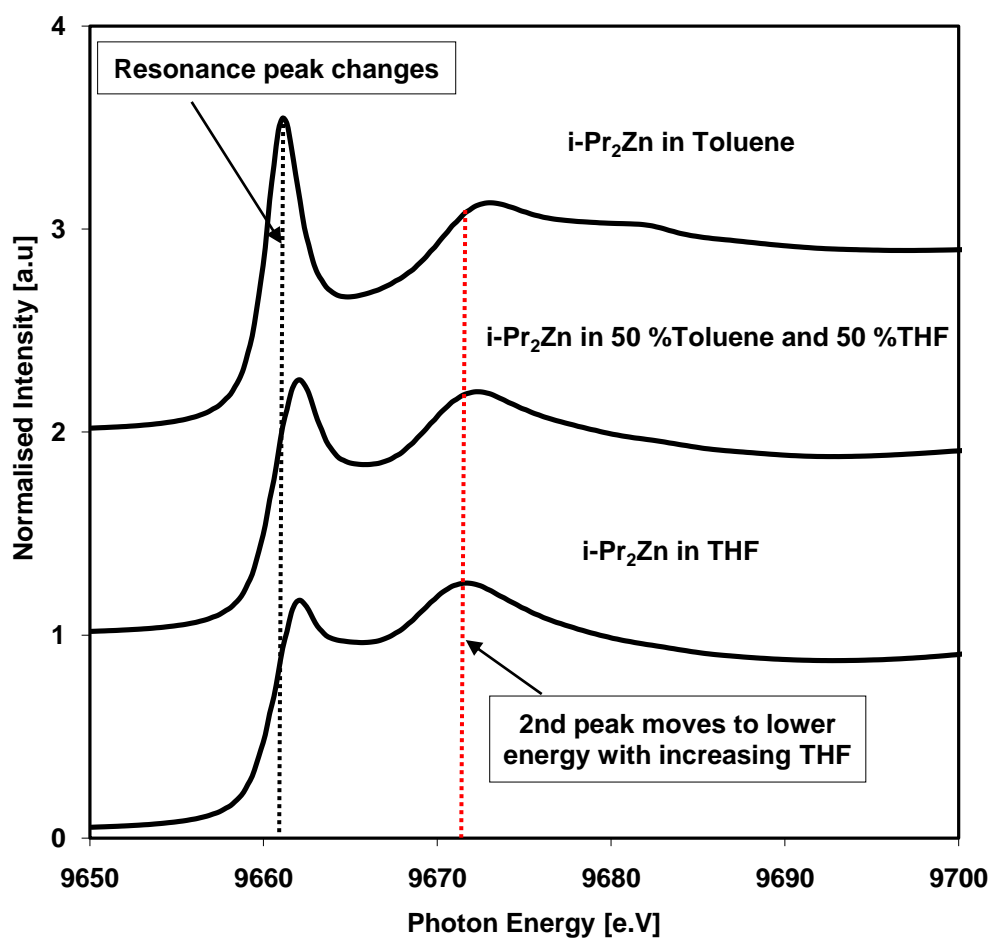
The local Zn structures in solution were determined from fitting experimental and theoretical data in *R* and *k* space (Figure 5.5). Theoretical data is from the structure of ZnO derived from a crystal structure database and imported into Iffefit. The extracted EXAFS function was weighted at *k*<sup>3</sup> and Fourier transforms calculated between a *k* range of 3-12 Å. The dialkylzinc models in different solvents were

assembled from the fits generated by FEFF8. The amplitude reduction factor was set at 0.82. The coordination number, radial distance, Debye-Waller factor and energy shifts were calculated considering only two shells.

## 5.3 Results and Discussion

### 5.3.1 *i*-Pr<sub>2</sub>Zn in toluene and THF

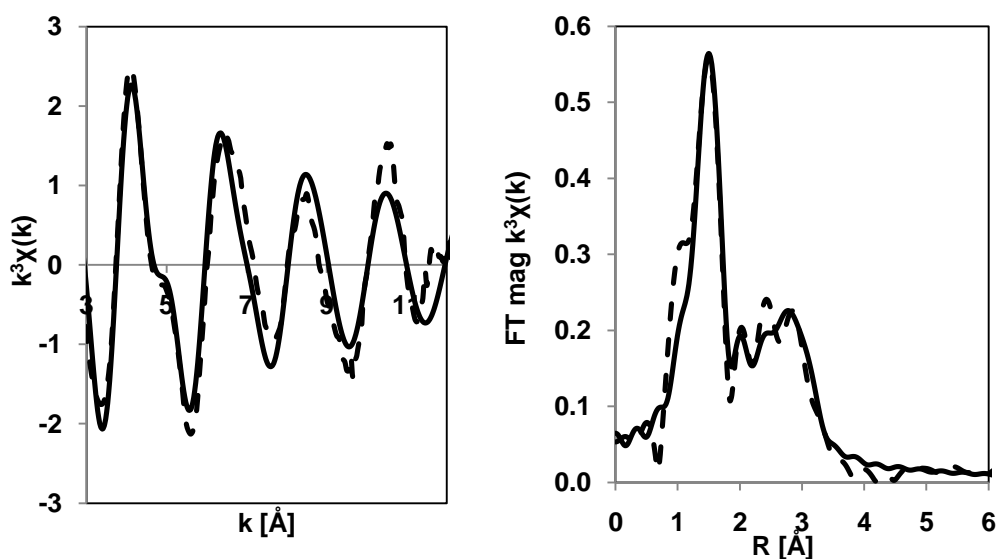
Initial experiments were carried out with diisopropylzinc in toluene and THF at the APS, Argonne National Laboratories, USA. The X-ray absorption near edge structure (XANES) region in both solvents is different as seen below. The XANES spectra of a 0.05 M *i*-Pr<sub>2</sub>Zn in toluene and THF are clearly dissimilar. A strong ‘white line’ near edge resonance is observed in toluene resulting from a 1s-4p transition. This peak is reduced with the introduction of THF, even when THF is diluted with toluene (black dotted line) as seen in Figure 5.2 below.



**Figure 5.2:** Zn K-edge XANES spectra of 0.1 M  $i\text{-Pr}_2\text{Zn}$  in toluene, THF and toluene/THF (1:1).

Considering the red dotted line in the XANES spectra (Figure 5.2), it is noticeable that with the addition of THF the second peak moves towards lower energy values. A small peak at 9684 eV of  $i\text{-Pr}_2\text{Zn}$  in toluene also disappears with THF addition. The similarity of the XANES spectra of  $i\text{Pr}_2\text{Zn}$  in THF and a toluene/THF mixture suggests a high affinity of THF to associate itself with Zn thus changing the Zn environment or electronegativity. A model of both  $i\text{Pr}_2\text{Zn}$  in toluene and THF was further calculated from the Extended X-ray Absorption Spectroscopy region.

The EXAFS fit of diisopropylzinc in toluene is shown in Figure 5.3 below.



**Figure 5.3:** Zn K-edge EXAFS spectra and FT of *i*-Pr<sub>2</sub>Zn in toluene. Dash lines: Experimental data and solid lines: best theoretical fit.

The model suggests that diisopropylzinc is not associated in toluene as seen by the EXAFS parameters in Table 5.3. The structural parameters obtained by the fitting analysis (Table 5.3) suggests that every Zn atom in the toluene solution has on average 1.5 C atoms at a distance of 1.89 Å. Also apparent is a second coordination shell of approximately 4 C atoms at a distance of approximately 3.4 Å. These data are compatible with a structural model of undissociated *i*Pr<sub>2</sub>Zn (Figure 5.5). As seen below, these structural parameters are compatible with the molecular structure of *i*Pr<sub>2</sub>Zn in the gas phase (Table 5.4). There is no evidence for Zn-Zn scattering in the data, supporting the conclusion that self-association of dissolved *i*Pr<sub>2</sub>Zn does not take place. The high statistical uncertainty on the coordination number of the second shell may indicate that complex but relatively weak interactions with toluene molecules take place in this region; such weak interactions are difficult to model in an EXAFS fit. This would also offer an explanation for the relatively lower fit quality.

The results of the EXAFS fitting analysis for diisopropylzinc in THF are also shown in Figure 5.4. A strong difference between the EXAFS of diisopropylzinc in toluene (Figure 5.3) and in THF (Figure 5.4) is already evident from visual inspection of the spectra.

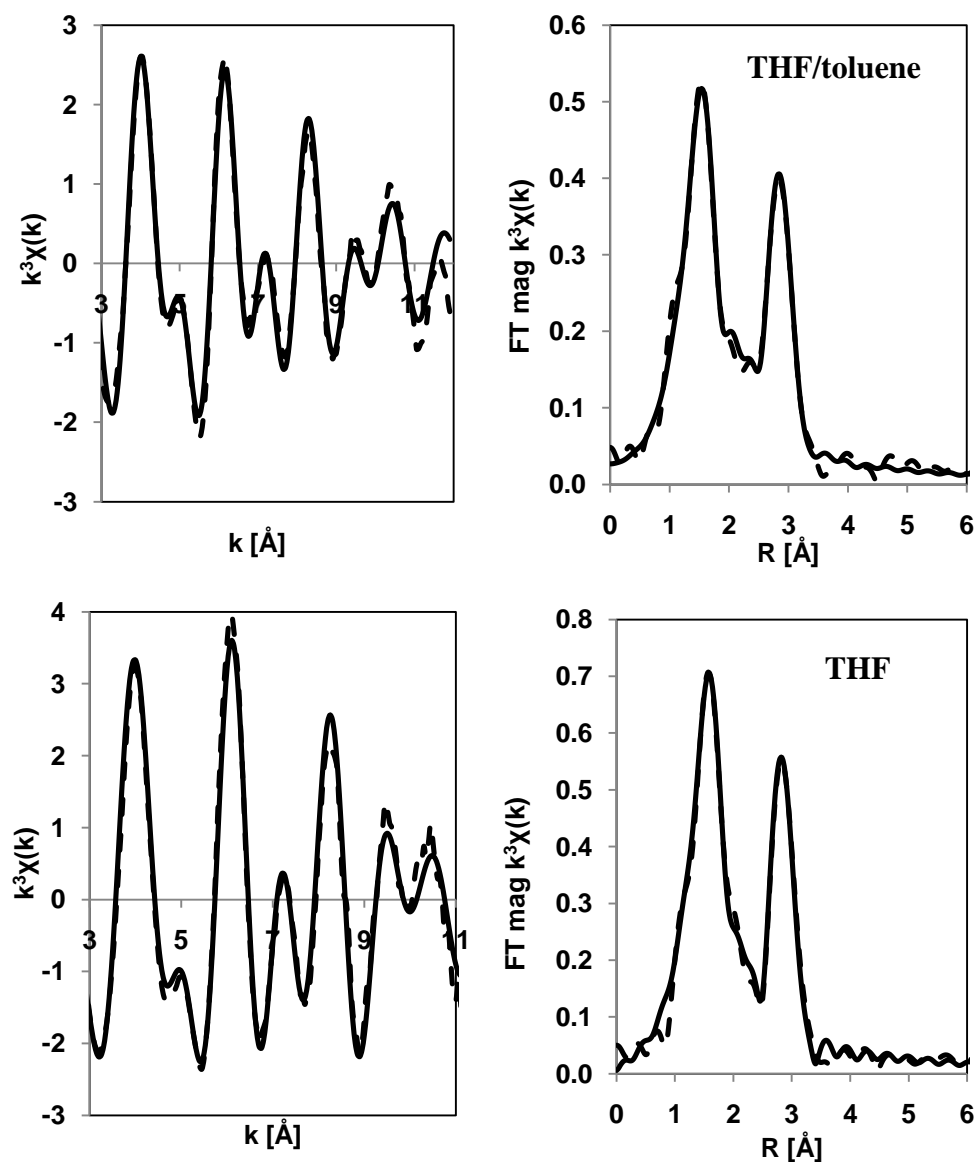


Figure 5.4: Zn K-edge EXAFS spectra and FT of  $i\text{-Pr}_2\text{Zn}$  in toluene and THF. Dash lines: experimental data and solid lines: best theoretical fit.

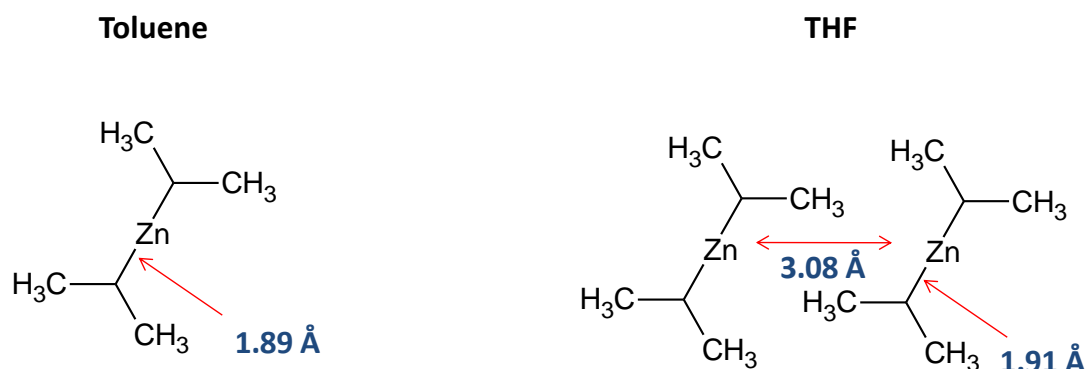
From the fitted EXAFS calculation in  $k$  and  $R$  space, it is noticeable that  $i\text{-Pr}_2\text{Zn}$  in the 1:1 Toluene/THF mixture is more similar to that in THF. In  $R$  space, a second peak resulting from Zn-Zn backscattering is absent in the case of toluene but present in THF or a THF/toluene mixture. A similarity is also seen in  $k$  space where there is more backscattering at higher  $k$  values in THF. In  $k$  space, there is a similarity in THF and toluene between 3 and 6 Å. However, changes are seen after this point at higher  $k$  values where more scattering (probably due to Zn...Zn scattering) is noticed with the introduction of THF. The EXAFS parameters used to fit these spectra are given in the table below (Table 5.3).

Sample	First shell (Zn-O/C/N)			Second shell (Zn-O/C/N) (Zn-Zn)							
	N	$R(\text{\AA})$	$\sigma^2(\text{\AA}^2)$	N	$R(\text{\AA})$	$\sigma^2(\text{\AA}^2)$	N	$R(\text{\AA})$	$\sigma^2(\text{\AA}^2)$	$E_0(\text{eV})$	R (%)
<b>Toluene <math>i\text{-Pr}_2\text{Zn}</math></b>	1.46 $\pm 0.141$	1.89 $\pm 0.005$	0.005 $\pm 0.001$	3.8 $\pm 1.583$	3.40 $\pm 0.013$	0.003 $\pm 0.007$				1.48 $\pm 0.318$	5.8
<b>THF <math>i\text{-Pr}_2\text{Zn}</math></b>	2.48 $\pm 0.171$	1.91 $\pm 0.005$	0.008 $\pm 0.001$	4.3 $\pm 0.83$	3.51 $\pm 0.013$	0.006 $\pm 0.002$	1.19 $\pm 0.318$	3.08 $\pm 0.006$	0.005 $\pm 0.002$	4.91 $\pm 0.714$	1.2
<b>Toluene/THF <math>i\text{-Pr}_2\text{Zn}</math></b>	1.71 $\pm 0.157$	1.96 $\pm 0.007$	0.007 $\pm 0.001$	5.82 $\pm 1.895$	3.48 $\pm 0.002$	0.013 $\pm 0.006$	0.89 $\pm 0.671$	3.08 $\pm 0.013$	0.008 $\pm 0.004$	3.48 $\pm 1.024$	1.9

**Table 5.3: Zinc K edge EXAFS parameters of  $i\text{-Pr}_2\text{Zn}$  in toluene and THF**



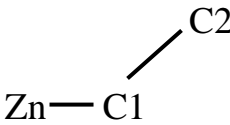
The R-factor, which is the goodness of the fit between experimental and theoretical spectrum is 1.2 and 1.9 % for  $i\text{Pr}_2\text{Zn}$  in THF and in the THF/toluene mixture, respectively. This means these fits are excellent and the predicted dimeric structures are therefore reliable. The structural parameters obtained by the fitting analysis (Table 5.3) suggests that every Zn atom in the THF solution has on average 2.5 C atoms at a distance of 1.91 Å (slightly more extended than in toluene). The second shell has approximately 4 C atoms at a distance of approximately 3.5 Å. The structural model of associated  $i\text{Pr}_2\text{Zn}$  is seen in Figure 5.5. There is evidence for Zn-Zn scattering in the data implying that self-association occurs in THF but not in toluene. In THF the existence of a dimer is evidenced by Zn-Zn backscattering.



**Figure 5.5: Models of  $i\text{Pr}_2\text{Zn}$  in toluene and THF from EXAFS calculations. Because of solvent interactions the Zn complex is likely to be a bent structure and therefore depicted as such, even though the actual coordination geometry cannot be determined from the XAFS data.**

Two distinct models of  $i\text{Pr}_2\text{Zn}$  can be seen from Figure 5.5 in toluene and THF.  $i\text{Pr}_2\text{Zn}$  exists as a monomer in toluene but dimerizes in THF. A possible link between both models and  $ee$  is suggested by Mahmoud.<sup>[75]</sup> The proposed dimer model has a Zn-Zn distance of approximately 3.08 Å. There is however no evidence of bond formation between the two Zn atoms because a Zn-Zn bond distance is typically reported to be about 2 Å i.e. approximately 1 Å less than the model proposed in this

study.<sup>[76]</sup> The Zn atoms are likely held together in a cluster by weak intermolecular forces. Using XAS it is otherwise not possible to distinguish Zn-O, Zn-N and Zn-C interactions as carbon, nitrogen and oxygen have similar backscattering contributions as a result of their close atomic numbers or similar number of electrons in the core of their atoms.<sup>[77]</sup> The EXAFS calculated bond distances are similar to those from other studies done by Haaland in which the bond length of zinc-carbon bonds was studied by density functional theory calculations, gas electron diffraction and photon electron spectroscopy.<sup>[76, 78]</sup>

	<b>Gas Phase<sup>[78]</sup></b>	<b>Solution (EXAFS)</b>	
Zn-C1	1.96 Å	1.89 Å	
Zn-C2	3.45 Å	3.40 Å	

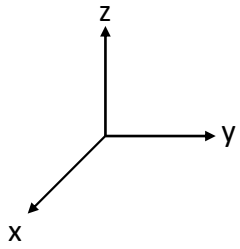

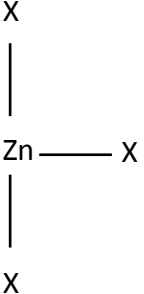
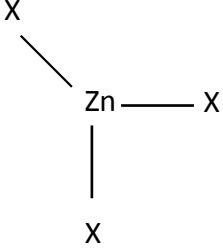
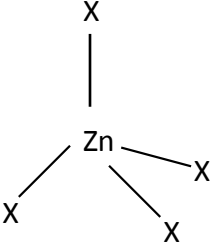
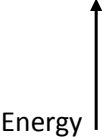
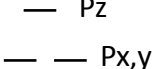
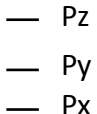
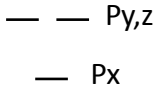

**Table 5.4: Comparison of bond distances in i-Pr<sub>2</sub>Zn gas phase and solution. Gas phase: Haaland's study,<sup>[78]</sup> Solution: EXAFS calculation.**

Assuming that bond angles in the gas phase and in solution are similar it would appear that the EXAFS-derived structural parameters are also compatible with the structures reported in Haaland's study. The Zn-C1-C2 angle adopted from the studies of Haaland is 114°.<sup>[78]</sup>

### *Near edge*

Based on the EXAFS derived models for iPr<sub>2</sub>Zn we can now understand the difference in the near-edge data for iPr<sub>2</sub>Zn dissolved in toluene and THF. Kau *et al*<sup>[79]</sup> and Fulton *et al*<sup>[80, 81]</sup> related the intensity of the near-edge resonance for Cu<sup>+</sup> to local coordination and geometry by considering the ligand field splitting of Cu<sup>+</sup>

valence orbitals as a function of site geometry.<sup>[79]</sup> In terms of the electron count,  $\text{Cu}^+$  corresponds to  $\text{Zn}^{2+}$ , so similar consideration should apply here (**Figure 5.6**). The position and intensity of the preedge of  $\text{Cu}^+$  is described by *Kau et al* as follows: A 2-coordinate complex exhibits a high intensity in the 8984 eV region, the intensity reduces in the same region for a 3-coordinate complex. In a 4-coordinate complex the reduced preedge peak moves upwards to the 8986 eV region.

Coordination number	2	3		4
	Linear	T-shaped	Trigonal Planar	Tetrahedral
				
				

**Figure 5.6: Ligand field splitting of  $\text{Zn}^{2+}$  4p orbitals as a function of site geometry.<sup>[79]</sup>**

The ligand field proposed by *Kau et al* predicts that the degeneracy in  $\text{Zn}^{2+}$  is split by the ligand field. In a coordinate linear molecule  $\text{Zn}^{2+}$  complexes, the energy of the antibonding  $4p_z$  is increased relative to  $4p_{x,y}$  levels due to repulsive interaction along the z axis (**Figure 5.6**). The intensity of the 1s to 4p transition is reduced by virtue of an overlap of the covalent ligand. A three coordinate complex is derived from a two coordinate electronic structure by introducing a ligand. The  $4p_{x,y}$  orbital then splits with the  $p_y$  to higher energy thus decreasing the 1s to  $4p_y$  intensity as observed with the addition of THF to diisopropylzinc in Figure 5.2. Furthermore from a three to

four coordinate structure the  $4p_{x,y,z}$  are close to degenerate but shifted to higher energy with each  $1s$  to  $4p$  transition having a reduced intensity as seen in **Figure 5.6**.<sup>[79]</sup>

### **5.3.2 Diethylzinc in different THF/toluene ratios**

Further XAS investigation, on the influence of solvents with dialkylzincs were done at the ESRF synchrotron in France. Different concentrations, solvent ratios and solvents were considered during measurements. An extensive XANES study was carried out with diethylzinc (DEZ) at different THF/toluene ratios to understand the interaction of the respective solvents. It was found that only a 10 % (vol %) of THF with toluene has a great influence on the zinc environment in DEZ (Figure 5.7). The XANES below is comparable to that of  $i\text{-Pr}_2\text{Zn}$  in toluene and THF previously seen.

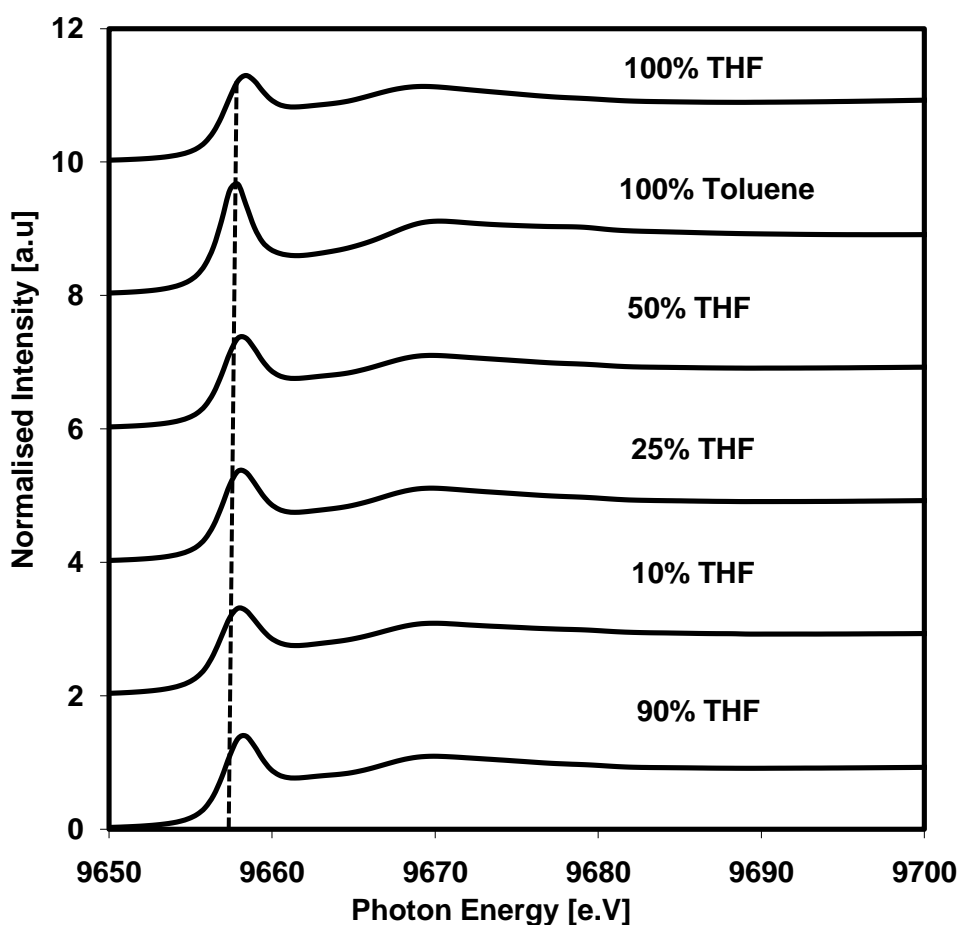
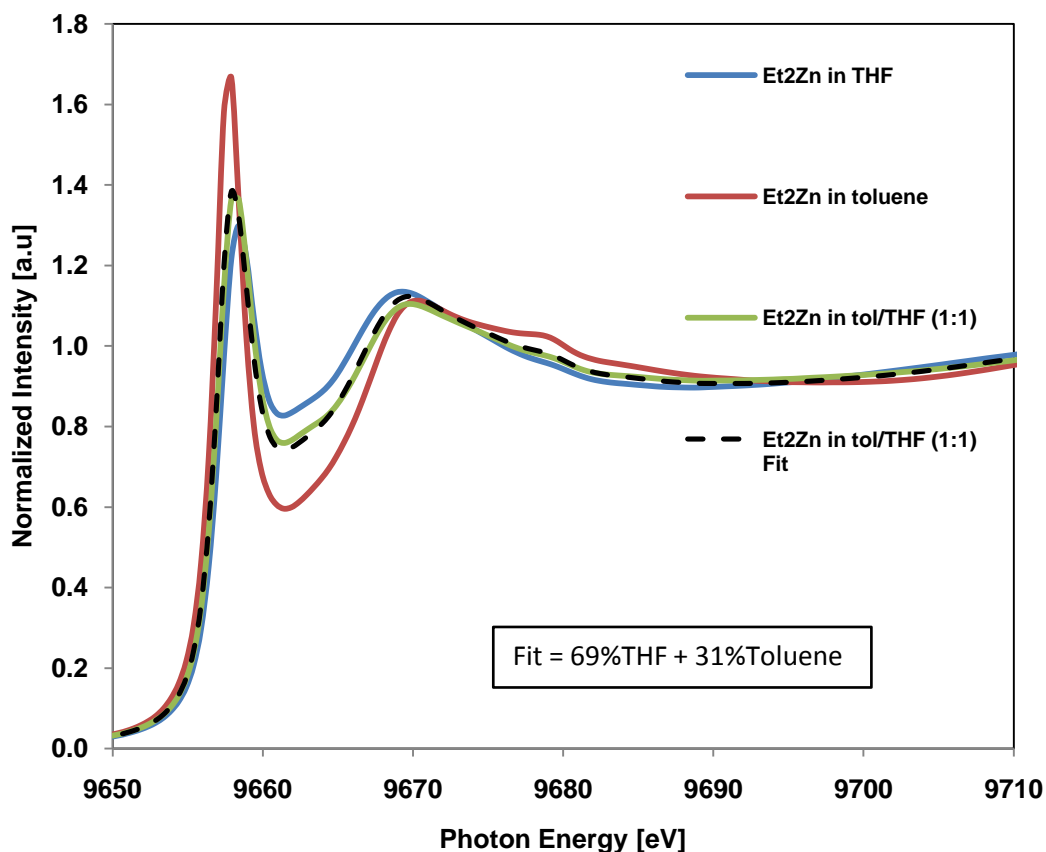


Figure 5.7: XANES spectra of 0.1M DEZ at different THF/toluene ratios

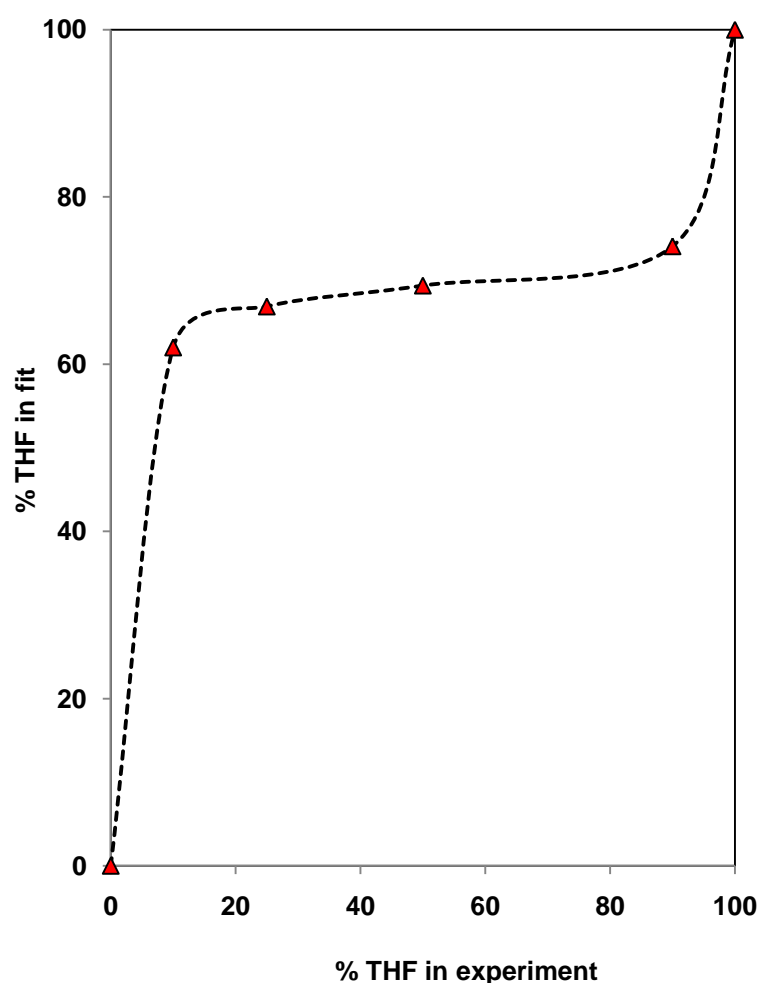
Evidently THF has a stronger influence than toluene on the resonance peak. From the black dash line it can be seen that the resonance peak of  $\text{Et}_2\text{Zn}$  reduces and moves to a higher photon energy with the addition of THF. With a 10 % presence of THF a strong reduction in the resonance peak is observed. Further drops are unnoticed when the amount of THF in the solvent mixture increases from 10% to 90%. A linear combination of the spectra from the toluene and THF solutions reproduces the XANES spectrum of diethylzinc in the 1:1 THF: toluene mixture very well ( **Figure 5.8**). The linear combination fit optimizes with a 69 % contribution from the THF and 31 % from the toluene XANES spectra. This suggests that the equimixture

has 69 % of zinc present as the dialkylzinc complex with THF. It appears that diethylzinc in THF has a significantly higher affinity for binding to diethylzinc than toluene.



**Figure 5.8: XANES spectra of 0.1 M DEZ in toluene and THF. Calculated XANES in 1:1 (toluene:THF) included.**

The linear combination analysis of XANES spectra was expanded to investigating a number of toluene/THF mixtures, from 10 to 90 % of THF in the solvent mixture. The results are shown in Figure 5.9. At 10, 25, 50 and 90 % of THF in the solvent mixture the calculated THF contributions were 62, 66.9, 70 and 74% respectively. This is a true indication of the strong influence of THF over toluene even at low concentrations of 10 %.



**Figure 5.9: Comparing the experimental and fitted XANES of 0.1 M  $\text{Et}_2\text{Zn}$  at different THF/toluene ratios (vol %).**

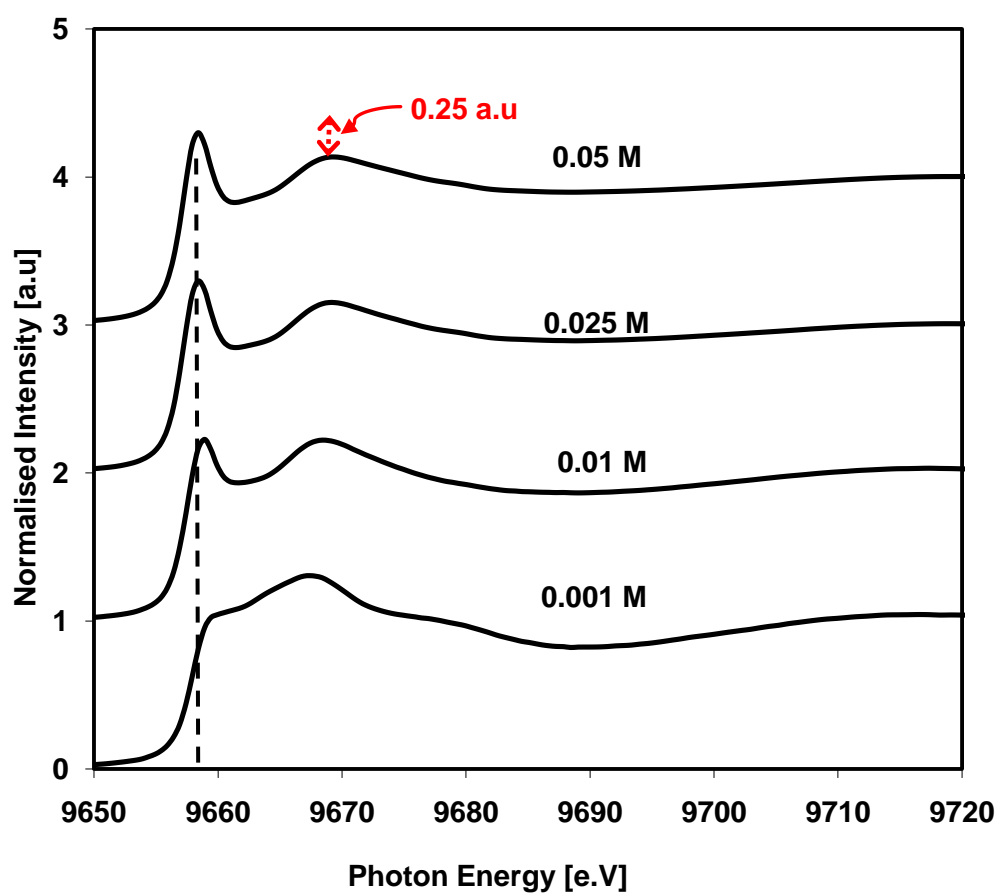
A remarkable increase is noticed at 10 % THF, which then stabilizes between 62 and 74%. At 90% THF, 74% was calculated in the fitted XANES suggesting the influence of toluene on diethylzinc. As the amount of THF increases from zero, a cooperative solvent effect is possible in which diethylzinc complexes predominantly with toluene when the THF concentration is low. It appears to bind predominantly with THF in toluene/THF mixtures when the toluene concentration is below approximately 90%, but toluene still appears to influence the electronic structure of the complex. In pure THF (less than ~10% toluene) a complex without toluene

influence appears to be formed. At high amounts of THF there is a possibility of slight decomposition with water molecules resulting in the reduction of the resonance peak, but this effect is not expected to dominate the observed spectra. This comparison indicates that diethylzinc has a strong affinity for pure toluene, and complexes formed in increasing amounts of THF do not completely overshadow complexes in toluene until almost pure THF is used.

### **5.3.3 Diethylzinc in THF as a function of concentrations**

Concentrations between 0.001 and 0.05 M of DEZ were investigated. Variations of the concentration were found to strongly influence the XANES Zn K-edge spectra of diethylzinc in THF (Figure 5.10).





**Figure 5.10: XANES spectra of DEZ in THF at different concentrations**

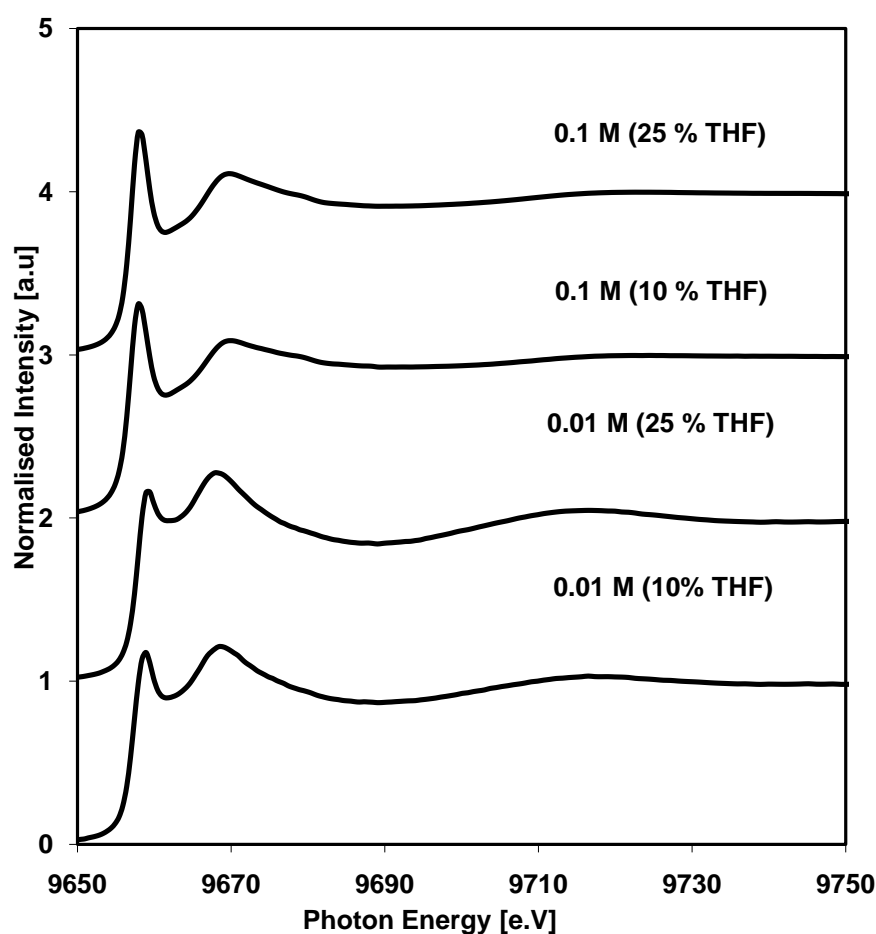
Concentrations beyond 0.2 M were not considered because of the problems associated with high absorption, fluorescence detector overload and self-absorption effects. At low concentrations (between 0.001 and 0.05 M) the sharp peak at about 9660 eV changes compared to that observed between 0.025 and 0.05 M. At 0.01 M the resonance peak reduces and maintains the same height as the second peak compared to higher concentrations considered. Between 0.025 and 0.05 M the difference between the 1<sup>st</sup> and 2<sup>nd</sup> peak is 0.25 a.u (Figure 5.10). Clearly there is a similarity in the XANES spectra between 0.01, 0.025 and 0.05 M which is undoubtedly different from 0.001 M. At 0.001 M the XANES structure is completely

different from the other measured XANES spectra and is reminiscent of ZnO/Zn(OH)<sub>2</sub>. The similarity between 0.025 and 0.05 M may suggest similar Zn species which are likely dimer species as previously seen in this study. At lower concentration values below 0.025 M, the DEZ molecules probably interact with impurities in the THF solvent, forming other products. Especially water contamination is expected to be an issue, and the spectrum obtained for a concentration of 0.001 M DEZ is very similar to the previously presented (Figure 4.11) spectrum of DEZ decomposed by deliberate exposure to water. It should be noted in this context that residual water concentration of 0.001 M corresponds to a THF purity of 99.9 % with 0.005 % water as impurity (Sigma Aldrich). It is evident that avoiding the influence of residual moisture becomes paramount at very low dialkylzinc concentrations in THF is reminiscent of the suggestion by Brown who suggests in one of his studies that the Soai autocatalytic reaction performs optimally between 0.05 and 0.2 M.<sup>[50]</sup> The influence of residual moisture content diminishes at higher concentrations, when DEZ is in excess over the interactions with impurities.

In line with the molecular orbital considerations by Kau *et al*<sup>[79]</sup> a 4 coordinate geometry is likely the case at 0.001 M with the reduction in the resonance peak and energy shift. This is confirmed by the EXAFS previously seen in Table 4.3 of decomposed diethylzinc of oxide/hydroxide species formed.

#### **5.3.4 Concentration versus solvent ratio of diethylzinc**

Another comparison was made to compare the influence of solvents and concentration of DEZ. At 0.1 M the resonance peak is higher than second peak in the presence of 10 and 25% THF.



**Figure 5.11: XANES spectra of DEZ in THF/toluene mixture at different concentrations**

At 0.01 M the first peak intensity equals that of the 2<sup>nd</sup> with 10 % THF and reduces slightly when increased to 25 %. The change of the resonance peak is more noticeable at 0.01 M than 0.1 M when THF is increased from 10 to 25% suggesting that a higher percentage of DEZ molecules form a complex with THF molecules at lower than at higher DEZ concentrations. In addition it appears that increasing the THF amount from 10 to 25 % at 0.1 M DEZ is not enough to observe a significant change in the electron density. This may indicate that, with an increase of 15% not enough THF molecules are available to change the DEZ Zn environment.

### 5.3.5 Interaction of dialkylzincs with different solvents

Other solvents and dialkylzincs were investigated. Interestingly DEZ in diethyl ether gave a massive resonance peak compared to THF. Both solvents are chemically the same except that THF, is a cyclic ether. The XANES below suggests that both solvents have may have different complexation behavior.

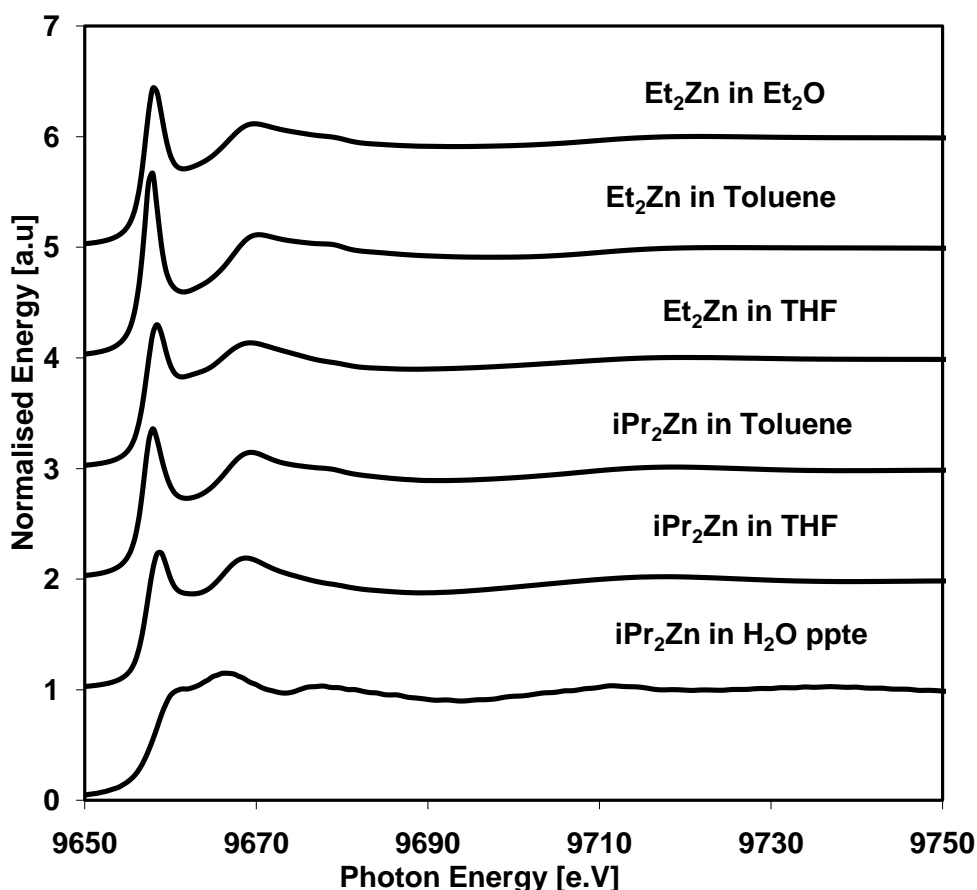


Figure 5.12: XANES spectra of 0.1 M dialkylzincs in THF, toluene and water.

From Figure 5.12, a tetrahedral Zn coordinate system can be associated to iPr<sub>2</sub>Zn in water. Considering studies by Denisov the strength of complex formation with DEZ would decrease in the following order: THF>DEE>toluene.<sup>[74]</sup> From EXAFS calculations however DEZ does not form a complex with toluene. The dipole moment of the solvents decreases from THF to toluene and this corresponds to the

decline in the ability of DEZ to form a complex with the respective solvent (Lewis basicity).<sup>[82, 83]</sup>

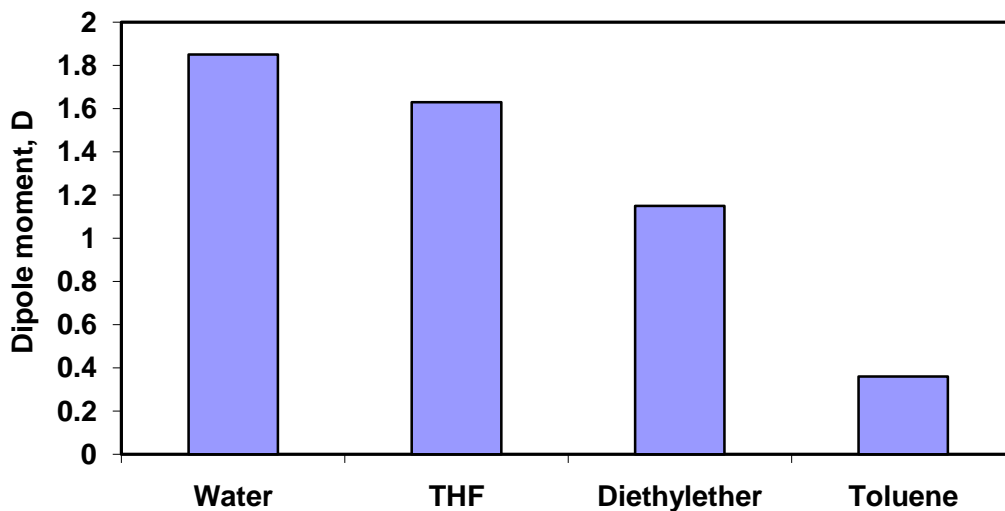


Figure 5.13: Comparing the dipole moment of water, THF, diethyl ether and toluene.

An increase in the dipole moment causes a change in the electron density of the zinc atom. In the case of water which has a dipole moment of 1.8 Debye and dielectric constant of 80, the change in electron density shift is greatest as can be seen in the former XANES spectra (Figure 5.12). The situation here is complicated by the fact that water is a protic solvent that can also lead to Bronsted acid-base reactions of the alkyl ligands. At low concentrations dialkylzinc interacts with water or oxidizing impurities in the solvent. The XANES spectra of  $i\text{-Pr}_2\text{Zn}$  in water, is also similar to that in a low concentration of DEZ in THF previously seen which may be indicative of hydrolyzed dialkylzinc.

### 5.3.6 Comparing diethylzinc in THF and toluene at ESRF, ANKA and APS

The benchmark XAS experiment at the ESRF, APS and ANKA was DEZ in THF and toluene. Even though the DEZ concentration of 0.1 M was the same at ANKA

and ESRF the XANES spectra from ESRF was similar to APS but not ANKA. This was observed in both THF and toluene. It is still unclear why the discrepancy exists. In all cases the supplier of DEZ and the solvents was Sigma Aldrich. However at ANKA, the solvents were dried, distilled and kept on molecular sieves.

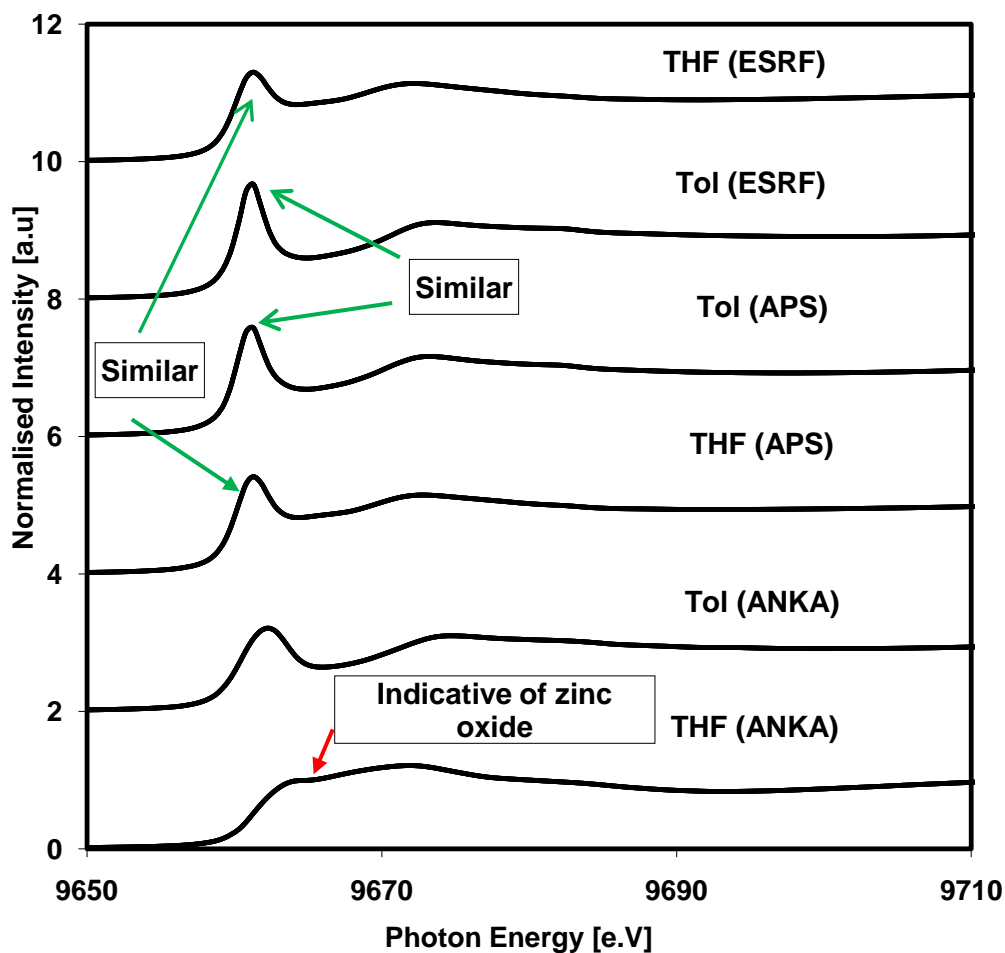


Figure 5.14: Comparing the XANES spectra of 0.1M DEZ obtained at different synchrotrons.

An expected massive white line which is the case at APS and ESRF is not the case at ANKA in toluene. The XANES measured at ANKA in toluene has a reduced peak and is similar to the XANES in THF at APS and ESRF. The difference between the measurement at ANKA in toluene and APS/ESRF in THF is that the 1<sup>st</sup> peak of the ANKA spectra is slightly broader. In THF the XANES spectra at ANKA is an

obvious reminder of zinc oxide suggesting tetrahedral zinc sites. From this XANES analysis at the different light sources, one may suspect the presence of trigonal planar or tetrahedral zinc sites in both toluene and THF based on the ANKA beam time results. One possible explanation could be the oxidation of DEZ or the presence of contaminants. The difference might perhaps be synchrotron related but is more likely to be the purity of DEZ. This study deals with this inconsistency by relying on the XAS measurements at APS and ESRF, in order to develop structural models.

### **5.3.7 Comparing the XANES of diethyl-, dimethyl- and diisopropylzinc**

Since the discovery of the Soai reaction, diisopropylzinc has been the only successful alkyl donating group capable of amplifying chirality. In this section we shall see the Zn K-edge spectra of diisopropyl-, diethyl- and dimethylzinc measured at the APS. The dialkylzincs which are pyrophoric were prepared in the same manner in an inert environment as previously mentioned. It should be noted that dimethylzinc is the most pyrophoric and easily ignites. Figure 5.15 illustrates the similarity in the XANES of dialkylzincs measured at APS with three characteristic peaks within this energy range. However, it can be seen that dimethylzinc (DMZ) shows a slightly different XANES from the other measured spectra.

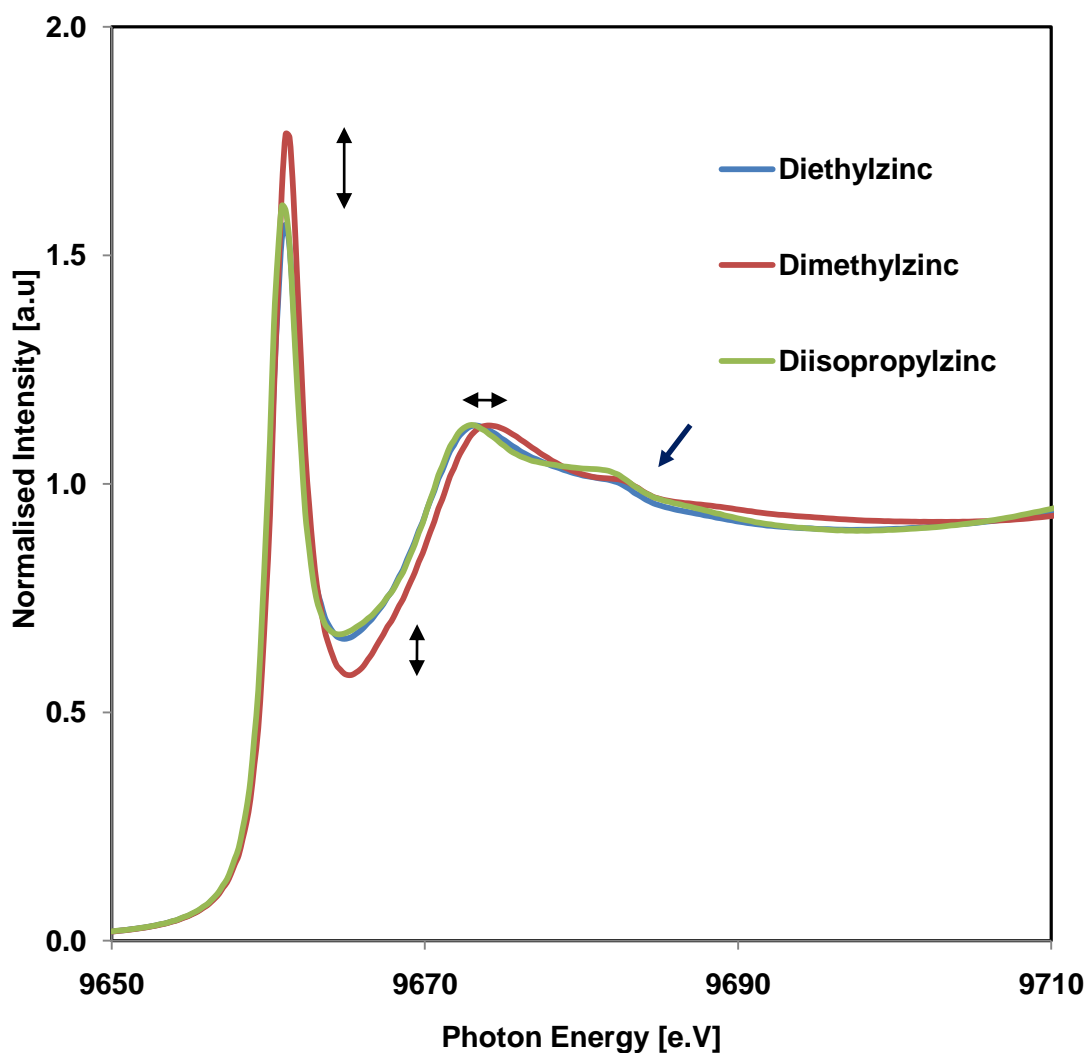


Figure 5.15: Zn K-edge spectra of 0.1 M dimethyl-, diethyl and diisopropylzinc in toluene

Dimethylzinc has a more intense resonance line than the other two. The discrepancy in their XANES spectra can be measured and is indicated by the black arrows in the above Zn K-edge XANES. With respect to DMZ the white line is higher by 0.2 a.u, the trough between the two peaks is 0.1 a.u deeper and the 2<sup>nd</sup> peak is shifted slightly to a higher energy level. The observed difference may be because of the electronic and steric effects present in these molecules. Diisopropylzinc and diethylzinc are both similar in size whereas dimethylzinc has a smaller radius and has less bulky



groups. In terms of the ability to release electrons, ethyl and isopropyl have a greater potential of donating electrons in comparison to methyl. Isopropyl is a better electron releasing substituent than ethyl even though their spectra are the same. This differentiation in the XANES spectra is partly or wholly as a result of the electronic effects on the zinc atom. On the other hand other potential causes must be considered including steric effects which could support the explanation of this disparity.

### 5.3.8 EXAFS analysis of diethylzinc in solvents

The EXAFS analysis provides evidence of the neighbouring atoms as well as bond distances from the central zinc atom in solution. We have established that dialkyl zincs tend to bind to polar solvents. According to EXAFS calculations DEZ does not form a complex with toluene. In toluene the 1<sup>st</sup> shell coordination number with carbon is 1.42 ( $\pm 0.121$ ) i.e. approximately 2 and the Zn-C bond distance in the first shell is 1.89 ( $\pm 0.010$ ) Å. This suggests a linear structure which is maintained in toluene.

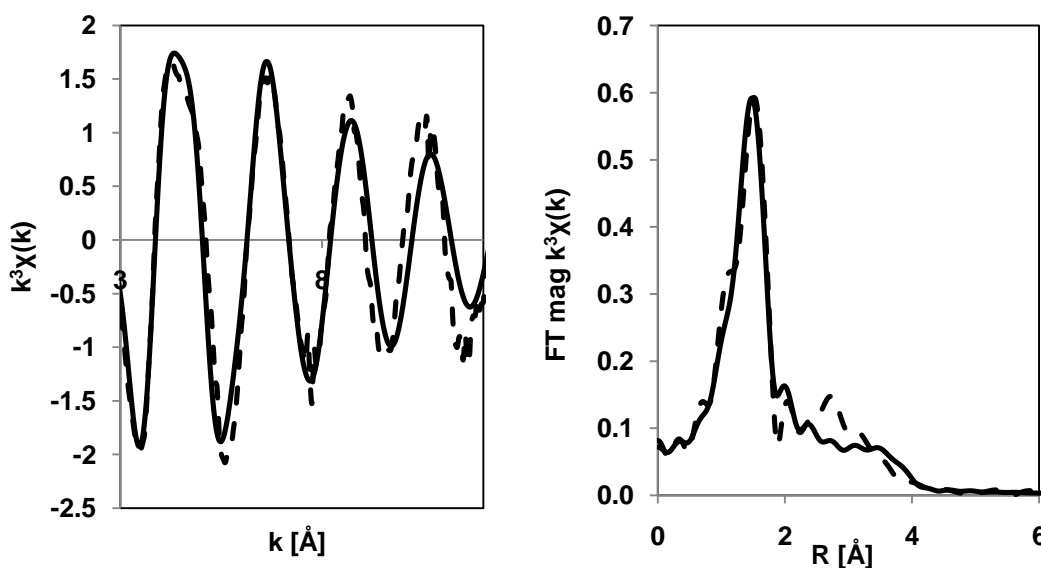


Figure 5.16: Zinc K edge EXAFS spectra of Et<sub>2</sub>Zn in Toluene. Dotted lines are the experimental data and the solid lines are the best theoretical fit.

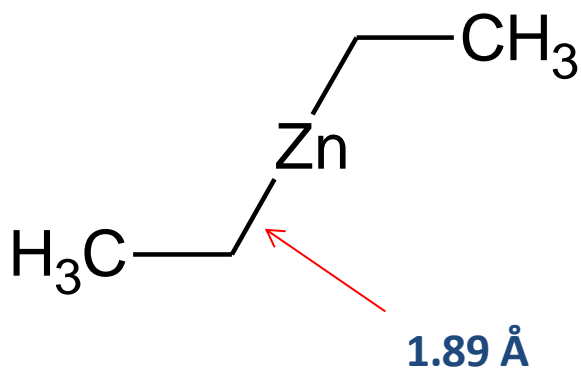
The fits in R and  $k$  space have an  $R$ -factor of 5.1% indicating a good fit between experimental and theoretical data. The table below contains the EXAFS parameters of diethyl zinc in toluene.

Sample	First shell (Zn-O/C/N)			Second shell (Zn-O/C/N) (Zn-Zn)							
	N	R(Å)	$\sigma^2(\text{\AA}^2)$	N	R(Å)	$\sigma^2(\text{\AA}^2)$	N	R(Å)	$\sigma^2(\text{\AA}^2)$	$E_0$ (eV)	$R$ (%)
<b>Et<sub>2</sub>Zn in toluene</b>	1.42 (±0.121)	1.89 (±0.010)	0.005 (±0.001)	6.18 (±6.279)	4.265 (±0.050)	0.016 (±0.027)	-	-	-	7.22 (±1.234)	5.1

**Table 5.5: EXAFS parameters of diethylzinc in toluene**

The above model of DEZ in toluene supports the Denisov study in that toluene which is non polar and does not form a complex with DEZ since it has a low dipole moment or dielectric constant. From the above EXAFS calculations the Zn-C bond distance of toluene is 1.89 Å as seen in Figure 5.17 below. The model has approximately 1.5 C neighbours to the Zn central atom. It is a monomer since no Zn...Zn interactions are present.

The EXAFS analysis is in accordance with the molecular orbital considerations by Kau *et al*<sup>[79]</sup> in which a 2 coordinated geometry system is predicted when diethylzinc is in toluene because of the increased resonance peak.



**Figure 5.17: Model of diethyl zinc in toluene from EXAFS calculations.**

The EXAFS fit of diethyl zinc in THF suggests that an association of DEZ molecules is promoted by the presence of the polar solution i.e. THF. Three EXAFS fit calculations were done on diethyl zinc in 100% THF in order to ascertain the nature of the structure in THF. The EXAFS fits in Figure 5.18 indicate that in THF it is very probable that there is a contribution due to a Zn...Zn interaction. The two best fits which include Zn seen in Figure 5.18 have a pronounced second peak at approximately  $3 \text{ \AA}$ . This pronounced second peak (mainly Zn...Zn) is absent in toluene. From the fits below it is obvious that the structure is more likely a tetramer or a dimer than a monomer as indicated by the number of neighbouring Zn atoms.

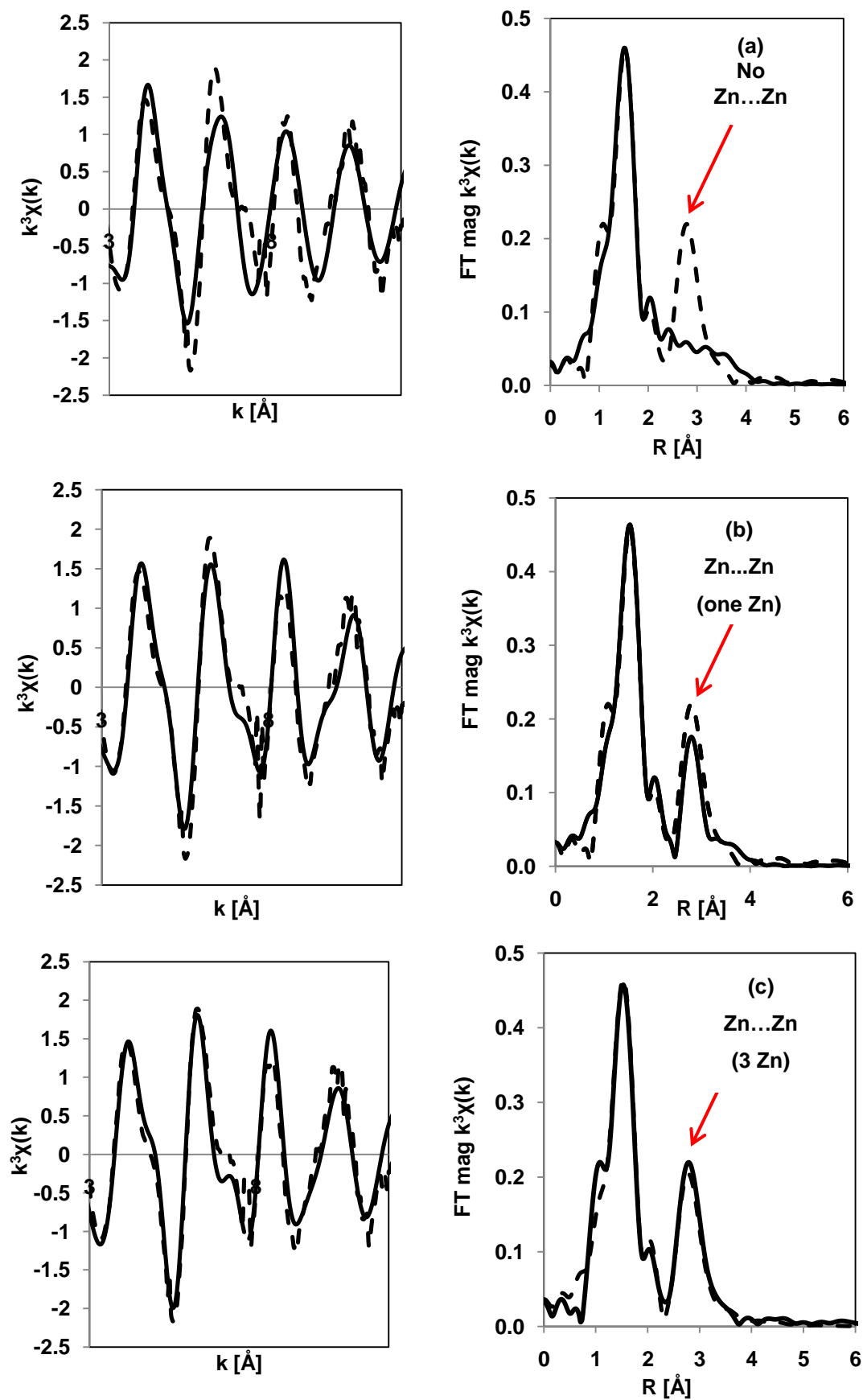


Figure 5.18: EXAFS fits of diethylzinc in THF (a) linear (b) dimer and (c) tetramer.

The EXAFS parameters of the most probable complexes in THF are seen below in Table 5.6.

Sample	First shell (Zn-O/C/N)			Second shell (Zn-O/C/N) (Zn-Zn)							
	N	R(Å)	$\sigma^2(\text{\AA}^2)$	N	R(Å)	$\sigma^2(\text{\AA}^2)$	N	R(Å)	$\sigma^2(\text{\AA}^2)$	$E_0$ (eV)	R %
Et <sub>2</sub> Zn in THF (Zinc set, N=1)	1.071 $\pm 0.098$	1.929 $\pm 0.006$	0.003 $\pm 0.001$	3.325 $\pm 4.047$	4.152 $\pm 0.056$	0.024 $\pm 0.023$	1	3.059 $\pm 0.010$	0.010 $\pm 0.001$	6.199 $\pm 1.204$	3.3
Et <sub>2</sub> Zn in THF (Zinc floating)	1.043 $\pm 0.072$	1.932 $\pm 0.004$	0.003 $\pm 0.001$	1.565 $\pm 1.722$	4.143 $\pm 0.050$	0.016 $\pm 0.017$	2.766 $\pm 0.641$	3.351 $\pm 0.009$	0.018 $\pm 0.002$	6.692 $\pm 0.859$	1.8

Table 5.6: EXAFS parameters of diethylzinc in THF

Table 5.6 shows the parameters from the calculations of diethylzinc in THF. The first case is calculated on the basis that there is one Zn neighbour i.e. coordination, N of Zn-Zn set to one. The complex which is a dimer is shown below with a Zn-Zn bond distance of approximately 3.059 Å. The complex also has only one neighbouring carbon atom and a Zn-C bond distance in the first shell is about 1.929 Å.

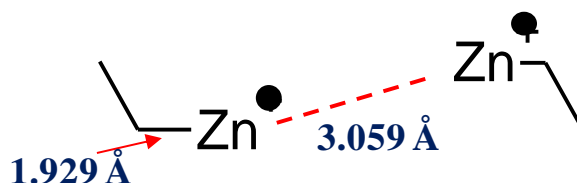
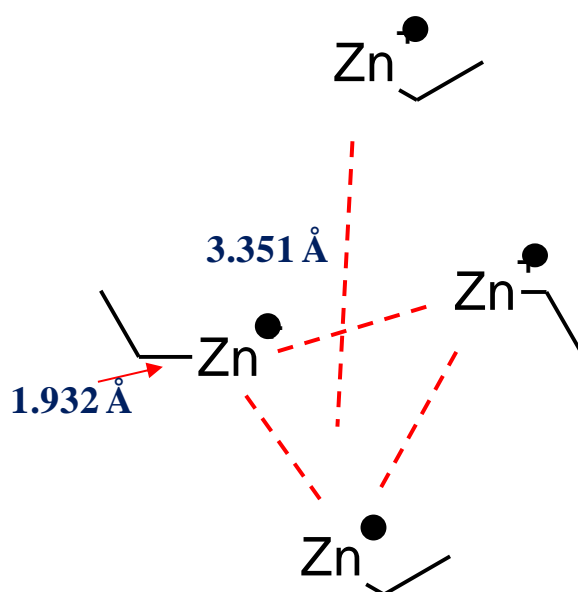


Figure 5.19: Structural calculated model of diethylzinc in THF (Dimer model).

The above model is derived from the dimer model has an *R*-factor of 3.3%. Allowing the Zn-Zn coordination number to float, results in the tetramer model (Figure 5.20). The EXAFS parameters that represent the tetramer model are seen in the bottom section of Table 5.6. As can be seen from Table 5.6 and Figure 5.18, the tetramer model has the best fit with an *R*-factor 1.8% (best fit). The structure of the tetramer model derived from the best fit is shown below.



**Figure 5.20: Structural calculated model of diethylzinc in THF (Tetramer model).**

The above models suggest that toluene molecules therefore do not interact with the diethylzinc like THF molecules which cause Zn...Zn interactions. Both the dimer and tetramer models in THF possess dissociated DEZ molecules i.e. monoalkylzinc (MEZ). Either two or four monoethylzinc molecules are then brought together by THF molecules (found between two MEZ molecules) to form a monoethylzinc (MEZ) dimer or tetramer respectively. From the EXAFS calculations it is very likely that the preferred structure of diethyl zinc in THF is the tetramer model which has a better fit in THF. The Zn-C bond distance is 1.932 Å and the Zn...Zn distances are

3.351 Å (longer than that of dimer model). It is also important to note that the Zn-C bond distance (1<sup>st</sup> shell) increases from toluene to THF from 1.89 to 1.93 Å. It is likely that monoethylzinc is a radical. This phenomenon, whereby a radical is formed by diethylzinc in THF has been proposed by other studies.<sup>[84, 85]</sup> Diethylzinc is known to promote radical formation possibly by its interaction with impurities which include oxygen present in THF. The ethyl radical formed then associates with other functional groups forming a new compound. Diethylzinc therefore functions as an initiator and transfer agent.<sup>[84, 85]</sup> The electronegative oxygen atom in THF, found between two MEZ molecules, is likely responsible for pulling the remaining MEZ molecules together thus the Zn...Zn interaction.

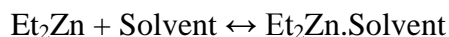
The association of THF molecules with zinc is still present with an excess of toluene molecules in a 3:1 ratio as previously seen in the XANES spectra. From this study the binding effect experienced with zinc atoms is less severe when less THF molecules are present. This finding is logical as fewer THF molecules are available to interact with zinc. Astonishingly according to this model, the diethylzinc molecules still dissociate to monoethylzinc with a deficiency of THF molecules in the solvent mixture.

In line with the molecular orbital considerations by Kau *et al*<sup>[79]</sup> a 3 fold coordinated geometry system is expected with the reduction in the resonance peak with the interaction of 0.1 M diethylzinc and THF. This is contradicted by a one coordinated geometry structure calculated by the EXAFS analysis. The formation of radicals of diethylzinc in THF already discussed may be the reason for this discrepancy.

### 5.3.9 Kinetic simulation studies of diethylzinc in solvents

In an attempt to relate the work of Denisov<sup>[74]</sup> to this XAFS study, equilibrium studies were carried out to compare the interaction of solvents with DEZ or dialkylzincs. Kinetic simulation studies were possible using a simulation program, Chemical Kinetic Simulator (CKS). The rate of reaction is determined by CKS using a stochastic algorithm technique.

The equilibrium constants derived from Denisov's work were used and the reversible reaction considered involved the association of DEZ and a solvent to form a complex.



DEZ and the solvent exist in equilibrium with the donor-acceptor complex. The kinetic calculation was done with initial amounts of 0.1 M and an inert solvent was assumed to be the medium. Equilibrium constants determined by Denisov i.e. THF: 0.68 l/m, DEE: 0.2 l/m were considered and the simulations were executed with a package called chemical kinetic simulator v1.01.<sup>[86]</sup> Assumptions made in the calculation include equilibrium constants of toluene and polar solvents as 0.05 and 1 l/mol respectively. The outcome of this calculation should hopefully support the findings derived from the XAFS studies.



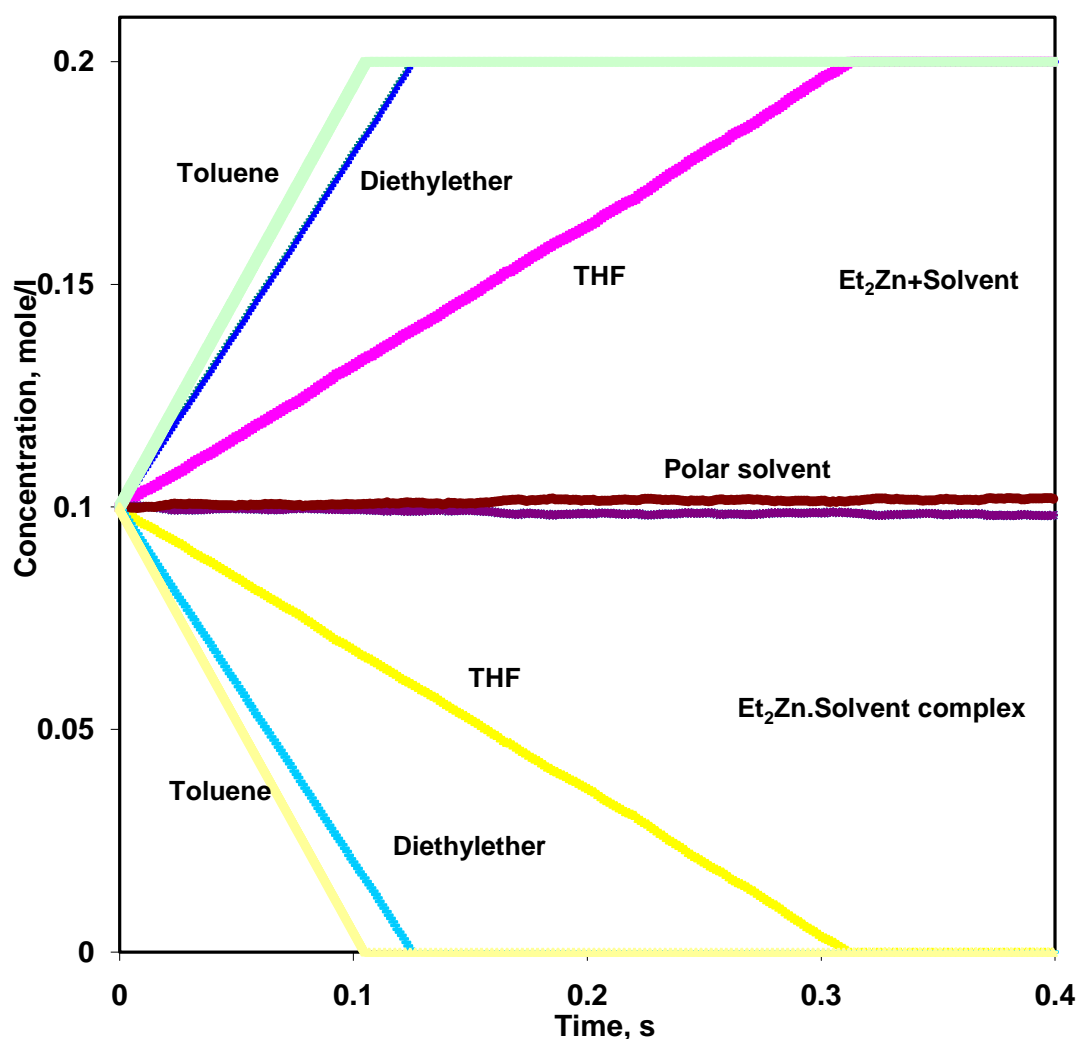


Figure 5.21: Kinetic simulation of DEZ, solvent and the complex. Initial concentration 0.1mol/l

It is clear from the simulation that the DEZ-solvent complex liberates DEZ at different rates. The fastest rate of DEZ release is the case of toluene and the least is with the polar solvent. The trend seen here is that the more basic the solvent, the slower the release of DEZ in the inert solvent. More polar solvents therefore coordinate a lot stronger. From the above kinetic plot DEZ is released from toluene within a tenth of a second meanwhile the release time triples in THF. There is possibly a correlation between this kinetic simulation and XAS studies. The XANES spectra of toluene and diethyl ether are similar and that of THF which has a reduced

resonance peak is different. In addition, the XANES of DEZ in 1:1 toluene/THF mixture shows a weight of THF three times that of toluene relating to the results obtained from this kinetic study in which toluene releases DEZ three times faster than THF from the complex. In the case of polar solvents the deviation of the XANES spectra and rate of release of DEZ is substantial compared to toluene or diethyl ether. This trend also follows work by Blackmond<sup>[45]</sup> (Figure 5.1) in which no amplification in THF but in toluene and diethyl ether is observed. This would therefore imply that the choice of a solvent in order to promote amplification of chirality is obviously from non-polar solvents which have a low affinity for zinc or lower complex formation ability. Zinc is electron deficient and would coordinate with Lewis bases which donate electrons to form bonds. The appropriate solvent to encourage chirality should therefore be able to release DEZ within 0.1 s or less from the complex if any is formed. This is likely to happen only with electron poor solvents that lack electrons to coordinate with zinc.

## 5.4 Conclusion

X-ray absorption and kinetic simulation studies have been used in this part to understand the behaviour of dialkyl zinc compounds in different solvents. Close to inert solvents such as toluene promote amplification of chirality meanwhile THF a strong Lewis base hinders autocatalysis probably by binding to zinc. Two distinguishable models in toluene and THF have been reported. THF causes the dimerization of diisoproylzinc and DEZ by pulling two molecules of the dialkylzincs together. The non association of toluene with zinc may clarify its outstanding functioning in asymmetric amplification in comparison to THF.

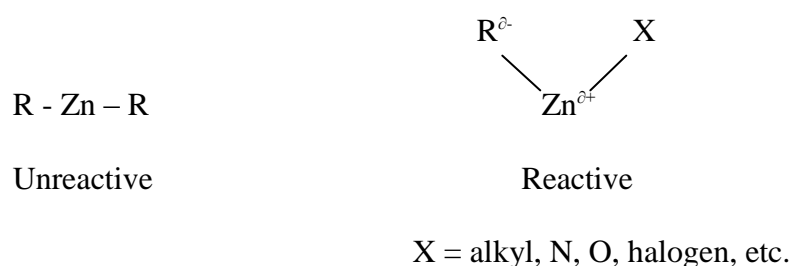
It has been observed that the presence of only 10 % of THF with toluene causes a major change in the XANES of different dialkylzinc species at a 0.1 M concentration. A major change is also noticed during the decomposition of dialkylzinc. At higher concentrations between 0.025 and 0.1 M, the XANES is different from that at lower concentration in toluene (between 0.01 and 0.001 M). This may be due to the interaction of DEZ with impurities present in the solvent including water and oxygen. Change in concentration has a greater influence on the XANES than the solvent ratio change. Denisov's study has been found to comply with this EXAFS and kinetic study where solvents with higher dipole moments such as THF have a higher ability to form a complex.<sup>[74]</sup> Non polar solvents therefore possess a higher ability to release DEZ.

The structural models from the EXAFS calculations rely on the XAS data from the ESRF and APS which are comparable. A linear structure is present in toluene but in THF this structure changes to a trigonal zinc site in a dimer or tetramer. From the EXAFS calculated model there is a difference between  $iPr_2Zn$  and DEZ in THF. In the latter both a dimer and tetramer model are possible. Further investigation suggests that DEZ is easily decomposed overtime as seen by the gradual drop in the white line. When dialkylzinc is exposed over longer periods or in interaction with water molecules the product likely formed is an oxidized-zinc compound, which is neither zinc oxide nor zinc hydroxide.

## 6. Characterisation of a ligand and alkylzinc complex

### 6.1 Introduction

The alkyl-zinc bond in dialkylzincs is rather non polar. Replacing an alkyl group by an electronegative substituent increases the polarity of the alkyl-Zn bond thereby strengthening the character of the alkyl group and zinc atom as a donor and acceptor respectively.



This explains the benefit of using chiral ligands which have an X substituent together with dialkylzincs. The nature of the aldehyde, alkylzinc and ligand is crucial in influencing the reactivity. Noyori suggested the scheme below in which DAIB (3-exo-(Dimethylamino)isoborneol) was mixed with dialkylzinc in a 1:1 ratio evolving the corresponding alkane. A dimeric compound, 1 is also produced among three isomers.<sup>[18]</sup>

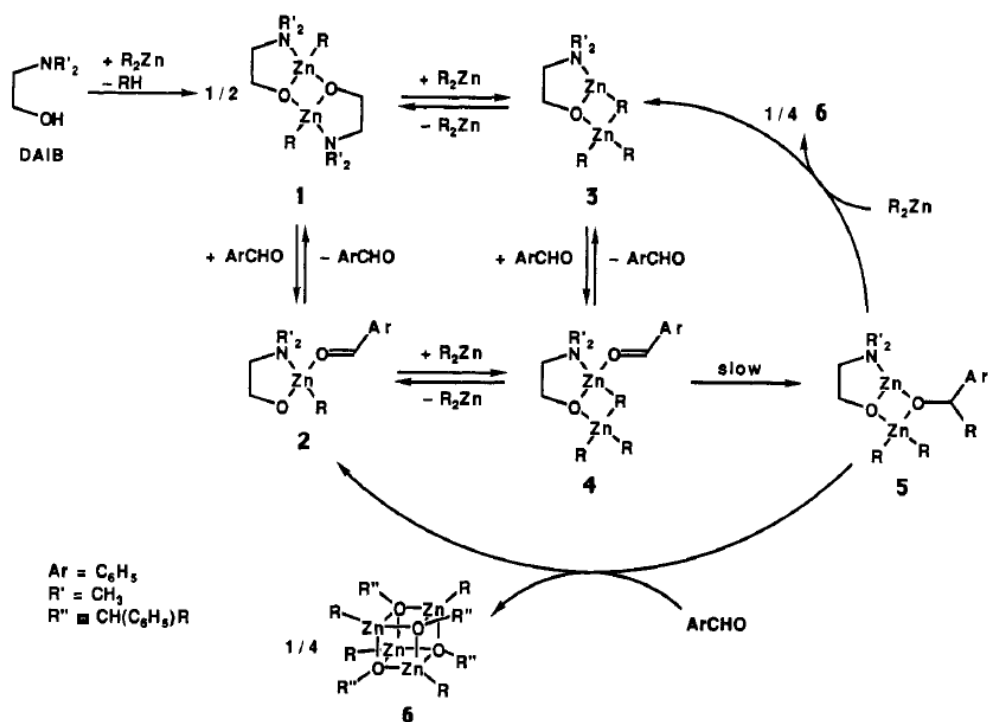


Figure 6.1: Catalytic cycle proposed by Noyori.<sup>[18]</sup>

The monomeric zinc chelate complexes (Figure 6.2) have been recognized by Noyori as the active catalyst in DAIB promoted alkylation of aldehydes while the dimeric catalysts are unreactive.<sup>[18]</sup> These catalysts are regarded to be vital in the amplification of chirality.

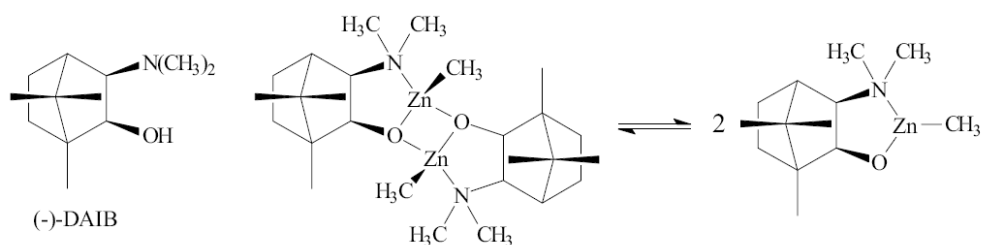


Figure 6.2: Noyori's DAIB and the dimer-monomer equilibrium of homochiral zinc chelate complexes.<sup>[87]</sup>

The equilibrium between the inactive dimer and active monomer according to Noyori provides evidence on the extent of turnover.<sup>[18]</sup>

Using XAS, our objective was to use conditions under which amplification of chirality is achieved according to Noyori, in order to characterize the zinc complex in solution. Experiments done by Noyori, indicate that a 1:2:1 mixture of the aldehyde, diethylzinc and ligand gives the highest yield and enantiomeric excess (corresponding to fourth row in Table 6.1).<sup>[18]</sup>

Ratio			(S)-1-phenyl-1-1-propanol	
C <sub>6</sub> H <sub>5</sub> CHO	(C <sub>2</sub> H <sub>5</sub> ) <sub>2</sub> Zn	(-) DAIB	% Yield	% <i>ee</i>
1	1	0	0	
1	1	1	1	0
1	2	2	0	
1	2	1	88	98
2	2	1	49	98
100	50	1	48	98
50	50	1	97	98

**Table 6.1: Effect of aldehyde: dialkylzinc: DAIB ratio on reactivity.**<sup>[18]</sup>

The main ligands studied in this report include DMAE (dimethylaminoethanol) and 2-butanol. Braese and co-workers have proven the suitability of ketimines with a [2.2] paracyclophane framework in the asymmetric addition of alkyl groups to aldehydes.<sup>[88-92]</sup> Soai and co-workers have also contributed to the growing interest in [2.2] paracyclophane as chiral ligands in enantioselective reactions.<sup>[93]</sup> For example, monosubstituted [2.2] paracyclophane were used as chiral initiators in the isopropylation of 2-alkynylpyrimidine-5-carbaldehyde to 2-alkynylpyrimidyl alkanol which gives a high enantiomeric excess (97%).

The objective of this investigation reported in the following sections is to examine the molecular structure of the active catalyst, and in particular whether it is a monomer, a dimer or perhaps some other species.

## 6.2 Experimental

The results in this section were obtained at the ESRF in a follow up beamtime to previous experiments carried out at ANKA in Karlsruhe, Germany. The paracyclophane ligand is mimicked by DMAE which has both O and N electronegative atoms. In the first instance the  $i\text{Pr}_2\text{Zn}$  and 2-butanol which have been used by Soai and coworkers will be studied followed by DMAE and DEZ.

## 6.3 Results and discussion

### 6.3.1 $i\text{-Pr}_2\text{Zn}$ and 2-butanol

XAS measurements were carried out at different concentrations of  $i\text{-Pr}_2\text{Zn}$  and 2-butanol mostly in toluene which is an ideal solvent to give a high *ee* and yield. The concentration of 0.1 M  $i\text{-Pr}_2\text{Zn}$  was maintained in all measurements.

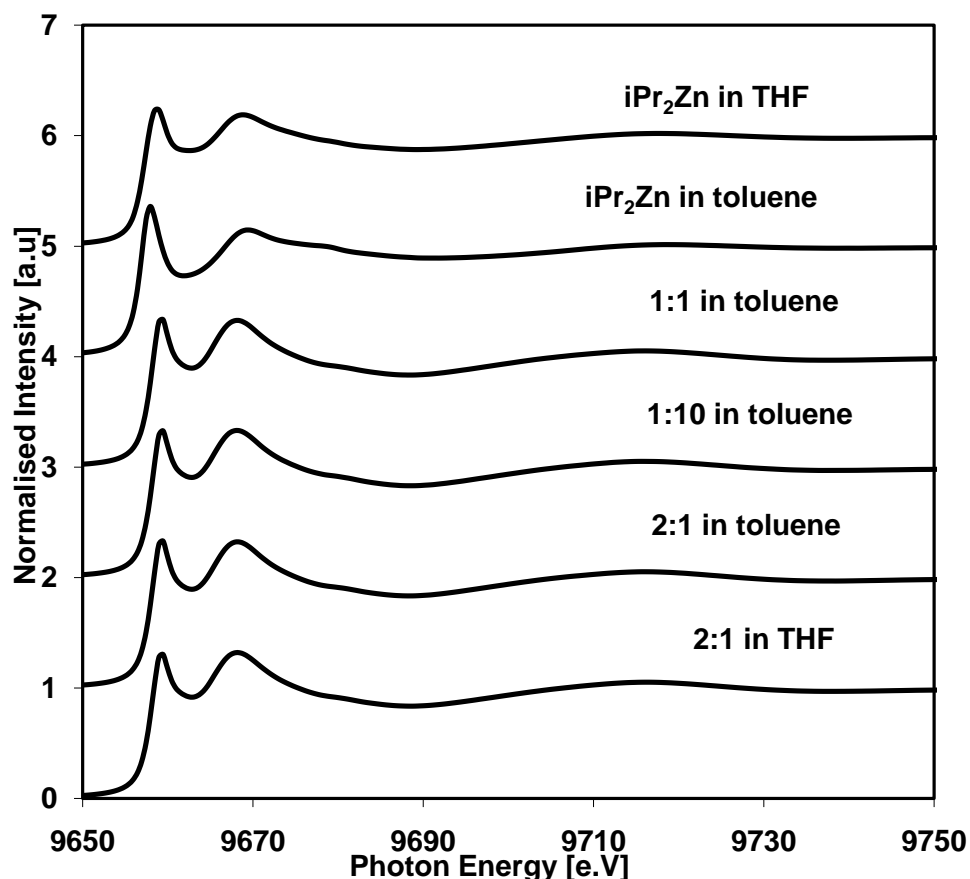


Figure 6.3: XANES Zn K-edge spectra of 0.1 M  $i\text{-Pr}_2\text{Zn}$  : 2-butanol molar ratios.

Mixing  $i\text{-Pr}_2\text{Zn}$  with 2-butanol causes a change in electronic state of the zinc atom as seen from the XANES spectra in which a drop of the resonance peak is visible compared to  $i\text{-Pr}_2\text{Zn}$  in toluene. However it is noticeable that decreasing the  $i\text{-Pr}_2\text{Zn}$ : 2-butanol molar ratio from 1:1 to 1:10 with the ligand in excess there is no visible change in the normalized XANES plot. This would imply the zinc environment remains unaltered probably because a point of saturation is attained for interaction between  $i\text{-Pr}_2\text{Zn}$  and 2-butanol molecules. By doubling the dialkylzinc amount, from 1:1 to 2:1 a similar XANES spectra is also observed in toluene and even THF. In such a scenario there is a surplus of  $i\text{-Pr}_2\text{Zn}$  molecules meaning all 2-butanol molecules will coordinate with  $i\text{-Pr}_2\text{Zn}$  and an excess of the dialkylzinc would be



present in solution. It is now well known that in THF amplification does not occur, the consideration of the 1:1 ratio in toluene is therefore ideal to determine the structure of the complex responsible for amplification of chirality.

The EXAFS fit of a 1:1 molar ratio of DEZ:2-butanol in toluene is seen below.

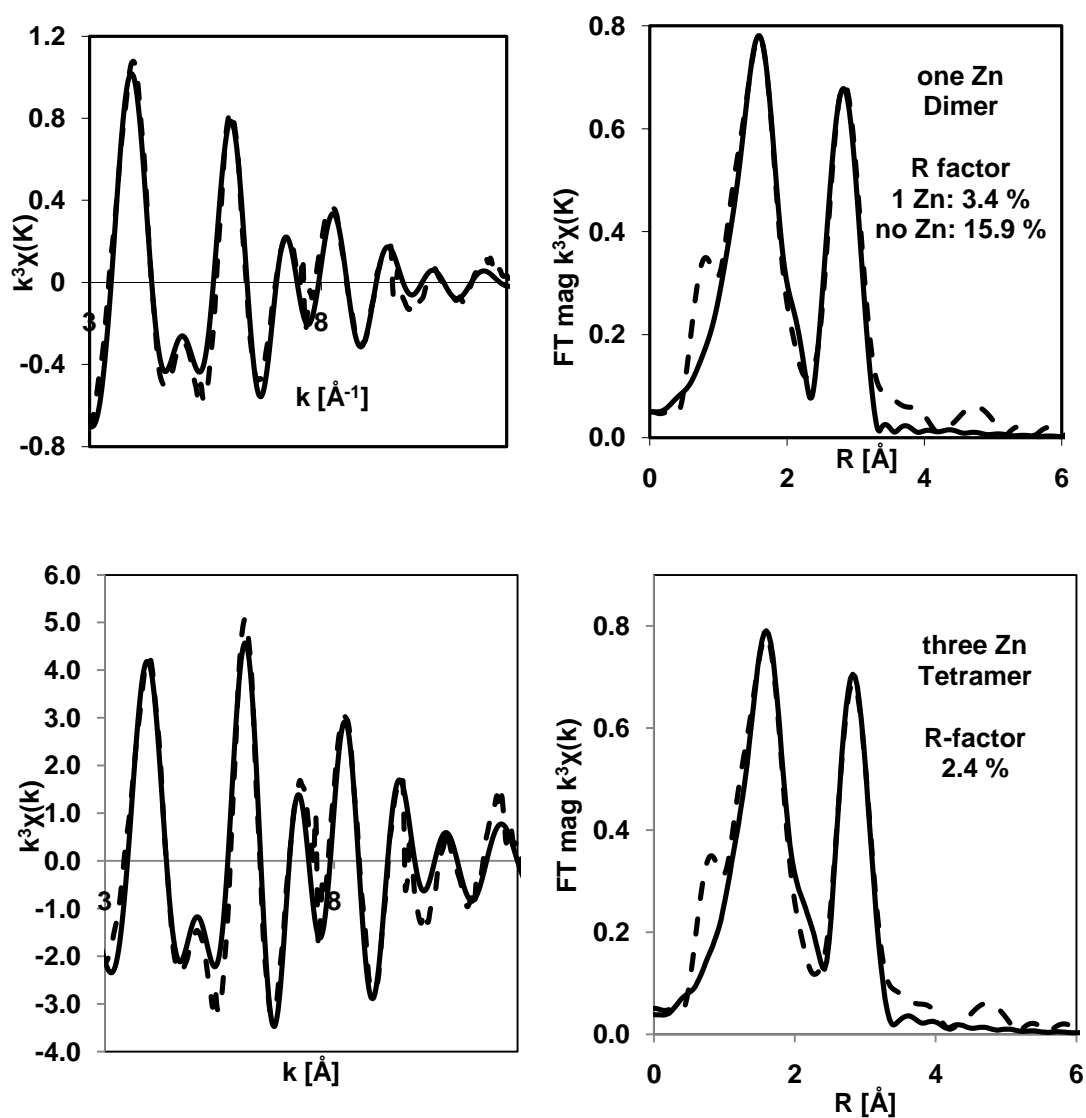


Figure 6.4: Zinc K edge EXAFS spectra of 0.1M  $i\text{-Pr}_2\text{Zn}$  with 2-butanol in 1:1 molar ratio in toluene (dimer and tetramer). Dotted lines are the experimental data and the solid lines are the best theoretical fit.

The data in Figure 6.4 indicate strong Zn...Zn interaction, either through the formation of a dimer or a tetramer. The R-factors of the dimer and tetramer model

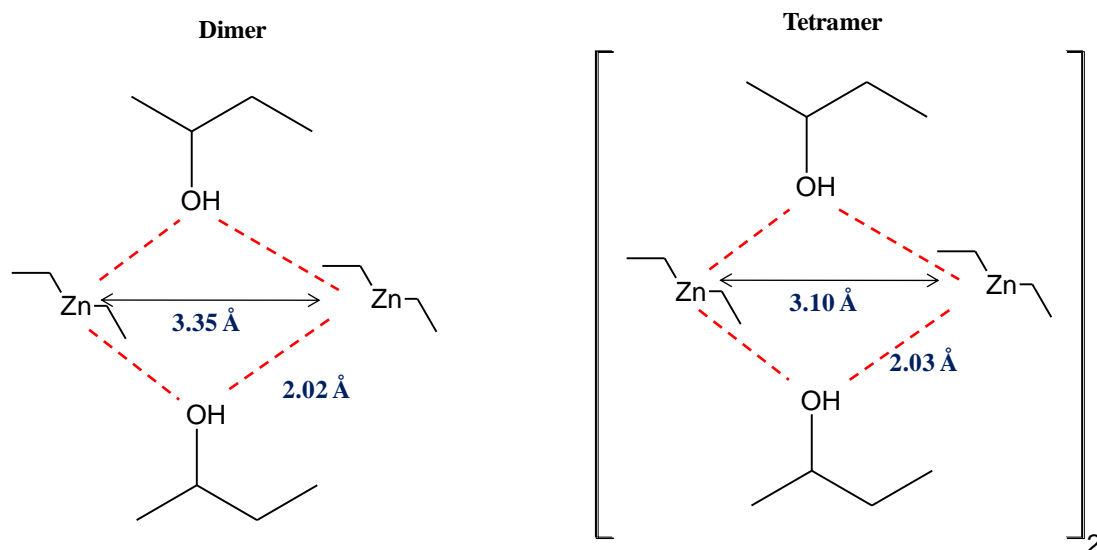
fits are 3.4 and 2.4 %. For comparison, the R-factor obtained using a monomer without Zn...Zn interaction is poor, at 15.9 %. The parameters used in the EXAFS fits are given in Table 6.2.

Model	First shell (Zn-O/C/N)			Second shell (Zn-O/C/N) (Zn-Zn)							
	N	R(Å)	$\sigma^2(\text{\AA}^2)$	N	R(Å)	$\sigma^2(\text{\AA}^2)$	N	R(Å)	$\sigma^2(\text{\AA}^2)$	$E_0$ (eV)	R %
<b>Dimer</b>	3.42 $\pm 0.394$	2.017 $\pm 0.011$	0.009 $\pm 0.002$	4.02 $\pm 0.991$	3.50 $\pm 0.016$	0.008 $\pm 0.003$	1	3.348 $\pm 0.010$	0.002 $\pm 0.001$	2.63 $\pm 1.014$	3.4
<b>Tetramer</b>	3.63 $\pm 0.394$	2.031 $\pm 0.009$	0.010 $\pm 0.001$	5.15 $\pm 1.719$	3.50 $\pm 0.016$	0.015 $\pm 0.003$	3	3.097 $\pm 0.007$	0.010 $\pm 0.001$	4.10 $\pm 1.555$	2.4

**Table 6.2: Zn K-edge EXAFS parameter of 0.1 M i-Pr<sub>2</sub>Zn with 2-Butanol in 1:1 molar ratio in toluene**

The XANES suggests that 2-butanol is reactive as can be seen by XANES of a 1:1 and 1:10 molar ratio which are similar compared to that of iPr<sub>2</sub>Zn in toluene. No visible difference is seen in both the XANES and EXAFS regions. This would imply that there is not enough butanol to react with all the zinc in solution.

The behavior of 2-butanol as observed from the XANES is similar to that of THF. The Zn-C bond distance in the 1<sup>st</sup> shell is 2.02 and 2.03 Å in the dimer and tetramer respectively. A difference of 0.25 Å is calculated between the dimer and tetramer complex with a Zn...Zn distance of 3.10 Å found in the tetramer.



**Figure 6.5: EXAFS calculated structural dimer and tetramer model of  $i\text{-Pr}_2\text{Zn}$  with 2-butanol in 1:1 molar ratio.**

A similar XANES and EXAFS with respect to other stoichiometric ratios means the same complex is present in solution. It is also likely that the structure model seen in Figure 6.5 represents the species also found when the amount of 2-butanol is in excess by tenfold. This XAFS study therefore proposes that the dimer or tetramer complex is more likely formed in toluene compared to the monomer proposed by Noyori.

### 6.3.2 $\text{Et}_2\text{Zn}$ and DMAE

The interaction between DEZ and DMAE was examined. The XANES of different molar ratios of  $i\text{-Pr}_2\text{Zn}$  and 2-butanol has been studied (Figure 6.3). However, not much change is seen in both the XANES and the EXAFS with a surplus of the ligand. Figure 6.6 illustrates the change in the zinc environment during the interaction of DEZ and DMAE. The illustration shows the XANES spectra with decreasing amounts of DEZ in the DEZ:DMAE mixture from top to bottom. The topmost spectrum has a mixture of DEZ and DMAE in a 2:1 molar ratio in toluene.

A weak 'white line' is present at approximately 9659 eV which disappears with the replacement of toluene with THF in the same molar ratio indicating the presence of new zinc species. The 'white line' reappears in an equimolar ratio DEZ and DMAE in toluene. Reducing the DEZ:DMAE ratio in toluene to 1:10 results in the disappearance of the white line at 9659 eV suggesting the emergence of new zinc species. The XANES of a 2:1 in THF and 1:10 in toluene are similar. The 2:1 mixture in THF probably has a mixture of DEZ-DMAE, and DEZ-THF complexes previously seen in section 5.3.8. On the other hand the 1:10 DEZ:DMAE mixture in toluene has DEZ-DMAE complexes since there is enough DMAE to react with all zinc centres. This behavior is evidence of the distinction between DMAE and 2-butanol. Both ligands are used in asymmetric synthesis as chiral initiators to activate the dialkylzinc.

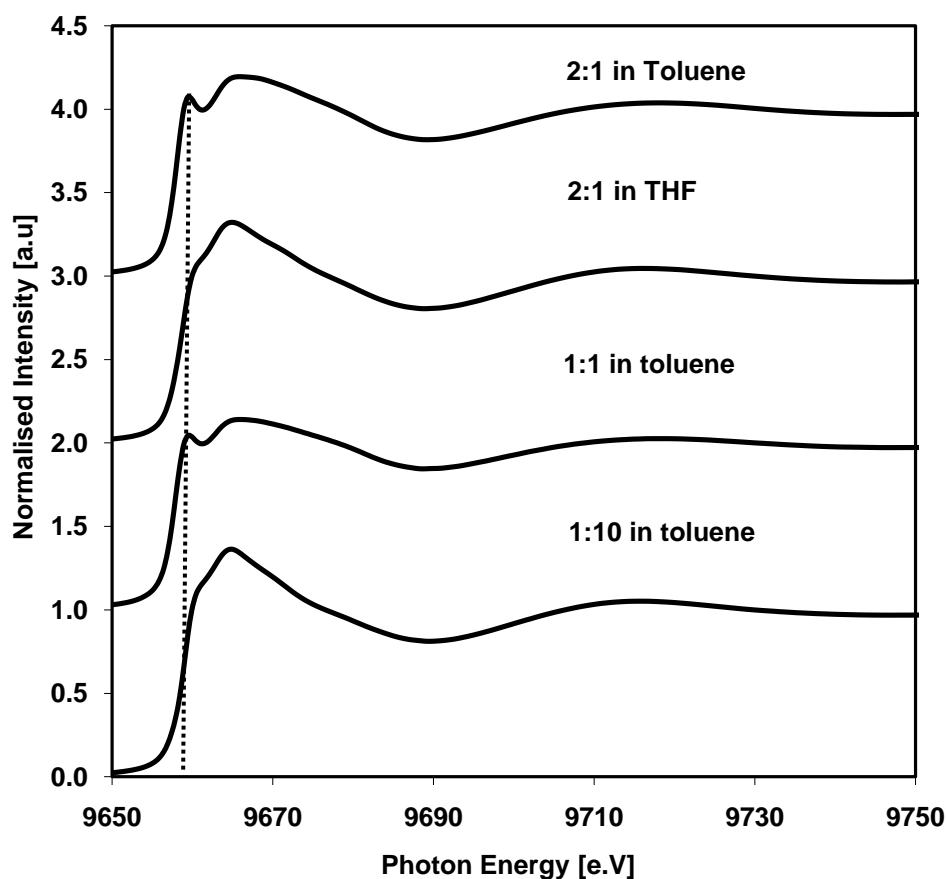
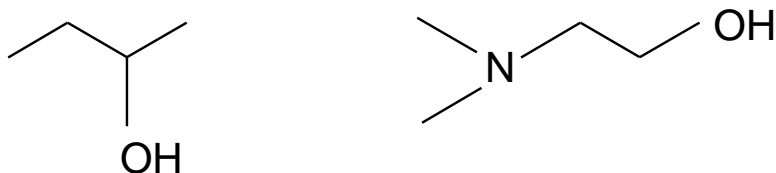


Figure 6.6: XANES Zn K-edge spectra of 0.1 M Et<sub>2</sub>Zn and DMAE.

The results seen in Figure 6.4 and Figure 6.6 suggest that the degree of interaction of both DMAE and 2-butanol with their corresponding dialkylzinc is diverse probably because DMAE is a chelating agent compared to 2-butanol. The XANES spectra of a 2:1 (DEZ: DMAE) in toluene with an excess of DEZ is found to be more similar to a 1:1 in toluene than a 2:1 mixture in THF. This likely because in toluene, DEZ-DMAE and DEZ species exist whereas in THF, DEZ-THF species are present in addition since THF binds to zinc. THF is known to stabilize diethylzinc.<sup>[94]</sup>

The presence of oxygen and a nitrogen atom in DMAE is seen in Figure 6.7. The dielectric properties of DMAE may therefore have a stronger electronic effect on the zinc atom than 2-butanol. DMAE is a chelating agent and 2-butanol is not. DMAE

appears to be less reactive in toluene because an excess is required to convert all DEZ.



**Figure 6.7: Structure of 2-butanol (left) and DMAE (right).**

Both oxygen and nitrogen in DMAE are capable of donating electrons to the zinc atom and are therefore likely to form a bidentate rather than a monodentate complex.<sup>[74]</sup> The similarity of the 1:10 in toluene and 2:1 in THF mixtures potentially supports the fact that DMAE is a better electron donor than 2-butanol.<sup>[95-97]</sup>

Further calculations were done to determine the structure of the DEZ/DMAE complex in a 1:1 ratio which according to studies by Noyori is represented by a monomeric active complex responsible for amplification of chirality.<sup>[18]</sup> Structural information in this study is ascertained by fitting the EXAFS in  $k$  and  $R$  space as seen in Figure 6.8. An evaluation of the EXAFS, advocates the possibility of dimer or tetramer complex formed between DEZ and DMAE.

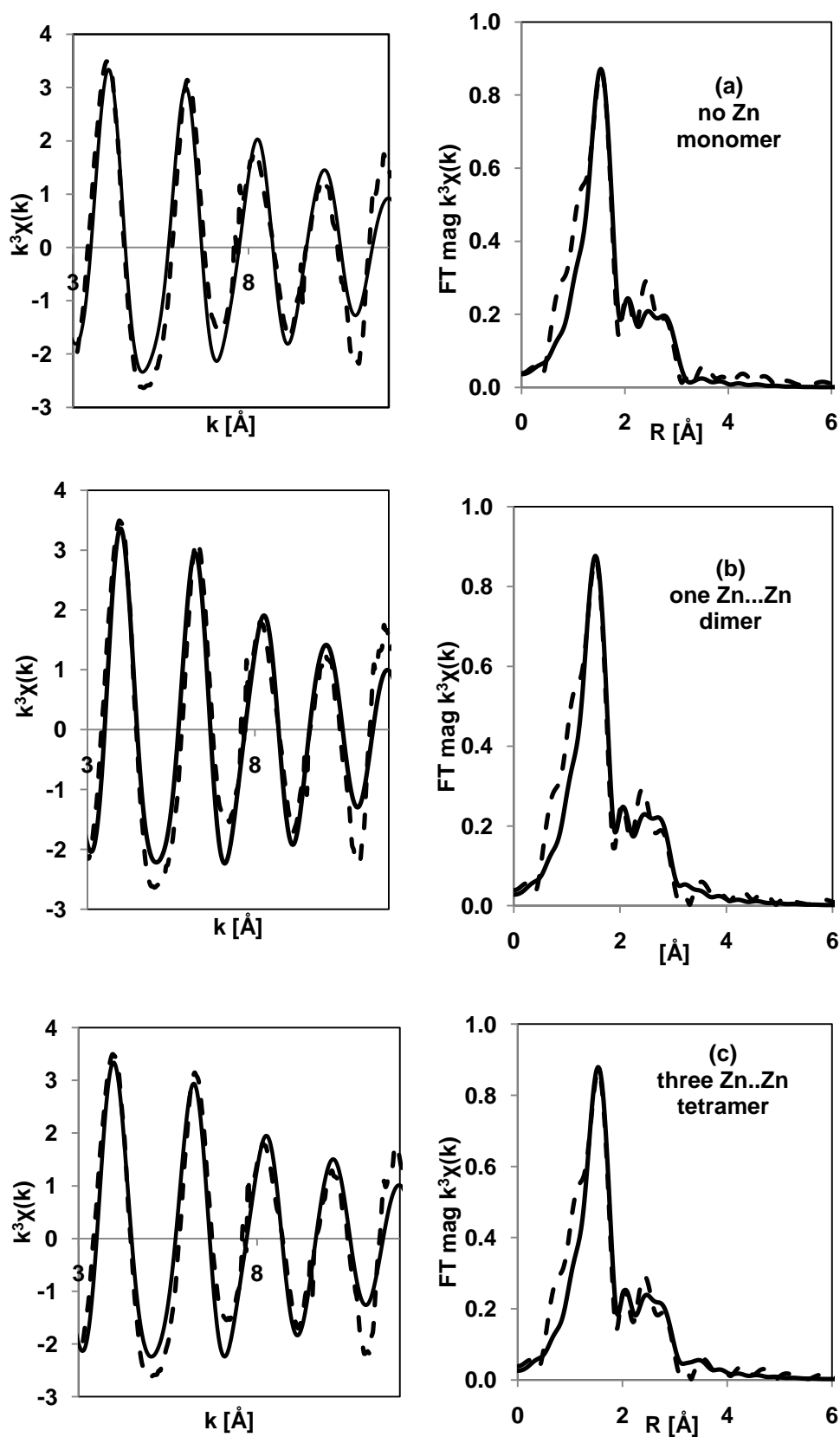


Figure 6.8: Zn K-edge EXAFS of 0.1 M Et<sub>2</sub>Zn/DMAE in 1:1 ratio (toluene) in k and R space. (a) monomer (b) dimer (c) tetramer. Dash lines are the experimental data and the solid lines are the best theoretical fit.

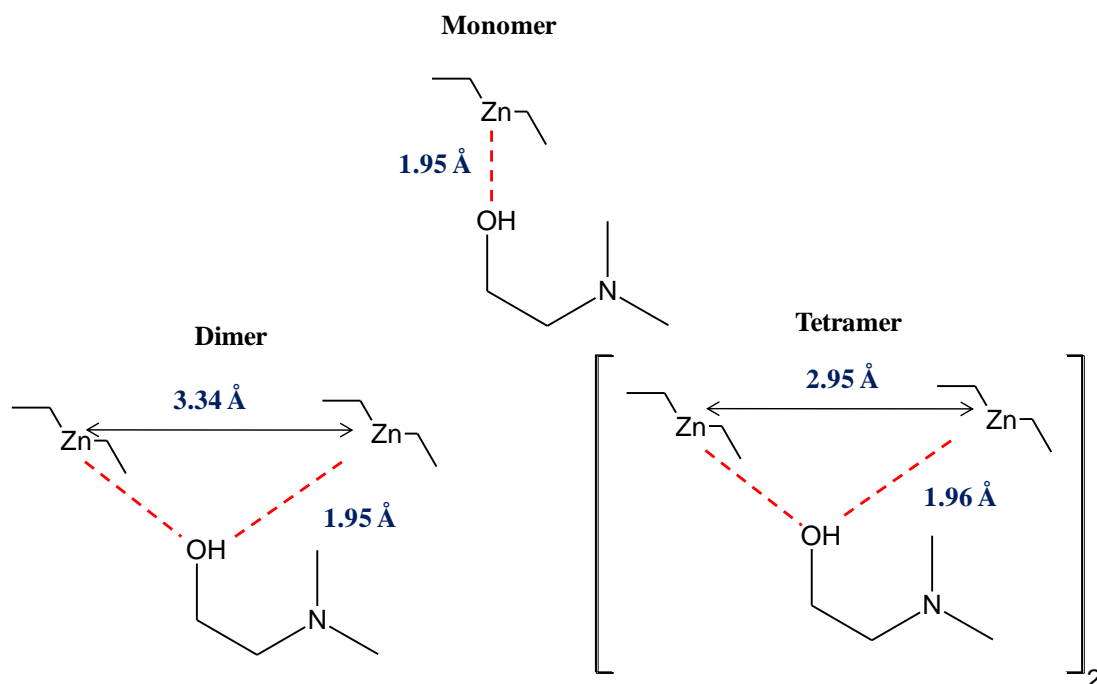
The EXAFS parameters derived from the above fits show the presence of Zn-Zn backscattering, thereby excluding the possibility of monomeric species. The Table below shows the monomer, dimer and tetramer model EXAFS parameters investigated.

Sample	First shell (Zn-O/C/N)			Second shell (Zn-O/C/N) (Zn-Zn)							
	N	R(Å)	$\sigma^2(\text{\AA}^2)$	N	R(Å)	$\sigma^2(\text{\AA}^2)$	N	R(Å)	$\sigma^2(\text{\AA}^2)$	$E_0$ (eV)	R (%)
<b>Monomer</b>	2.52 $\pm 0.198$	1.955 $\pm 0.005$	0.006 $\pm 0.001$	2.40 $\pm 1.009$	3.385 $\pm 0.020$	0.009 $\pm 0.005$				-0.203 $\pm 0.947$	2.8
<b>Dimer</b>	2.54 $\pm 0.201$	1.956 $\pm 0.006$	0.007 $\pm 0.001$	1.82 $\pm 1.159$	3.391 $\pm 0.006$	0.008 $\pm 0.006$	1	3.343 $\pm 0.179$	0.026 $\pm 0.011$	0.088 $\pm 0.997$	2.5
<b>Tetramer</b>	2.57 $\pm 0.198$	1.958 $\pm 0.006$	0.007 $\pm 0.001$	1.29 $\pm 1.098$	3.385 $\pm 0.034$	0.007 $\pm 0.007$	3	2.959 $\pm 0.179$	0.034 $\pm 0.008$	0.259 $\pm 0.977$	2.4

**Figure 6.9: Zn K-edge EXAFS parameters of 0.1 M Et<sub>2</sub>Zn/DMAE in 1:1 ratio in toluene (different models).**

Their R-factor values are between 2.4 % in the tetramer and dimer and 2.8 % in the monomer. The closeness of these values may suggest that one model does not entirely dominate the others even though the dimer and tetramer have slightly higher R-factor values. It is extremely difficult to decide which model could be considered but a mixture of species could be possible. The monomer model is likely because the Zn...Zn feature in the Fourier transform is not significant.





**Figure 6.10: Monomer, Dimer and Tetramer structural models proposed from EXAFS parameters of 0.1 M Et<sub>2</sub>Zn/DMAE in 1:1 ratio (toluene).**

Using XAS it is not possible to distinguish Zn-O, Zn-N and Zn-C interactions as carbon, nitrogen and oxygen have similar backscattering contributions as a result of their close atomic numbers or similar number of electrons. Other studies propose comparable Zn-O, Zn-N and Zn-C bond distances.<sup>[98, 99]</sup>

## 6.4 Conclusion

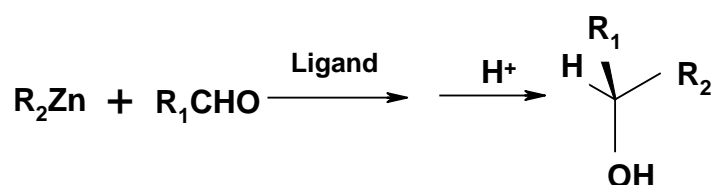
According to Noyori the monomer species is responsible for catalysis. The EXAFS calculations in this study indicate that a monomer, dimer, tetramer or a mixture of complexes is formed between DEZ and DMAE in a 1:1 molar ratio. From the XANES it is apparent that the interaction of dialkylzinc and DMAE is different to its interaction with 2-butanol. DEZ is found to be more reactive than 2-butanol. This difference in interaction may be because of the presence of two electronegative atoms (N and O) in DMAE, which causes a stronger interaction with the zinc centre.

The objective of this chapter which is to determine the nature of the complex formed between dialkylzinc and the ligand has therefore been successfully resolved. Two ligands which include 2-butanol and DMAE were investigated with DEZ. DMAE which has both O and N electronegative atoms is similar to paracyclophane ketimine ligand which is also of great interest in this study. From the findings of this chapter using both ligands, it is therefore very probable that a dimer or tetramer complex is formed with 2-butanol, indicating that the monomer complexes, as suggested by Noyori, are probably present only in low concentrations. In the case of DMAE a monomer, dimer and tetramer complex is possible based on the EXAFS calculations. This difference in the structures may also be attributed to DMAE which is less reactive with DEZ than 2-butanol.

## 7. Characterisation of the alkylation of aldehydes

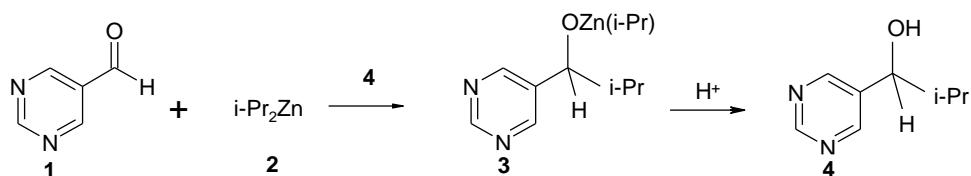
### 7.1 Introduction

In the Soai reaction and in many non-autocatalytic stereoselective synthesis reactions prochiral carbonyl compounds react with dialkylzinc in the presence of a chiral ligand to give the corresponding chiral secondary alcohol after hydrolysis. This reaction is capable of giving up to 99% *ee*.

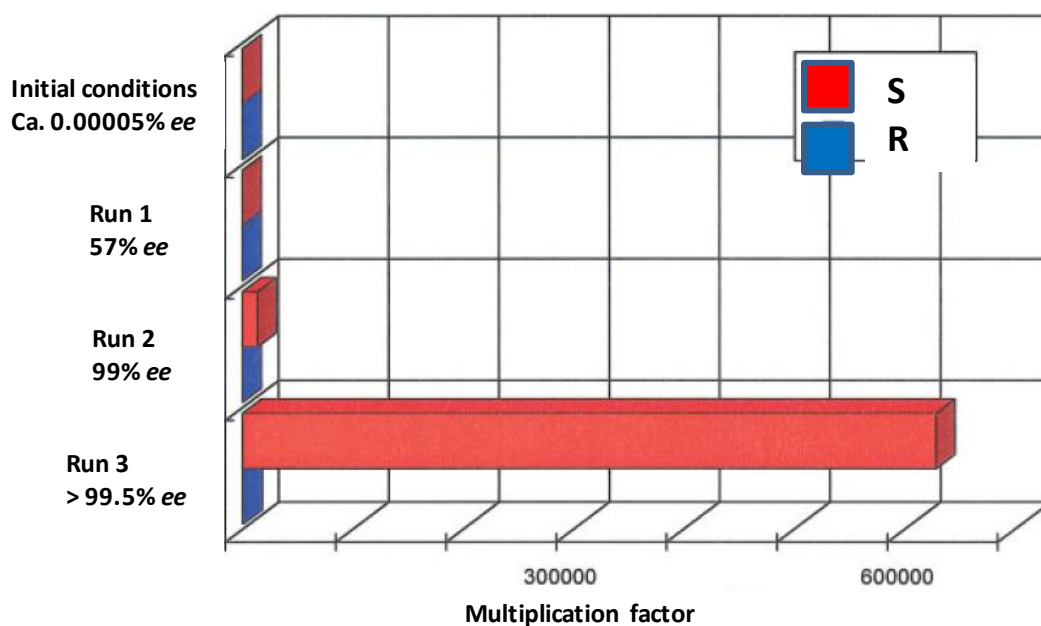


Several studies<sup>[17, 18, 22, 25, 33, 45, 49, 51]</sup> have been reported on the enantioselective addition of dialkylzincs to aldehydes but a deep understanding of the nature of the reaction products is lacking. Two types of reactions that generate chirality will be examined in this section. They include the Soai autocatalytic reaction and non-autocatalytic asymmetric reactions. Both reactions are highly enantioselective but the autocatalytic asymmetric reactions are of great interest since the product acts as the catalyst which is never depleted.

As earlier mentioned, the principle of autocatalytic chiral amplification was first theoretically suggested by Frank, who established that spontaneous asymmetric synthesis is a natural property of life which may be present in simpler autocatalytic systems.<sup>[16]</sup> A laboratory demonstration of the antagonistic principle by Frank was first possible by Soai and coworkers who first reported the asymmetric autocatalytic reaction.<sup>[19, 26, 27]</sup>



In the Soai autocatalytic reaction, chiral 5-pyrimidyl, 3-quinolyl, and 5-carbamoyl-3-pyridyl alkanols act as highly enantioselective asymmetric autocatalysts in the isopropylation of the respective aldehydes such as pyrimidine-5-carbaldehyde. An initial amount of 0.6% of chiral 2-alkynylpyrimidyl alkanol as a result of consecutive asymmetric autocatalysis multiplies to the product with up to >99.5% *ee*.<sup>[102]</sup>



**Figure 7.1: The increase in the amounts of S and R pyrimidyl alcohol in consecutive asymmetric autocatalysis.**<sup>[102]</sup>

Approaches so far used to study the reaction mechanism include computational, kinetic, NMR and calorimetric methods. Different studies propose different transition state structures which include monomers, dimers, trimers and tetramers in solution. The transition state structure remains unclear.<sup>[34, 45, 46, 49, 103]</sup> This section aims to

show results derived from EXAFS and XANES analysis that contribute to the possible structural models of the active catalysts responsible for autocatalysis. The advantage of using X-ray absorption spectroscopy is the possibility of acquiring both electronic and structural properties.

## 7.2 Experimental

Zn K-edge measurements of the main reaction between dialkylzinc and different aldehydes were carried out at ESRF and APS synchrotron light sources.

## 7.3 Results and discussion

The results discussed here include the reaction of dialkylzinc compounds with pyrimidine-5-carbaldehyde, benzaldehyde and cinnamaldehyde in presence of DMAE and 2-butanol. The studies described here are therefore a logical continuation of the work presented in chapter 6, which examined the interaction of the ligand and dialkylzinc compounds.

### 7.3.1 *i*-Pr<sub>2</sub>Zn and benzaldehyde

In the first instance the reaction of 0.1 M *i*-Pr<sub>2</sub>Zn with benzaldehyde (BA) is presented. The molar ratios were varied and changes were observed in the XANES. *i*-Pr<sub>2</sub>Zn perfectly works in the Soai autocatalytic reaction but chiral amplification up to 99% *ee* achieved with benzaldehyde. Figure 7.2 illustrates the Zn K-edge XANES of the *i*-Pr<sub>2</sub>Zn/benzaldehyde system. The strong white line resulting from a 1s-4p transition of *i*-Pr<sub>2</sub>Zn in toluene decreases on addition of benzaldehyde indicating a change in the local Zn environment. The two peaks in the XANES region are found between 9650 and 9670 eV. Increasing the amount of benzaldehyde from a 1:1 ratio

with  $i\text{-Pr}_2\text{Zn}$  to 1:20, we notice a lowering of the first peak which eventually equals the second peak at high benzaldehyde concentrations.

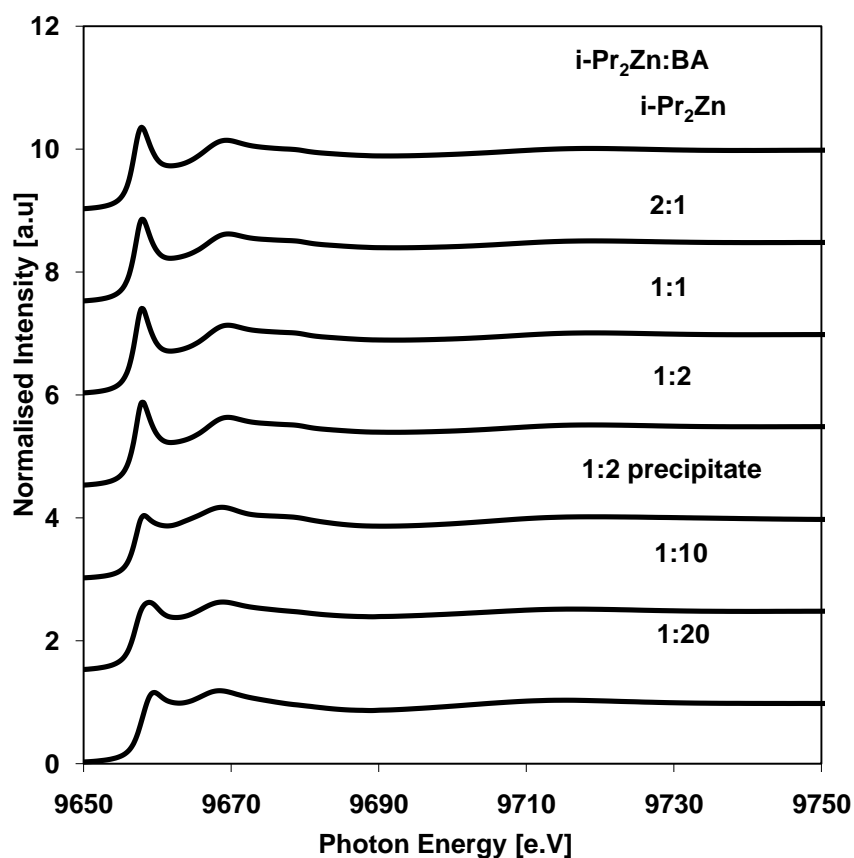


Figure 7.2: Zinc K-edge of 0.1 M  $i\text{-Pr}_2\text{Zn}$ :BA in toluene.

With an excess of  $i\text{-Pr}_2\text{Zn}$  in the molar ratio 2:1 of 0.1 M of  $i\text{-Pr}_2\text{Zn}$  with 0.05 M benzaldehyde we see a slight drop of the near-edge peak. However the resonance peak is higher than the 2<sup>nd</sup> peak. These changes in the XANES suggest the presence of different Zn species or a change in their oxidation states. It would appear that at room temperature the reaction is rather sluggish or resulting in equilibrium with significant amounts of unconverted reactants, since slight changes can be seen even when the amount of benzaldehyde is increased from 10 to 20 times that of  $i\text{-Pr}_2\text{Zn}$ .

It was observed that a precipitate was deposited at the bottom of the microcentrifuge tube which gradually formed as the reaction progressed. The strong difference

between the near-edge resonance intensity in the XANES of the precipitate (1:2 precipitate) at the bottom of the tube as compared to the supernatant solution (Figure 7.2) suggests that the solution may contain significant unreacted  $i\text{-Pr}_2\text{Zn}$ . This suggestion is supported by the fact that the XANES of the 1:2 precipitate is similar to that of the species present in solution at a benzaldehyde excess of 1:20, which would be compatible with the above mentioned equilibrium shifted to products by addition of reactant excess, and formation of a product with low solubility.

### **7.3.2 $i\text{-Pr}_2\text{Zn}$ and pyrimidine-5-aldehyde**

The XANES spectra of  $i\text{Pr}_2\text{Zn}$  and pyrimidine-5-carbaldehyde, PA shown below follow a similar trend to the reaction with benzaldehyde.

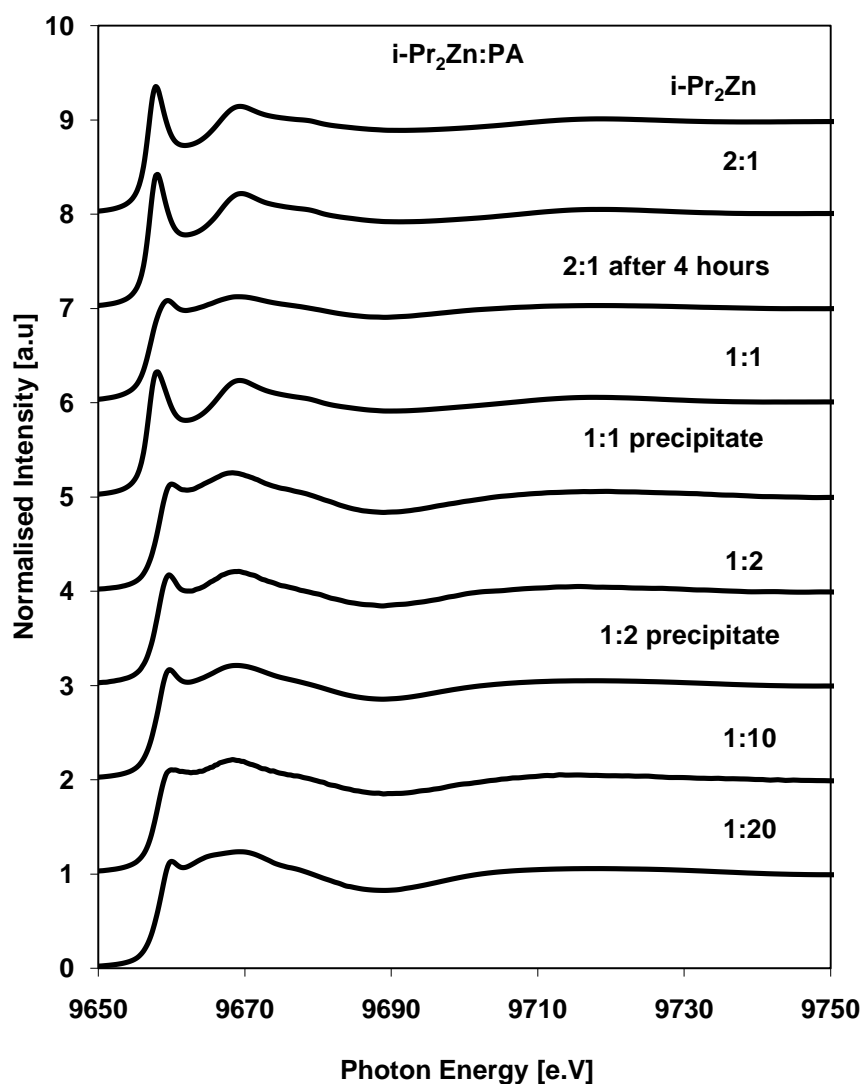


Figure 7.3: Zinc K-edge spectra of 0.1 M  $i\text{-Pr}_2\text{Zn:PA}$  in toluene.

As also observed for the benzaldehyde system, an increase in the amount of the aldehyde, results in a drop of the intensity of the white line resonance. There are two peaks between 9650 and 9670 eV which level out with an excess of pyrimidine-5-carbaldehyde. The XANES of the 1:1 in solution is different from that observed for the precipitate at the same molar ratio suggesting the presence of significantly different chemical composition of supernatant solution and precipitate most likely characterized by the presence of significant amounts of unreacted  $i\text{-Pr}_2\text{Zn}$ . Increasing



the amount of aldehyde from 1:1 by a factor of 10 results in more subtle XANES change in the case of the pyrimidylaldehyde compared to benzaldehyde. This is also the case when increased to a factor of 20 whereby one peak almost disappears. Comparing the XANES spectra one could therefore conclude that pyrimidine-5-aldehyde is more reactive with  $i\text{Pr}_2\text{Zn}$  than benzaldehyde.

An EXAFS analysis of the Soai reaction products, formed by diisopropylzinc with pyrimidylaldehyde (PA) in toluene is carried out.

Sample	First shell (Zn-O/C/N)			Second shell (Zn-O/C/N) (Zn-Zn)							
	N	$R(\text{\AA})$	$\sigma^2(\text{\AA}^2)$	N	$R(\text{\AA})$	$\sigma^2(\text{\AA}^2)$	N	$R(\text{\AA})$	$\sigma^2(\text{\AA}^2)$	$E_0$ (eV)	R (%)
<b><math>i\text{Pr}_2\text{Zn}</math> : PA 1:1</b>	2.39 $\pm 0.289$	1.95 $\pm 0.008$	0.010 $\pm 0.002$	4.4 $\pm 0.877$	3.51 $\pm 0.015$	0.003 $\pm 0.003$	1	3.38 $\pm 0.012$	0.002 $\pm 0.002$	3.03 $\pm 0.987$	3.9

Table 7.1: Zn K-edge EXAFS parameter of 0.1 M  $i\text{-Pr}_2\text{Zn}$  with PA in 1:1 molar ratio in toluene.

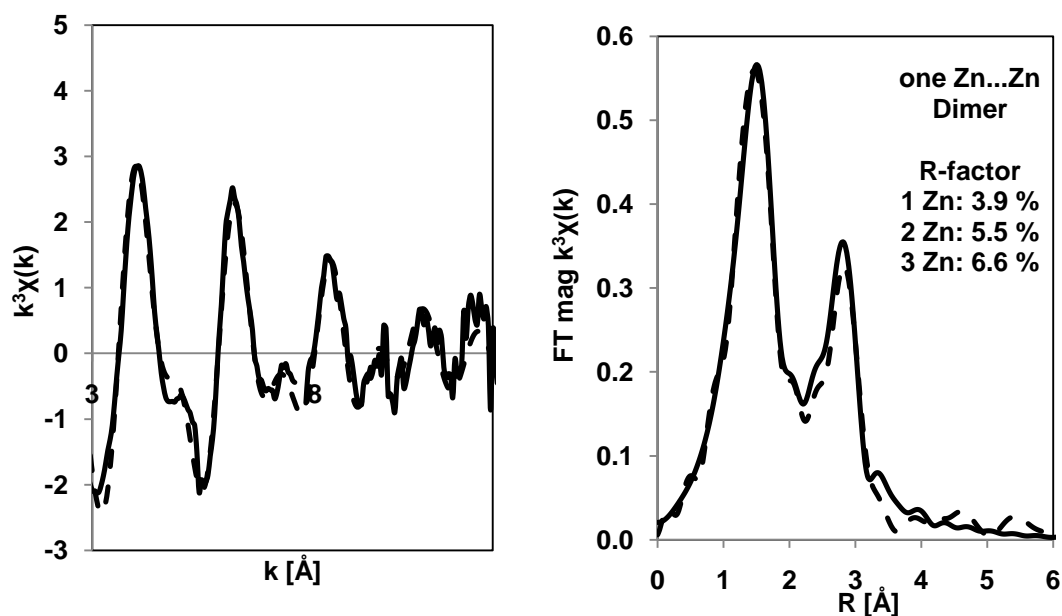


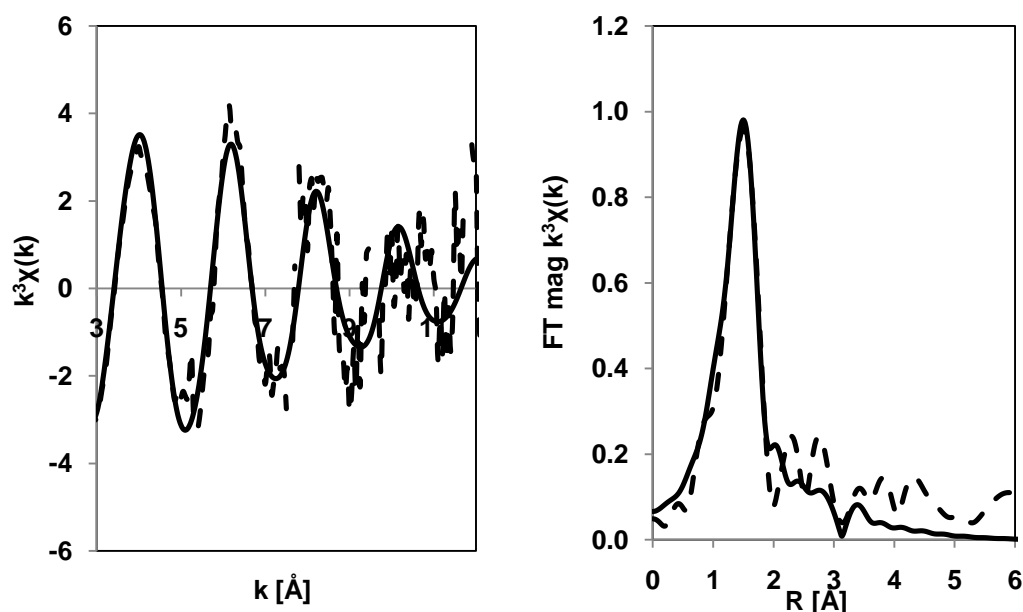
Figure 7.4: Zinc k-edge EXAFS spectra of  $i\text{-Pr}_2\text{Zn}$  with pyrimidyl aldehyde in 1:1 molar ratio (toluene). Dash lines are the experimental data and the solid lines are the best theoretical fit.

A fit of the EXAFS obtained for the 1:1 molar ratio in toluene (Table 7.1, Figure 7.4) suggests that in a 1:1 solution of  $i\text{-Pr}_2\text{Zn}$  and pyrimidyl aldehyde a dimer exists which is so far typical for Zn-O moieties. This dimer structural model is derived from an EXAFS fit with R-factor of 3.9 % in the dimer compared to 5.5 % and 6.6 % in the trimer and tetramer respectively. Based on the EXAFS calculations around the central Zn atom in the 1<sup>st</sup> shell, there are about 3 atoms: possibly 2 oxygen and 1 carbon atom distant approximately 1.95 Å from zinc. The bulky pyrimidyl group on oxygen probably prevents the formation of higher aggregates. One Zn neighbouring atom is also found with a distance 3.34 Å from the zinc central atom. The square core of the dimer is a Zn-O-Zn-O around which an isopropyl group is attached to zinc and the pyrimidyl group is attached to the oxygen. The 1:1 molar ratio of the precipitate formed at the bottom of the 1:1 solution of  $i\text{-Pr}_2\text{Zn}$  and pyrimidyl aldehyde (PA) was also investigated as tabulated below.

Sample	First shell (Zn-O/C/N)			Second shell (Zn-O/C/N) (Zn-Zn)							
	N	$R(A)$	$\sigma^2(A^2)$	N	$R(A)$	$\sigma^2(A^2)$	N	$R(A)$	$\sigma^2(A^2)$	$E_0$ (eV)	R (%)
<b><math>i\text{Pr}_2\text{Zn}</math>: PA 1:1 precipitate</b>	3.68 $\pm 0.901$	1.96 $\pm 0.017$	0.007 $\pm 0.002$	86 $\pm 2854$	3.85 $\pm 0.969$	0.132 $\pm 1.006$	1	3.49 $\pm 0.069$	0.012 $\pm 0.008$	-0.16 $\pm 0.322$	16.4

**Table 7.2: Zinc K edge EXAFS parameters of  $i\text{-Pr}_2\text{Zn}$  with pyrimidyl aldehyde in 1:1 molar ratio (precipitate). Some results are rather unusual due to nonhomogeneity of sample in solution, thus the high R-factor.**

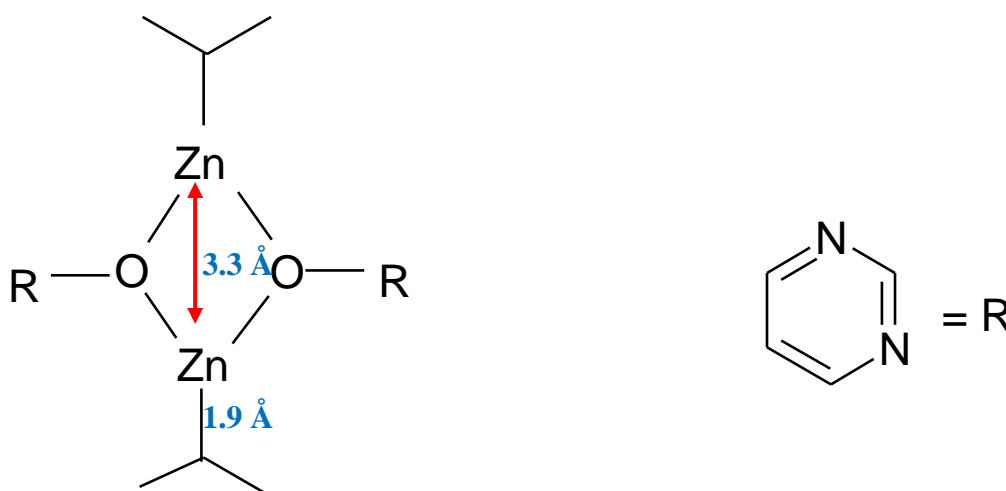
One obvious difference between the solution and precipitate that may influence the XAS measurements is that the solution is more homogenous than the precipitate. Homogeneity is a fundamental requirement for acquiring good XAS data. The EXAFS fit in a 1:1 precipitate is noisy likely because of the heterogeneity of the solid/liquid suspension, with precipitate particles moving in and out of the X-ray beam.



**Figure 7.5:** Zinc K edge EXAFS spectra of  $i\text{-Pr}_2\text{Zn}$  with pyrimidyl aldehyde in 1:1 molar ratio (precipitate). Dotted lines are the experimental data and the solid lines are the best theoretical fit. Not significant evidence of  $\text{Zn}\dots\text{Zn}$  from the fourier transform.

Even though the fit is not very good because of the high noise level in the measured data, the EXAFS fit in this case suggests on an average, 4-fold coordinated zinc atom similar to the 1:1 molar ratio in solution with 2 O, 1 C and 1 N atom from the pyrimidine. The Zn-O/C distance in the 1<sup>st</sup> shell is 1.96  $\text{\AA}$  slightly shorter than in solution. The Zn-Zn distance was calculated to be 3.49  $\text{\AA}$ . The EXAFS model of the precipitate was based on a fit with a high R-factor of 16.4%. In building the model

only the 1<sup>st</sup> shell is considered similar to all cases in this study. The derived model therefore reveals an alkoxide dimer with a Zn-O-Zn-O plane at the centre.



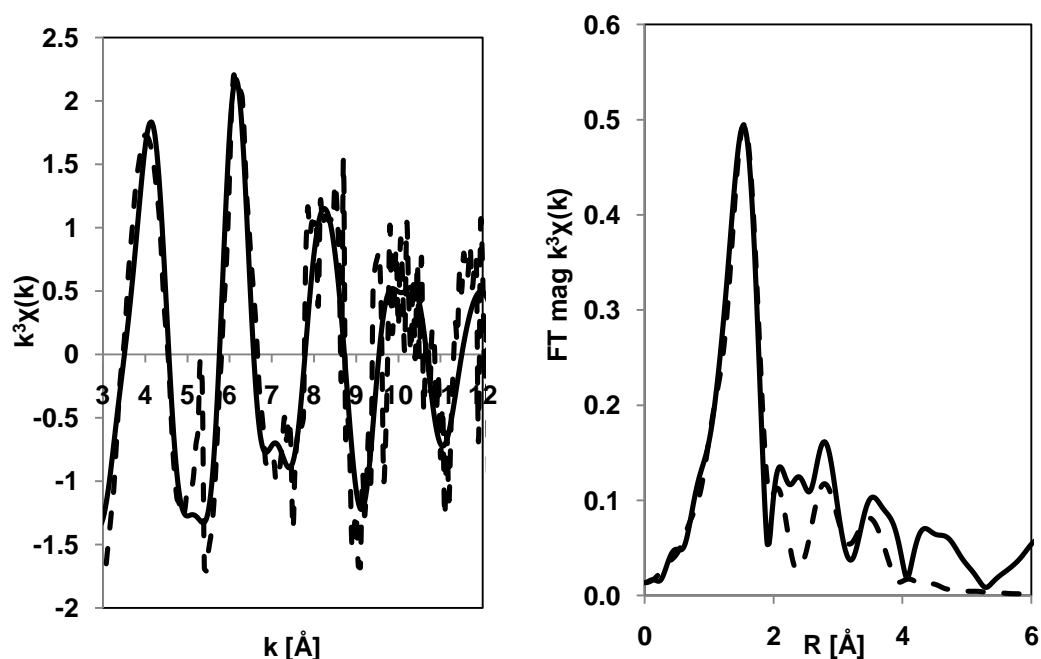
**Figure 7.6:** EXAFS model of  $i\text{-Pr}_2\text{Zn}$  with pyrimidyl aldehyde in 1:1 molar ratio. Model of dimer alkoxide in solution. The oxygen attaches opposite the both Ns' in the pyrimidyl ring.

Further EXAFS measurements were carried out for the 2:1 molar ratio of  $i\text{-Pr}_2\text{Zn}$  and PA. In this case an excess of  $i\text{-Pr}_2\text{Zn}$  molecules was present in solution suggesting that most of the PA molecules would be reacted.  $i\text{-Pr}_2\text{Zn}$  molecules have a linear coordination (5.3.1). We have previously seen that with a 1:1 molar ratio of  $i\text{-Pr}_2\text{Zn}$  and PA a dimer complex is formed which possesses a trigonal zinc coordination. One would therefore logically expect a combination of both linear and trigonal coordinated Zn centres in the first instance. From the EXAFS calculations three C/O atoms are around the zinc centre in the 1<sup>st</sup> shell. The Zn-C/O and Zn-Zn bond distances are 1.97 and 3.06 Å respectively. This fit with an R-factor of 12.9% therefore complies with the prediction of having excess  $i\text{-Pr}_2\text{Zn}$  molecules in solution. EXAFS is a bulk technique and in this case two significant zinc species are

found in solution which includes the zinc alkoxide dimer and unreacted  $i\text{-Pr}_2\text{Zn}$  molecules as seen in the model below (Figure 7.9).

Sample	First shell (Zn-O/C/N)			Second shell (Zn-O/C/N) (Zn-Zn)							
	N	$R(\text{\AA})$	$\sigma^2(\text{\AA}^2)$	N	$R(\text{\AA})$	$\sigma^2(\text{\AA}^2)$	N	$R(\text{\AA})$	$\sigma^2(\text{\AA}^2)$		
<b><math>i\text{Pr}_2\text{Zn}</math> :</b>	1.54	1.97	0.005	2.83	3.98	-0.013	1	3.06	0.013	3.23	12.9
<b>PA 2:1</b>	$\pm 0.284$	$\pm 0.013$	$\pm 0.002$	$\pm 2.612$	$\pm 0.046$	$\pm 0.015$		$\pm 0.030$	$\pm 0.003$	$\pm 2.409$	

**Table 7.3: Zinc K edge EXAFS parameter of  $i\text{-Pr}_2\text{Zn}$  with pyrimidyl aldehyde in 2:1 molar ratio (solution) at  $t_0$  (initial).**



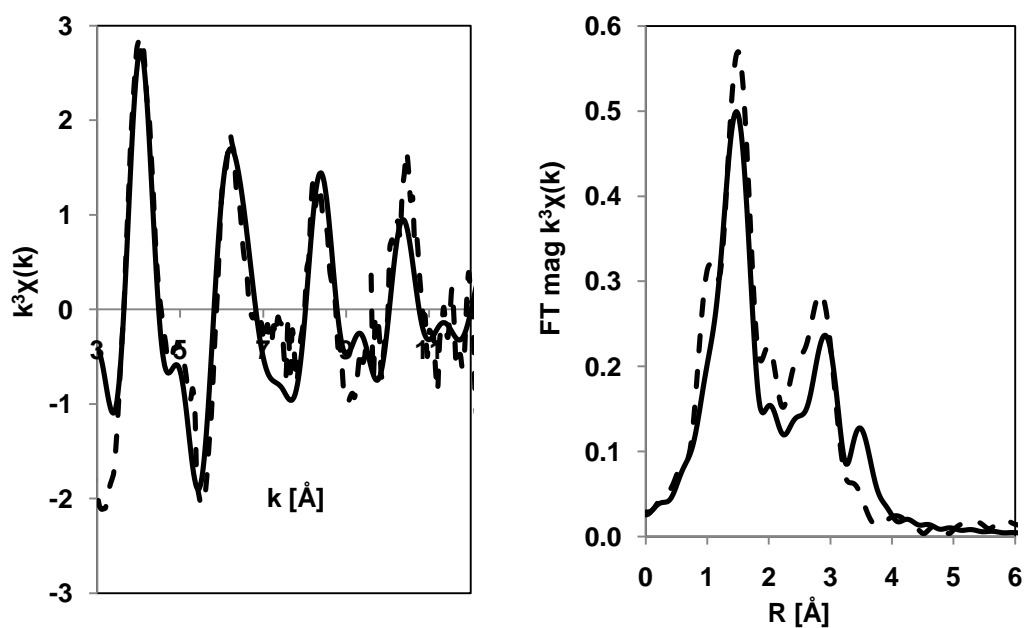
**Figure 7.7: Zinc K edge EXAFS spectra of  $i\text{-Pr}_2\text{Zn}$  with pyrimidyl aldehyde in 2:1 molar ratio (solution) at  $t_0$  (initial). Dotted lines are the experimental data and the solid lines are the best theoretical fit.**

The EXAFS fits in  $R$ - and  $k$ - space as seen above (Figure 7.7) are similar to that seen with  $i\text{-Pr}_2\text{Zn}$  in toluene. The radial distance fit has only one peak suggesting a low Zn...Zn contribution. After 3 hours of the previously measured 2:1 solution,

according to the EXAFS calculations the Zn-Zn distance increases as well as the intensity but the structural model likely remains the same.

Sample	First shell (Zn-O/C/N)			Second shell (Zn-O/C/N) (Zn-Zn)							
	N	$R(A)$	$\sigma^2(A^2)$	N	$R(A)$	$\sigma^2(A^2)$	N	$R(A)$	$\sigma^2(A^2)$	$E_0$ (eV)	R (%)
<b>iPr<sub>2</sub>Zn : PA 2:1</b>	1.84 $\pm 0.343$	1.91 $\pm 0.013$	0.007 $\pm 0.002$	18.48 $\pm 13.720$	4.04 $\pm 0.047$	-0.031 $\pm 0.014$	1	3.42 $\pm 0.022$	0.008 $\pm 0.002$	-2.08 $\pm 2.162$	10.9

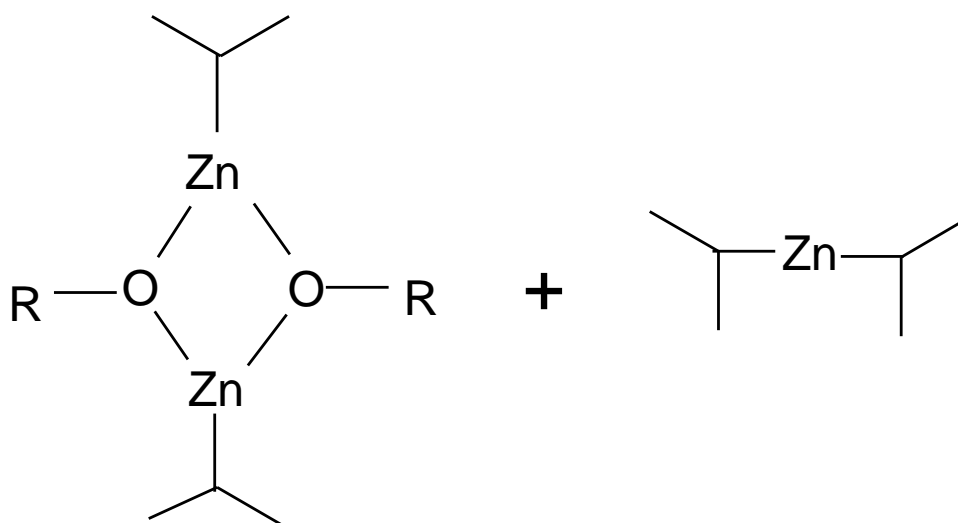
**Table 7.4: Zinc K-edge EXAFS spectra of i-Pr<sub>2</sub>Zn with pyrimidyl aldehyde in 2:1 molar ratio (solution) after 3 hours.**



**Figure 7.8: Zinc K edge EXAFS spectra of i-Pr<sub>2</sub>Zn with pyrimidyl aldehyde in 2:1 molar ratio (solution) after 3 hours. Dash lines are the experimental data and the solid lines are the best theoretical fit.**

The EXAFS fit in Figure 7.8 has an R-factor of 10.9% and the Debye Waller Factors.

The Zn-C/O and Zn-Zn bond distances are 1.91 and 3.4 Å respectively.

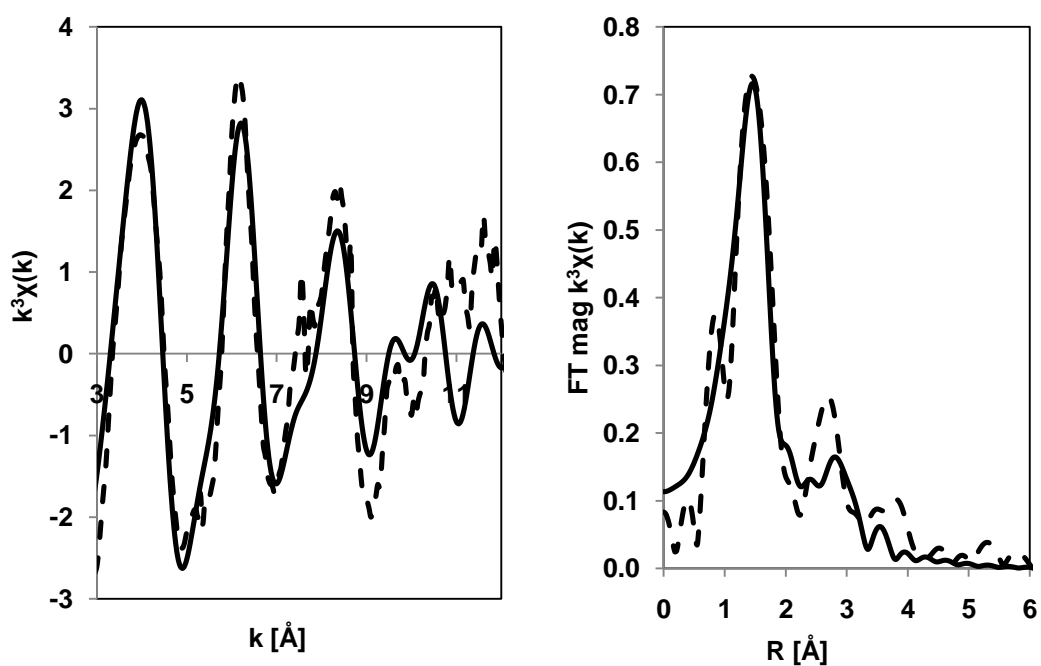


**Figure 7.9:** EXAFS model of  $i\text{-Pr}_2\text{Zn}$  with pyrimidyl aldehyde in 2:1 molar ratio in solution at start and after 3 hours.

A molar ratio of 1:2 ( $i\text{-Pr}_2\text{Zn}$ :PA) was also considered with an excess of the aldehyde in the precipitate. From first instance, one would expect trigonal zinc sites with a Zn-O-Zn-O plane centre considering the Zn K-edge. An EXAFS fit with an R-factor of 10.6% reveals a tetrahedral zinc site with calculated Debye Waller Factors between 0.007 and 0.012  $\text{\AA}^2$ . The Zn-C/O and Zn-Zn bond distances were calculated to be 1.95 and 3.37  $\text{\AA}$  respectively (see Figure 7.10 and Table 7.5).

Sample	First shell (Zn-O/C/N)			Second shell (Zn-O/C/N) (Zn-Zn)							
	N	$R(\text{\AA})$	$\sigma^2(\text{\AA}^2)$	N	$R(\text{\AA})$	$\sigma^2(\text{\AA}^2)$	N	$R(\text{\AA})$	$\sigma^2(\text{\AA}^2)$	$E_0$ (eV)	R (%)
<b><math>i\text{Pr}_2\text{Zn}</math>:PA 1:2 (precipitate)</b>	3.88 $\pm 0.746$	1.95 $\pm 0.015$	0.010 $\pm 0.002$	2.52 $\pm 3.629$	3.90 0.057	0.012 $\pm 0.014$	1	3.37 $\pm 0.023$	0.007 $\pm 0.002$	-4.4 $\pm 2.44$	10.6

**Table 7.5:** Zinc K edge EXAFS spectra of  $i\text{-Pr}_2\text{Zn}$  with pyrimidyl aldehyde in 1:2 molar ratio (precipitate).



**Figure 7.10:** Zinc K edge EXAFS spectra of  $i\text{-Pr}_2\text{Zn}$  with pyrimidyl aldehyde in 1:2 molar ratio (precipitate). Dash lines are the experimental data and the solid lines are the best theoretical fit.

The proposed model from the above fit in  $R$ - and  $k$ - space suggests that tetrahedral sites are possible with an excess of PA molecules if they attach themselves to the zinc. The difference in electronegativity between  $\text{Zn}^{2+}$  and  $\text{O}^{2-}$  attracts the excess PA molecules (intermolecular attraction) causing the transformation from a trigonal to tetrahedral zinc environment.



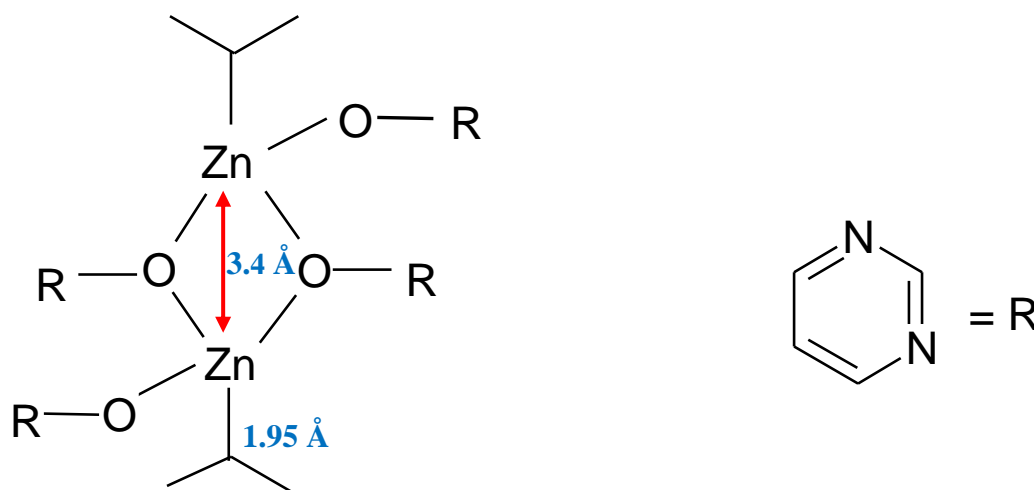


Figure 7.11: EXAFS model of  $i\text{-Pr}_2\text{Zn}$  with pyrimidyl aldehyde in 1:2 molar ratio (precipitate).

Increasing the excess of PA over  $i\text{-Pr}_2\text{Zn}$  by 10 and then 20 times results in a change in the XANES as observed suggesting a further change in the zinc environment. The XANES of a 1:1 precipitate was however similar to a 1:10 and 1:20 solution. This may suggest that the chemical composition is similar. Unfortunately the EXAFS calculations at high ratios of PA were not successful and had extremely high R-factors of up to 17.9%. Interestingly, it was found that at higher PA amounts over  $i\text{-Pr}_2\text{Zn}$ , there was a uniform distribution in solution which may mean that the excess PA molecules solubilize the formed zinc alkoxide molecules. However, it is also possible that the excess PA molecules intermolecularly aggregate amongst themselves and therefore prevent the association of zinc alkoxide dimers in solution to form aggregates.

### 7.3.3 $\text{Et}_2\text{Zn}$ and pyrimidyl aldehyde

Diethylzinc is widely used as an alkylating agent in organozinc chemistry. Although the only suitable alkylating agent in the Soai autocatalytic reaction is  $i\text{-Pr}_2\text{Zn}$ , studies

on DEZ would be beneficial because it is similar to  $i\text{-Pr}_2\text{Zn}$  in its functioning and size.

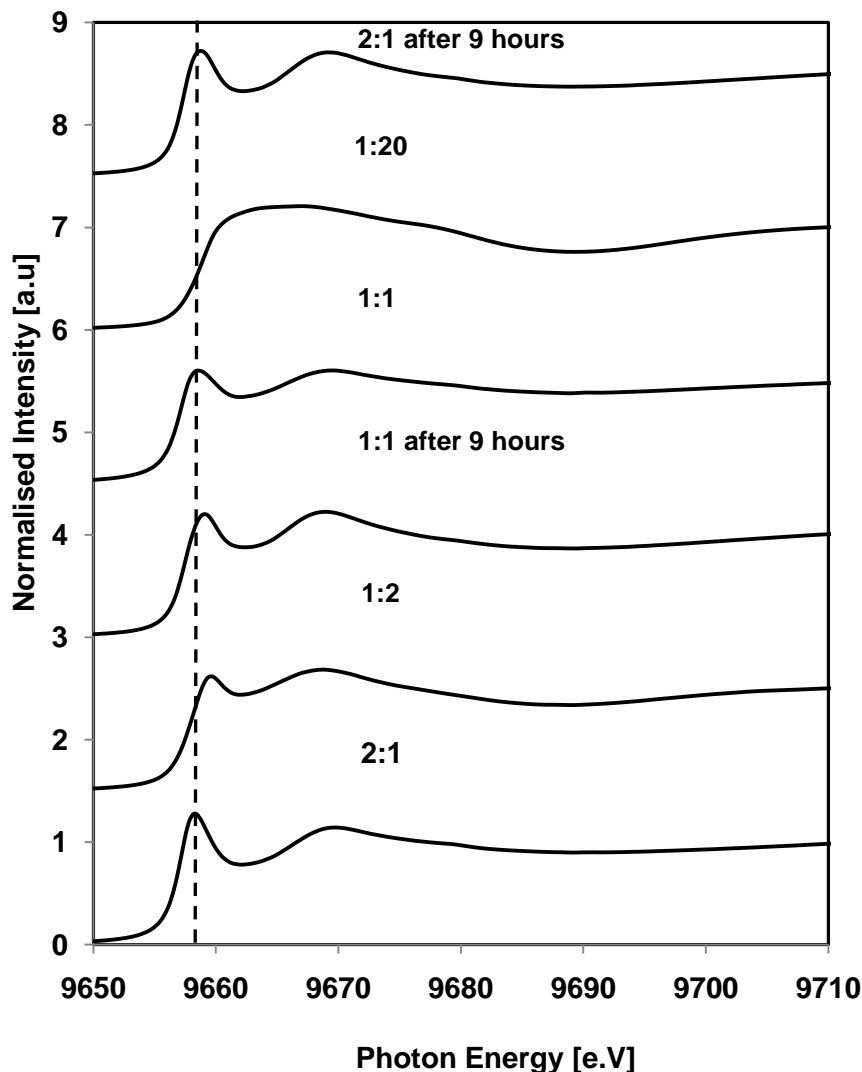


Figure 7.12: Zinc K-edge XANES spectra of 0.1 M DEZ:PA in toluene.

The XANES spectra of the reaction of DEZ and PA illustrated above were measured under different stoichiometric conditions. The trend of the XANES spectra of DEZ is similar to  $i\text{-Pr}_2\text{Zn}$ . In toluene a DEZ molecule has a linear zinc arrangement with a large white line resonance peak (see 5.3.2). In the case of the reaction of PA and DEZ the resonance peak drops implying a change in the zinc environment from the

linear structure observed in toluene. The DEZ:PA molar ratios considered in the XANES include 1:1, 1:2, 2:1 and 1:20 in toluene. With an increase in DEZ over PA the resonance peak increases. The initial XANES spectrum of the 1:1 mixture is similar to that observed after 9 hours. On the other hand the XANES of the 2:1 mixture changes after 9 hours. The resonance peak decreases over time; indicating the formation of new zinc species with time. By doubling the amount of PA over DEZ, the section between the first two peaks increases. This is even more noticeable at a stoichiometric molar ratio of 1:20, where both peaks merge to one large peak.

For the 1:1 solution, EXAFS measurements of the fresh solution are seen below in  $k$ - and  $R$ - space. The Zn K edge EXAFS spectra is rather noisy as seen in Figure 7.13.

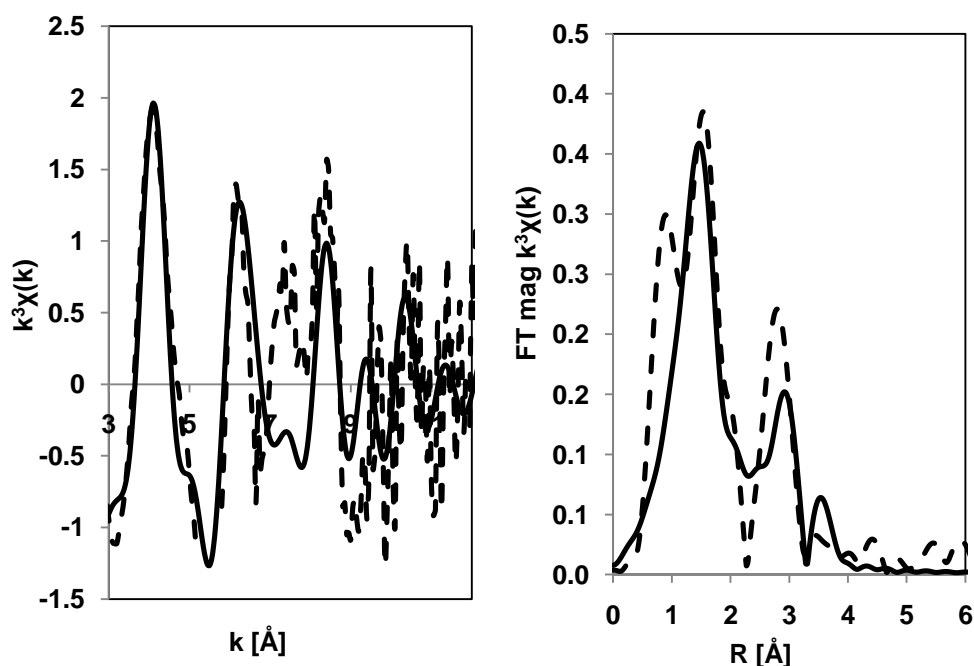
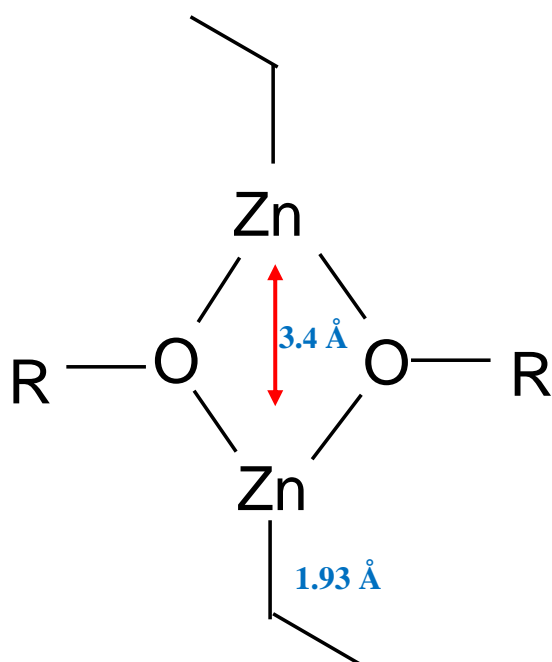


Figure 7.13: Zinc k edge EXAFS spectra of 0.1 M DEZ with pyrimidyl aldehyde in 1:1 molar ratio (toluene). Dotted lines are the experimental data and the solid lines are the best theoretical fit.

Sample	First shell (Zn-O/C/N)			Second shell (Zn-O/C/N) (Zn-Zn)							
	N	$R(A)$	$\sigma^2(A^2)$	N	$R(A)$	$\sigma^2(A^2)$	N	$R(A)$	$\sigma^2(A^2)$	$E_0$ (eV)	R (%)
<b>DEZ:PA</b>	1.78	1.93	0.002	4.68	4.04	0.015	1	3.43	0.008	0.36	21.8
<b>1:1</b>	$\pm 0.537$	$\pm 0.022$	$\pm 0.004$	$\pm 5.177$	$\pm 0.027$	$\pm 0.016$		$\pm 0.027$	$\pm 0.002$	$\pm 3.115$	

**Table 7.6: Zinc K edge EXAFS spectra of DEZ with pyrimidyl aldehyde in 1:1 molar ratio (toluene).**

The noisy XAS data resulted in an R-factor of the EXAFS fit of 21.8%. The Debye-Waller factors were between 0.002 and 0.015 Å<sup>2</sup>. The proposed model has upto about 3 neighbouring atoms to the zinc centre atom i.e. C or O and a zinc atom. The Zn-O-Zn-O exists and the Zn-Zn distance is 3.43 Å. The Zn-C/O bond distance in the 1<sup>st</sup> shell is 1.93 Å. From the XANES after 9 hours the plot of the normalized intensity versus photon energy looks the same suggesting that the zinc species are similar or same.



**Figure 7.14: EXAFS model of DEZ with pyrimidyl aldehyde in 1:1 molar ratio (solution).**

The EXAFS data are compatible with the presence of a mixture of linear DEZ and 1:1 trigonal species, as seen above (Figure 7.14). An EXAFS fit of a 2:1 stoichiometric ratio with an R-factor of 6.7% confirms this prediction. The DWF calculated were between 0.005 and 0.010  $\text{\AA}^2$  and the Zn-C/O and Zn-Zn bond distances of 1.87  $\text{\AA}$  and 3.39  $\text{\AA}$  respectively.

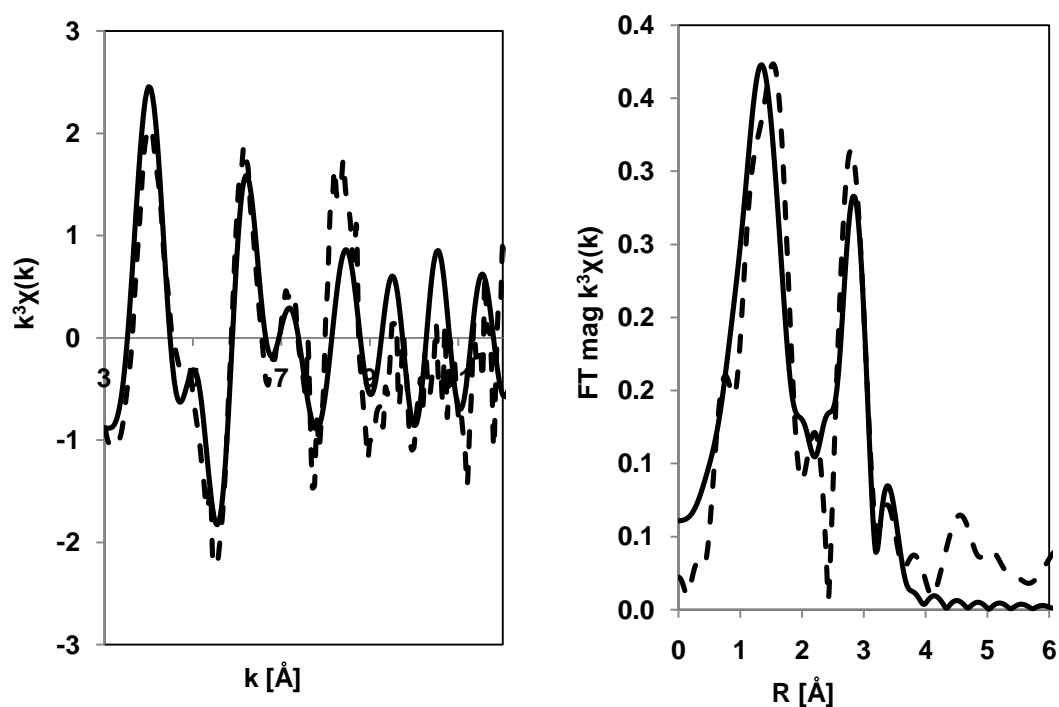
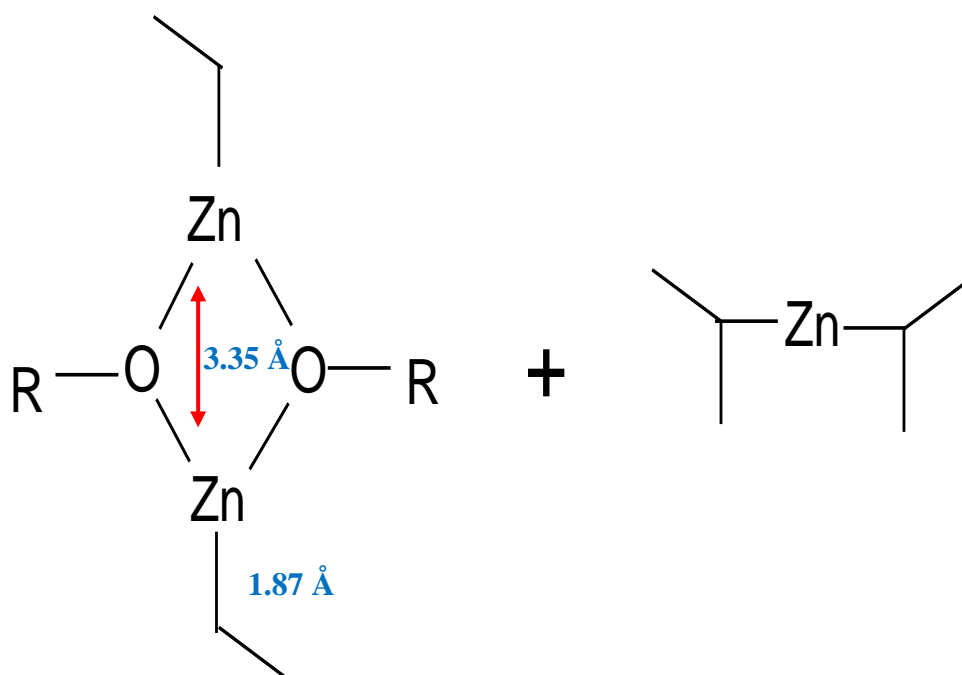


Figure 7.15: Zinc k edge EXAFS spectra of DEZ with pyrimidyl aldehyde in 2:1 molar ratio (toluene). Dotted lines are the experimental data and the solid lines are the best theoretical fit.

Sample	First shell			Second shell							
	(Zn-O/C/N)			(Zn-O/C/N)			(Zn-Zn)				
	N	<i>R</i> (Å)	σ²(Å²)	N	<i>R</i> (Å)	σ²(Å²)	N	<i>R</i> (Å)	σ²(Å²)	E <sub>0</sub> (eV)	R (%)
DEZ:PA	3.19	1.87	0.018	6.79	3.88	0.012	1	3.35	0.005	-9.77	22.4
2:1	±1.519	±0.026	±0.007	±5.641	±0.048	±0.009		±0.023	±0.001	±3.239	

Table 7.7: Zinc K edge EXAFS spectra of DEZ with pyrimidyl aldehyde in 2:1 molar ratio (toluene).

The above EXAFS fit suggests that in the first shell there 3 C/O atoms or less around the zinc centre. As earlier mentioned this confirms that there is a mixture of zinc species with linear and trigonal sites as seen in the model below (Figure 7.6).



**Figure 7.16: EXAFS model of DEZ with pyrimidyl aldehyde in 2:1 molar ratio (solution).**

From the XANES (Figure 7.12) there is evidence of the formation of new zinc species since there is a change with an increase in the stoichiometric amount of PA over diethylzinc. All the diethylzinc in toluene will obviously be consumed by excess PA. The EXAFS calculations at 1:2 and 1:20 were unfortunately extremely noisy and not fully interpretable because increasing the amount of PA increases the amount of solid particles in solution. With this increase in PA there is a change in the XANES spectra implying that the excess PA molecules still interact with the formed alkoxide dimer leading possibly to solubilisation. Another reason for the change in the XANES may be the physical state. Increasing the amount of PA gradually moves from a liquid solution to a solid. It may also be possible that higher aggregates e.g. Figure 7.17, may be formed especially with the possibility of intermolecular interaction although no direct evidence is immediately available.

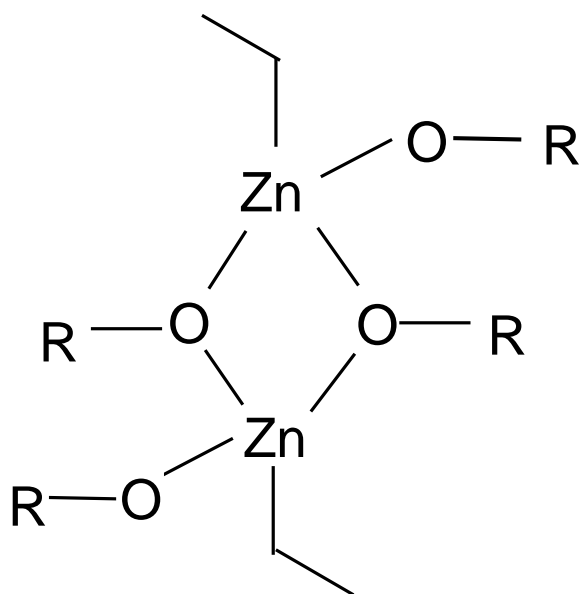


Figure 7.17: Possible model of DEZ with surplus pyrimidyl aldehyde in solution.

#### 7.3.4 Et<sub>2</sub>Zn, DMAE and cinnamaldehyde

In this section the XANES spectra of diethylzinc, DMAE and cinnamaldehyde (CA) will be examined. Basically the main reaction is between the aldehyde and alkylzinc. DMAE acts as a chiral ligand that makes the alkylzinc more reactive by replacing one alkyl group by an electronegative substituent thereby increasing the polarity of the alkyl-Zn bond. Noyori *et al*<sup>[18]</sup> report the effect of changing the molar ratio of BA: DEZ: DAIB (see Table 6.1).

From Table 6.1, the optimum *ee* and yield of the secondary alcohol product are obtained with an excess of DEZ. The work by Noyori *et al* suggests that two Zn atoms per aldehyde account for the alkylation reaction. The reaction mechanism proposed by their work involves several structural complexes (see Figure 6.1).<sup>[18]</sup> From the molar ratios studied by Noyori and co-workers, XANES studies were made to appreciate the structural changes. We have already seen that the XANES of DEZ



gives a huge resonance peak. The addition of DMAE in a 1:1 molar ratio brings about a change in the zinc as seen in the peak which reduces. From the XANES below it can be seen that increasing the substituents from 2 to 3, lessens the number of peaks from 2 to 1 between 9650 and 9670 eV. This may be a hint that the zinc species present are not the same. Relating the XANES Zn K-edge spectra to table 3.1, the best *ee* and yield are at molar ratios of 2:1:1 then 2:1:2. Molar ratios of 1:1:1 are reported to deliver a poor *ee* and yield.

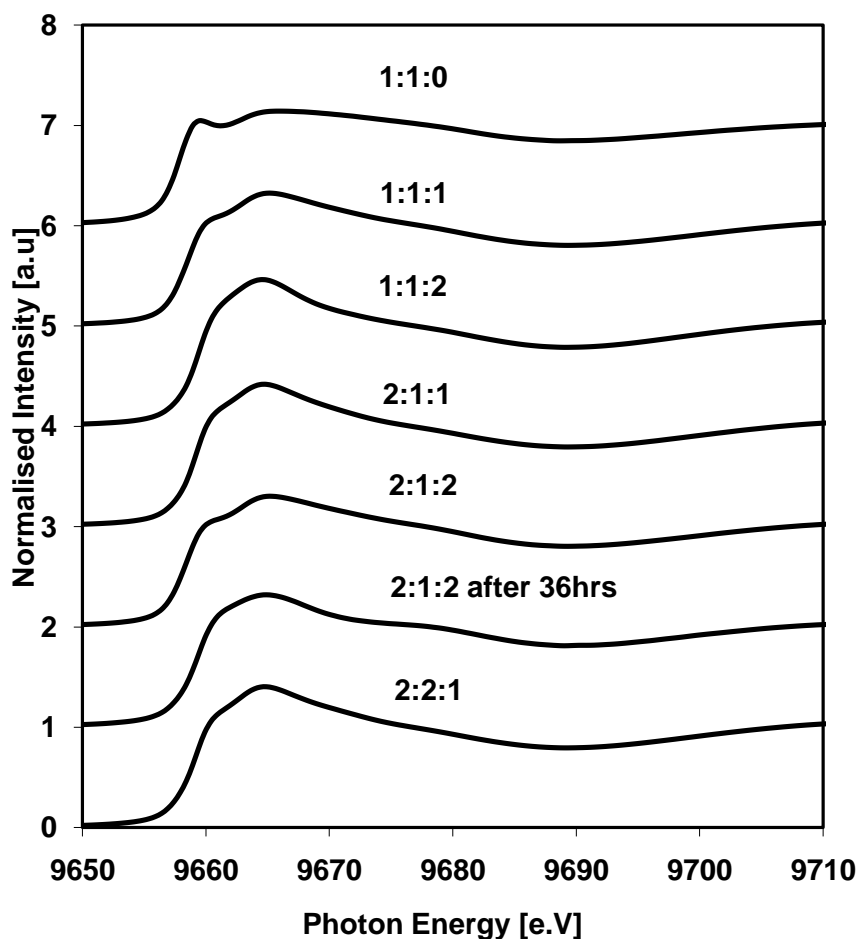


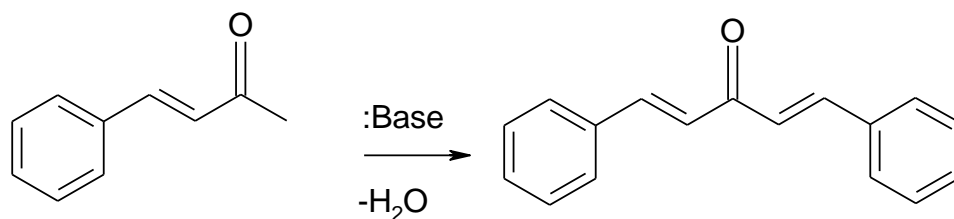
Figure 7.18: Zinc k-edge spectra of 0.1 M DEZ:DMAE:CA in toluene.

It is noted that the colour of the DEZ/DMAE/Cinnamaldehyde mixture changes from straw green to orange then to red. After 36 hours the following colours were observed for different stoichiometric amounts.

<b>Molar ratio (DEZ:DMAE:CA)</b>	<b>Colour observed</b>
1:1:1	Red
2:1:1	Bright orange
2:1:2	Red
2:2:1	Red
1:1:2	Bright Orange

**Table 7.8: Colour change at different molar ratios of DEZ:DMAE:CA after 36 hours**

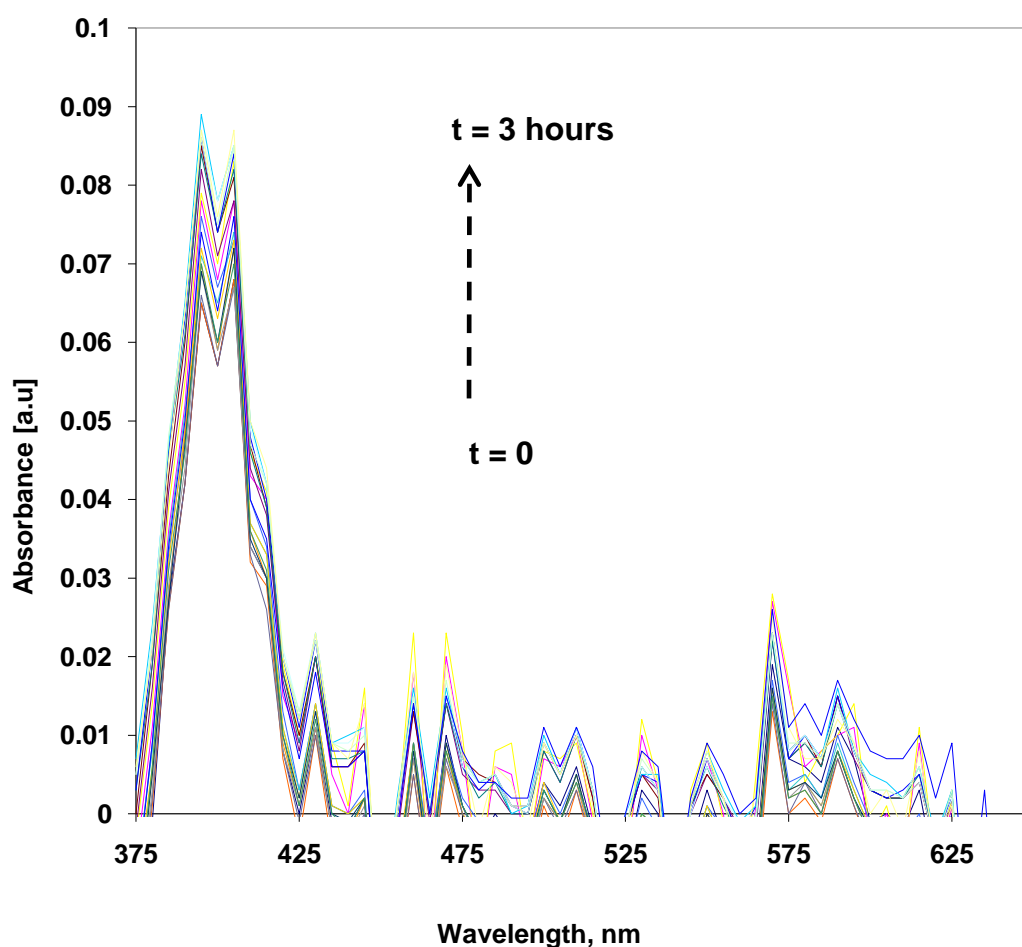
The first suspicion for the colour<sup>[104, 105]</sup> to intensify over 36 hours is likely because of Claisen-Schmidt condensation<sup>[106-108]</sup> which involves the reaction of aldehydes with the removal of water to form longer chain compounds in the presence of a base. In this case two cinnamaldehyde molecules react together in the presence of DMAE which is the base to form long chain organic compounds as seen in the reaction below.



Organic compounds especially those with a high degree of conjugation absorb visible light in the electromagnetic spectrum. Cinnamaldehyde which is conjugated absorbs UV and visible light and the absorbance increases in the presence of the base DMAE

because of the formation of a longer chain conjugated compound as seen in the scheme. The intensity therefore likely changes from an initial pale green to red as a result of longer chain conjugation and concentration.

An investigation to understand the change in colour was carried out using an in house high throughput system capable of taking UV measurements. Initially only cinnamaldehyde and DMAE were considered as seen in the plot below (Figure 7.19).



**Figure 7.19: Absorption Spectra of reaction of DMAE and cinnamaldehyde**

The green colour from mixing DMAE and cinnamaldehyde (CA) does not change as seen in the above absorption spectra measured over three hours. The change of absorbance is insignificant i.e. 0.03 a.u and the wavelength is constant overtime. The maximum wavelength of the maximum intensity,  $\lambda_{\text{max}}$  was measured at 400 nm

corresponding to the green colour observed. Adding DEZ to the above combination changes the situation as seen in the absorption spectra below (Figure 7.20). An increase in the absorbance and the wavelength is observed. From Figure 7.20,  $\lambda_{\text{max}}$  moves from 475 nm to 515 nm which corresponds to the change from green to red observed in the reaction over time. The deduction from this change in wavelength is the formation of new absorbing species. This may confirm the fact that a longer conjugated compound is formed with time which causes an increase in the intensity probably due to an increase in concentration over time.

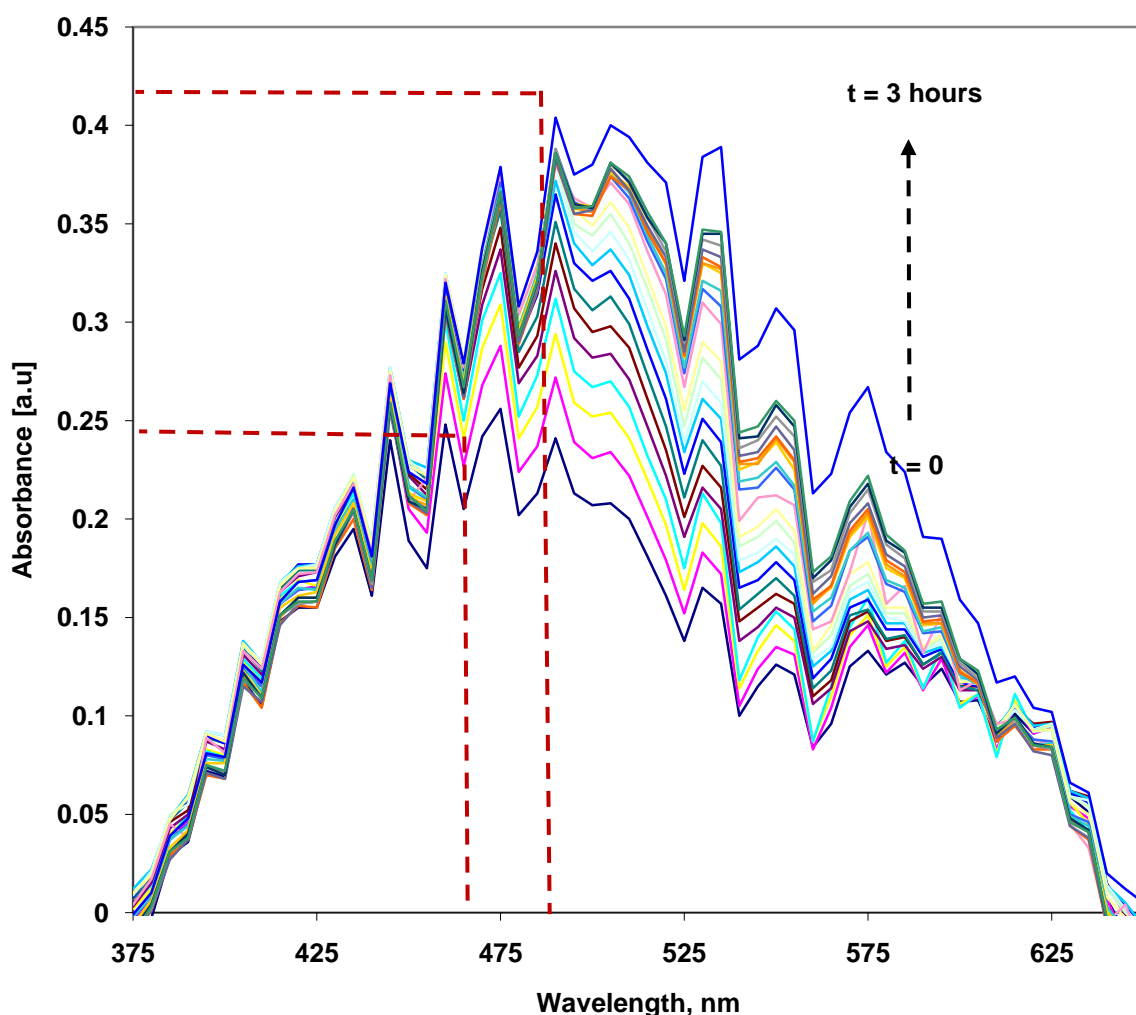
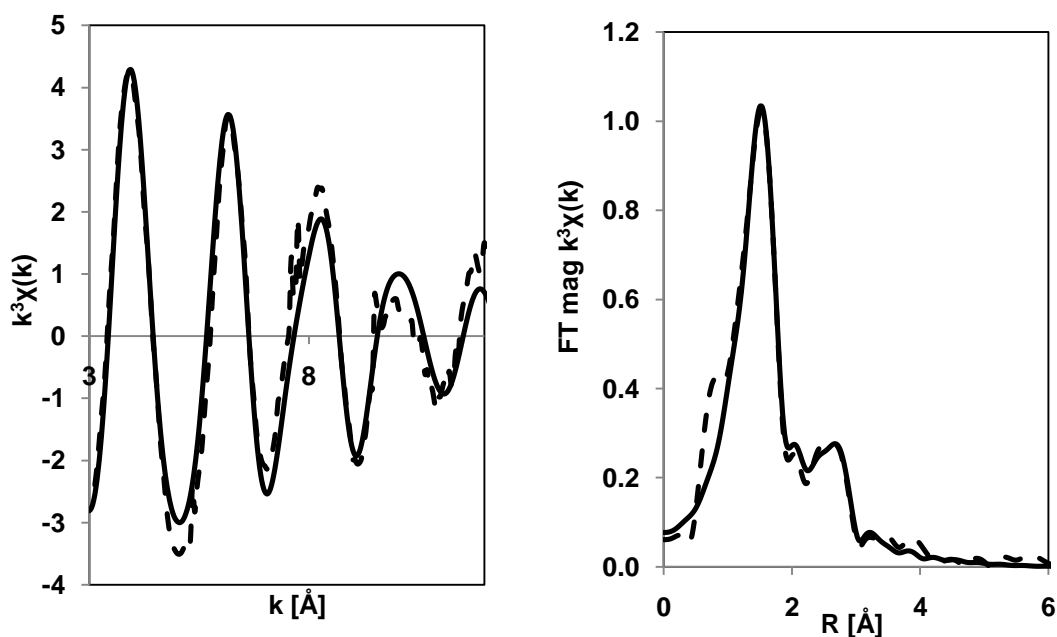


Figure 7.20: Absorption Spectra of reaction of DMAE, cinnamaldehyde and DEZ

From this examination there is no change in colour when DMAE and CA are mixed. It was also observed that there was no change in colour when DEZ was mixed with CA. These facts imply that the reaction may be zinc catalyzed. DMAE and CA initially combine to form a complex which is green in a condensation reaction. The presence of Zn tetrahedral sites possibly promotes the formation of monomer complex which eventually polymerizes because of the conjugated bonds in CA which open and link with other monomers.

An EXAFS analysis with  $k$  values considered between 3 and 12  $\text{\AA}^{-1}$  is presented here with an excellent R-factor of 0.8%. The Debye Waller factors calculated are between 0.005 and 0.009  $\text{\AA}^2$ .



**Figure 7.21:** Zinc K edge EXAFS spectra of 0.1 M DEZ:DMAE:CA (2:1:2) in toluene. Dotted lines are the experimental data and the solid lines are the best theoretical fit.

Sample	First shell (Zn-O/C/N)			Second shell (Zn-O/C/N) (Zn-Zn)							
	N	R(A)	$\sigma^2(\text{\AA}^2)$	N	R(A)	$\sigma^2(\text{\AA}^2)$	N	R(A)	$\sigma^2(\text{\AA}^2)$	E <sub>0</sub> (eV)	R (%)
<b>Et<sub>2</sub>Zn:DMAE:</b>											
<b>CA</b>	4.0	1.97	0.008	3.1	3.47	0.003	1	3.32	0.006	-0.10	0.8
<b>2:1:2</b>	±0.18	±0.003	±0.001	±0.69	±0.015	±0.004		±0.012	±0.002	±0.545	

**Table 7.9: Zinc K edge EXAFS spectra of DEZ, DMAE and CA.**

The model proposes four C/O neighbouring atoms to Zn in the 1<sup>st</sup> shell, with a Zn-C distance approximately 1.97 Å. This EXAFS calculation therefore suggests a dimer specie with two zinc centres separated by 3.42 Å. The dimer complex may be a polymer or conjugated complex based on the red colour seen in the UV measurements (Table 7.8).

### 7.3.5 Characterisation of dimer species formed in the Soai reaction

The results of this section were measured at the APS to confirm the nature of the products formed during the autocatalytic Soai process. EXAFS calculations reported in the previous sections so far disclosed the distinct possibility of a dimer alkoxide complex with specific bond distances, but other possibilities include admixtures of monomers, trimers, tetramers and higher oligomers.

First, the XANES spectra of four different aldehydes that were allowed to react with iPr<sub>2</sub>Zn were considered. The aldehydes examined include: benzaldehyde, pyrimidyl aldehydes and pyridyl aldehydes. It is worth mentioning that so far the best performing aldehyde discovered by Soai and co-workers is 2-(tert-butylethynyl)

pyrimidine-5-carbaldehyde which gives an *ee* of 99.5 % in a few reaction cycles. The influence of the group at 2-position of the pyrimidine ring has been reiterated although it has not yet been fully studied. The Zn K-edge XANES spectra of 0.5 M equimolar mixtures of  $i\text{Pr}_2\text{Zn}$  and the respective aldehydes were measured. A similar trend is observed with the reduction of the resonance peak in the XANES spectra of  $i\text{Pr}_2\text{Zn}$  with the addition of all tested aldehydes.

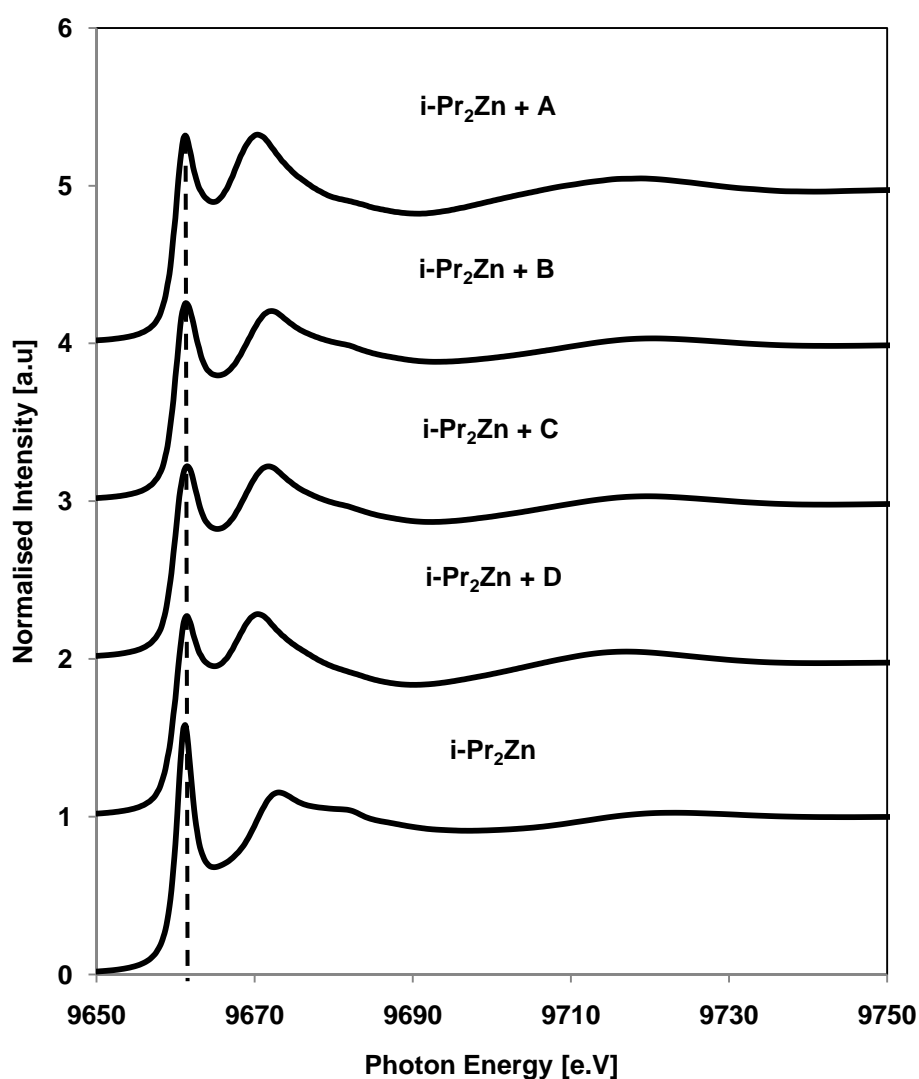
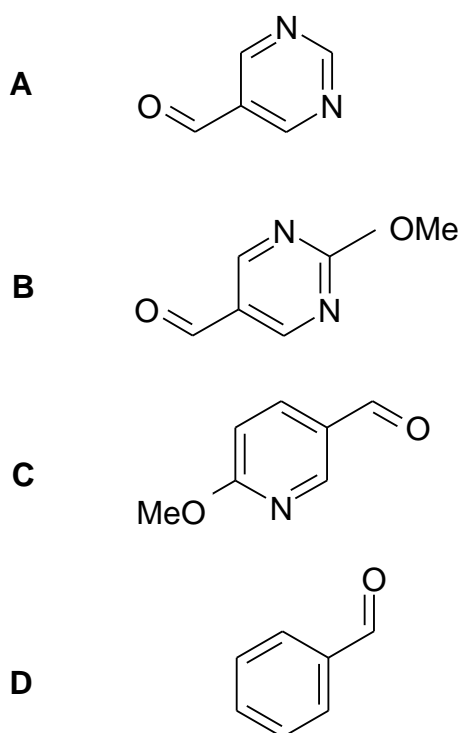


Figure 7.22: Zinc K-edge spectra of 0.05M  $i\text{Pr}_2\text{Zn}$  and different aldehydes (molar ratio 1:1 in toluene). Reaction products of  $i\text{-Pr}_2\text{Zn}$  with A: pyrimidyl- B: methoxypyrimidyl- C: methoxypyridyl- D: benzaldehyde (APS).

The XANES (Figure 7.22) shows that the reaction of  $i\text{Pr}_2\text{Zn}$  with different aldehydes, probably forms similar or the same zinc species because of their similarity. The addition of each aldehyde causes the drop of the resonance peak depicted by the dash line compared to  $i\text{Pr}_2\text{Zn}$  seen at the bottom of the XANES plot. The different structures of the aldehydes are shown below.

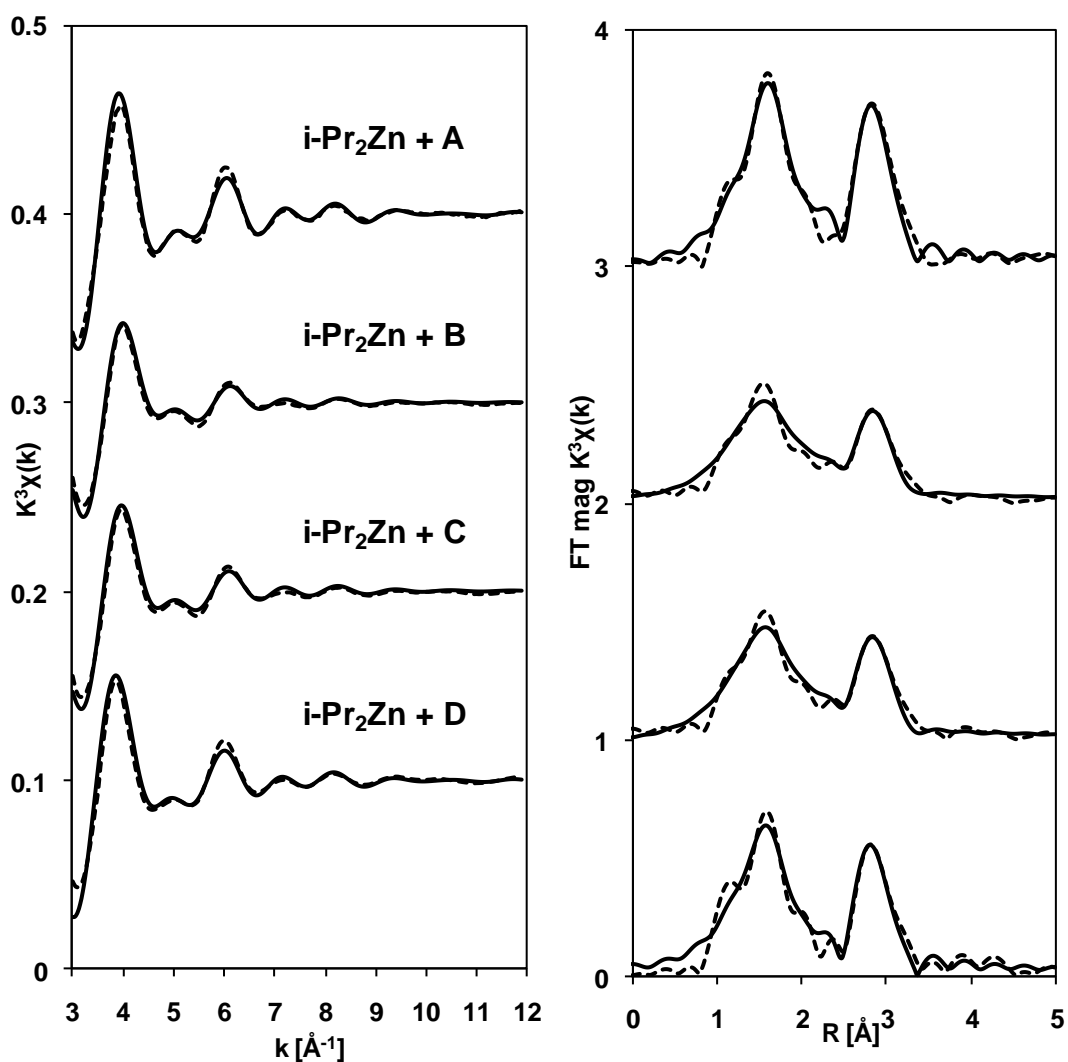


**Figure 7.23: Structure of the different aldehydes. A: pyrimidyl- B: methoxypyrimidyl- C: methoxypyridyl- D: benzaldehyde.**

The Zn K-edge XANES spectra of the product of 0.05 M  $i\text{-Pr}_2\text{Zn}$  with pyrimidyl aldehyde compared to the reference spectra of  $i\text{-Pr}_2\text{Zn}$  is distinct. The XANES spectra of A, B, C, and D reacting with  $i\text{-Pr}_2\text{Zn}$  have peak at 9660 eV caused by the strong 1s-4p white line transition mentioned in previous sections. The characteristics of the Zn absorption edge is different among the samples due to the different chemical environments. The four aldehydes studied show similar XANES spectra suggesting similar chemical environment around the zinc atom.

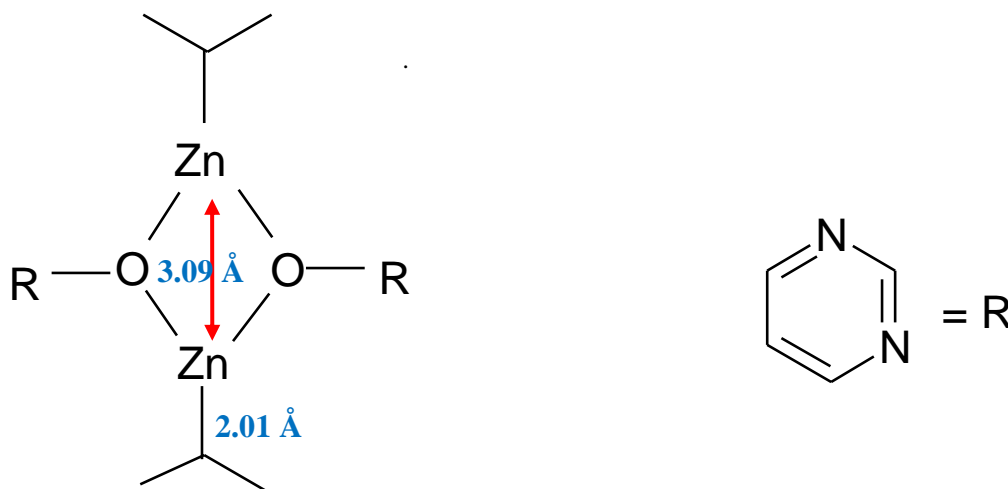


Both methoxy groups are para-substituted. Previous studies by Soai and co-workers prove that asymmetric amplification only occurs with pyrimidyl aldehydes. Para substitution with a methoxy group (electron withdrawing), should improve the yield and enantiomeric excess. The first asymmetric autocatalytic reactions were observed by Soai and co-workers when pyridyl aldehydes were allowed to form pyridyl alcohol. They were found not to be highly enantioselective like pyrimidylaldehydes. Benzaldehydes do not exhibit asymmetric autocatalysis. The XANES can only inform us on the  $\text{Zn}^{2+}$  oxidation state and also that the zinc coordination of the alkoxide complex formed from each aldehyde is likely the same. The EXAFS fit in  $k$  and  $R$ - space seen below shows that the fit of the experimental and theoretical data is reliable.



**Figure 7.24:** Zn K-edge EXAFS and Fourier Transform of 0.5 M  $i\text{Pr}_2\text{Zn}$  and different aldehydes (A, B, C and D) in 1:1 molar ratio in k and R space in toluene.

The R- and Debye-Waller factors calculated from the EXAFS analysis in each case were 3.6 - 6.7 % and  $0.001\text{-}0.010 \text{ \AA}^2$  respectively. The EXAFS calculation proposes a dimer model with a Zn-O-Zn-O square core for all aldehydes.



**Figure 7.25:** EXAFS model of alkoxide model from  $i\text{-Pr}_2\text{Zn}$  with pyrimidyl aldehyde in 1:1 molar ratio. Pyrimidylalkoxide dimer (APS).

From this analysis three low scattering atoms C/O are found in the 1<sup>st</sup> shell approximately 2 Å away from zinc. These results do not indicate that the alkoxide is predominantly a homo- or hetero- dimer even though one would suspect the latter to be energetically more stable. Details of the EXAFS parameters are shown in

Table 7.10. The table shows three models i.e. monomer, dimer and tetramer and justifies why the dimer model is chosen as seen in Figure 7.25. A monomer cannot be selected due the poorest fit reflected by a high R-factor of 18.6 %. The dimer is preferred over the tetramer model mainly because of the higher R-factor and Debye Waller factor in the tetramer.

Sample	First shell (Zn-O/C)			Second shell (Zn-O/C) (Zn-Zn)							
	N	R (Å)	$\sigma^2$ (Å <sup>2</sup> )	N	R (Å)	$\sigma^2$ (Å <sup>2</sup> )	N	R (Å)	$\sigma^2$ (Å <sup>2</sup> )	E <sub>0</sub> (eV)	R (%)
<i>i</i> -Pr <sub>2</sub> Zn	1.46 ±0.141	1.89 ±0.005	0.005 ±0.001	3.8 ±1.583	3.40 ±0.013	0.003 ±0.007				1.48 ±0.318	5.8
<i>i</i> -Pr <sub>2</sub> Zn + A											
monomer (0 Zn...Zn)	2.29 ±0.621	1.92 ±0.014	0.004 ±0.002	9.39 ±3.305	3.46 ±0.295	0.007 ±0.004				1.12 ±1.892	18.6
dimer (1 Zn...Zn)	2.44 ±0.295	2.01 ±0.008	0.006 ±0.001	5.44 ±1.376	3.52 ±0.015	0.004 ±0.002	1 <sup>s</sup>	3.09 ±0.008	0.003 ±0.001	5.32 ±1.061	3.9
tetramer (3Zn...Zn)	2.46 ±0.299	2.03 ±0.008	0.006 ±0.001	4.17 ±1.595	3.54 ±0.022	0.005 ±0.004	3 <sup>s</sup>	3.10 ±0.009	0.010 ±0.001	6.19 ±1.218	4.1

**Table 7.10: Zn K-edge EXAFS parameters of *i*Pr<sub>2</sub>Zn and aldehyde A. s: fixed**

The Zn-O/C and Zn-Zn bonds in the first shell are similar in all alkoxide models. In the second shell the Zn-C bond distances and coordination number varies from 3.46 in the monomer to 3.54 Å in the tetramer. The most important shell using in this study is the 1<sup>st</sup> shell which has a higher level of accuracy compared to higher shells. It is now evident from the XAS data analysed from the APS and ESRF that the transition state complex is a dimer.

## 7.4 Conclusion

The reaction of *i*Pr<sub>2</sub>Zn with benzaldehyde, pyrimidylaldehyde, pyridylaldehyde and cinnamaldehyde was examined through XANES and EXAFS measurements. The reaction of DEZ and pyrimidylaldehyde has also been closely investigated. The XANES indicates pyrimidylaldehydes form more strongly bound products with

iPr<sub>2</sub>Zn than benzaldehyde. Increasing the amount of benzaldehyde results in less drastic changes in the XANES compared to pyrimidylaldehydes where the changes are more obvious. The XANES of the reaction products held in solution and deposited as a precipitate are different and it appears that in solution the diversity of zinc species is greater than in the precipitate. Alkylation of the aldehyde occurs over time as seen from the XANES, which changes with time. This EXAFS study does not explain why iPr<sub>2</sub>Zn is preferred to DEZ which is similar in size. The XANES and EXAFS analysis of both dialkylzincs are similar and no solid justification has been made for the outstanding performance of iPr<sub>2</sub>Zn in chiral amplification. Considering that by using XAS both structural and electronic information can be acquired, one may conclude that the performance of iPr<sub>2</sub>Zn over DEZ may be based on its energetic stability. Strangely the Zn...Zn distances calculated (iPr<sub>2</sub>Zn: PA; 1:1) are not the same. The calculations based on experiments at ESRF (Table 7.3) compared to the APS (Table 7.10) propose an average Zn-Zn distance of 3.38 and 3.01 Å respectively. This difference is likely due to noise caused by the inhomogeneous solution. The most important information derived from both data is the existence of a dimer complex which is the main objective of this work. From an energetic perspective a thorough look at the bond distance in the dimer alkoxide complex formed by DEZ and iPr<sub>2</sub>Zn may be a breakthrough. Considering only the 1<sup>st</sup> shell, it is remarkable to know that the Zn-C/O is shorter in the DEZ- than the iPr<sub>2</sub>Zn-alkoxide complex. This applies to the 1:1 and 2:1 complexes formed in solution where the bond distances are shorter by 0.04 and 0.02 Å respectively. This may advocate that the transition state structure of the DEZ-complex has a higher Gibbs free energy than that formed by iPr<sub>2</sub>Zn. The enantioselectivity may be instigated by the difference in free energy between both transition structures. Klankermayer reports

that the apparent size of iPr is similar to Et and that the presence of longer H-H repulsion may be responsible.<sup>[52]</sup> Other studies justify the relationship between structure and dynamics.<sup>[110-112]</sup> In spite of this, recognition must be given to DEZ because it gives the best yield and enantiomeric excess in asymmetric reactions in which the product is not the catalyst. It is now understandable that this XAS study clearly defines the transition state structure to be a dimer with a Zn-O-Zn-O plane. This is a great achievement which also provides distinct bond distances and coordination numbers. The distance between the two centre Zn atoms are approximately 3 Å and Zn-O bond distances are about 2 Å. This model suggests that there is no significant bonding between the Zn atoms in the core.

A further investigation of the mixture of DEZ, DMAE and CA suggest a similar XANES of three components compositions which are different from DEZ/DMAE. This is probably because of the absence of the aldehyde in the latter which suggest that it is more reactive than DMAE. The colour change from pale green to red in the different DEZ:DMAE:CA molar ratios is because of the formation of long conjugated organic compounds formed in Claisen-Schmidt condensation which involves the reaction of aldehydes with the removal of water to form longer chain compounds in the presence of a base. An increase in the concentration of the conjugated organic compound forces the colour to intensify thus the colour change.

From other studies  $\text{Zn}^{2+}$  coordinates exists as tetra-, penta- and hexa- complexes. The Cambridge Structural Database also a library of  $\text{Zn}^{2+}$  coordination numbers of 4, 5 and 6. Other studies show that changing the concentration could influence the degree of complexation. Berquist<sup>[113]</sup> also proposes a zinc alkoxide complex and according to Lebedeva<sup>[114]</sup> tetrahedral zinc complexes are energetically more stable.

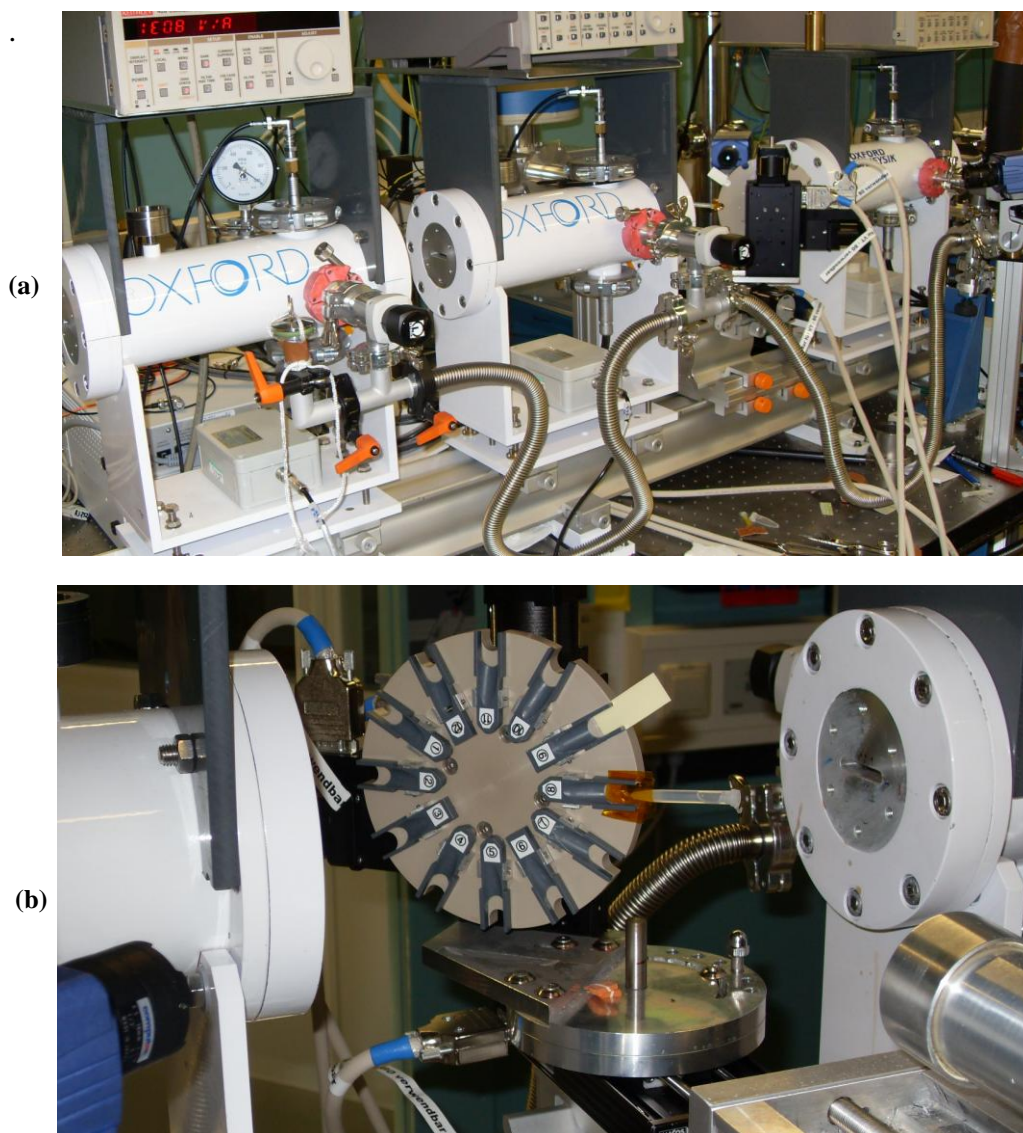
## 8. Additional work

An initial beamtime at ANKA, Karlsruhe in Germany was performed to determine the nature of diethylzinc/ligand complex. Four different dialkylzincs, two aldehydes, four ketones, two imines and two ligands were examined within 5 allocated days.

As will be reported below, for a combination of reasons, this beamtime did not provide conclusive results but indicators for further work summarised in the previous chapters. For example, the nature of DMAE and paracyclophane compounds with dialkylzinc compounds was later thoroughly examined at the ESRF in France (see chapter 6).

### 8.1 Experimental

X-ray absorption spectroscopy (XAS) experiments were carried out at ANKA with a beamline energy range from 2.4 to 25 K.eV. A Si(111) monochromator was used with a focused beam size of 8mm  $\times$  1mm. At room temperature Zn K-edge measurements were done in transmission (3 ionization chambers) and fluorescence mode (Ge-detector) as seen in Figure 8.1. The experimental set up described below was static i.e. microcentrifuge tube and the samples were prepared with the exclusion of oxygen by purging with argon and evacuating with a pump (Figure 8.2). Prior to this the solvents used in the experiments were thoroughly dried with sodium and then by distillation. The solvents were stored over molecular sieves. The microcentrifuge tube was fixed horizontally on a sample holder between two ionization chambers. The focused beam was then allowed to impinge on the sample and XAS data was collected by transmission and fluorescence.



**Figure 8.1: (a) Ionisation chambers(IC) (b) Sample holder between IC**

The influence of oxygen and other electronegative atoms is obvious to the Zn K-edge spectra as seen in preceding chapters. The Schlenk technique was conveniently used in defence against atmospheric intrusion in the absence of a glove box. The Schlenk line shown below was found to be less tedious and less cumbersome compared to glove boxes previously used.





**Figure 8.2: Air free sample preparing set up**

XAS data was then acquired after mounting the prepared sample contained in an Eppendorf tube (5cm × 0.6cm). Materials used include dialkylzincs, organic solvents, aldehydes, N/O ligands, imines and ketones.

<b>Dialkyl -zinc</b>	<b>Organic solvents</b>	<b>Aldehyde</b>	<b>Ketones</b>	<b>N/O ligands</b>
i-Pr <sub>2</sub> Zn	THF	t-Cinnamaldehyde	Benzylidene Acetone	Paracyclophane
Et <sub>2</sub> Zn	Toluene	Trans-2-Hexenal	Benzyliden acetophenone	N,N-dimethyl aminoethanol
Me <sub>2</sub> Zn	Hexane		Cyclohexenone	
n-Bu <sub>2</sub> Zn	Diethylether			

**Table 8.1: Chemicals used during experiment**

## 8.2 Results and discussion

XAS acquisition at the Zn K-edge was optimal at a concentration of 0.05 M. This concentration was used at the APS prior to this experiment. The results of this section include processing the XANES and EXAFS refinement. The applications used in data processing include Athena and Artemis (Ifeffit packages).

### 8.2.1 Alkylating agents

Alkyl donating groups investigated include dimethyl-, diethyl-, dibutyl- and diisopropylzinc. Diisopropylzinc has been the only successful alkyl donating group in the Soai autocatalytic reaction<sup>[19, 102]</sup> meanwhile diethylzinc gives the best yield and enantiomeric excess in asymmetric reactions in which the product is not the catalyst. Clearly noticeable from the Zn K-edge spectra is a similar resonance peak with all measured dialkylzincs (Figure 8.3).

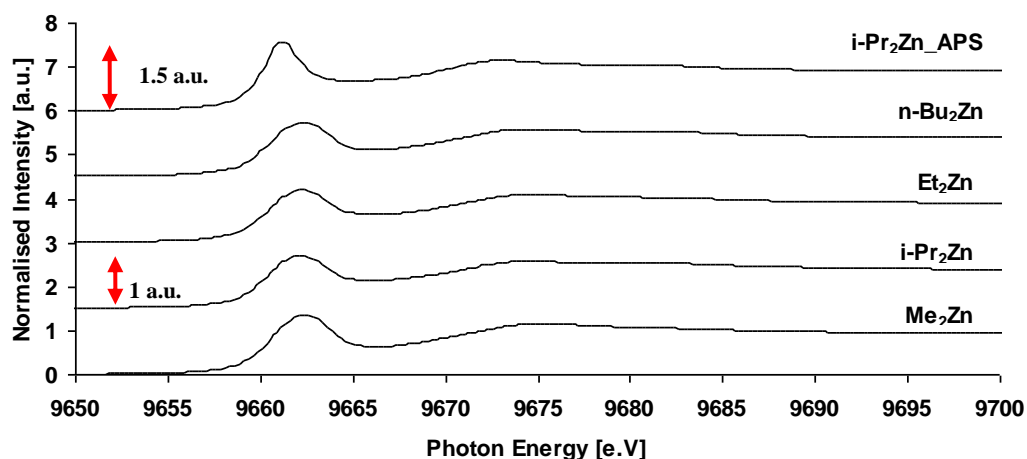


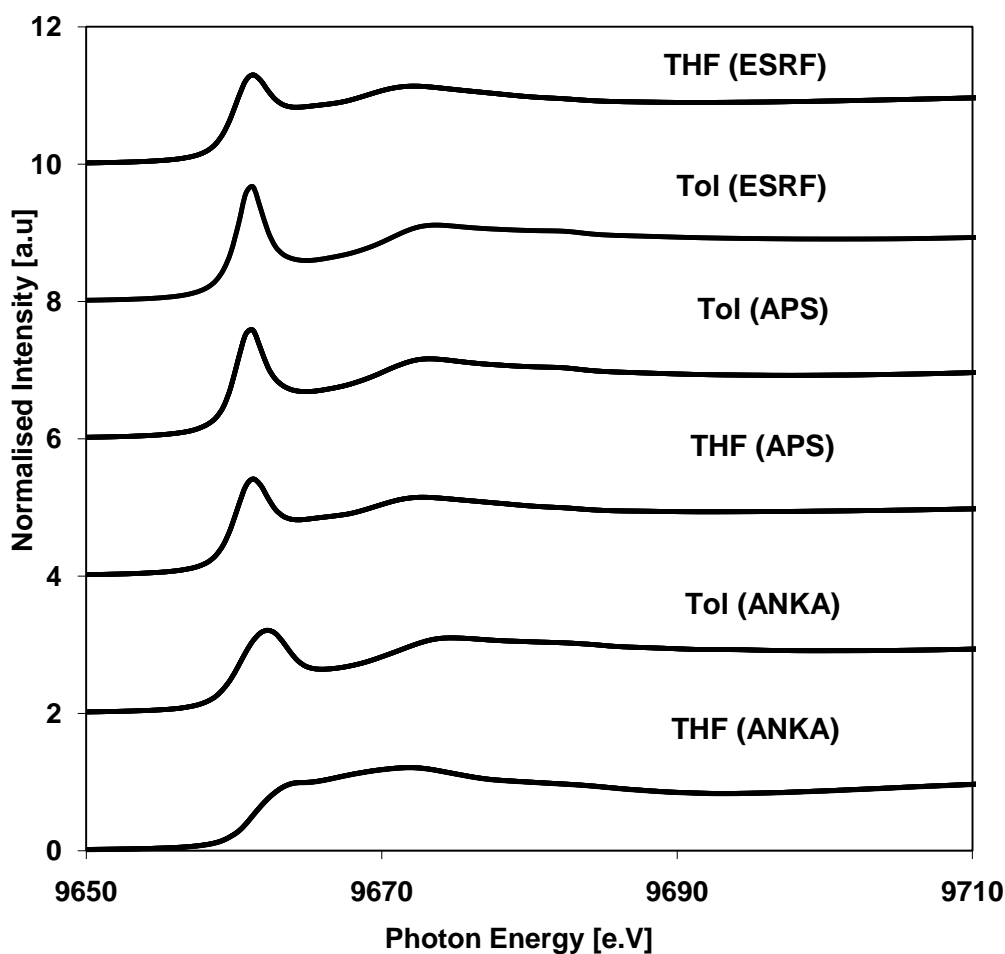
Figure 8.3: XANES of different alkylzincs in Toluene. APS-labeled; ANKA-unlabeled

The top most spectra shows that the normalized intensity of  $i\text{-Pr}_2\text{Zn}$  at APS, changes with the photon energy. The resonance peak is 1.5 a.u and is higher than the spectra

of  $i\text{-Pr}_2\text{Zn}$  at ANKA by 0.5 a.u. This discrepancy which raises questions was observed to be the same for other dialkylzinc measurements at ANKA. Nonetheless, attention must be drawn to the fact that the XANES results of the different dialkylzinc measured were consistent. From fundamental XAFS principles, exciting the Zn atom with an X-ray source causes a change in the electronic configuration; one or more electrons populate unoccupied bound or continuum states. A  $1s\text{-}4p$  transition results in the abrupt increase in the absorption coefficient at the Zn K absorption edge. This transition is responsible for the resonance peak which is overwhelmingly lower than anticipated.

### 8.2.2 Solvent effect

Solvent choice is crucial in asymmetric reactions. Polar solvents tend to give a poorer enantiomeric excess than non-polar. A detailed study is seen in Chapter 5, which shows how different solvents, both polar and non polar affect zinc geometry. At both APS and ANKA diethylzinc showed different tendencies in toluene and THF. It is important to mention that the chronological beam time order was APS, ANKA and then ESRF. The yard stick was therefore a massive resonance peak of dialkylzinc in toluene. This imperative confirmation was reached at the ESRF subsequent to the inquiry at ANKA as seen in the plot below. DEZ according to APS has a huge white line in toluene which reduces in THF. The first peak in THF, noticeable still exists even though it is trimmed down.



**Figure 8.4: Comparing XANES of diethylzinc in Toluene and THF. (APS/ANKA data)**

The results of DEZ at ANKA are not in harmony with APS. In toluene the first peak is shorter by 0.5 a.u and in THF no real resonance peak is present. The peak is reduced and then flattened. Based on the outcome at ANKA the observable change of the Zn K-edge resonance peak from a non polar to a polar solvent indicates a change in the electron density. The zinc environment evidently changes. The XANES spectra of the same sample should have the same signature, clearly this is not the case. Synchrotron instrumentation may affect factors such as the signal/noise ratio but not the shape of the XANES spectra. The suspicion at this juncture is whether the labeling represents the content of the individual chemicals used in the

experiment. There may be contamination of some kind on the chemicals or solvents either from the beam time at ANKA or APS.

### **8.2.3 Ethylation with paracyclophane based and dimethylaminoethanol ligands**

The use of N,O-ligands such as paracyclophane is important in enantioselectivity generally giving a high yield and enantiomeric excess. In this section the Zn K-edge of the interaction of DEZ and N,O-ligands such as paracyclophane and dimethylaminoethanol are studied.<sup>[88-91]</sup> The essence of this is to determine the zinc environment with different combinations. The main aim was to provide structural information of the nature of the complex formed between DEZ and the ligand. The illustration below shows the XANES of DEZ with DMAE/Paracyclophane in toluene. It also includes the interaction of the DEZ-ligand combination with aldehydes and ketones. From basic chemistry ketones are generally less reactive than aldehydes because of steric hindrance. Ketones generally have bulky groups compared to aldehydes which hinder attacking molecules from reacting. Obvious changes are seen from the XANES plot below implying a change in zinc geometry. It is also observed that changing the solvent from toluene to a polar solvent, in this case THF changes the XANES substantially as previously seen in this work. Only the behavior of ketones can be appreciated in the following example.

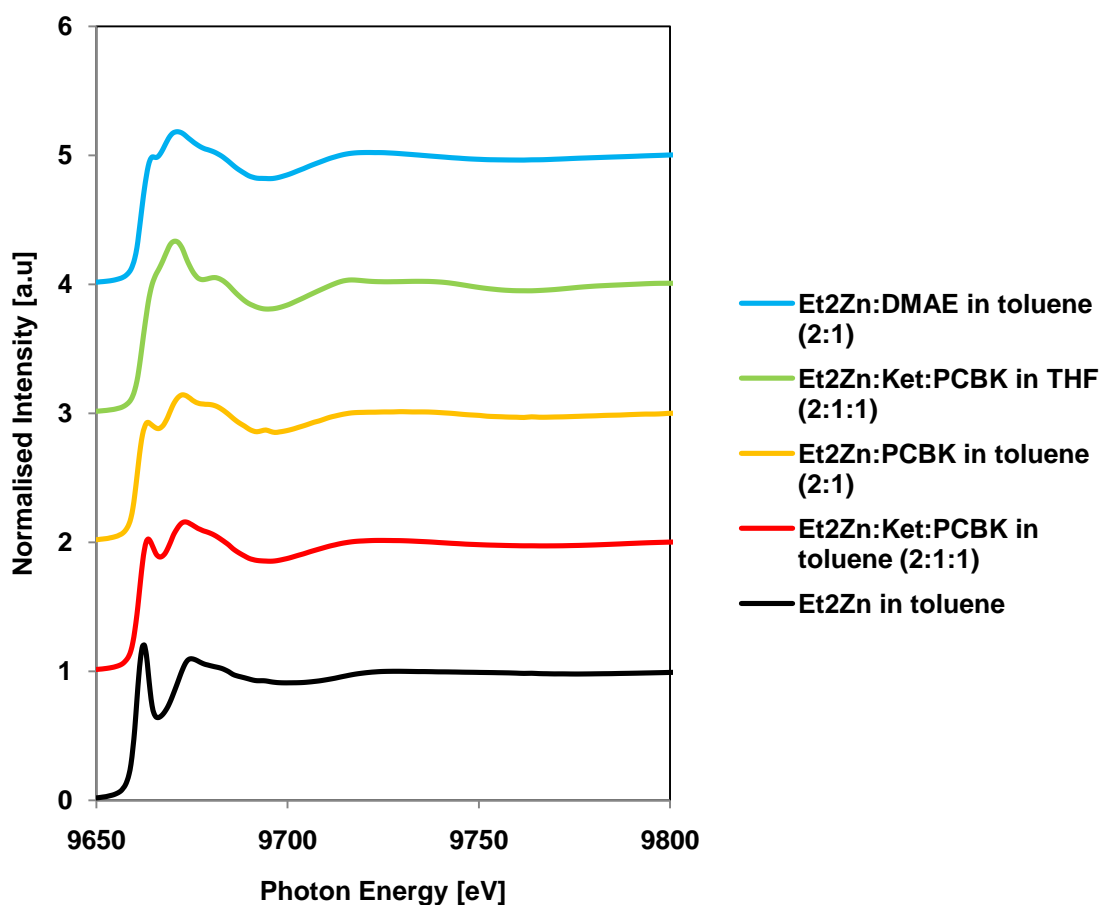


Figure 8.5: XANES spectra of 0.1 M diethylzinc with ligands and Ketone (ANKA data).

The resonance peak of  $\text{Et}_2\text{Zn}$  in toluene is strangely about the same height with the second peak seen at a photon energy of 9675 eV. This drops and flattens with the addition of DMAE and PCBK. The trough between both peaks in DEZ in toluene however increases with the addition of PCBK until both peaks of DEZ and PCBK vanish by merging. The above Zn K-edge spectra provides information that in a 2:1:1 molar ratio of DEZ:Ketone:PCBK there is a change in the XANES from DEZ alone. Comparing 2:1:1 and 2:1 it is noticeable that the XANES spectra are similar suggesting similar or slightly different Zinc species. The change in the XANES from DEZ to 2:1 is observed to be significant than from 2:1 to 2:1:1 which may mean that ketone molecules do not react effectively over the period of the XANES

measurement. It should be noted that the diethylzinc: ligand: ketone ratio of 2:1:1 was intentionally taken and is optimal in understanding the structure of the complex responsible for catalysis. The influence of THF can also be seen when compared with toluene during the ethylation of the ketone in the presence of the paracyclophane ligand. This might imply a likely binding of THF molecules to zinc as studied in earlier chapters.

#### **8.2.4 Diethylzinc addition to Imines**

Further XAS studies on the asymmetric diethylzinc addition to imines with paracyclophane were also carried out. The XANES below compares DEZ and the influence of paracyclophane, the ketone and the imine. The influence of the former has been discussed and focus will now be on the later which shows an interesting trend over time. From the following illustration the resonance peak of DEZ at 9662 eV clearly drops and moves to the right with the addition of the paracyclophane ligand. A shift in the 2<sup>nd</sup> peak of DEZ at 9675 eV to lower photon energy is also observed. The same trend is seen in the 2:1:1 molar ratio where a slightly deeper trough is seen compared to the 2:1.

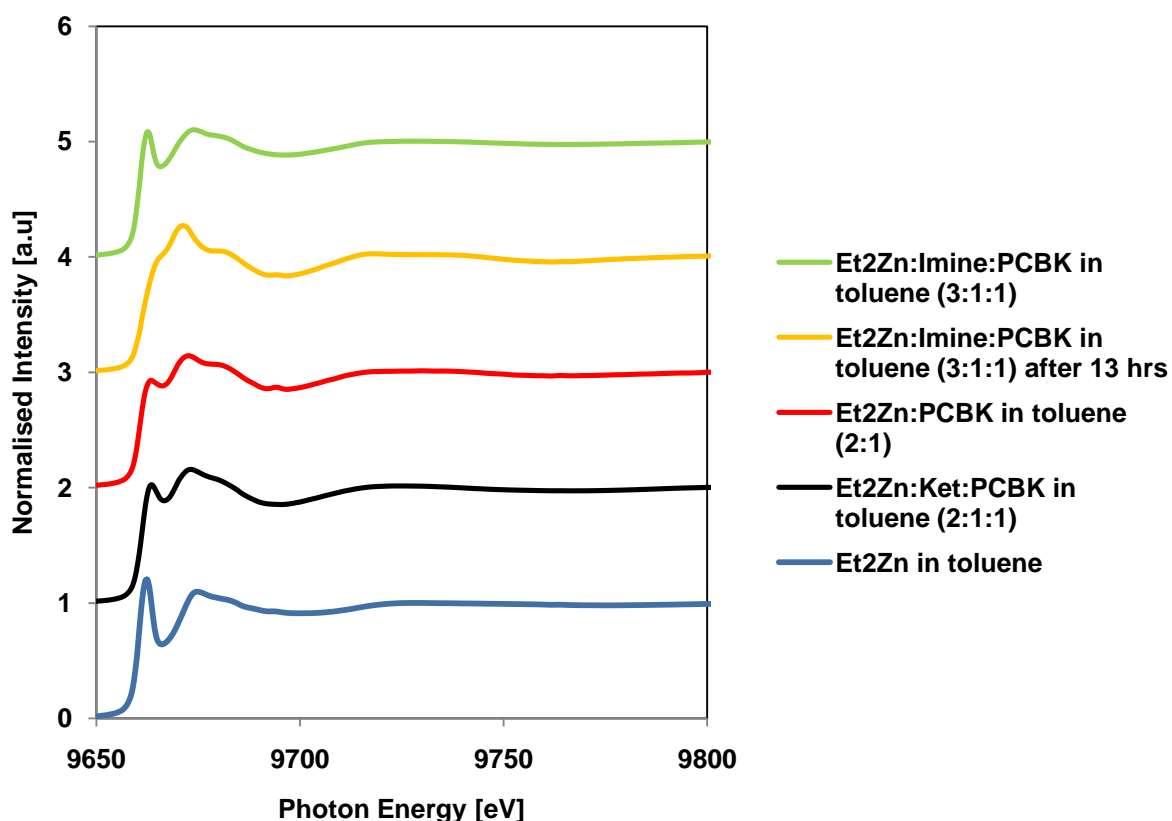


Figure 8.6: XANES spectra of diethylzinc addition to imines (ANKA data).

An obvious change in the zinc environment can be seen from the XANES of diethylzinc to the addition of imine. The molar ratio of ethylzinc: ligand: imine measured was 3:1:1. The above XANES in the 3:1:1 molar ratio after an hour has an excess of DEZ as seen in the 1<sup>st</sup> huge peak at 9662 eV and a 2<sup>nd</sup> broad peak is found at 9675 eV. The situation changes after 13 hours were a change in the XANES is palpable. The maximum peak moves to 9672 eV and the resonance peak previously seen at 9662 eV vanishes. This modification of the XANES can only be justified by the formation of new zinc species over a period of 13 hours. A defined structure of the zinc complex formed can only be calculated by an EXAFS analysis in which the coordination number and bond distances will be characterized. A potential reason for the radical transformation in the Zn K-edge XANES after 13 hours may be due to the



low solubility of Imine. The XANES after an hour therefore displays the interaction of DEZ and paracyclophane. In addition, it has been reported that deprotonation to give the intermediate is the rate-limiting step and the alkyl- addition itself is fast.<sup>[115, 116]</sup>

#### **8.2.5 EXAFS Refinement of ANKA data**

As seen in other sections of this report, the XANES compliments the EXAFS analysis. The EXAFS analysis is vital in understanding zinc geometry. The core of this study is to contribute to the reaction mechanism by describing the nature of the zinc complexes in solution. As afore mentioned the same experiments carried out at APS were not alike with that at ANKA. This obviously led to suspicion of the reliability of the results at ANKA which were arduous to fit. Fitting experimental and theoretical data was not possible with the results from ANKA in contrast to APS. Only unacceptably high R-factor values were achievable. The reasons for the intolerable fit may be a hint of contaminated samples. The EXAFS analysis was not possible and therefore not considered in this section.

### **8.3 Conclusion**

In this chapter the XANES spectra of dimethyl-, diethyl-, dibutyl and diisopropylzinc are comparable though the XANES Zn K edge spectra at ANKA and APS were poles apart with a conspicuously huge resonance peak seen in the XAS data collected from the APS and ESRF.

From the beamtime at ANKA, THF reduces the resonance probably as a result of the binding of THF molecules to the zinc atom thus changing the zinc environment. Its influence is not only seen in dialkylzincs alone but also on the ethylating of ketones

in the presence of paracyclophane. The XANES spectra of diethylzinc and DMAE is different from that with paracyclophane suggesting difference in the change in the electron density of the zinc atom. A surplus of DEZ over the ligand results in a modification of the XANES compared to the 1:1 mixture where the resonance peak is comparably lower and more to the right i.e. higher photon energy values.

Significant changes can be seen in the XANES during the ethylating of imines over time. This may be as a result of the reported low solubility of imines since deprotonation to give the intermediate occurs rapidly.

No full explanation is available for the discrepancy concerning the XAS data acquired at ANKA and APS. Both light sources have an international reputation and have S/N ratios within acceptable limits. The results from both lights sources should therefore be comparable. Assuming that the reason for the inconsistency is not from the light source, the only other source of error would be from the sample. This is broad ranging from the content of the chemicals to the manner in which the samples were prepared. It should be noted that the method of sample preparation at ANKA was different from APS where the solvents were not distilled but bought as anhydrous solvents from Sigma Aldrich. In addition at APS air exclusion during sample preparation was achieved by using a glove bag filled with nitrogen. At ANKA a Schlenk line was put in place and the samples were prepared under argon.

No structures were determined from the EXAFS analysis as only unacceptable results were obtained. The benefit of the study at ANKA was the XANES which was different depending on the experiment and also coherent. In addition, repeatable results were possible meaning that the results in terms of trend were believable. It must be noted that a follow up of this beam time was the previously seen

experiments at the ESRF, Grenoble, France which tally with the results from the APS.

## 9. Summary

This dissertation reports a series of studies that address the structural properties of key organometallic species involved in dialkylzinc-catalysed enantioselective reactions, with a particular view to the Soai chiral amplification process.

Structural causes of solvent effects were revealed through XANES of dialkylzinc species in various solvents. According to this study non polar solvents such as toluene are favourable in asymmetric amplification because they do not bind to the zinc centres, which remain monomeric in the absence of the prochiral reactants. EXAFS calculations propose dimers or tetramers in the presence of THF. The binding of THF to zinc may also be responsible for the slow turnover, thus producing low yield and little enantiomeric excess. The interaction with THF is, relative to that with toluene, so strong that even small vol% (~10%) of THF in a mixture with toluene cause a significant change to the XANES. Furthermore the influence of concentration is more dramatic on the XANES than the polar/non polar solvent ratio. The XANES at higher concentrations is different than at lower concentrations where the dialkylzinc molecules may be interacting with water molecules (impurities). In conjunction with Denisov's NMR study from 1975, which has previously not been considered in studies on the Soai reaction, the tendency of different solvents to form solvate species with dialkylzinc has been introduced as an important concept for solvent selection. The EXAFS models also show a distinction between  $iPr_2Zn$  and DEZ in THF. Dimethylzinc on the other hand has a slightly higher first resonance peak compared to the other two. This work also demonstrates that over a long period dialkylzinc decomposes to a product similar to zinc oxide when slow air ingress into

the reactor takes place. There is however also a possibility of the presence of zinc hydroxide due to residual H<sub>2</sub>O which was found to have a higher R-factor than ZnO. An examination of the complex formed between a chiral ligand and dialkylzinc suggests that dimers or tetramers are possibly formed. The XANES does not change drastically with changes in the stoichiometric amount of dialkylzinc and 2-butanol. The contrary is the case with DMAE where a considerable change is observed probably because it is less reactive. This is likely attributed to the presence of two electronegative atoms (O and N) in DMAE which cause a significant electronic effect. Overall the XAFS study confirms the possible presence of a monomer, dimer, tetramer or a mixture of species in a 1:1 molar ratio of DEZ:DMAE, suggesting that no specific specie can be identified, which are central for the Noyori mechanistic schemes for chiral amplification.

One of the most significant contributions of this study is the determination of the complex responsible for the catalysis in the Soai autocatalytic reaction. Despite the numerous scientific studies no proposal has been made that provides electronic and structural information of the proposed dimer structures. For the first time using X-ray absorption spectroscopy, we are able to confirm that the transition state structure is a dimer built around a centre with a Zn-Zn distance of approximately 3 Å, with no significant metal-metal bonding between zinc atoms. Such dimer complexes are formed with all aldehydes studied.

However, the reason for the outstanding performance of iPr<sub>2</sub>Zn over Et<sub>2</sub>Zn could not be substantiated. From the XANES it appears that pyrimidyl aldehydes bind more strongly than benzaldehyde, suggesting that a strongly bound complex is preferable for the Soai autocatalytic reaction. This is observed by varying the stoichiometric amount of dialkylzinc and aldehyde. Different structures have been established in

this evaluation by changing the stoichiometric ratios of dialkylzinc and aldehyde. The EXAFS investigation confirms the possibility of trigonal and tetrahedral zinc sites in the alkoxide complex depending on the stoichiometric amounts.

The XANES of a mixture of DEZ, DMAE and cinnamaldehyde is distinct from that of DEZ and DMAE. The colour change from pale green (DEZ and DMAE) to red (DEZ, DMAE and cinnamaldehyde) over time is likely because of zinc catalyzed polymerization. Evidence of this transformation is seen from UV and X-ray absorption analysis.

Results from several synchrotron radiation sources and using a number of experimental approaches to the organometallic synthesis at a synchrotron radiation source were considered in this study. The findings from Schlenk and glove box laboratory experimentation at ANKA were consistent but different from those obtained with small volume glove bag experiments at APS and ESRF. An expected huge resonance peak of dialkylzinc in toluene was not seen at ANKA suggesting that the small volume glove bag approach is more reliable than transferring home laboratory techniques to a synchrotron setting.

The accomplishment of the microcentrifuge tube reactor work overshadows that of the continuous flow reactor which is limited due to the formation of a precipitate on the inner reactor wall.

Mainly three coordination numbers of the different measurements of this study can be identified as seen in the table below. The table compares the coordination numbers predicted from the XANES analysis based on Kau *et al* (coordination number determined from the nature of the resonance peak) and the EXAFS calculations.

	1 <sup>st</sup> shell coordination number derived from XANES analysis (Based on Kau <sup>[79]</sup> <i>et al</i> )	Characteristic of white line of XANES at approximately 9661 eV (Based on Kau <sup>[79]</sup> <i>et al</i> )	1 <sup>st</sup> shell coordination number derived from EXAFS analysis
iPr <sub>2</sub> Zn in toluene	2	Strong	2
Et <sub>2</sub> Zn in toluene	2	Strong	2
iPr <sub>2</sub> Zn in THF	3	Reduced	3
Et <sub>2</sub> Zn in THF	3	Reduced	1
Et <sub>2</sub> Zn in toluene (ANKA)	3	Reduced	-
Et <sub>2</sub> Zn in THF (ANKA)	4	None	-
iPr <sub>2</sub> Zn in H <sub>2</sub> O	4	None	-
Et <sub>2</sub> Zn exposed to air	4	None	4
iPr <sub>2</sub> Zn and 2-butanol	3	Reduced	3-4
Et <sub>2</sub> Zn and DMAE	3	Reduced	3
iPr <sub>2</sub> Zn and aldehyde	3	Reduced	3-4
Et <sub>2</sub> Zn and aldehyde	3	Reduced	2-4
Et <sub>2</sub> Zn, DMAE and aldehyde	4	None	4

**Table 9.1: Comparing the 1<sup>st</sup> shell coordination number analysed by the XANES and EXAFS.**

From the comparison above it is obvious that the coordination number from XANES and EXAFS analysis correspond except in the case of diethylzinc in THF. Three main Zn coordinate systems have been identified in this study, which include 2-coordinate linear, 3-coordinate trigonal and 4-coordinate tetrahedral structures.

## 10. Future Work

Precise time resolved measurements are essential in order to fully understand the molecular mechanism of organozinc reactions. The continuous tubular flow reactor is excellent in design but poor in providing persuasive results. Highly rated results can only be achieved if the deposit which builds in the inner wall is eliminated. This system may benefit a reaction that does not produce a precipitate. Experiments using a stop flow reactor<sup>[117]</sup> would be essential towards the development of an efficient continuous flow reactor. In addition to X-ray absorption spectroscopy it would be beneficial to integrate different methods such as IR and XRD simultaneously with the XAS measurements.

From this study the rationale behind the excellence of  $i\text{Pr}_2\text{Zn}$  has not been fully endorsed. It is important to carry out further investigation on the difference between  $i\text{Pr}_2\text{Zn}$  and DEZ. It may also be beneficial to do XAFS studies on a mixture of dialkylzincs to understand their interaction with the intention of getting more information on their diversity.

Based on the different stoichiometric amounts of reactants it would make sense to correlate the XAFS studies with kinetic models that should explain the reaction mechanism. The kinetic together with XAFS data should build a mathematical model capable of explaining asymmetric autocatalysis.

The Mannich reaction<sup>[118-120]</sup> is another example of an autocatalytic reaction. Studying this reaction using X-ray absorption spectroscopy would be of great interest and may provide information on the molecular mechanism.

More emphasis should be placed on *ab initio* calculations based on the structural models derived from this EXAFS study. The structures produced from X-ray



absorption analysis should be converted to XYZ coordinates in order to generate Feff files. Feff calculations should reveal a theoretical XANES which should be compared to the experimental. The agreement between theoretical and experimental data should provide evidence on the accuracy of the model.

Homogenous reactions in which the product is not the catalyst should be studied using the continuous flow and batch reactor. Catalysts such as copper<sup>[121, 122]</sup> have been reported in asymmetric synthesis. It would be attention-grabbing to understand the change of the catalysts with increasing residence time.

## 11. Peer reviewed work

“Reducibility of supported gold (III) precursors: influence of the metal oxide support and consequences for CO oxidation activity.” Laurent Delannoy, Norbert Weiher, Nikolaos Tsapatsaris, Angela M. Beesley, Luanga Nchari, Sven L. M. Schroeder and Catherine Louis: (Top. Catal.). (2007)

“Continuous Tubular Flow Reactor for XAFS Studies of Organometallic Reactions: Possibilities and Limitations for Studies of the Soai Reaction.” Nchari L.N, Hembury, G. A.; Beesley, A. M.; Meehan D.J.; Tsapatsaris N.; Schroeder S. L. M., (Journal of Physics, Conference proceeding). (2009)

## 12. References

- [1] T. Shibata, T. Hayase, J. Yamamoto, K. Soai, *Tetrahedron-Asymmetry* **1997**, 8, 1717.
- [2] R. Morrison, R. Boyd, *Organic Chemistry* **1992**, 6th Edition.
- [3] T. Graham Solomons, C. Fryhle, *Organic Chemistry* **2007**, 9th edition.
- [4] F. A. Carey, *Organic Chemistry* **1992**, 2nd Edition.
- [5] J. D. Carroll, *Chirality* **2009**, 21, 354.
- [6] W. Fuss, *Chirality* **2009**, 21, 299.
- [7] L. Rosaria, A. D'Urso, A. Mammana, R. Purrello, *Chirality* **2008**, 20, 411.
- [8] C. A. Challener, *Chiral intermediates*, Ashgate, Aldershot, **2001**.
- [9] A. N. Collins, G. N. Sheldrake, J. Crosby, *Chirality in industry : the commercial manufacture and applications of optically active compounds*, Wiley, Chichester ; New York, **1992**.
- [10] M. A. Fox, *Organic Chemistry* **2004**, 3rd Edition.
- [11] S. N. Kilnyi, R. A. Aitken, *Asymmetric synthesis*, Blackie Academic & Professional, London, **1992**.
- [12] V. Davankov, *Chirality* **2006**, 18, 459.
- [13] J. G. Smith, *Organic Chemistry* **2006**.
- [14] M. Breuer, K. Ditrich, T. Habicher, B. Hauer, M. Keßeler, R. Stürmer, T. Zelinski, *Angew. Chem., Int. Ed.* **2004**, 43, 788.
- [15] J. Clayden, N. Greeves, S. Warren, P. Wothers, *Organic Chemistry* **2001**.
- [16] F. C. Frank, *Biochimica Et Biophysica Acta* **1953**, 11, 459.
- [17] C. Girard, H. B. Kagan, *Angew. Chem., Int. Ed.* **1998**, 37, 2923.
- [18] M. Kitamura, S. Okada, S. Suga, R. Noyori, *J. Am. Chem. Soc.* **1989**, 111, 4028.
- [19] I. Sato, D. Omiya, K. Tsukiyama, Y. Ogi, K. Soai, *Tetrahedron-Asymmetry* **2001**, 12, 1965.
- [20] I. Sato, H. Urabe, S. Ishiguro, T. Shibata, K. Soai, *Angew. Chem., Int. Ed.* **2003**, 42, 315.
- [21] T. Shibata, S. Yonekubo, K. Soai, *Angew. Chem., Int. Ed.* **1999**, 38, 659.
- [22] K. Soai, T. Kawasaki, *Chirality* **2006**, 18, 469.
- [23] K. Soai, T. Kawasaki, *Amplification of Chirality* **2008**, 284, 1.
- [24] K. Soai, T. Shibata, H. Morioka, K. Choji, *Nature* **1995**, 378, 767.
- [25] K. Soai, T. Shibata, I. Sato, *Acc. Chem. Res.* **2000**, 33, 382.
- [26] K. Soai, T. Shibata, I. Sato, *Nippon Kagaku Kaishi* **2001**, 141.
- [27] K. Soai, T. Shibata, I. Sato, *Bull. Chem. Soc. Jpn.* **2004**, 77, 1063.
- [28] D. Indar, *MEng Dissertation University of Manchester* **2009**.
- [29] C. Puchot, O. Samuel, E. Dunach, S. Zhao, C. Agami, H. B. Kagan, *J. Am. Chem. Soc.* **1986**, 108, 2353.
- [30] M. Kitamura, S. Suga, H. Oka, R. Noyori, *J. Am. Chem. Soc.* **1998**, 120, 9800.
- [31] F. Lutz, T. Igarashi, T. Kinoshita, M. Asahina, K. Tsukiyama, T. Kawasaki, K. Soai, *J. Am. Chem. Soc.* **2008**, 130, 2956.
- [32] I. Sato, D. Omiya, H. Igarashi, K. Kato, Y. Ogi, K. Tsukiyama, K. Soai, *Tetrahedron-Asymmetry* **2003**, 14, 975.
- [33] T. Shibata, H. Morioka, T. Hayase, K. Choji, K. Soai, *J. Am. Chem. Soc.* **1996**, 118, 471.

- [34] I. D. Gridnev, J. M. Brown, *Proc. Natl. Acad. Sci. U. S. A.* **2004**, *101*, 5727.
- [35] S. P. Mathew, H. Iwamura, D. G. Blackmond, *Angew. Chem., Int. Ed.* **2004**, *43*, 3317.
- [36] K. Soai, T. Shibata, *J. Synth. Org. Chem. Jpn.* **1997**, *55*, 994.
- [37] S. Sugiyama, Y. Aoki, K. Ishii, *Tetrahedron-Asymmetry* **2006**, *17*, 2847.
- [38] M. H. Todd, *Chemical Society Reviews* **2002**, *31*, 211.
- [39] D. G. Blackmond, *J. Am. Chem. Soc.* **1997**, *119*, 12934.
- [40] F. G. Buono, D. G. Blackmond, *J. Am. Chem. Soc.* **2003**, *125*, 8978.
- [41] D. G. Blackmond, *Proc. Natl. Acad. Sci. U. S. A.* **2004**, *101*, 5732.
- [42] D. G. Blackmond, C. R. McMillan, S. Ramdeehul, A. Schorm, J. M. Brown, *J. Am. Chem. Soc.* **2001**, *123*, 10103.
- [43] D. G. Blackmond, *Acc. Chem. Res.* **2000**, *33*, 402.
- [44] D. G. Blackmond, *Tetrahedron-Asymmetry* **2006**, *17*, 584.
- [45] F. G. Buono, H. Iwamura, D. G. Blackmond, *Angew. Chem., Int. Ed.* **2004**, *43*, 2099.
- [46] D. G. Blackmond, *Adv. Synth. Catal.* **2002**, *344*, 156.
- [47] T. Buhse, *Tetrahedron-Asymmetry* **2003**, *14*, 1055.
- [48] J. R. Islas, D. Lavabre, J. M. Grevy, R. H. Lamonedá, H. R. Cabrera, J. C. Micheau, T. Buhse, *Proc. Natl. Acad. Sci. U. S. A.* **2005**, *102*, 13743.
- [49] I. D. Gridnev, J. M. Serafimov, H. Quiney, J. M. Brown, *Org. Biomol. Chem.* **2003**, *1*, 3811.
- [50] I. D. Gridnev, J. M. Serafimov, J. M. Brown, *Angew. Chem., Int. Ed.* **2004**, *43*, 4884.
- [51] J. M. Brown, I. Gridnev, J. Klankermayer, *Amplification of Chirality* **2008**, 284, 35.
- [52] J. Klankermayer, I. D. Gridnev, J. M. Brown, *Chem. Commun.* **2007**, 3151.
- [53] P. Coppens, J. Penner-Hahn, *Chem. Rev.* **2001**, *101*, 1567.
- [54] NSLS, *EXAFS Data Collection and Analysis Workshop* **2003**.
- [55] H. D. Kelly S.D, Ravel B, *Soil Science of America* **2008**, Part 5, 367.
- [56] D. C. Koningsberger, B. L. Mojet, G. E. van Dorssen, D. E. Ramaker, *Top. Catal.* **2000**, *10*, 143.
- [57] A. Filippini, A. Diccio, T. A. Tyson, C. R. Natoli, *Solid State Commun.* **1991**, *78*, 265.
- [58] B. Ravel, M. Newville, *J. Syn. Rad.* **2005**, *12*, 537.
- [59] G. Bunker, "XAFS class notes"; <http://sparky.csrri.iit.edu/xafsdocs/>. **1983**.
- [60] B. K. Teo, *EXAFS-Basic principles and Data Analysis* **1986**.
- [61] M. Newville, J. J. Kas, J. J. Rehr, *14th International Conference on X-Ray Absorption Fine Structure (Xafs14), Proceedings* **2009**, 190.
- [62] ATOMS, <http://leonardo.phys.washington.edu/~ravel/atoms/> **Manual**.
- [63] M. Brivio, W. Verboom, D. N. Reinhoudt, *Lab on a Chip* **2006**, *6*, 329.
- [64] P. Watts, *Abstracts of Papers of the Am. Chem. Soc.* **2005**, 229, 024.
- [65] P. Watts, S. J. Haswell, C. Wiles, *Abstracts of Papers of the Am. Chem. Soc.* **2005**, 230, 700.
- [66] C. Wiles, P. Watts, S. J. Haswell, *Abstracts of Papers of the Am. Chem. Soc.* **2005**, 230, 293.
- [67] P. D. I. Fletcher, S. J. Haswell, E. Pombo-Villar, B. H. Warrington, P. Watts, S. Y. F. Wong, X. L. Zhang, *Tetrahedron* **2002**, *58*, 4735.
- [68] J. Rolland, X. C. Cambeiro, C. Rodriguez-Escrich, M. A. Pericas, *Beilstein J. Org. Chem.* **2009**, 5.

- [69] NSLS, *EXAFS Data Collection and Analysis Workshop* **2001**.
- [70] D. R. Roberts, R. G. Ford, D. L. Sparks, *J. Colloid Interface Sci.* **2003**, 263, 364.
- [71] X. C. Liu, E. W. Shi, Z. Z. Chen, B. Y. Chen, W. Huang, L. X. Song, K. J. Zhou, M. Q. Cui, Z. Xie, B. He, S. Q. Wei, *J. Alloys Compd.s* **2008**, 463, 435.
- [72] L. N. Nchari, G. A. Hembury, A. M. Beesley, D. J. Meehan, N. Tsapatsaris, M. Hudson, M. Thomason, S. L. M. Schroeder, *14th International Conference on X-Ray Absorption Fine Structure (Xafs14), Proceedings* **2009**, 190.
- [73] D. J. Meehan, *PhD Thesis, University of Manchester* **2009**.
- [74] V. M. Denisov, Y. P. Kuznetsov, *Bulletin of the Academy of Sciences of the USSR Division of Chemical Science* **1975**, 24, 2595.
- [75] G. Mahmoud, *MSc Dissertation, University of Manchester* **2010**.
- [76] A. Haaland, S. Samdal, R. Seip, *J. Org. Chem.* **1978**, 153, 187.
- [77] J. Weston, *Organometallics* **2001**, 20, 713.
- [78] A. Haaland, J. C. Green, G. S. McGrady, A. J. Downs, E. Gullo, M. J. Lyall, J. Timberlake, A. V. Tutukin, H. V. Volden, K. A. Ostby, *Dalton Trans.* **2003**, 4356.
- [79] L. S. Kau, D. J. Spirasolomon, J. E. Pennerhahn, K. O. Hodgson, E. I. Solomon, *J. Am. Chem. Soc.* **1987**, 109, 6433.
- [80] J. L. Fulton, M. M. Hoffmann, J. G. Darab, *Chem. Phys. Lett.* **2000**, 330, 300.
- [81] J. L. Fulton, M. M. Hoffmann, J. G. Darab, B. J. Palmer, E. A. Stern, *J. Phys. Chem. A* **2000**, 104, 11651.
- [82] T. Jarusuwannapoom, W. Hongroijanawiwat, S. Jitjaicham, L. Wannatong, M. Nithitanakul, C. Pattamaprom, P. Koombhongse, R. Rangkupan, P. Supaphol, *Eur. Polym. J.* **2005**, 41, 409.
- [83] L. Wannatong, A. Sirivat, P. Supaphol, *Polym. Int.* **2004**, 53, 1851.
- [84] M. P. Bertrand, L. Feray, R. Nougier, P. Perfetti, *J. Org. Chem.* **1999**, 64, 9189.
- [85] T. Akindele, K. I. Yamada, K. Tomioka, *Acc. Chem. Res.* **2009**, 42, 345.
- [86] F. A. Houle, W. D. Hinsberg, *Annual Reports in Computational Chemistry* **2006**, 2,3.
- [87] B. Goldfuss, M. Steigelmann, *Journal of Molecular Modeling* **2000**, 6, 166.
- [88] F. Lauterwasser, J. Gall, S. Hofener, S. Brase, *Adv. Synth. Catal.* **2006**, 348, 2068.
- [89] S. Brase, S. Dahmen, S. Hofener, F. Lauterwasser, M. Kreis, R. E. Ziegert, *Synlett* **2004**, 2647.
- [90] S. Dahmen, S. Brase, *Tetrahedron-Asymmetry* **2001**, 12, 2845.
- [91] S. Dahmen, S. Brase, *Org. Lett.* **2001**, 3, 4119.
- [92] M. Kreis, M. Nieger, S. Brase, *J. Org. Chem.* **2006**, 691, 2171.
- [93] S. Tanj, A. Ohno, I. Sato, K. Soai, *Org. Lett.* **2001**, 3, 287.
- [94] W. J. E. Beek, R. A. J. Janssen, in *Hybrid Nanocomposites for Nanotechnology*, Springer US, **2009**, pp. 1.
- [95] A. Daprano, D. I. Donato, V. Agrigento, *J. Solution Chem.* **1981**, 10, 673.
- [96] J. J. Makosz, *Acta Phys. Pol. A* **1990**, 78, 907.
- [97] T. Thenappan, U. Sankar, *J. Mol. Liq.* **2006**, 126, 38.
- [98] A. Lennartson, A. Hedstrom, M. Hakansson, *Acta Crystallographica Section E-Structure Reports Online* **2007**, 63, M123.

- [99] P. O'Brien, M. B. Hursthouse, M. Motevalli, J. R. Walsh, A. C. Jones, *J. Org. Chem.* **1993**, 449, 1.
- [100] D. G. Blackmond, M. Klussmann, *Aiche Journal* **2007**, 53, 2.
- [101] R. Plasson, H. Bersini, A. Cornmeyras, *Proc. Natl. Acad. Sci. U. S. A.* **2004**, 101, 16733.
- [102] K. Soai, I. Sato, T. Shibata, *Chemical Record* **2001**, 1, 321.
- [103] P. D. Bailey, *Journal of the Chemical Society-Chem. Commun.* **1995**, 1797.
- [104] Y. Park, S. Kim, J. H. Lee, D. H. Jung, C. C. Wu, J. Park, *Organic Electronics* **2010**, 11, 864.
- [105] Y. Tanaka, T. Ishisaka, A. Inagaki, T. Koike, C. Lapinte, M. Akita, *Chemistry-a European Journal* **2010**, 16, 4762.
- [106] Y. Y. Wang, X. X. Gong, L. Y. Dai, *Chinese J. Org. Chem.* **2009**, 29, 1470.
- [107] A. Dhakshinamoorthy, M. Alvaro, H. Garcia, *Adv. Synth. Catal.*, 352, 711.
- [108] K. Mogilaiah, T. K. Swamy, A. V. Chandra, N. Srivani, K. Vidya, *Indian J. Chem., Sect. B: Org. Chem. Incl. Med. Chem.*, 49, 382.
- [109] C. E. Sabel, J. L. Shepherd, S. Siemann, *Anal. Biochem.* **2009**, 391, 74.
- [110] A. de Meijere, S. I. Kozhushkov, A. A. Fokin, I. Emme, S. Redlich, P. R. Schreiner, *Pure Appl. Chem.* **2003**, 75, 549.
- [111] R. V. Muralidhar, R. R. Chirumamilla, R. Marchant, V. N. Ramachandran, O. P. Ward, P. Nigam, *World Journal of Microbiology & Biotechnology* **2002**, 18, 81.
- [112] C. Orrenius, F. Haeffner, D. Rotticci, N. Ohrner, T. Norin, K. Hult, *Biocatal. Biotransform.* **1998**, 16, 1.
- [113] C. Bergquist, H. Storrie, L. Koutcher, B. M. Bridgewater, R. A. Friesner, G. Parkin, *J. Am. Chem. Soc.* **2000**, 122, 12651.
- [114] N. S. Lebedeva, N. A. Pavlycheva, E. V. Parfenyuk, A. I. Vyugin, *J. Chem. Thermodyn.* **2006**, 38, 165.
- [115] S. Dahmen, S. Brase, *J. Am. Chem. Soc.* **2002**, 124, 5940.
- [116] S. Hofener, F. Lauterwasser, S. Brase, *Adv. Synth. Catal.* **2004**, 346, 755.
- [117] J. A. Marafie, J. D. Moseley, *Org. Biomol. Chem.* **2010**, 8, 2219.
- [118] P. Galzerano, D. Agostino, G. Bencivenni, L. Sambri, G. Bartoli, P. Melchiorre, *Chemistry* **2010**, 16, 6069.
- [119] X. Wang, Y. Zhang, H. Tan, Y. Wang, P. Han, D. Z. Wang, *J. Org. Chem.* **2010**, 75, 2403.
- [120] J. Xia, R. H. Qiu, S. F. Yin, X. W. Zhang, S. L. Luo, C. T. Au, K. Xia, W. Y. Wong, *J. Org. Chem.* **2010**, 695, 1487.
- [121] M. L. McIntosh, C. M. Moore, T. B. Clark, *Org. Lett.* **2010**, 12, 1996.
- [122] T. Arai, A. Mishiro, N. Yokoyama, K. Suzuki, H. Sato, *J. Am. Chem. Soc.* **2010**, 132, 5338.